AAA Workshop Series Volume 7
Asociación Argentina de Astronomía

# Proceedings of the Second Argentinian-Brazilian Meeting on Gravitation, Relativistic Astrophysics and Cosmology

April 22 - 25, 2014
Buenos Aires, Argentina

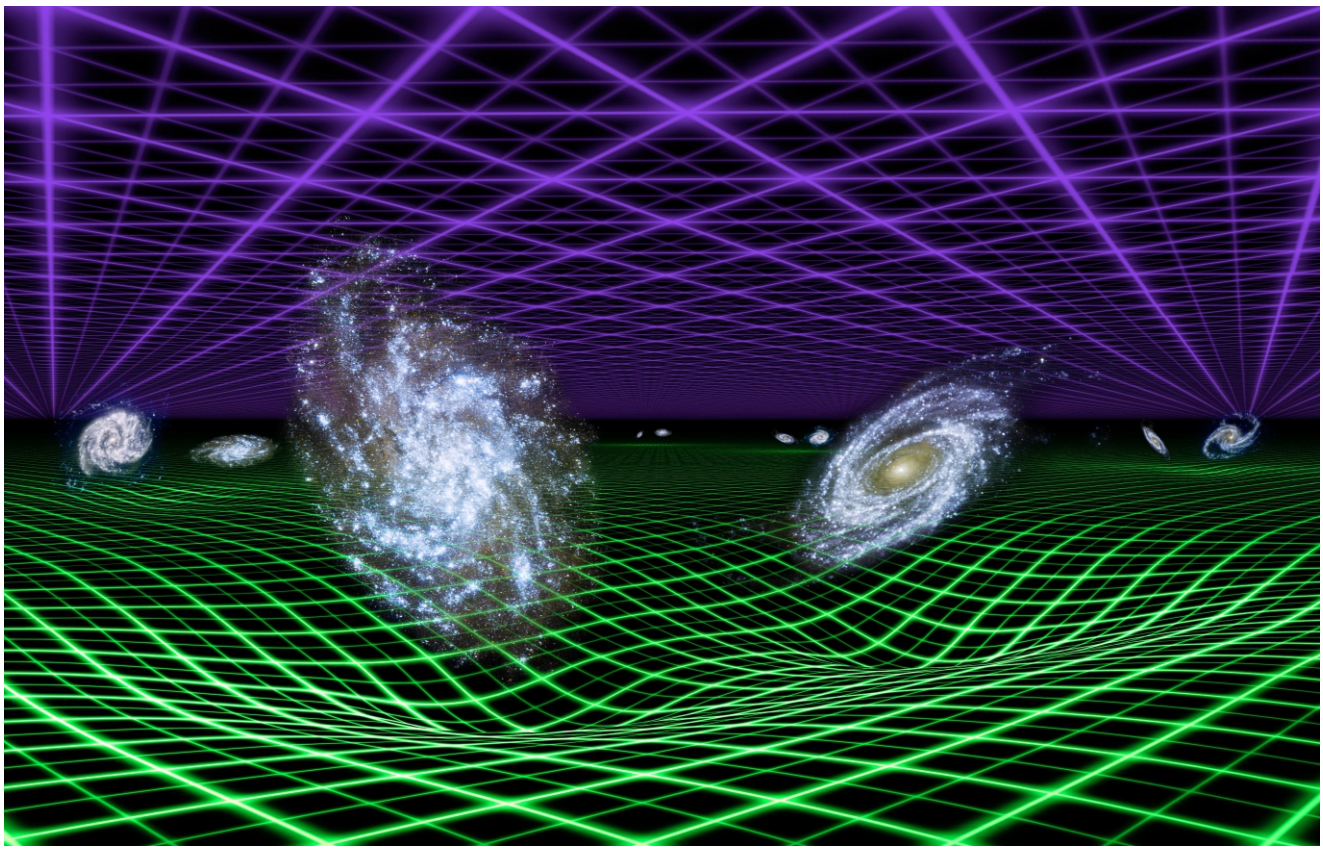

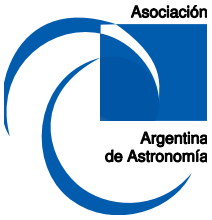


Asociación Argentina de Astronomía

# Proceedings of the 2nd Argentinian-Brazilian Meeting on Gravitation, Relativistic Astrophysics and Cosmology (GRACo II)

Gabriela S. Vila, Florencia L. Vieyro and Júlio C. Fabris, eds.

*Buenos Aires, Argentina, April 22-25, 2014*

**Credits:**
Cover image: Dark Energy and Gravity: Yin and Yang of the Universe (Artist's Concept). Courtesy NASA/JPL-Caltech.
Cover design: Gabriela S. Vila
LaTeX editor: Gabriela S. Vila
using LaTeX's 'confproc' package, version 0.8

Vila, Gabriela
Proceedings of the Second Argentinian-Brazilian Meeting on Gravitation, Relativistic Astrophysics and Cosmology / Gabriela Vila ; Florencia Laura Vieyro ; Julio Fabris. - 1a ed volumen combinado. - La Plata : Asociación Argentina de Astronomía, 2015.
250 p. ; 22 x 16 cm. - (Asociación Argentina de Astronomía Workshop Series / Bosch, Guillermo; 7)

ISBN 978-987-24948-2-7

1. Gravitación. 2. Cosmología. 3. Teoría de la Relatividad. I. Vieyro, Florencia Laura II. Fabris, Julio III. Título
CDD 520

# Asociación Argentina de Astronomía

## Fundada en 1958

Personería Jurídica (Legajo 21.459 - Matr. 1.421), Pcia. de Buenos Aires

## Comisión Directiva

(2014 – 2017)

| | |
|---|---|
| Presidente: | Guillermo Bosch |
| Vicepresidente: | Andrea Costa |
| Secretario: | Roberto Venero |
| Tesorera: | Mónica Cardaci |
| Vocal 1ro: | Javier Ahumada |
| Vocal 2do: | Jorge Combi |
| Vocal Sup. 1ro: | Sergio Dasso |
| Vocal Sup. 2do: | Federico González |

## Comisión Revisora de Cuentas

| | |
|---|---|
| Titulares: | Cristina Cappa |
| | Gabriela Castelletti |
| | Alejandro Córsico |

## Comité Nacional de Astronomía

| | |
|---|---|
| Secretaria: | Estela Reynoso |
| Miembros: | Andrea Torres |
| | Christian Giuppone |
| | Rene Rohrmann |
| | Mariano Domínguez |

# Asociación Argentina de Astronomía

**Proceedings of the 2nd Argentinian-Brazilian Meeting on Gravitation, Relativistic Astrophysics and Cosmology (GRACo II)**

*Buenos Aires, Argentina, April 22-25, 2014*

# Foreword

Research on Gravitation, Astrophysics, and Cosmology in Argentina and Brazil has reached a substantial degree of development. However, the interaction between groups of both countries working in these areas is still not strong enough to undertake long-term, successful joint research programs. The series of Argentinian-Brazilian Meetings on Gravitation, Astrophysics, and Cosmology was started with the goal of stimulating this kind of collaboration.

The second meeting of the series was successfully held in Buenos Aires, Argentina, in April 2014, with the attendance of more than a hundred researchers and students from both countries. It aimed at strengthening the links between both communities, and increasing the number of researchers and students involved in the discussions. The presentations offered an up-to-date picture of the research lines of both communities, and explored particularly the applications of the binational project Long Latin American Millimeter Array (LLAMA) in the fields of Astrophysics and Cosmology.

The present volume contains the set of invited and contributed papers presented at the meeting. It is our hope that it would stimulate the collaboration between researchers and groups in both countries.

Leonardo J. Pellizza
La Plata, Argentina, November 2015

# Contents

## Posters

# Invited Talks

*Gravitation, Relativistic Astrophysics and Cosmology*
*Second Argentinian-Brazilian Meeting, 2014*
*G. S. Vila, F. L. Vieyro and J. Fabris, eds.*

# Shape of black holes

María Eugenia Gabach Clement

*FaMAF-UNC, IFEG CONICET, Córdoba, Argentina*

**Abstract.** It is well known that celestial bodies tend to be spherical due to gravity and that rotation produces deviations from this sphericity. We discuss what is known and expected about the shape of black holes' horizons from their formation to their final, stationary state. We present some recent results showing that black hole rotation indeed manifests in the widening of their central regions, limits their global shapes and enforces their whole geometry to be close to the extreme Kerr horizon geometry at almost maximal rotation speed. The results depend only on the horizon area and angular momentum. In particular they are entirely independent of the surrounding geometry of the spacetime and of the presence of matter satisfying the strong energy condition. We also discuss the the relation of this result with the Hoop conjecture.

## 1. Introduction

This article is inspired by and based on a recent article [Gab2013] by MEGC and Martin Reiris. We refer the reader to [Gab2013] for further discussions and technical details.

The problem we wish to address is how to describe and characterize the shape of black holes. By this we mean the shape of their horizons, how we can measure it, what the restrictions on it are, if there are any, and how some physical parameters affect and determine this shape.

This problem has three important roots that we would like to refer to: the first one is the connection between the shape of a black hole and the shape of the matter configuration that collapsed to form it. If general black holes were close to spherical, what would that say about highly non- spherical collapse? One possibility would be that the deformations away from sphericity were in a sense, lost during the collapse that leads to the black hole. Another possibility would be that non-spherical configurations would not collapse into a black hole at all, resulting in naked singularities or other compact configurations instead. In this sense, the allowed shapes of black holes might shed light into this very complicated collapse scenarios. The second root of the problem is the relation with the uniqueness theorems for the Kerr black hole and the basic questions here are the following. Are generic black hole solutions really that different from the Kerr black holes? Do they share any important property? Do they look similar in shape? The final point we want to remark is the connection between Newton's predictions on the shape of (non-relativistic) objects, with those of general relativity on black holes. We know that for small velocities and weak fields, general relativity reduces to Newton's gravitation. There are many relativistic phenomena that get lost in the Newtonian limit and we would like to understand if some of them manifest though the shape of black holes but are absent in the shape of "Newtonian" objects.

We will discuss these issues with a bit more detail through this article and a good place to start is to take a look at objects that are more accessible to us than black holes, *i.e.* stars and planets.

To a first approximation, celestial objects are spherical. The main reason for this is gravity, one expects that when enough mass is gathered close together, the resultant gravity will pull equally in all directions. Then, if there were no other effects present, the resulting shape would be a perfect sphere. But clearly this is not the case, as there are other ingredients involved, like the mass of the object, its rotation, the material it is made of, the magnetic fields, the surrounding fields and bodies. And these all combine to produce the different shapes we see in the sky.

Of all these deformations away from sphericity, maybe the most common and easy to measure is a flattening due to rotation, resulting in configurations that become ever more oblate for increasingly rapid rotation. This effect, that we observe in the Sun, the Earth and most celestial bodies, can be described using Newtonian physics, with General Relativity playing no role.

The natural questions are then: can we expect the same behavior for black holes, the paradigm of relativistic objects? How do they look like?

As black holes can not be directly seen, the fine aspects of the shape of these objects can not be easily extracted from the images obtained by telescopes. Therefore, we resort to theoretical models of realistic black holes.

## 2. A model for realistic black holes

One of the most used models to represent real black holes is the solution of Einstein's equations found by Kerr [Ker1963]. It is stationary, vacuum, axisymmetric and asymptotically flat. It is characterized by two parameters, usually taken to be the total ADM mass $m$ and total angular momentum $J$. For different values of these two parameters, we get completely different spacetimes. When $|J| > m^2$ we find a naked singularity. But when $J \leq m^2$ it gives a stationary, rotating black hole. Within the Kerr black hole family, when the angular momentum attains its maximum allowed value, $|J| = m^2$, the resulting black hole is called extreme Kerr black hole. The opposite case, that is, when the angular momentum is zero, leads to a static solution, the Schwarzschild black hole.

All through this article, we will refer to the Kerr black hole, with $|J| \leq m^2$, no naked singularities will be considered.

The location and properties of Kerr horizon can be easily read out from the explicit form of the metric (see, for instance, [Wal1984]). One can check that none of the rotating Kerr-horizons are exactly metrical spheroids.

Moreover, the Kerr black holes satisfy

$$8\pi|J| \leq A \tag{1}$$

where $A$ is the horizon area. This inequality is relevant for the horizon description as it involves only quasi-local quantities that can be defined on the black hole horizon. Note that the equality in (1) corresponds to the extreme Kerr black hole, with $|J| = m^2 = A/(8\pi)$. Therefore, for fixed area, the extreme Kerr black hole is the one that spins the fastest (within the family).

The problem of measuring the shape of Kerr's horizon and the deformations away from sphericity can be approached by computing the flattening coefficient due to rotation.

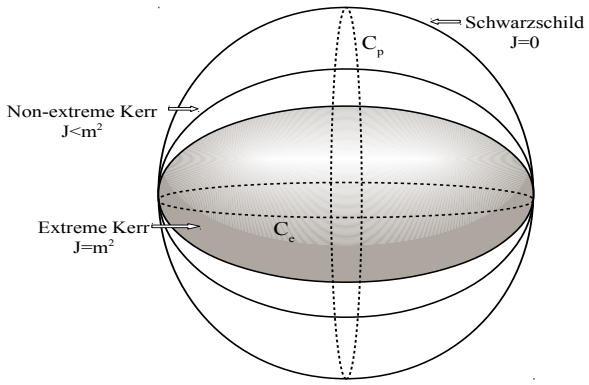


Figure 1. Schematic representation of Kerr black hole horizons for equal values of mass and different values of the angular momentum. Also displayed are the quantities $C_p$ and $C_e$ for the Schwarzschild case. As the angular momentum increases from zero (Schwarzschild black hole) to the maximum value $|J| = m^2$ (extreme Kerr black hole) the horizon becomes ever more oblate.

It is defined as

$$f := 1 - \frac{C_p}{C_e} \tag{2}$$

where $C_p$, and $C_e$ are respectively the lengths of the polar circle, that measures twice the distance between the poles, and the equatorial circle, which is the greatest circle normal to the symmetry axis, see Figure 1.

For the Kerr family we find, by explicit computation, that $0 \leq f \leq 0.36$, and it increases as the angular momentum increases (or the area decreases), which is in agreement with what is observed in stars and planets. The fastest the rotation, or the smaller the object, the strongest the flattening. When there is no rotation at all (Schwarzschild black hole), the horizon is spherically symmetric, with zero flattening. Moreover, to the maximum value of $J$ corresponds the maximum flattening value, $f = 0.36$, which is achieved by the extreme Kerr black hole. Keep in mind that a value of unity would mean a deformation to a disk.

To make contact with non-relativistic celestial bodies, note that the Sun has $f \sim 10^{-5}$ and the Achernar star, the most flattened star known so far, has $f = 0.17$ [Dom2003]. Quite remarkably, this last value coincides with the flattening of a Kerr black hole with $J \sim 0.88m^2$.

The above description shows that the Kerr family presents roughly a similar connection between rotation and flattening as most celestial bodies. But what about more general black holes? Especially black holes that are not vacuum, stationary or axisymmetric like Kerr. Is the Kerr solution really that relevant in this more general scenario?

In the next section we will see that Kerr black holes indeed turn out to be fundamental in the evolution of more complex black holes and play a key role there.

## 3. The final state

Consider a spinning, very massive object that is collapsing to form a black hole. Independently of the very complicated and dynamical process that takes place, the "black hole uniqueness theorem" say that once the dust has settled, and the system has calmed down, the final black hole is simple [Bar1973-Chr1994]. It can be completely described in terms of a few parameters: the total mass, angular momentum and the electric charge of the black hole. Once these parameters are chosen, the system is determined completely. This striking property of black holes has been popularized as "the no-hair theorem" by Wheeler. The name alludes to the fact that only very few parameters are needed to describe those solutions, apart from the values of those parameters, black holes have no distinguishing characteristics (no "hair").

How do black holes become so simple? The answer is gravitational waves. In general relativity, gravitational radiation escaping to infinity or to the interior of a black hole carry almost all the complicated features present during the dynamical evolution stage. The gravitational field radiates away everything that can be radiated away, and the final stationary black hole is Kerr black hole, or its Kerr-Newman generalization when non- vanishing electric charge is considered [Chr2012].

In summary, the uniqueness theorems give us detailed information about the final black hole and therefore, about the shape of its horizon, namely, the final shape will be that of a member of Kerr family. But what about the beginnings? Right before the collapse? And during the middle, dynamical stage? What do we know about black hole's shape then?

## 4. The initial state

One of the first results dealing with shapes and black holes is the Hoop conjecture, formulated by Thorne in 1972 [Tho1972]. It reads "*Horizons form when and only when a mass* $m$ *gets compacted onto a region whose circumference in every direction is less than or equal to* $4\pi m$". According to this conjecture, the circumference around the region must be bounded in every direction, and hence, a thin but long body of given mass would not necessarily evolve to form a horizon.

In principle, this conjecture talks about collapsing bodies, and not black holes. But if it were true, one would naively expect black holes not to be very elongated, but localized in every direction, like the matter configuration they collapsed from.

Unfortunately, the impreciseness of Thorne's statement had made this heuristic conjecture difficult to state, approach and prove. Since its formulation there has been a great amount of work making the idea more precise and attempting to establish its correctness or otherwise [Sch1983-Sen2008-Gib2009].

The main problems with the original formulation of the Hoop conjecture can be summarized as follows: in practice, it is impossible to determine the existence of an event horizon, a global concept accessible only to omniscient observers. A remedy has been the use of alternative, local, definitions of horizons, mainly apparent horizons or closed marginally trapped surfaces. Another major problem is the notion of mass

encircled by a hoop, which does not have a solution already in Newtonian physics. There is no notion of region encircled by a hoop. In fact, one can pass arbitrarily small hoops around any concentration of matter by letting appropriate portions of the hoop move relativistically. Finally, the uncertainty about the numeric constants to be used in the conjecture, several possibilities have appeared in the literature.

Yet, despite all difficulties, the Hoop Conjecture has been successful. It was settled in spherical symmetry, and discussed in some special non-spherical cases. Many numerical and/or analytical idealized examples have given it robust support. The problems in the original formulation and the subsequent studies have not only given insight as to what to expect at the initial stage in the black hole evolution, but also inspired and guided the technical aspects in the study of shape of black holes.

In 2013, Gabach Clement and Reiris study the shape of dynamical, axisymmetric, rotating black holes and use measures solely in terms of the area and angular momentum of the black hole horizon.

## 5. Dynamical stage

We discuss here some of what is known and the expectation about the properties of the shape of black hole horizons in the middle stage, namely, after the black hole formation and before the stationary, final phase.

There are two fundamental issues one must resolve in order to describe the shape of a black hole. First is how one will represent the black hole horizon, and second, how its shape will be measured. As to the first issue, apparent horizons or marginally outer trapped surfaces have been the preferred choice during the last years [And2008, And2009]. As to the measures of shape, one possibility is to find a background, well known configuration to compare with. Another possibility would be to construct coefficients, like the flattening mentioned in connection with the Kerr back hole that give an intrinsic notion of deformation. Finding a well defined and practical notion is an important and complicated point that, as we will show in Section 5.1., has a straightforward solution in axial symmetry.

Gibbons [Gib2009-Gib2012] considers apparent horizons as representations of black hole horizons and studies two measures of shape: the length of the shortest non trivial closed geodesic $\ell$ and the Birkhoff's invariant $\beta$. Remarkably he finds that if the surface admits an antipodal isometry and that Penrose inequality holds, then $\ell \leq 4\pi m$. Gibbons goes further and conjectures that $\ell \leq \beta \leq 4\pi m$ hold in the general case, without antipodal symmetry.

### 5.1. Axial symmetry

Gabach Clement and Reiris [Gab2013] study axially symmetric black holes and represent their horizons by stable marginally outermost trapped surfaces. These surfaces are such that the outgoing null expansion is zero. The stability property is crucial and plays a central role in many features of black-holes, in particular, the horizon's shape. In axial symmetry the study of shape of the horizon is somewhat simplified because the symmetry axis defines two meaningful hoops on the surface. One is given by the greatest meridian and the other, by the great circle or greatest axisymmetric orbit, see Figure 2. In analogy with the analysis for Kerr black hole, denote the lengths of these curves by $C_e$ and $C_p$ respectively

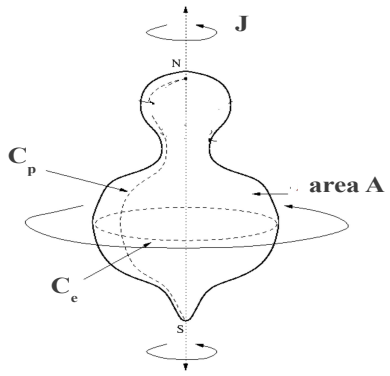


Figure 2. Schematic representation of an axisymmetric black hole horizons, together with the great circle of length $C_e$ and the polar circle of length $C_p$ (image partly taken from [Gab2013]).

In rotating, axially symmetric black holes, the extreme Kerr black hole plays a key role. This can be in part seen from the following inequality

$$8\pi|J| \leq A \tag{3}$$

valid for *all* dynamical, axially symmetric black holes [Hen2008, Ace2011, Dai2011, Jar2011, Gab2013a]. Note that (3) looks exactly the same as the inequality (1) we described for the Kerr family. Moreover, the extreme Kerr black hole saturates (3) among axially symmetric black holes. Therefore one can think of this black hole as the smallest one for a given angular momentum, or the most rapidly rotating one for given size. These observations suggest that extreme Kerr black hole may be a good candidate to compare the shape of a general black hole with.

The study of the shape of black holes in [Gab2013] is done through the comparison with extreme Kerr black hole and the estimation of the horizon's lengths $C_p, C_e$ and the flattening coefficient $f$. The main results of that article are discussed below.

*Bounds on $C_e, C_p$ and $f$.*

The most noticeable effect of rotation is a thickening of the bulk of the horizons. More precisely, the length $C_e$ of the great circle is subject to the lower bounds

$$\frac{16\pi|J|^2}{A} \leq \frac{8|J|}{\delta + \sqrt{\delta^2+4}} \leq \left(\frac{C_e}{2\pi}\right)^2, \tag{4}$$

where

$$\delta = 2\sqrt{\left(\frac{A}{8\pi|J|}\right)^2 - 1}. \tag{5}$$

These formulae say that rotation imposes a minimum (non-zero) value for the length of the greatest circle. For a given angular momentum, the horizon can not be too thin, but it gets thickened perpendicular to the rotation axis. Nevertheless they do not say whether the greatest circle lies in the "middle region" of the horizon or "near the poles", nor does it say anything about the size of other axisymmetric circles.

On the other hand, there is an upper bound on the length of the great circle, given by

$$\left(\frac{C_e}{2\pi}\right)^2 \leq 4|J|\frac{\delta+\sqrt{\delta^2+4}}{2} \leq \frac{A}{\pi} \tag{6}$$

showing that ultimately, the area controls the maximum size of the great circle. Note that for a perfect sphere, $\left(\frac{C_e}{2\pi}\right)^2 = A/(4\pi)$, and more importantly, for extreme Kerr black hole, $\left(\frac{C_e}{2\pi}\right)^2 = A/(2\pi)$, giving a factor of 2 with the right hand side of (6).

Putting (4) and (6) together, one sees that they coincide when $\delta = 0$ at $C_e/2\pi = 2\sqrt{|J|}$ which is the value for the extreme Kerr horizon. This is not a coincidence and will be discussed below.

The final relation that is presented, is connected with the flattening factor $f$ and reads

$$f := 1 - \frac{C_p}{C_e} \leq 1 - \frac{1}{\sqrt{2}\pi} \sim 0.77 \tag{7}$$

which shows that stable rotating horizons of a given area $A$ and angular momentum $J \neq 0$, cannot be arbitrarily oblate or "thick". Let us pause a moment to analyze this bound. Recall that the extreme Kerr black hole has $f_{eKerr} = 0.36$ which is roughly half right hand side of (7). As extreme Kerr black hole is the black hole that, given the horizon area, rotates the fastest (because it is the only axisymmetric solution that saturates the bound (3)), then one would expect that it is the most flattened black hole. Therefore, naively we expect $f \leq f_{eKerr}$ for all axisymmetric black holes. Nevertheless, we get twice that value in (7), which leaves room to improve.

*Rotational stabilization*. Rotation stabilizes the shape of stable horizons in such a way that for given A and J their entire shapes are controlled (not just $C_p$ or $C_e$).

$$\|g - g_{eKerr}\|_{C^0} \leq F(\delta) \tag{8}$$

for a certain finite function $F(\delta)$, where $g$ is the 2-metric on the horizon, $g_{eKerr}$ is the 2-metric on the extreme Kerr horizon with angular momentum $J$ and $\delta$ was defined in (5). In [Gab2013] it is shown that not only the metric (and therefore, the whole geometry of the horizon) is controlled in that way, but also the rotational potential are completely controlled by $A$ and $J \neq 0$. It also shows that stable holes with $A/8\pi|J|$ close to one must be close to the extreme Kerr horizon.

*Enforced shaping*

At very high rotations all the geometry of the horizon tends to that of the extreme Kerr horizon, regardless of the presence of any type of matter, as long as it satisfies the Strong Energy Condition:

*Hoop like inequality*.

The following result makes contact with Thorne's Hoop conjecture. Consider a stable, axisymmetric, outermost minimal surface[1] on a maximal axisymmetric and asymptotically flat initial data for Einstein equations. Matter satisfying the strong energy condition is also allowed. Then, assuming that Penrose inequality $16\pi m^2 \geq A$ [Mar2009] holds, it is deduced that the length of the great circle of the minimal surface satisfies

$$C_e \leq 8\pi m, \tag{9}$$

where $m$ is the ADM mass.

Note that again, there is a factor of 2 (as in (7)) on the right hand side with respect to the Thorne conjectured value of $4\pi m$.

Finally, regarding Gibbons' conjecture on the Birkhoff's invariant mentioned earlier, $\beta \leq 4\pi m$, using the above results, in [Gab2013] it is proved that for axisymmetric outermost minimal spheres one has $\beta \leq C_e$ and therefore from (9), $\beta \leq 8\pi m$. Whether $8\pi$ instead of Gibbon's $4\pi$ is the right coefficient for $m$ is not known. Nevertheless, the $8\pi$ factor in (9) is not sharp. If one expects the Penrose inequality to hold also for apparent horizons, then the argument before would work the same and one would obtain $C_e \leq 8\pi m$ as well.

## 6. Final comments

There are many open problems that still need attention.

Regarding the Hoop conjecture, there have been works on establishing a precise formulation and extensions to other theories, higher dimensions and special spacetimes [Sen2008-Yos2008-Gib2009-Khu2009-Yoo2010-Muj2012], nevertheless, a clear and general statement and proof is lacking.

With respect to the shape of black holes, one would like to take into account other ingredients like matter content and type and the influence of magnetic fields. Another issue of great relevance is the condition of axial symmetry imposed in [Gab2013]. In the absence of this symmetry, as we mentioned before, the measures of shape and the study of the horizon geometry become much more complicated, as is manifest in the work of Gibbons [Gib2012]. But even within axial symmetry, as it was mentioned, there is still room for improvement in the bounds found in [Gab2013].

Finally, it would be interesting to analyze what general relativity has to say about the shape of material objects, instead of black holes, in the spirit of [Sch1983].

**Acknowledgments.** It is a pleasure to thank the organizers of the *Gravitation, Relativistic Astrophysics and Cosmology Second Argentinian-Brazilian Meeting* that took place in Buenos Aires in April 2014 for their kind invitation and hospitality.

## References

[Ace2011] Acena, A., Dain, S. & Gabach Clement M. E. 2011, Class. Quant. Grav., 28, 105014

[1] See [Gab2013a] for a connection between stable axisymmetric minimal surfaces and stable axisymmetric trapped surfaces in the context of geometrical inequalities involving angular momentum and area.

[And2008] Andersson, L., Mars, M. & Simon, W. 2008, Adv. Theor. Math. Phys., 12

[And2009] Andersson, L. & Metzger J. 2009, Commun. Math. Phys., 290, 941-972

[Bar1973] Bardeen, J. M., Carter, B. & Hawking, S. W. 1973, Commun. Math. Phys. 31, 161-170

[Bra2001] Bray, H. L. 2001, J. Differential Geom., 59(2), 177-267

[Chr1994] Chrusciel, P. 1994, Contemp. Math. 170, 23-49

[Chr2012] Chrusciel, P., Lopes Costa, J. & Heusler, M. 2012, Living Rev. Relativity, 15, 7

[Dai2011] Dain, S. & Reiris, M. 2011, Phys. Rev. Lett., 107(5), 051101

[Dom2003] Domiciano de Souza, A., Kervella, P., Jankov, S. et al. 2003, A&A, 407, L47-L50

[Gab2013] Gabach Clment, M. E. & Reiris, M. 2013, Phys. Rev. D, 88, 044031

[Gab2013a] Gabach Clement, M. E., Jaramillo, J. L. & Reiris, M. 2013, Class. Quant. Grav., 30, 065017

[Gib2009] Gibbons, G. W. 2009, arXiv:0903.1580

[Gib2012] Gibbons, G. W. 2012, AIP Conf. Proc., 1460, 90-100

[Hen2008] Hennig, J., Ansorg, M. & Cederbaum, C. 2008, Class. Quant.Grav., 25, 162002

[Jar2011] Jaramillo, J. L., Reiris, M. & Dain, S. 2011, Phys. Rev. Lett. D, 84(12), 121503

[Ker1963] Kerr, R. P. 1963, Phys. Rev. Lett., 11, 237-238

[Khu2009] Khuri, M. A. 2009, Phys. Rev. D, 80, 124025

[Mar2009] Mars, M. 2009, Class. Quant. Grav., 26, 193001

[Muj2012] Mujtaba, A. H. & Pope, C. N. 2013, Phys. Lett. B, 719, 454-457

[Sen2008] Senovilla, J. M. M. 2008, Europhys. Lett., 81, 20004

[Sch1983] Schoen, R. & Yau, S. T. 1983, Commun. Math. Phys., 90, 575-579

[Tho1972] Thorne, K. S. 1972, "Nonspherical gravitational collapse: A short review", in Magic Without Magic: John Archibald Wheeler. A Collection of Essays in Honor of his Sixtieth Birthday, J. R. Klauder (ed.), W. H. Freeman, San Francisco

[Yoo2010] Yoo, C., Ishihara, H., Kimura, M. & Tanzawa, S. 2010, Phys. Rev. D, 81, 024020

[Yos2008] Yoshino, H. 2008, Phys. Rev. D, 77, 041501

[Wal1984] Wald, R. 1984, "General Relativity", The University of Chicago Press

*Gravitation, Relativistic Astrophysics and Cosmology*
*Second Argentinian-Brazilian Meeting, 2014*
*G. S. Vila, F. L. Vieyro and J. Fabris, eds.*

# New geometries for the characterization of dark matter phenomena

Osvaldo M. Moreschi, Ezequiel Boero, and Emanuel Gallo

*FaMAF, Universidad Nacional de Córdoba,*
*Instituto de Física Enrique Gaviola (IFEG), CONICET,*
*Ciudad Universitaria, (5000) Córdoba, Argentina.*

**Abstract.** We present some new geometries with spheroidal symmetry, with and without mass, that involve new kind of energy momentum tensors, and which are suitable for the description of dark matter phenomena.

## 1. Introduction

The standard characterization of dark matter phenomena is through models that assume the generally accepted cold dark matter model. However, when studying dark matter phenomena with different techniques one often finds non-trivial disagreement among the measurements.

Notably, when estimating the matter content in a region using gravitational weak lensing effects and dynamical studies, the different techniques do not coincide (Serra & Romero 2011) in the estimated value.

These problems might be related to the way in which one normally deals with inhomogeneities in cosmology. We will comment briefly on the inherent problems involved in the notion of averaging of tensors; that contribute to unexpected terms in the energy momentum tensor.

In a previous study of weak lensing we have noticed that a spacelike contribution of the energy-momentum tensor has been neglected (Gallo & Moreschi 2011) in previous works. This is the source of inspiration for the suggestion of a family of solutions with a nontrivial contribution to the geometry but with less requirement of mass content. In the past we have presented static spherically symmetric solutions (Gallo & Moreschi 2012); in this case we generalize to spheroidal symmetry,

We present some new geometries that involve new kind of energy momentum tensors which are suitable for the description of dark matter phenomena.

### 1.1. What could be missing from the standard picture?

*The problem with implicit averages:* In a simple cosmological model one can consider a Universe made out of small pieces of matter distributed in corresponding islands. If a photon would reach us from one of those bodies it would feel: a vanishing Ricci tensor and a non-vanishing Weyl tensor, namely:

$$R_{ab} = 0 \qquad , \qquad W_{abc}{}^{d} \neq 0.$$

While in a smooth averaged description, one would have the contrary, that is: a non-vanishing Ricci tensor and a vanishing Weyl tensor:

$$R_{ab} \neq 0 \qquad , \qquad W_{abc}{}^{d} = 0;$$

as is the case in the Robertson-Walker spacetimes.

One normally thinks that the Robertson-Walker spacetimes are a good model for the large scale structure of the Universe in which the small scales inhomogeneities are smooth out in some kind of averaging process. However, there is no notion of average that coming from a zero tensor would produce a non-zero average. As is the case with the Ricci tensor as mention above.

*The standard approach to weak lenses:* In standard textbooks, such as *Gravitational lenses* (Schneider, Ehlers & Falco 1992), one finds that the deflection angle is expressed by:

$$\hat{\alpha}(\vec{\xi}) = \frac{4G}{c^2}\int_{\mathbb{R}^2}\Sigma(\vec{\xi}')\frac{\vec{\xi}-\vec{\xi}'}{|\vec{\xi}-\vec{\xi}'|^2}d^2\xi', \tag{1}$$

where $\Sigma(\vec{\xi})$ is the mass density projected onto a plane perpendicular to the light path, $\vec{\xi}$ describes the position of the light ray in the lens plane.

Instead we have shown in Gallo & Moreschi (2011) the following expressions for the bending angle in terms of energy-momentum components and the mass content $M(r)$, of a spherically symmetric stationary spacetime

$$\boxed{\alpha(J) = J\int_{-d_l}^{d_{ls}}\left[\frac{3J^2}{r^2}\left(\frac{M(r)}{r^3}-\frac{4\pi}{3}\varrho(r)\right)+4\pi\left(\varrho(r)+P_r(r)\right)\right]dy}\,; \tag{2}$$

where $J = |\vec{\xi}|$ is the impact parameter and $r = \sqrt{J^2+y^2}$.

Let us observe the appearance of a term proportional to the radial component of the energy-momentum tensor; namely $P_r$.

This suggested us to consider a simple model with $P_r \neq 0$ and $M(r) = 0$ (zero mass), $\rho(r) = 0$ (zero mass density); which describes fairly well dark matter phenomena; id.est. rotation curves, weak lens, scape velocities; as we have shown in previous works (Gallo & Moreschi 2012).

Here we present a new exact solution of Einstein equations with prolate and oblate spheroidal symmetry and zero mass, which is the natural generalization of our previous construction with spherical symmetry. We also present a family of solutions with mass resembling well known profiles.

## 2. A spacetime with prolate spheroidal symmetry and zero mass

### 2.1. Using the hyperbolic coordinate

**The metric**

We will consider spacetimes with spheroidal symmetry of the form

$$\begin{aligned} ds^2 =& a(\xi,t)dt^2 - b(\xi,t)r_\mu^2(\sinh^2(\xi)+\sin^2(\theta))d\xi^2 \\ & - r_\mu^2\left((\sinh^2(\xi)+\sin^2(\theta))d\theta^2 \ + \sinh^2(\xi)\sin^2(\theta)d\phi^2\right); \end{aligned} \tag{3}$$

where $r_\mu$ characterizes the position of the focus, for the spheroidal geometry, as it will become more clear later when we relate the geometric coordinate $\xi$ with the radial coordinate $r$.

In particular we present the static solution given by

$$a = a_0(\xi + C)^2, \tag{4}$$

and

$$b = 1; \tag{5}$$

so that the whole geometry is characterized by the two constants $a_0$ and $C$.

**The Einstein tensor**

The corresponding components of the Einstein tensor which are different from zero are:

$$G_{\xi\xi} = -\frac{(2\cosh^2(\xi) - 2 + \sin^2(\theta))\cosh(\xi)\sinh(\xi)}{(\cosh^2(\xi) + \sin^2(\theta) - 1)(\cosh^2(\xi) - 1)(\xi + C)}, \tag{6}$$

$$G_{\xi\theta} = -\frac{\cos(\theta)\sin(\theta)}{(\cosh^2(\xi) - 1 + \sin^2(\theta))(\xi + C)}, \tag{7}$$

$$G_{\theta\theta} = -\frac{\cosh(\xi)\sin^2(\theta)\sinh(\xi)}{(\cosh^2(\xi) - 1 + \sin^2(\theta))(\cosh^2(\xi) - 1)(\xi + C)}. \tag{8}$$

## 2.2. Using the radial coordinate

**The metric**

From the relation

$$\xi = \operatorname{arcsinh}\left(\frac{r}{r_\mu}\right) = \ln\left(\frac{r}{r_\mu} + \sqrt{(\frac{r}{r_\mu})^2 + 1}\right); \tag{9}$$

or alternatively $r = r_\mu \sinh(\xi)$; one can express the metric as:

$$ds^2 = a(r)dt^2 - \left((r^2 + r_\mu^2\sin^2(\theta))\left(\frac{dr^2}{r^2 + r_\mu^2} + d\theta^2\right) + r^2\sin^2(\theta)d\phi^2\right), \tag{10}$$

and the timelike component of the metric is

$$a = a_0\left(\ln\left(\frac{r}{r_\mu} + \sqrt{(\frac{r}{r_\mu})^2 + 1}\right) + C\right)^2. \tag{11}$$

**The Einstein tensor**

The corresponding components of the Einstein tensor which are different from zero are:

$$G_{rr} = -\frac{(2r^2 + r_\mu^2\sin^2(\theta))}{\sqrt{r^2 + r_\mu^2}(\ln\left(\frac{\sqrt{r^2+r_\mu^2}+r}{r_\mu}\right) + C)(r_\mu^2\sin^2(\theta) + r^2)r}, \tag{12}$$

$$G_{r\theta} = -\frac{r_\mu^2\cos(\theta)\sin(\theta)}{\sqrt{r^2 + r_\mu^2}(\ln\left(\frac{\sqrt{r^2+r_\mu^2}+r}{r_\mu}\right) + C)(r_\mu^2\sin^2(\theta) + r^2)}, \tag{13}$$

$$G_{\theta\theta} = -\frac{(r^2 + r_\mu^2) r_\mu^2 \sin^2(\theta)}{\sqrt{r^2 + r_\mu^2}(\ln\left(\frac{\sqrt{r^2+r_\mu^2}+r}{r_\mu}\right) + C)(r_\mu^2 \sin^2(\theta) + r^2) r}. \tag{14}$$

**The Riemann tensor**

The components of the Riemann tensor which are different from zero are:

$$R_{trtr} = \frac{-(\ln\left(\frac{\sqrt{r^2+r_\mu^2}+r}{r_\mu}\right) + C) a_0 r}{\sqrt{r^2 + r_\mu^2}(\sin(\theta)^2 r_\mu^2 + r^2)}, \tag{15}$$

$$R_{trt\theta} = \frac{-(\ln\left(\frac{\sqrt{r^2+r_\mu^2}+r}{r_\mu}\right) + C) \cos(\theta) \sin(\theta) a_0 r_\mu^2}{\sqrt{r^2 + r_\mu^2}(\sin(\theta)^2 r_\mu^2 + r^2)}, \tag{16}$$

$$R_{t\theta t\theta} = \frac{(\ln\left(\frac{\sqrt{r^2+r_\mu^2}+r}{r_\mu}\right) + C)(r^2 + r_\mu^2) a_0 r}{\sqrt{r^2 + r_\mu^2}(\sin(\theta)^2 r_\mu^2 + r^2)}, \tag{17}$$

$$R_{t\phi t\phi} = \frac{(\ln\left(\frac{\sqrt{r^2+r_\mu^2}+r}{r_\mu}\right) + C)(r^2 + r_\mu^2) \sin(\theta)^2 a_0 r}{\sqrt{r^2 + r_\mu^2}(\sin(\theta)^2 r_\mu^2 + r^2)}. \tag{18}$$

## 3. A prolate spheroidal distribution as a gravitational lens

### 3.1. The adapted coordinate system

We have in mind a gravitational lens configuration in which the source is located far away close to the $y$ axis, the lens is near the origin of the frame, and the observer along negative values of the $y$ axis; as depicted in Figure 1. We use coordinates $(x, z)$ for the plane of the lens.

### 3.2. A rotated spheroid

The spheroidal distribution is assumed to be at an angle $\iota$ from the $z$ axis in the direction of $y$.

### 3.3. Gravitational lens geometry for prolate spheroidal distributions

In the calculation of gravitational lens, one needs to calculate the spinor components of the Ricci tensor $\Phi_{00}$ and the Weyl component $\Psi_0$, with respect to a null tetrad adapted to the null geodesic congruence of the photons.

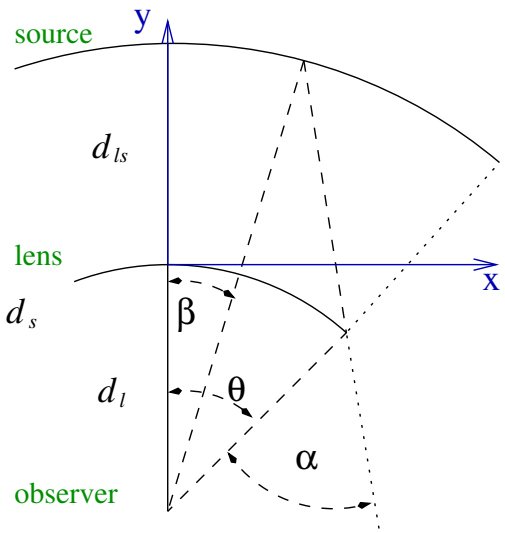


Figure 1. Standard notation for deviation angles and background coordinate system. $d_s$ denotes the distance to the source of the image; $d_l$ to the lens and $d_{ls}$ the lens-source distance.

We choose the null tetrad in the flat background as in our previous article; so that in the $(t, x, y, z)$ frame, one has

$$l^{\underline{a}} = (-1, 0, 1, 0), \tag{19}$$

$$m^{\underline{a}} = \frac{1}{\sqrt{2}}(0, i, 0, 1), \tag{20}$$

$$\bar{m}^{\underline{a}} = \frac{1}{\sqrt{2}}(0, -i, 0, 1), \tag{21}$$

$$n^{\underline{a}} = \frac{1}{2}(-1, 0, -1, 0). \tag{22}$$

Let us note that the Ricci component is:

$$\Phi_{00} = -\frac{1}{2}R_{ab}l^a l^b = -\frac{1}{2}G_{ab}l^a l^b. \tag{23}$$

The Weyl component is given by:

$$\Psi_0 = C_{abcd}l^a m^b l^c m^d. \tag{24}$$

We finally obtain the expression

$$\begin{aligned}\Phi_{00} =& -\frac{1}{2}\left(G_{rr}l^r l^r + 2G_{r\theta}l^r l^\theta + G_{\theta\theta}l^\theta l^\theta\right)\\ =&\frac{1}{2\sqrt{r^2+r_\mu^2}\left(\ln\left(\frac{\sqrt{r^2+r_\mu^2}+r}{r_\mu}\right)+C\right)\left(r_\mu^2\sin^2(\theta)+r^2\right)r}\\ &\Big(\left(2r^2+r_\mu^2\sin^2(\theta)\right)l^r l^r + 2\,r\,r_\mu^2\cos(\theta)\sin(\theta)l^r l^\theta +\\ &\left(r^2+r_\mu^2\right)r_\mu^2\sin^2(\theta)l^\theta l^\theta\Big);\end{aligned} \tag{25}$$

while the Weyl component is given by:

$$\begin{aligned}\Psi_0 =&\frac{1}{g_{tt}}R_{tbtd}\,m^b\,m^d\\ =&\frac{1}{g_{tt}}R_{trtr}(m^r)^2+\frac{2}{g_{tt}}R_{trt\theta}\,m^r\,m^\theta+\frac{1}{g_{tt}}R_{t\theta t\theta}(m^\theta)^2+\frac{1}{g_{tt}}R_{t\phi t\phi}(m^\phi)^2\\ =&\frac{1}{\left(\ln\left(\frac{\sqrt{r^2+r_\mu^2}+r}{r_\mu}\right)+C\right)\sqrt{r^2+r_\mu^2}\left(\sin(\theta)^2r_\mu^2+r^2\right)}\\ &\Big(-r(m^r)^2-2\cos(\theta)\sin(\theta)\,r_\mu^2\,m^r\,m^\theta+\\ &(r^2+r_\mu^2)r(m^\theta)^2+(r^2+r_\mu^2)r\sin(\theta)^2(m^\phi)^2\Big).\end{aligned} \tag{26}$$

### 3.4. The optical scalars

Let us recall from Gallo & Moreschi (2011) that the optical scalars, namely, the expansion $\kappa$ and the shear components $\gamma_1$ and $\gamma_2$, in the thin lens approximation, are given by:

$$\kappa = \frac{d_l d_{ls}}{d_s}\hat{\Phi}_{00}, \tag{27}$$

$$\gamma_1 + i\gamma_2 = \frac{d_l d_{ls}}{d_s}\hat{\Psi}_0, \tag{28}$$

where

$$\begin{aligned}\hat{\Phi}_{00} &= \int_0^{d_s}\Phi_{00}d\lambda,\\ \hat{\Psi}_0 &= \int_0^{d_s}\Psi_0 d\lambda,\end{aligned} \tag{29}$$

are the projected curvature scalars along the line of sight.

## 4. Numeric calculation of the optical scalars

### 4.1. The expansion

For the numerical calculation we have taken the following values: The parameter $C$ was taken as $-\ln(\mu)$, from Gallo & Moreschi (2012) which it was adjusted to the observations of weak lens in the Coma cluster. The radius $r_\mu$ was arbitrarily taken to have the value 3 Mpc. The rotation angle $\iota$ was chosen to be $\frac{\pi}{4}$. The lens distances were taken as: $d_l = 97.10$ Mpc, $d_s = 1068.03$ Mpc, $d_{ls} = 970.92$ Mpc; which are values from the Coma cluster used in our previous work. The integration was carried out using Chebyshev-Gauss techniques. The number of points evaluated was automatically adjusted to a chosen tolerance. The results are presented in the graphics of Figures 2, 3 and 4.

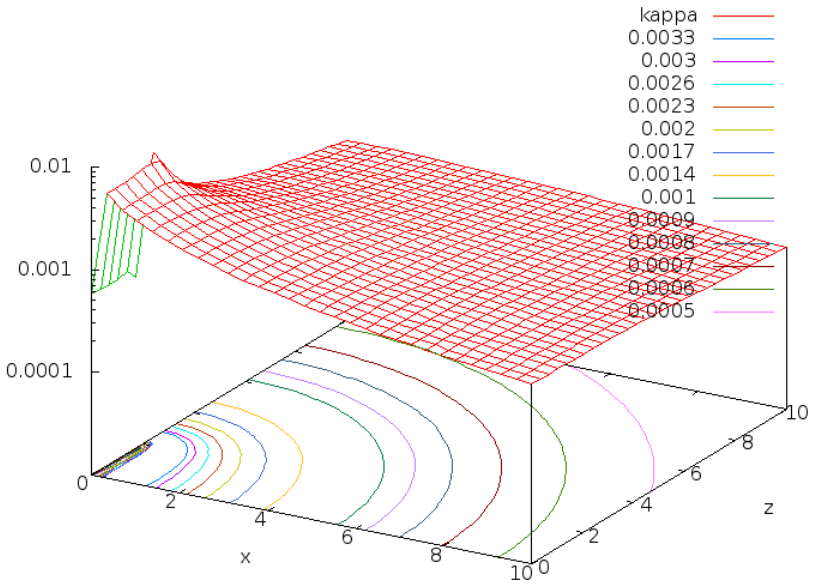


Figure 2. The expansion $\kappa$ plotted in a log scale. One can see that it copies the geometry of the projected spheroids.

In Figure 2 we plot the expansion optical scalar $\kappa$, with the contour level at the bottom. One can see that the contours copy very well the projection of the spheroidal geometry, to the $(xz)$ plane.

Figure 3 shows the plot of the modulus of shear optical scalar $\gamma$, with the contour level at the bottom. It is observed that in this case the structure is much more complicated, and that in the inner region the behaviour of the modulus does not follow the projection of the spheroidal geometry. However, in Figure 4; where the shear is represented by small segments, it is easier to follow and understand the effects of the spheroidal geometry

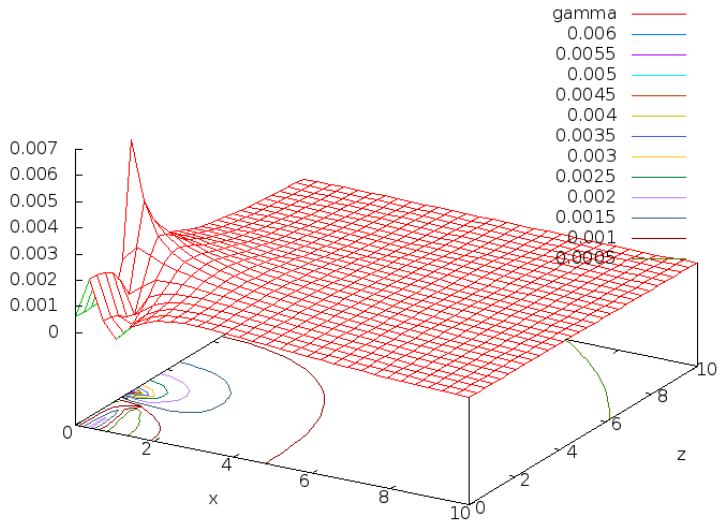


Figure 3. The modulus $\gamma$ of the shear expansion. The contour curves are more complicated in this case.

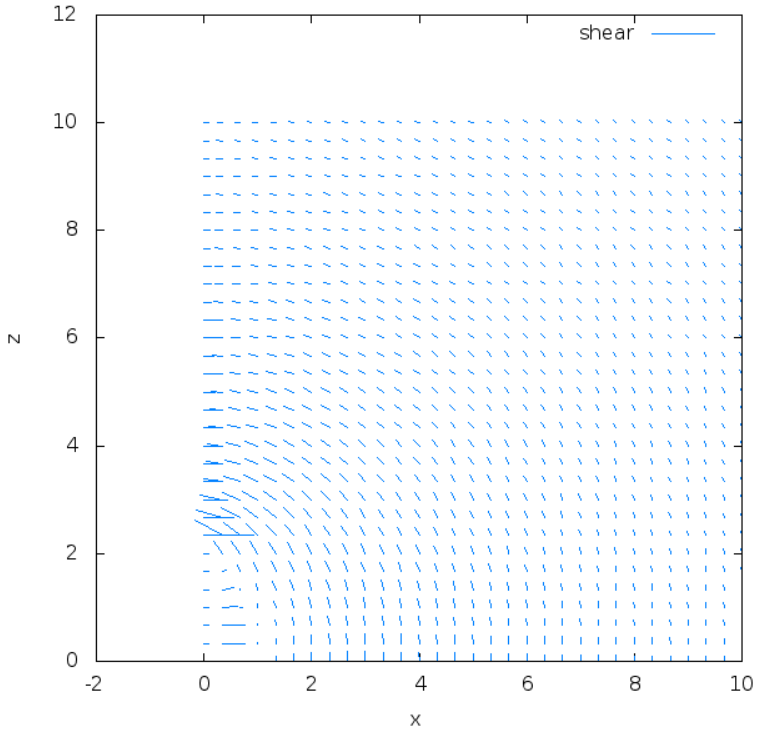


Figure 4. The shear plotted as segments in the plane of the lens.

on the gravitational lens. The segments represent the direction of the maximum shear deformation.

## 5. Spacetimes with prolate spheroidal symmetry and mass

The zero mass spacetime just presented can be generalized to spacetimes with mass content; as we do next.

### The metric

Here we present a new stationary solution with mass content, spheroidal symmetry and a non-trivial spacelike component of the energy momentum tensor whose metric is:

$$ds^2 = a(r)dt^2 - \left((r^2 + r_\mu^2 \sin^2(\theta))\left(\frac{dr^2}{r^2 - 2M(r)r + r_\mu^2} + d\theta^2\right) + r^2 \sin^2(\theta) d\phi^2\right), \tag{30}$$

and the timelike component of the metric is:

$$a = a_0\left(\ln\left(\frac{r}{r_\mu} + \sqrt{(\frac{r}{r_\mu})^2 + 1}\right) + C\right)^2, \tag{31}$$

and where $M(r)$ is:

$$M(r) = \frac{M_*}{r_*} r \quad \text{for} \quad r \leqslant r_* \text{ and } M(r) = M_* \quad \text{for} \quad r > r_* \text{ (isothermal) or} \tag{32}$$

$$M(r) = 4\pi\rho_* r_*^3\left(\ln(1 + \frac{r}{r_*}) - \frac{\frac{r}{r_*}}{1 + \frac{r}{r_*}}\right) \qquad \text{(NFW);} \tag{33}$$

where the constant $M_*$ is the mass of the generalized isothermal distribution, $r_*$ denotes the maximum radius for the isothermal distribution, or the characteristic radius for the generalized Navarro-Frenk-White (NFW) distribution, and $\rho_*$ the density parameter. These two mass distributions, considered in these solutions, are the natural generalization of the isothermal mass density and of the NFW profile to the spheroidal geometry.

## 6. A spacetime with oblate spheroidal symmetry and zero mass

We generalize here the previous discussion to oblate spheroidal symmetry.

### 6.1. Using the radial coordinate

### The metric

From the relation $r = r_\mu \sinh(\xi)$; one can express the metric as:

$$ds^2 = a(r)dt^2 - \left((r^2 + r_\mu^2 \cos^2(\theta))\left(\frac{dr^2}{r^2 + r_\mu^2} + d\theta^2\right) + (r^2 + r_\mu^2)\sin^2(\theta) d\phi^2\right), \tag{34}$$

and the timelike component of the metric is

$$a = a_0\left(\ln\left(\frac{r}{r_\mu} + \sqrt{(\frac{r}{r_\mu})^2 + 1}\right) + C\right)^2. \tag{35}$$

## 7. Spacetimes with oblate spheroidal symmetry and mass

The zero mass spacetime just presented can be generalized to spacetimes with mass content; as we do next.

### The metric

Here we present a new stationary solution with mass content, spheroidal symmetry and a non-trivial spacelike component of the energy momentum tensor. The metric is:

$$\begin{aligned} ds^2 = a(r)dt^2 - (r^2 + r_\mu^2\cos^2(\theta))\frac{dr^2}{r^2 - 2M(r)r + r_\mu^2} \\ -\Big((r^2 + r_\mu^2\cos^2(\theta))d\theta^2 + (r^2 + r_\mu^2)\sin^2(\theta)d\phi^2\Big), \end{aligned} \tag{36}$$

and the timelike component of the metric is

$$a = a_0\left(\ln\left(\frac{r}{r_\mu} + \sqrt{(\frac{r}{r_\mu})^2 + 1}\right) + C\right)^2, \tag{37}$$

and where $M(r)$ is:

$$M(r) = \frac{M_*}{r_*}r \quad \text{for} \quad r \leqslant r_* \text{ and } M(r) = M_* \quad \text{for} \quad r > r_* \text{ (isothermal) or} \tag{38}$$

$$M(r) = 4\pi\rho_* r_*^3\left(\ln(1 + \frac{r}{r_*}) - \frac{\frac{r}{r_*}}{1 + \frac{r}{r_*}}\right) \qquad \text{(NFW).} \tag{39}$$

These mass distributions are the natural generalization of the isothermal mass density to the spheroidal geometry and of the NFW distribution to spheroidal geometry.

## 8. Final comments

We have presented several new static exact solutions of the Einstein equations, with spheroidal symmetry. Some of them have $T_{tt} = 0$, and therefore they have *zero mass*, although with a non-trivial geometry whose gravitational effects are of interest for the explanation of dark matter phenomena.

They are the natural generalization of a previous geometry we presented before (Gallo & Moreschi 2012), with spherical symmetry; that adequately represents *dark mater observations*.

The behaviour of the shear in the weak lens calculation, for the prolate zero mass case, is not yet well understood; but it might indicate a non-trivial behaviour of the spin 2 nature of the Weyl $\Psi_0$ component.

These geometries have the property that they can naturally be generalize to other matter distributions with spheroidal symmetry; using the same form of the metric. That is they represent a family of solutions with multiple possibilities.

We wish to develop these techniques for applications to typical non-spheric systems as binary systems, irregular clusters, galaxies, and others.

**Acknowledgments.** We are very grateful for the corrections and suggestions of an anonymous referee. We acknowledge support from CONICET, SeCyT-UNC and Foncyt.

**References**

Serra, A. L. & Romero, M. J. L. D. 2011, MNRAS Letters, 415, L74–L77

Gallo, E. & Moreschi, O. M. 2011, Phys. Rev. D, 83, 083007,

Gallo, E. & Moreschi, O. M. 2012, Mod. Phys. Lett., A27, 1250044

Schneider, P., Ehlers, J. & Falco, E. 1992, “Gravitational lenses”, Springer-Verlag

*Gravitation, Relativistic Astrophysics and Cosmology*
*Second Argentinian-Brazilian Meeting, 2014*
*G. S. Vila, F. L. Vieyro and J. Fabris, eds.*

# Radiation production and stochastic effects during inflation

Rudnei O. Ramos

*Departamento de Física Teórica, Universidade do Estado do Rio de Janeiro, 20550-013 Rio de Janeiro, RJ, Brazil*

**Abstract.** Nonisentropic (warm) inflation models are characterized by radiation production due to the decay of fields coupled to the inflaton during inflation. The continuous radiation production might sustain a thermal radiation bath during inflation as a result of the dissipative particle production. The presence of the radiation bath can impact on the dynamics of inflation and, consequently, on the observable quantities measured from the cosmic microwave background radiation (CMBR). Besides of dissipative effects, these are also accompanied by stochastic fluctuations. Both the origin and the impact of these effects on the inflationary dynamics are reviewed here.

## 1. Introduction

Inflation is the most acceptable paradigm that solves the flatness and horizon problems of the standard Big-Bang cosmological model (Liddle & Lyth 2000). We generically defines inflation as an early accelerated expansion dominated by vacuum energy density and driven by a fluid with negative pressure:

$$\text{Inflation} \quad \Rightarrow \quad \ddot{a} > 0, \quad p < -\rho/3.$$

Besides of solving the flatness and horizon problems of the hot Big-Bang theory, inflation also provides a solution of how inhomogeneities can originate, thus giving a mechanism through which large-scale structures can form. Inflation is typically driven by a scalar field, the inflaton field. Density perturbations are sourced by perturbations of this inflaton field, which can be either of quantum and/or thermal origin. Inflation also solves some outstanding problems related to Grand-Unified theories (GUT), like the problem of dangerous heavy relics (e.g., magnetic monopoles).

In the standard scenario of inflation, which we call *cold inflation*, the interactions of the inflaton field with other field degrees of freedom are negligible during inflation. In this case the universe enters in a vacuum dominated phase and any previous (if any) initial radiation energy density, $\rho_r$, quickly redshifts away. In cold inflation, the inflationary phase must end with a reheating phase, through which the universe enters in the radiation dominated phase, such that the standard Big-Bang cosmological evolution follows. The standard theory of inflation, as a bonus, predicts that the large scale distribution of galaxies can be traced back to quantum vacuum fluctuations of a weakly coupled field, the inflaton, during the inflationary era (Liddle & Lyth 2000).

However, there can be regimes of parameters such that the inflaton interactions with other field degrees of freedom are not negligible. It then happens that these interactions can generate dissipation terms, such that a small fraction of vacuum energy density

can be converted to radiation. If the magnitude of these dissipation terms are strong enough to compensate the redshift of the radiation by the expansion, then a steady state can be produced, with the inflationary phase happening in a thermalized radiation bath. This scenario is called *warm inflation* (WI) (for a recent review see Berera, Moss & Ramos 2009). In warm inflation, the evolution equation for the radiation gets modified to $\dot{\rho}_r + 4H\rho_r = \Upsilon\dot{\phi}^2$, where $H = \dot{a}/a$ and $\Upsilon$ is a dissipation term that can be a function of both the inflaton field $\phi$ and temperature $T$. Typically, in warm inflation it is assumed that $T \gtrsim H$, in which case thermal fluctuations dominate over the quantum ones. As a consequence, density fluctuations are now sourced by thermal fluctuations as opposite to quantum fluctuations in the cold inflation scenario.

WI dynamics can be viewed as an analogous of that of open systems. Dissipative dynamics along with stochastic forces are typical manifestations for the dynamics of a system interacting with some large environment. We can think of such similar dynamics to also manifest in the early universe. For instance, when the matter content of the universe can be split into a subsystem interacting with a large energy reservoir, then physical processes may be represented through effective dissipation and stochastic noise terms.

The presence of a radiation bath in WI can impact on the dynamics of inflation and, consequently, on the observable quantities measured from the cosmic microwave background radiation. In particular, the amplitude of primordial curvature perturbations is enhanced and this is particularly significant when a non-trivial statistical ensemble of inflaton fluctuations is also maintained. Since gravitational modes are decoupled from the radiation bath for energies well below the Planck scale, the presence of the thermal radiation bath and/or a non vanishing statistical ensemble for the inflaton generically lowers the tensor-to-scalar ratio and yields a modified consistency relation for warm inflation, as well as changing the tilt of the scalar spectrum. This is able to alter the landscape of observationally allowed inflationary models, with for example the quartic chaotic potential being in very good agreement with the Planck results for nearly-thermal inflaton fluctuations, whilst essentially ruled out for an underlying vacuum state. Besides of dissipative effects, these are also accompanied by stochastic fluctuations. Both the origin and the impact of these effects on the inflationary dynamics is reviewed in the next sections. We show how the dissipative and stochastic forces associated are able to alter the landscape of observationally allowed inflationary models, with for example the quartic chaotic potential being in very good agreement with the Planck results for nearly-thermal inflaton fluctuations. We also connect the results obtained from warm inflation with the recent BICEP2 measurement of a B-mode in the CMBR, believed to come from gravitational waves of primordial origin, and how warm inflation can conciliate both Planck and BICEP2 results.

## 2. Warm inflation dynamics

Warm inflation is defined in terms of the effective evolution equation for the inflaton field when averaging out (functionally integrating over) the other field degrees of freedom. This produces a stochastic (Langevin-like) equation of motion for the inflaton which is of the form (Ramos & Silva 2013)

$$\ddot{\phi}(\mathbf{x},t) + 3H\dot{\phi}(\mathbf{x},t) + \int d^4x' \Sigma_R(x,x')\phi(x') + V_{,\phi} - \frac{1}{a^2}\nabla^2\phi(\mathbf{x},t) = \xi_q + \xi_T \,, \quad (1)$$

where $\Sigma_R(x,x')$ is a self-energy contribution and $\xi_q$ and $\xi_T$ are stochastic fields, with Gaussian distributions, describing quantum and thermal (noise) fluctuations, respectively. They satisfy appropriate fluctuation and dissipation relations. For example, two-point correlation function for $\xi_T$ is related to thermal part of $\Sigma_R(x,x')$. The self-energy term can be put in the form of a dissipative term in the adiabatic approximation, $\dot{\phi}/\phi, H, \dot{T}/T < \Gamma$, where $\Gamma$ is a decay rate term. In the most recent implementations of warm inflation (Berera, Moss & Ramos 2009), $\Gamma$ is the decay width of a heavy scalar field coupled to the inflaton field and that can decay into light radiation fields. Under the adiabatic approximation, we can approximate the self-energy term in Eq. (1) as $\int d^4x' \Sigma_R(x,x')\phi(x') \approx \Upsilon\dot{\phi}(\mathbf{x},t)$ and the two-point correlation function for the stochastic source $\xi$ turns into a local correlation function: $\langle \xi_T(\mathbf{x},t)\xi_T(\mathbf{x}',t')\rangle = a^{-3}\Upsilon T\delta(\mathbf{x}-\mathbf{x}')\delta(t-t')$. Likewise, the two-point correlation function for the quantum noise term can be expressed as $\langle \xi_q(\mathbf{x},t)\xi_q(\mathbf{x}',t')\rangle = H^2\,(1+2\mathcal{N})\,/2\,a^{-3}\delta(\mathbf{x}-\mathbf{x}')\delta(t-t')$, where $\mathcal{N}$ accounts for the possibility of a non-trivial distribution of inflaton particles, produced as a result of the dissipative processes occurring during inflation. For sufficiently fast interactions, this is expected to approach a Bose-Einstein distribution: $\mathcal{N} \approx n_{\rm BE}(k) = 1/[\exp(k/aT) - 1]$.

The dissipation coefficient $\Upsilon$ is found to have the following generic power law dependence with $\phi$ and $T$ (Bastero-Gil, Berera & Ramos 2011, Bastero-Gil, Berera, Ramos & Rosa 2013),

$$\Upsilon = C_\phi \frac{T^c}{\phi^{c-1}}, \tag{2}$$

where the value of the power $c$ dependent on the specifics of the model construction for WI and on the temperature regime of the thermal bath. Typically, it is found that $c = 3$ (low temperature), $c = -1$ (high temperature) or $c = 0$ (constant dissipation).For example, $c = 3$ corresponds to the case where the inflaton interacts with a heavy (scalar) boson field, which in turn decays into light scalars. This is the case we use throughout this work, unless otherwise specified. The effectiveness of WI can be parametrized by the ratio $Q \equiv \Upsilon/3H$. The strong dissipative regime for WI is for $Q \gg 1$, while for $Q \ll 1$, it is the weak dissipative regime for WI.

As usual, we can study the dynamics by splitting the inflaton field in a background homogeneous part and perturbations, $\phi(\mathbf{x},t) = \phi(t) + \delta\varphi(\mathbf{x},t)$. The background quantities $\phi(t)$ and the radiation energy density $\rho_r(t)$ satisfy

$$\ddot{\phi} + (3H + \Upsilon)\dot{\phi} + V_{,\phi} = 0, \tag{3}$$

$$\dot{\rho}_r + 4H\rho_r = \Upsilon\,\dot{\phi}^2, \tag{4}$$

$$3H^2 = 8\pi G\rho\,. \tag{5}$$

Prolonged inflation requires the slow-roll conditions $|\epsilon_X| \ll 1$, where $\epsilon_X = -d\ln X/H dt$, and $X$ is any of the background field quantities. These slow-roll coefficients in WI satisfy

$$\begin{aligned}
\epsilon &= \frac{m_{\rm P}^2}{2}\left(\frac{V_{,\phi}}{V}\right)^2 \ll 1+Q, \\
\eta &= m_{\rm P}^2\left(\frac{V_{,\phi\phi}}{V}\right) \ll 1+Q, \\
\beta &= m_{\rm P}^2\left(\frac{\Upsilon_{,\phi}V_{,\phi}}{\Upsilon V}\right) \ll 1+Q,
\end{aligned} \tag{6}$$

where $m_{\rm P}$ is the reduced Planck mass, $m_P = 1/\sqrt{8\pi G} = 2.4\times 10^{18}$GeV.

## 3. Perturbations and connection with CMBR measurable quantities

From Eq. (1) in the local approximation, the equation of motion for the fluctuations $\delta\varphi(\mathbf{x},t)$ at linear order (in Fourier momentum space) is given by

$$\ddot{\delta\varphi}(\mathbf{k},t) + (3H+\Upsilon)\dot{\delta\varphi}(\mathbf{k},t) + V''(\phi)\delta\varphi(\mathbf{k},t) + \frac{k^2}{a^2}\delta\varphi(\mathbf{k},t) = \tilde{\xi_T}(\mathbf{k},t) + \tilde{\xi_q}(\mathbf{k},t)\ . \tag{7}$$

The solution of this equation can be expressed in terms of a Green function and from it we define the power spectrum for the inflaton field perturbations,

$$P_{\delta\varphi}(z) = \frac{k^3}{2\pi^2}\int \frac{d^3k'}{(2\pi)^3}\langle\delta\varphi(\mathbf{k},z)\delta\varphi(\mathbf{k}',z)\rangle\,, \tag{8}$$

where $z = k/(aH)$. These perturbations at some scale $k$ get frozen as soon these scales cross the horizon, $z_* = 1$ and are imprinted in the CMBR when they reenter the horizon again at the decoupling era. The power spectrum can then be related to the CMBR quantities like the amplitude $\Delta_R$ for the curvature perturbation (defined in terms of the gauge invariant curvature perturbation $\xi = -H\delta\varphi/\dot{\phi}$) and the spectral index $n_s$,

$$\Delta_R^2 = \frac{H^2}{\dot{\phi}^2}P_R = \Delta_R^2(k_0)\left(\frac{k}{k_0}\right)^{n_s-1}\ , \tag{9}$$

and the spectral index $n_s$, is the spectral index ($N_e$ is the number of e-folds of inflation):

$$n_s - 1 = \frac{d\ln\Delta_R^2}{dN_e} = \frac{d\ln\Delta_R^2}{d\ln k}\,, \tag{10}$$

where $N_e$ is the number of e-folds of inflation.

For a generic inflaton phase-space distribution at the time when observable CMB scales leave the horizon during inflation, $z = z_*$, the dimensionless power spectrum of curvature perturbations in WI found to be given by (Ramos & Silva 2013)

$$\Delta_R^2 = \left(\frac{H_*}{\dot{\phi}_*}\right)^2\left(\frac{H_*}{2\pi}\right)^2\left[1+2n_* + \left(\frac{T_*}{H_*}\right)\frac{2\sqrt{3}\pi Q_*}{\sqrt{3+4\pi Q_*}}\right]\,, \tag{11}$$

which yields the standard cold inflation result, $\left(H_*/\dot{\phi}_*\right)^2 [H_*/(2\pi)]^2$, in the limit $n_*, Q_*, T_* \to 0$.

Another quantity that can be used to constrain the many different inflation models is the tensor to scalar curvature perturbation ratio, $r = \Delta_T^2/\Delta_R^2$. Inflation in general also predicts a spectrum of gravitational waves. Gravitational wave perturbations also gets amplified during inflation, just like vacuum and thermal (in WI) perturbations of the inflaton field. Gravity waves are weakly coupled to the thermal bath and the spectrum of tensor modes retains its vacuum form, $\Delta_T^2 = (2/\pi^2)(H_*^2/m_P^2)$. This therefore suppresses the tensor-to-scalar ratio, yielding a modified consistency relation in the case of WI,

$$r \simeq \frac{8|n_t|}{1 + 2n_* + 2\pi Q_* T_*/H_*} , \tag{12}$$

where $n_t = -2\epsilon_*$ is the tensor index, while the spectral index $n_s$ in WI is (Bartrum, Bastero-Gil, Berera, Cerezo, Ramos & Rosa 2014)

$$n_s - 1 \simeq 2\eta_* - 6\epsilon_* + \frac{2\kappa_*}{1+\kappa_*}\left(7\epsilon_* - 4\eta_* + 5\sigma_*\right) , \tag{13}$$

where $\sigma = m_P^2 V'/(\phi V) < 1+Q$ and we have used the slow-roll equations, $3H(1+Q)\dot{\phi} \simeq -V'(\phi)$ and $\rho_R \simeq (3/4)Q\dot{\phi}^2$, to determine the variation of $\kappa \equiv 2\pi QT/H$ as different scales become super-horizon during inflation.

Modifications are, however, more prominent in the opposite limit of nearly-thermal inflaton fluctuations, with $n_* \simeq n_{BE*}$. For $T_* \gtrsim H_*$ and $Q_* \ll 1$ we then obtain:

$$n_s - 1 \simeq 2\sigma_* - 2\epsilon_* , \tag{14}$$

which is, in particular, independent of the curvature of the potential, which only determines its running:

$$n_s' \simeq 2\sigma_*(\sigma_* + 2\epsilon_* - \eta_*) - 4\epsilon_*(2\epsilon_* - \eta_*) . \tag{15}$$

In this case, a red-tilted spectrum, $n_s < 1$, corresponds to either potentials with a negative slope, such as hill-top models, or large field models where $\epsilon_* > 2(m_P/\phi_*)^2$.

The above results for $r$ and $n_s$ in WI also easily goes to the cold inflation result when $n_*, Q_*, T_* \to 0$. In cold inflation (see, e.g., Liddle & Lyth 2000), it is found that $r = 16\varepsilon$, $n_s = 1 + 2\eta - 6\varepsilon$.

The observed amplitude of curvature perturbations from the recent measurements from Planck (Ade et al. 2013) gives $\Delta_{\mathcal{R}}^2 \simeq 2.2 \times 10^{-9}$. The recently released Planck results also give for the tensor to scalar amplitude ratio the result $r < 0.11$ at 95% CL (when the high-$\ell$ CMB ACT+SPT data are added) and for the spectral index $n_s = 0.9600 \pm 0.0072$, while when including the Planck lensing likelihood gives $n_s = 0.9653 \pm 0.0069$ and $r < 0.13$, and by also adding BAO data, it gives $n_s = 0.9643 \pm 0.0059$ and $r < 0.12$.

## 4. Results

Let us show some of the results that the above expressions derived in the context of WI produces. For that, we specialize in the particular case of a chaotic quartic inflation potential,

$$V(\phi) = \lambda\phi^4 \ . \tag{16}$$

In the cold inflation case, it is known that such potential for inflation is not consistent with the present data, since it predicts a tensor-to-scalar ratio $r$ and spectral index $n_s$ outside of the allowed region as recently determined by the results from Planck (Ade et al. 2013).

Our results for WI (Bartrum, Bastero-Gil, Berera, Cerezo, Ramos & Rosa 2014) are shown in Fig. 1.

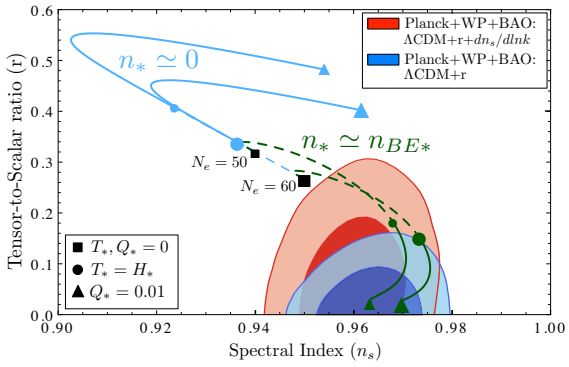


Figure 1. Trajectories in the $(n_s, r)$ plane for $V(\phi) = \lambda\phi^4$ as a function of the dissipative ratio, $Q_* < 0.01$, 50-60 e-folds before the end of inflation, compared with the Planck results (Ade, et al. 2013), for $g_* = 228.75$ relativistic degrees of freedom. The dark green (light blue) curves correspond to nearly-thermal (negligible) inflaton occupation numbers $n_*$, with dashed branches for $T_* \leq H_*$. Note that corresponding curves converge in the cold inflation limit, $T_*, Q_* \to 0$.

The results in Fig. 1 for the trajectories in the $(n_s, r)$ plane show that depending on the values of dissipation ratio $Q$ and the statistical state for the inflatons, particularly in the case where the inflatons are in a quasi-thermalized state with a Bose-Einstein distribution $n_{\rm BE}$, the trajectories fall just easily in the allowed region from Planck.

## 5. The BICEP2 recent results and possible consequences for WI

The BICEP2 experiment (Ade, et al. 2014) has recently reported evidence for a large tensor-to-scalar ratio $r = 0.20^{+0.07}_{-0.05}$ (without foreground dust subtraction) from the observation of B-mode polarization in the CMBR at degree angular scales. While this is good news for the inflationary paradigm (Liddle & Lyth 2000), which predicts a primordial tensor component in the CMBR spectrum, BICEP2's value seems to be in tension with the constraint on the tensor-to-scalar ratio reported by the Planck collaboration last year (Ade et al. 2013). The Planck collaboration has, in particular, placed an upper bound $r < 0.11$ (95% CL), assuming that primordial scalar curvature perturbations are described solely by an adiabatic component with a simple power-law spectrum, i.e. no running of the spectral index.

The constraints obtained by BICEP2 in the $(n_s, r)$ plane is illustrated in Fig. 2, where we superimpose them in the same figure 1 that includes the WI trajectories. Note from the figure that WI can also be consistent with the BICEP2 results. The figure also illustrates the discrepancy (at the 2-$\sigma$ level) of the BICEP2 results from that from Planck in the absence of a running for the spectral index ($n_s' = dn_s/d\ln k$).

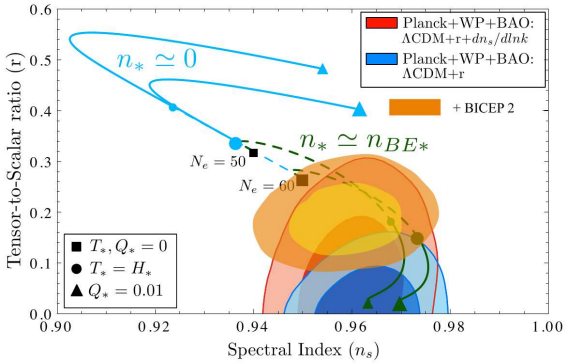


Figure 2. Trajectories in the $(n_s, r)$ plane. Same as in Fig. 1, but now including the contours from BICEP2.

On the one hand, Planck has also confirmed a significant deficit of power on large angular scales with respect to their best-fit ΛCDM model, with a primordial spectrum characterized by a constant red-tilted spectral index, so that any additional contributions like gravity waves are naturally rather constrained. On the other hand, any modification of the primordial spectrum that tends to reduce the power on large scales will help relaxing the above constraint on $r$. Several possibilities were already mentioned by the Planck collaboration, and they have been further explored in view of the BICEP2 result, for example a negative running of the scalar spectral index, sterile neutrinos as extra relativistic degrees of freedom, a blue-tilted tensor spectrum, or isocurvature perturbations (Kawasaki & Yokoyama 2014). In particular the tension in the bound on the tensor-to-scalar ratio $r$ between Planck and BICEP2 can be resolved by introducing isocurvature perturbations that are anti-correlated with the main adiabatic component.

As shown in Bastero-Gil, Berera, Ramos & Rosa 2012, a cosmological baryon asymmetry can be produced through dissipative particle production during inflation, a mechanism known as *warm baryogenesis*. The produced baryon-to-entropy ratio $\eta_s = n_b/s$ was shown in that reference to be consistent with the observed cosmological asymmetry $7.2\times10^{-11} < \eta_s < 9.2\times10^{-11}$. Since the produced asymmetry $\eta_s$ depends on the inflaton field and temperature, super-horizon fluctuations of the inflaton field will also be imprinted in the CMB temperature anisotropies in the form of baryon isocurvature perturbations. These have the same origin and will thus be fully (anti-)correlated with the main adiabatic curvature perturbations. This is a very distinctive feature of warm baryogenesis and makes it a testable model, which is not the case of most of the baryogenesis mechanisms proposed in the literature. Besides baryon isocurvature perturbations, dark matter isocurvature ones can equally be produced by the same mechanism during WI. These isocurvature perturbations $B_m$ can be produced at a level still consistent with the upper bounds set by Planck, $|B_m| < 0.079$, yet, they can affect the CMB temperature anisotropies $\langle(\Delta T/T)^2\rangle$ strongly,

$$\langle (\Delta T/T)^2 \rangle \sim P_\zeta \left(1 + \frac{5}{6} r_{\rm eff}\right) , \tag{17}$$

where

$$r_{\rm eff} = r + \frac{6}{5}\left(4B_m^2 + 4B_m\right), \tag{18}$$

such that for anti-correlated isocurvature perturbations a smaller effective tensor-to-scalar ratio can be obtained.

It is important to mention that in deriving the bounds on the tensor-to-scalar ratio $r$ from CMB temperature anisotropies, the Planck collaboration has assumed that primordial scalar curvature perturbations are described uniquely by an adiabatic component. The effects of any other component such as baryon isocurvature modes are then necessarily absorbed into an effective tensor-to-scalar ratio, $r_{eff}$, which is smaller than the true tensor contribution if the additional components are anti-correlated with the dominant adiabatic modes. Using this effect of an anti-correlated matter isocurvature perturbation that can be generated during WI, an either partial or even full screening is naturally present and may reconcile the BICEP2 detection of B-mode polarization with the upper bound on the tensor-to-scalar ratio placed by Planck, as shown in details in Bastero-Gil, Berera, Ramos & Rosa (2014). A partial screening would, in particular, be interesting if there is future evidence for a non-zero tensor-to-scalar ratio in the temperature power spectrum that is somewhat smaller than the value inferred from the polarization data. This screening can, in fact, be effective for a wide range of values for the tensor-to-scalar ratio and is not inherent to the large value obtained by the BICEP2 collaboration, which is presently is under scrutiny.

An example of this effect of screening of the tensor-to-scalar ratio is shown in Fig. 3, again for the case of a quartic inflaton potential in WI.

## 6. Summary and perspectives

We have seen that warm inflation is able to describe in a concomitantly and natural way the effects of both quantum and thermal fluctuations. While the observational constraints involving the spectral index $n_s$ and the tensor to scalar curvature ratio $r$ already rule out a large class of inflaton polynomial potentials $V \sim \phi^p$, with $p > 3$, dissipative effects and thermal fluctuations can make these higher polynomial inflaton potentials compatible again with the observational constraints, as shown recently in the references Ramos & Silva (2013) and in Bartrum, Bastero-Gil, Berera, Cerezo, Ramos & Rosa (2014). We have here shown the results for the particular case of a quartic inflaton potential and seen how easily WI can make it in concordance with the recent results from Planck. The most important effect of dissipation and/or a non-trivial inflaton particle distribution is the lowering of the tensor-to-scalar ratio in the modified consistency relation in Eq. (12), so we expect next upcoming Planck release and future CMB B-mode polarization searches to shed new light on the nature of inflaton fluctuations.

We have also seen that WI can naturally account for the baryon asymmetry of the universe. As an additional bonus, we predicts the production of anti-correlated isocurvature perturbations as a result of the matter production due to dissipative effects

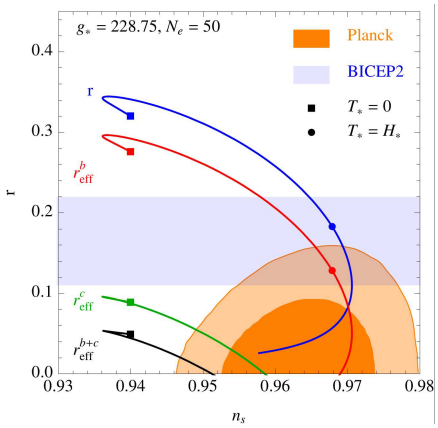


Figure 3. Trajectories in the $n_s - r$ plane for the quartic model (thermal inflaton occupation numbers) with 50 e-folds of inflation and $g_* = 228.75$, with baryon ($r^b_{eff}$), CDM ($r^c_{eff}$), and full matter isocurvature perturbations ($r^{b+c}_{eff}$). The shaded regions show the 68% and 95% CL Planck contours (Ade, et al. 2013), including the results of WMAP and BAO observations, and the $1\sigma$ interval for $r$ derived by the BICEP2 collaboration (Ade, et al. 2014) after taking into account dust contributions. These results correspond to the range $T_*/H_* = 0 - 13$ ($Q_* = 0 - 0.01$).

during WI. The obtained results for chaotic models suggest that a large tensor-to-scalar ratio could be accommodated by the current Planck results due to the presence of these matter isocurvature modes associated with an asymmetric dissipation of the inflaton's energy density into baryonic or CDM species. This provides a way of reconciling the Planck results with the recent results from the BICEP2 experiment on B-modes measurements on the CMB.

**Acknowledgments.** The author would like to thank financial support from research grants from CNPq and FAPERJ (Brazilian funding agencies). I also would like to thank the organizers for the invitation and for putting together a stimulating program.

## References

Ade, P. A. R., et al. 2014 [Planck Collaboration], A&A, 571, A22

Ade, P. A. R., et al. 2014 [BICEP2 Collaboration], Phys. Rev. Lett., 112, 241101

Bartrum, S., Bastero-Gil, M, Berera, A., Cerezo, R., Ramos, R. O. & Rosa, J. G. 2014, Phys. Lett. B, 732, 116

Bastero-Gil, M, Berera A. & Ramos, R. O. 2011, JCAP, 1109, 033

Bastero-Gil, M, Berera A., Ramos, R. O. & Rosa, J. G. 2012, Phys. Lett. B, 712, 425

Bastero-Gil, M, Berera A., Ramos, R. O. & Rosa, J. G. 2013, JCAP, 1301, 016

Bastero-Gil, M, Berera A., Ramos, R. O. & Rosa, J. G. 2014, JCAP 10, 053

Berera, A., Moss, I. G. & Ramos, R. O. 2009, Rept. Prog. Phys., 72, 026901

Kawasaki, M. & Yokoyama, S. 2014, JCAP, 5, 46

Liddle, A. R. & Lyth, D. H. 2000, "Cosmological inflation and large scale structure", Cambridge University Press, Cambridge, U.K.

Ramos, R. O. & Silva, L. A. 2013, JCAP, 1303, 032

*Gravitation, Relativistic Astrophysics and Cosmology*
*Second Argentinian-Brazilian Meeting, 2014*
*G. S. Vila, F. L. Vieyro and J. Fabris, eds.*

# Stability of gravitational waves and the new perspectives for Quantum Gravity below the Planck scale

Ilya L. Shapiro,[1,2] Ana M. Pelinson,[3] and Filipe de O. Salles[1]

[1]*Departamento de Física, ICE, Universidade Federal de Juiz de Fora, MG, Brazil*
[2]*Tomsk State Pedagogical University and Tomsk State University, Tomsk, Russia*
[3]*Departamento de Física, CFM, Universidade Federal de Santa Catarina, SC, Brazil*

**Abstract.** One can say that the theory of gravity with higher derivatives terms is one of the most relevant models of quantum gravity. The main reason is that the action of gravity should include fourth derivative terms to provide renormalizability in the vacuum sector at the semiclassical level. At the same time, including the generic fourth derivative terms means the presence of massive ghosts, which are gauge-independent massive states with negative kinetic energy. At both classical and quantum level these ghosts may violate stability of the vacuum state and hence the theory becomes inconsistent. In order to check to which extent this situation depends on the energy scale, we explore the dynamics of the gravitational waves on the background of classical solutions. There are strong arguments that massive ghosts produce instability only when they are present as physical particles and this requires a very high energy scale. In the case of a cosmological background one can observe that if the initial frequency of the metric perturbations is much smaller than the mass of the ghost, no instabilities are present.

## 1. Introduction

The QFT in curved space requires introducing a generalized action of external gravity field. One can prove that the theory can be renormalizable only if such a vacuum action includes four derivative terms. We will not go into details, but just refer the reader to the books in Birell & Davies (1982), Buchbinder et al. (1992) for a general introduction, and to the recent paper in Lavrov & Shapiro, (2010) for the most complete proof, including the case when non-covariant gauge fixing conditions are used. The necessary form of the gravitational vacuum action is as follows:

$$S_{vac} \;=\; S_{EH} \,+\, S_{HD}\,, \tag{1}$$

where

$$S_{EH} \;=\; -\,\frac{1}{16\pi G}\int d^4x\sqrt{-g}\,\{R+2\Lambda\} \tag{2}$$

is the Einstein-Hilbert action with the cosmological constant and the higher derivative term $S_{HD}$, can be recast in the most useful form as

$$S_{HD} = \int d^4x\sqrt{-g}\left\{a_1C^2 + a_2E + a_3\Box R + a_4R^2\right\} . \quad (3)$$

Here

$$C^2 = R^2_{\mu\nu\alpha\beta} - 2R^2_{\alpha\beta} + 1/3\, R^2 \quad (4)$$

is the square of the Weyl tensor and

$$E = R_{\mu\nu\alpha\beta}R^{\mu\nu\alpha\beta} - 4\, R_{\alpha\beta}R^{\alpha\beta} + R^2 \quad (5)$$

is the integrand of the topological Gauss-Bonnet term.

In quantum gravity, higher derivative term like the square of the Weyl tensor indicate the presence of massive ghost, namely, a spin-two particle with negative kinetic energy. This leads to the problem with unitarity, at least at the tree level. But, in the semiclassical theory, gravity is external and unitarity of the gravitational $S$-matrix can be not requested. Therefore, the consistency conditions in this case can be relaxed to the existence of physically reasonable solutions and their stability under small metric perturbations. Perhaps the most important point here is that the theory without the fourth-derivative terms (3) can not be consistent. If we do not include them into the classical action, these terms will emerge in the quantum corrections anyway, with infinite coefficients. The difference with the theory (1) would be that, without these terms in the classical action one can not control higher derivatives by means of multiplicative renormalization.

The higher derivative QG based on the fourth-derivative action (1), possesses a massive spin-two gauge-independent excitation called massive ghost,

$$G_{\text{spin}-2}(k) \sim \frac{1}{m^2}\left(\frac{1}{k^2} - \frac{1}{k^2+m^2}\right), \quad m \propto M_P . \quad (6)$$

In the framework of linearized theory one can separate the massless and massive degrees of freedom. It is an easy exercise to check that the kinetic energy of the massive component is negative. For this reason this particle is called massive ghost. Indeed, the mass of this ghost is huge, of the Planck order of magnitude. The main point of this review is a new proposal concerning ghosts, which was originally done in F. de O. Salles & Shapiro (2014).

Including even more derivatives was initially thought to move massive pole to a much higher mass scale. In Asorey et al. (1997) the following action was proposed

$$\begin{aligned} S &= S_{EH} + \int d^4x\sqrt{-g}\left\{a_1R^2_{\mu\nu\alpha\beta} + a_2R^2_{\mu\nu} + a_3R^2 + \ldots\right. \\ &+ \left. c_1R_{\mu\nu\alpha\beta}\Box^k R^{\mu\nu\alpha\beta} + c_2R_{\mu\nu}\Box^k R^{\mu\nu} + c_3R\Box^k R + b_{1,2,..}R^{k+1}_{...}\right\} . \end{aligned} \quad (7)$$

A simple analysis shows that this theory is superrenormalizable, but the massive ghost is still here. For the case of real poles one can prove that the spin-two part of the propagator has the structure

$$G_2(k) = \frac{A_0}{k^2} + \frac{A_1}{k^2 + m_1^2} + \frac{A_2}{k^2 + m_2^2} + \cdots + \frac{A_{N+1}}{k^2 + m_{N+1}^2}, \tag{8}$$

where for any sequence $0 < m_1^2 < m_2^2 < m_3^2 < \cdots < m_{N+1}^2$, the signs of the corresponding terms alternate, $A_j \cdot A_{j+1} < 0$. Therefore, the situation when the ghost is shifted to an infinite energy level is ruled out.

## 2. Stability of classical solutions at low energies

In our opinion, the most risky assumption which is usually done to rule out the higher derivative theory is that the Ostrogradsky instabilities or Veltman scattering are relevant independent on the energy scale. There is a relatively simple way to check this assumption. Let us take a higher derivative theory of gravity and verify the stability with respect to the linear perturbations on some, physically interesting, dynamical background. If the mentioned assumption is correct, we will observe rapidly growing modes even for the low-energy background and for the low initial frequencies of the gravitational perturbation. On the contrary, if there are no growing modes at the linear level, there will not be such modes even at higher orders. One has to remember that the ghost issue is essentially a tree-level problem, so the study of classical solution is sufficient to draw conclusions about the general situation.

Up to the present moment, the program formulated above has been realized in the following three cases:

a) Cosmological background. In the particular case of de Sitter metric the result is partially known for more than thirty years (Starobinsky 1979) and has been repeatedly confirmed (Hawking et al. 2001), including by using the effective action method (Fabris et al. 2001). In these papers the theory with semiclassical corrections to the classical action (3) has been used. On the other hand, recently the same investigation has been repeated for other cosmological metrics, such as radiation- and dust-dominated Universes (Fabris et al. 2012). At the same time, in all these papers the relation between instabilities and higher derivative ghosts was never traced back explicitly. This last part has been explored in F. de O. Salles & Shapiro (2014) and in what follows we shall review the main results of this work.

b) Black hole background. In this case there are conflicting data in the literature, namely the statements about stability (Whitt 1985) and instability (Myung 2013) of this solution. The analysis of this case is too complicated and we will not discuss it here. Let us only note that it is not clear to which extent the results depend on the choice of the boundary conditions and on the frequency of initial seeds of perturbations.

c) General curved background which is close to a flat space-time in a sense that the curvature tensor components are very small compared to the mass scale of the ghost. Since the non-linearities of the perturbations can be taken into account by means of a non-trivial metric background, it looks natural to consider a weak (albeit arbitrary) gravitational field. Such consideration is, in principle, possible by using Riemann normal coordinates and local momentum representation (F. de O. Salles & Shapiro 2014) but goes beyond the present short review.

## 3. Background cosmological solutions

In principle, one can explore the stability of the classical solution in the theory (1), but for the sake of generality we can include also the semiclassical corrections coming from the massless fields. It is supposed that the effects of massive fields are negligible at the sufficiently low energies.

In the case of massless conformal fields one can set to zero the coefficient of the $R^2$-term, $a_4 = 0$, in the action (3), without violating renormalizability. Therefore, the theory of our interest is described by the sum of a classical action (1) with $a_4 = 0$ and with the additional anomaly-induced (Riegert 1984; Fradkin & Tseytlin 1984) quantum contribution[1],

$$\begin{aligned}\Gamma_{ind} &= S_c[g_{\mu\nu}] - \frac{3c+2b}{36(4\pi)^2}\int_x R^2(x) + \frac{\omega}{4}\int_x\int_y C^2(x)\,G(x,y)\,(E-\frac{2}{3}\Box R)_y \\ &+ \frac{b}{8}\int_x\int_y (E-\frac{2}{3}\Box R)_x\,G(x,y)\,(E-\frac{2}{3}\Box R)_y\,, \end{aligned} \tag{9}$$

where we used compact notations

$$\int_x = \int d^4x\sqrt{-g}\,, \quad \text{and} \quad \Delta_4\,G(x,y) = \delta(x,y)\,. \tag{10}$$

Furthermore,

$$\Delta = \Box^2 + 2R^{\mu\nu}\nabla_\mu\nabla_\nu - \frac{2}{3}\,R\Box + \frac{1}{3}\,(\nabla^\mu R)\nabla_\mu \tag{11}$$

is the conformal self-adjoint Paneitz operator, coefficients $\omega$, $b$, $c$ depend on the number of quantum fields and $S_c\,[g_{\mu\nu}]$ is an arbitrary conformal invariant functional of the metric. Further details about derivation of (9) can be found, e.g., in Fabris et al. (2001).

In order to understand the effect of quantum terms on the conformal factor of the metric, let us consider the equation for this factor $a(t)$, Consider unstable inflation, matter (or radiation) dominated Universe and assume that the Universe is close to the classical FRW solution. The equation is

$$\begin{aligned}&\frac{\dddot{a}}{a} + \frac{3\dot{a}\ddot{a}}{a^2} + \frac{\ddot{a}^2}{a^2} - \left(5+\frac{4b}{c}\right)\frac{\ddot{a}\dot{a}^2}{a^3} - 2k\left(1+\frac{2b}{c}\right)\frac{\ddot{a}}{a^3} \\ &\quad -\frac{M_P^2}{8\pi c}\left(\frac{\ddot{a}}{a} + \frac{\dot{a}^2}{a^2} + \frac{k}{a^2} - \frac{2\Lambda}{3}\right) = -\frac{1}{3c}\,\rho_{matter}\,, \end{aligned} \tag{12}$$

where we have also introduced the matter term for illustrative purpose. Also, $k = 0, \pm 1$ and $\Lambda$ is the cosmological constant. It is easy to see how the things change in this equation when the time change. First of all, let us consider the empty universe, with

[1] Since we are mainly interested in the tensor gauge-independent mode of the metric perturbations, there is no problem to assume that the classical $R^2$-term is absent, since this term does not influence essentially the dynamics of this mode.

$\rho_{matter} \to 0$. In this case one can find particular solutions (see Starobinski 1980, and also Pelinson et al. 2003 for the case with cosmological constant)

$$a(t) = \begin{cases} a_o \exp(Ht), & k = 0 \\ a_o \cosh(Ht), & k = 1 \\ a_o \sinh(Ht), & k = -1 \end{cases}, \tag{13}$$

where Hubble parameter takes two constant values

$$H = H_\pm = \frac{M_P}{\sqrt{-32\pi b}} \left( 1 \pm \sqrt{1 + \frac{64\pi b}{3} \frac{\Lambda}{M_P^2}} \right)^{1/2}. \tag{14}$$

Let us note that the coefficient $b$ is negative for any particle content of the theory contributing to quantum terms. For the small cosmological constant $\Lambda \ll M_P^2$ the two solutions (14) boil down to

$$H_+ = \frac{M_P}{\sqrt{-16\pi b}}, \qquad H_- = \sqrt{\frac{\Lambda}{3}}. \tag{15}$$

Obviously, the first solution here is usual Starobinsky inflation (initial part of it, better say) and the second one is the usual dS solution without quantum corrections. What we need here is the stability of the second of these solutions with respect to the tensor perturbations of the metric.

One can first perform a simple test of the model, by considering the stability of the low-energy solution with $H_-$ with respect to the perturbations of the conformal factor (Pelinson et al. 2004). Consider $H \to H_- + const \cdot e^{\lambda t}$ and arrive at

$$\lambda^3 + 7H_0\lambda^2 + \left[ \frac{(3c - b)4{H_0}^2}{c} - \frac{M_P^2}{8\pi c} \right] \lambda - \frac{32\pi b{H_0}^3 + M_P^2 H_0}{2\pi c} = 0. \tag{16}$$

The solutions of this equation have positive real parts

$$\lambda_1 = -4H_0, \qquad \lambda_{2/3} = -\frac{3}{2} H_0 \pm \frac{M_P}{\sqrt{8\pi|c|}} i, \tag{17}$$

indicating the absence of growing modes. Obviously, the positive cosmological constant $\Lambda > 0$ protects the low-energy dS solution from higher-derivative instabilities in this case, even in the presence of higher derivatives.

One can regard the two dS solutions (15) as extreme states of the Universe (Shapiro 2002). The first of these solutions is the initial phase of the Starobinsky inflation and the last one is the distant future of the Universe when the effect of all kinds of matter becomes irrelevant and only cosmological constant will drive the accelerated expansion. What is important for us is that, in the low-energy regime of a late Universe, the solution with $H_-$ provides an extremely precise approximation for the solution with quantum terms taken into account. In the absence of quantum term (9) this is an exact solution, because Eq. (3) with $a_4 = 0$ does not affect the dynamics of the conformal factor. But even if the quantum term (12) is taken into account, it is still a perfect approximation. The reason that the theory without matter has only two dimensional parameters, $M_P$

and $\Lambda$. Any correction to $H_-$ is given by a positive power of the ratio $\Lambda/M_P^2$, which is of the order of $10^{-120}$. So, we can safely use this background solution at low energies.

Let us now consider the case with the nontrivial matter contents, $\rho_{matter}$. Consider the late time epoch. It is easy to see that the terms of the first line of (12), which are of the quantum origin, behave like $t^{-4}$. At the same time the second-line terms, of the classical origin, all behave like $t^{-2}$ (see Pelinson & Shapiro 2011 for more detailed discussion). Obviously, the quality of the classical approximation for the solution $a(t)$ becomes better for $t \to \infty$ and can be considered a very good one in the late epoch of the Universe.

## 4. Gravitational waves and ghosts

Now we are in a position to explore the dynamics of the gravitational waves on the background of cosmological solutions described in the previous section. For this end we consider small perturbation

$$g_{\mu\nu} \to g_{\mu\nu} + h_{\mu\nu}\,, \qquad h_{0\mu} = 0\,, \qquad \partial_i\, h^{ij} = 0 \qquad \text{and} \qquad h_{ii} = 0\,, \tag{18}$$

where the last three conditions mean synchronous coordinate condition and fixing the gauge freedom such that we deal with the tensor mode only. The background metric should be $g^0_{\mu\nu} = \{1,\ -\delta_{ij}\, a^2(t)\}$, where $a(t)$ can be chosen as cosmological constant-, radiation- or dust-dominated classical solution. Finally, our notations are $\mu = 0, i$ and $i = 1, 2, 3$. In order to explore the time dynamics of the gravitational waves one can make a partial Fourier transformation

$$h_{\mu\nu}(t, \vec{r}) \;=\; \int \frac{d^3k}{(2\pi)^3}\, e^{i\vec{r}\cdot\vec{k}}\, h_{\mu\nu}(t, \vec{k}) \tag{19}$$

and assume that the modes with different momenta do not interact between each other. Then $k = |\vec{k}|$ becomes a constant parameter and one can deal with an ordinary differential equation instead of a partial one.

In the original papers we worked with both classical case described only by the action (1) in F. de O. Salles & Shapiro (2014) and with the theory which includes semiclassical corrections (9) in Fabris et al. (2012). It was shown that the effect of these semiclassical corrections is negligible when we deal with the sufficiently small perturbations and sufficiently weak background. The qualitative explanation of this fact is that all the terms in (9) are at least of the third order in curvature tensor, or reduce to the less relevant $R^2$-term. Therefore, for the reason of compactness we will restrict ourselves by the purely classical case and also keep the cosmological constant zero and the space section of the space-time manifold plane. Then the equation for the perturbations have the form

$$\begin{aligned}\dddot{\dddot{h}} + 6H\,\dddot{h} + \Big(11H^2 + 4\dot{H} + \frac{{M_P}^2}{32\pi a_1}\Big)\ddot{h} + \Big(\frac{1}{2}\frac{\nabla^4 h}{a^4} - 2\frac{\nabla^2 \ddot{h}}{a^2} - 2H\frac{\nabla^2 \dot{h}}{a^2}\Big) - \\ \Big[7H\dot{H} + \ddot{H} + 6H^3 - \frac{3{M_P}^2\, H}{32\pi a_1}\Big]\dot{h} - \Big(\frac{{M_P}^2}{32\pi a_1}\Big)\frac{\nabla^2 h}{a^2} + \\ \Big[\frac{{M_P}^2}{16\pi a_1}(2\dot{H} + 3H^2)\Big]h = 0.\end{aligned} \tag{20}$$

Already at this level one can see that the equation depends only on the coefficient of the Weyl-squared term $a_1$ in the action (3) and not on other terms, as one should expect.

The analysis of the equation (20) and its semiclassical generalization has been done in F. de O. Salles & Shapiro (2014) and Fabris et al. (2012), correspondingly. Let us present here only qualitative results, which were achieved by both analytical and numerical methods. The analytical method was based on the following idea. One can approximately treat all coefficients as constants, assuming that the time variation of the Hubble parameter and its derivatives performs slower that the one of the perturbations. In this case the consideration can be performed by conventional elementary methods. The numerical methods included the CMBEasy software or Wolfram's Mathematica, and provided the results which were perfectly consistent with the mentioned analytic approach.

The net result is that the stability is completely defined by the sign of the coefficient $a_1$ of the Weyl-squared term.[2] The most relevant observation is that the sign of this term defines whether graviton or ghost has positive or negative kinetic energy!

One can distinguish the following three cases:

- The coefficient of the Weyl-squared term is negative, $a_1 < 0$. Then

$$G_{\text{spin}-2}(k) \sim \frac{1}{m^2}\left(\frac{1}{k^2} - \frac{1}{k^2+m^2}\right), \quad m \propto M_P\,. \tag{21}$$

In this case there are no growing modes up to the Planck scale, $\vec{k}^2 \approx M_P^2$. For the dS background this is in a perfect agreement with the previous results of Starobinsky (1979) and Hawking et al. (2001). It is remarkable that when the frequency $k = |\vec{k}|$ is getting close to the Planck scale, the growing modes start to show up. From the physical side this means that the higher derivative theory (1) is actually stable against ghost-induced perturbations, but only for the frequencies below the Planck cut-off. Some plots illustrating this situation are shown in Figure 1.

- The classical coefficient of the Weyl-squared term is positive, $a_1 > 0$ and also the sign $M_P^2 \to -M_P^2$. Then the propagator of the tensor mode has the form

$$G_{\text{spin}-2}(k) \sim \frac{1}{m^2}\left(-\frac{1}{k^2} + \frac{1}{k^2+m^2}\right), \quad m \propto M_P\,. \tag{22}$$

With this "wrong" sign of $a_1$, the massless graviton is becoming a ghost. On the contrary, massive spin-2 particle in this case has positive energy. As one could expect, in this case there is no Planck-mass threshold and, as we have found, there are rapidly growing modes at any scale of frequencies. This example is artificial, but very illustrative, for it explicitly shows the relation between mass of the ghosts and the stability of classical solutions.

Coming back to the physical case $a_1 < 0$, the natural interpretation of the result is that, at low energies, the massive ghosts are present only in the vacuum state. There are no even one of such excitations "alive" until the typical energy scale remains below the Planck mass threshold. As far as the frequency comes close to $M_P$, the ghosts start to be generated from vacuum and we observe strong instabilities.

---

[2] Let us mention that the same is true in the semiclassical case with the non-zero coefficient $c$, which corresponds to the classical $a_4$.

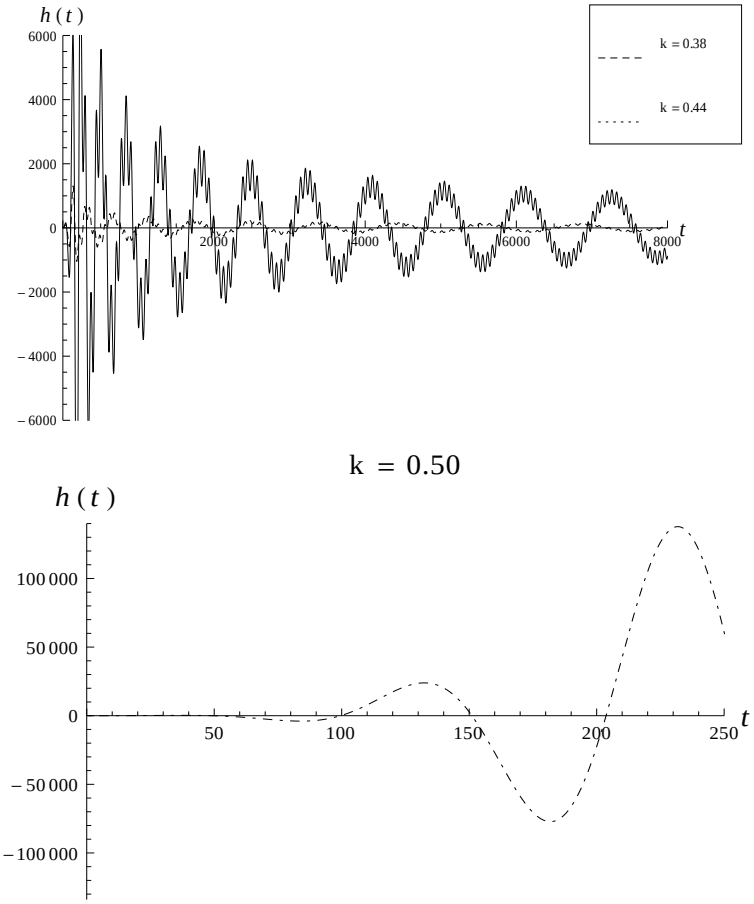


Figure 1. Illustrative plots for the case of radiation-dominated Universe. There are no growing modes up to the frequency $k \approx 0.5$ in Planck units. Starting from this value, one can observe the massive ghost making destructive work.

## 5. Conclusions and further perspectives

One should definitely quantize both matter and gravity, for otherwise the theory would not be complete. Indeed, the quantum matter is something essentially more certain than the quantum metric, simply because quantization of matter is really experimentally supported, in all senses. Since it is not possible to deal with the quantization of matter fields without higher derivatives terms (3), the main question is not whether we like these terms or not. In our opinion the question is to explain why these terms do not produce destructive instabilities in the classical gravitational solutions.

For QG with higher derivatives, the propagator includes massive nonphysical mode(s) called ghosts. These massive ghosts are capable to produce terrible instabilities, but for some unknown reason our world is stable and it is interesting to understand why this happens. At least in the cosmological case, ghosts are not produced at the energy scales far below the Planck mass. If there is no at least one such ghost excitation in the

initial spectrum, there are no instabilities at the linear approximation and the Lyapunov theorems guarantee that this will be the case, also, at the non-linear level.

Assuming that our conjecture about the situation with ghosts "sleeping" in the vacuum state is correct, the higher derivative gravity becomes a perfect candidate to be an effective QG below the Planck scale. Then we have to answer the question of whether the effect of this theory at low energies is the same of the low-energy quantum GR or not, as it was discussed in Shapiro (2009).

It is clear that the energy scale below Planck mass covers most of the possible applications. On the other hand, there is a conceptually important question of what happens with the ghosts above $M_P$. In this case we need some new ideas. The solution can be related to string theory, or to some new principles of Physics which we do not know yet. In principle, on of the options would be some principle which forbids the Planck densities of energy to form. For instance, some hypothesis which closely fit this requirements, can be found in the recent works (Dvali et al. 2011), but, in general, this problem remains open.

**Acknowledgments.** This work is based on original papers by the authors and their collaborators. We are grateful to them, especially to Júlio Fabris, for the contributions to these works. Another source of this review are seminars, mainly given by I. Sh. between 2012 and 2014. We appreciate the contribution of those who invited him to speak about the subject and also those who asked questions. The work of the authors was partially supported by CNPq, CAPES, FAPEMIG and (in case of I. Sh.) ICTP.

## References

Asorey, M., López, J. L. & Shapiro, I. L. 1997, Int. Journ. Mod. Phys. A, 12, 5711

Birell, N. D. & Davies, P. C. W. 1982, "Quantum Fields in Curved Space", Cambridge University Press, Cambridge

Buchbinder, I. L., Odintsov, S. D. & Shapiro, I. L. 1992, "Effective Action in Quantum Gravity", IOP Publishing, Bristol

de O. Salles, F. & Shapiro, I. L. 2014, Phys. Rev. D, 89, 084054

Dvali, G., Folkerts, S. & Germani, C. 2011, Phys. Rev. D, 84, 024039

Dvali, G. & Gomez, C. 2013, Fortschr. Phys., 63, 742

Fabris, J. C., Pelinson, A. M. & Shapiro, I. L. 2001, Nucl. Phys. B, 597, 539 [Erratum-ibid., 602, 644 (2001)]

Fabris, J. C., Pelinson, A. M., de O. Salles, F. & Shapiro, I. L. 2012, JCAP, 02, 019

Fradkin, E. S. & Tseytlin, A. A. 1984, Phys. Lett. B, 134, 187

Hawking, S. W., Hertog, T. & Reall, H. S. 2001, Phys. Rev. D, 63, 083504

Lavrov P. M. & Shapiro, I. L. 2010, Phys. Rev. D, 81, 044026

Myung, Yu. S. 2013, Phys. Rev. D, 88, 024039

Ostrogradski, M. 1985 Mem. Ac. St. Petersbourg VI, 4, 385

Pelinson, A. M., Shapiro, I. L. & Takakura, F. I. 2003, Nucl. Phys. B, 648, 417

Pelinson, A. M., Shapiro, I. L. & Takakura, F. I. 2004, Nucl. Phys. Proc. Suppl. B, 127, 182

Pelinson, A. M. & Shapiro, I. L. 2011, Phys. Lett. B, 694, 467

Pelinson, A. M. & Shapiro, I. L. 2011, Intern. Journ. Mod. Phys. A, 26, 3759
Riegert, R. J. 1984, Phys. Lett. B, 134, 56
Shapiro, I. L. 2002, Int. Journ. Mod. Phys. D, 11, 1159
Shapiro, I. L. & Solà, J. 2002, Phys. Lett. B, 530, 10
Shapiro, I. L. 2009, Int. J. Mod. Phys. A, 24, 1557
Starobinsky, A. A. 1979, JETP Lett., 30, 682
Starobinsky, A. A. 1979, Pisma Zh. Eksp. Teor. Fiz., 30, 719
Starobinski, A. A. 1980, Phys. Lett. B, 91, 99
Starobinsky, A. A. 1981, Zh. Eksp. Teor. Fiz., 34, 460
Starobinsky, A. A. 1983, Sov. Astron. Lett., 9, 302
Veltman, M. J. G. 1963, Physica, 29, 186
Whitt, B. 1985, Phys. Rev. D, 32, 379

*Gravitation, Relativistic Astrophysics and Cosmology*
*Second Argentinian-Brazilian Meeting, 2014*
*G. S. Vila, F. L. Vieyro and J. Fabris, eds.*

# Neutrino emission from gamma-ray bursts

F. L. Vieyro[1,2]

[1]*Instituto Argentino de Radioastronomía (IAR, CCT La Plata, CONICET), C.C.5, (1894) Villa Elisa, Buenos Aires, Argentina*
[2]*Facultad de Ciencias Astronómicas y Geofísicas, Universidad Nacional de La Plata, Paseo del Bosque s/n, (1900) La Plata, Argentina*

**Abstract.**

Gamma-ray bursts (GRBs) are the most violent and energetic events in the universe. Short GRBs seem to be the result of the final merger of two compact objects, whereas long GRBs are probably associated with the gravitational collapse of very massive stars (*collapsars*).

The central engine of a GRB can collimate relativistic jets, where shocks are produced and particles can be accelerated. Although the exact location of the region where the gamma rays are created is still under debate, it is widely accepted that the prompt emission has a different origin from the afterglow. The latter is emitted at a much greater distance from the central engine, when the fireball is decelerated by its interaction with the interstellar medium.

It seems reasonable to assume that if the prompt gamma-ray radiation and the afterglows are generated by relativistic electrons accelerated in shocks, then the same shocks should also accelerate baryons. These high-energy protons can produce neutrinos through $pp$ inelastic collisions and $p\gamma$ interactions, making GRBs candidates to be sources of high-energy neutrinos.

In this review, I discuss different scenarios where high-energy neutrinos (GeV-EeV) can be generated.

## 1. Introduction

Gamma-ray bursts (GRBs) are the most energetic explosions known to occur in the universe since the Big Bang. The initial prompt phase can last from milliseconds to several tenths of seconds, and in this short time an energy of $\sim 10^{53}$ ergs is released (e.g., Piran, 2000; Mészáros, 2002). The peak of the spectra is in the gamma-ray band (100 keV $< E <$ MeV), hence the name of these sources.

The first event was detected in July 2, 1967, by the satellites of a military program called Vela. These satellites were built by the United States to detect gamma radiation pulses emitted by possible nuclear weapon tests in space.[1] Since the features of these bursts were unlike any known nuclear weapon, its origin was a mistery, and their existence was kept as a secret for more than 6 years. Finally, in 1973, a team at Los Alamos Scientific Laboratory, led by Ray Klebesadel, rejected the possibility of these bursts being produced within the Solar System. The observations of the new gamma ray

[1]The *Partial Test Ban Treaty* signed in 1963, banned all nuclear testing on space, underwater and atmosphere. All testing was to be driven underground.

sources, which were called Gamma-ray bursts, were then published (Klebesadel et al., 1973).

For almost 20 years little progress was made in the understanding of the origin, until 1991, when the Compton Gamma Ray Observatory was launched. The observatory was equipped with the instrument BATSE (*Burst and Transient Source Explorer*), a sensitive gamma-ray detector, designed for detecting transient events. In the 9 years of the mission, BATSE registered more than 2700 events, an average of one gamma-ray burst event per day (Paciesas et al., 1999).

This instrument provided crucial data regarding the origin of GRBs. The bursts distribute isotropically on the sky, a fact that indicates an extragalactic origin.

The first afterglow in X-rays was found in 1997, by the Italian-Dutch X-ray astronomy satellite BeppoSAX. A few months later, the first optical spectrum was measured, rendering a determination of the host galaxy redshift. This detection finally confirmed that GRBs have an extragalactic origin. The host galaxies of several long bursts were found to have typical redshifts $z = 1 - 2$, which means that those GRBs occurred on very distant galaxies.

Once the GRB distance scale was identified, a new conundrum arised: what is the central engine of GRBs that is capable of generating more than $10^{50}$ ergs? The Swift observatory and the Fermi Gamma-ray Space Telescope are the missions that have helped unveiling the enigma.

Swift was launched in 2004 and is still operational. Swift is the first gamma-ray observatory designed with GRBs as the main target. It is equipped with the Burst Alert Telescope (BAT), which is a very sensitive gamma-ray detector, capable of localizing a burst with arcmin accuracy within a few seconds. It also has on board the X-ray Telescope (XRT) and the Ultraviolet/Optical Telescope (UVOT), both dedicated to study the afterglow emission.

The Fermi Gamma-ray Space Telescope was launched in 2008. One of its two main instruments is the Gamma-ray Burst Monitor (GBM); it can localize a burst with 10−degree accuracy, and has been detecting GRBs at a rate of $\sim 300$ per year (Gehrels et al., 2009).

These instruments have provided precise observations of hundreds of bursts, and have been crucial to understand many aspects of these sources.

The main topic of this article is the neutrino emission from GRBs; nevertheless, a basic discussion on GRB physics is presented in the first two sections. For more details and a complete discussion on phenomenology and theory of GRBs see, e.g., Zhang & Mészáros (2004), Gehrels et al. (2009) and Zhang & Kumar (2013).

## 2. Classification

There is a great variety of light curves of GRBs, unlike other transient sources (e.g., novas, supernovas, etc). Several categories of GRBs can be found depending on the property used as classifier. The historical classification is made considering the duration of the prompt emission, and leads to two populations of bursts: one with an average duration of $\sim 0.3$ s, and the other centered around $\sim 30$ s (see Fig. 1). Although there is a significant overlapping region where it is not clear to which category the events belong, short and long GRBs are the standard categories.

The classification in long and short relates to two different progenitors. Long GRBs make approximately 75% of the bursts. The study of long GRB afterglows shows

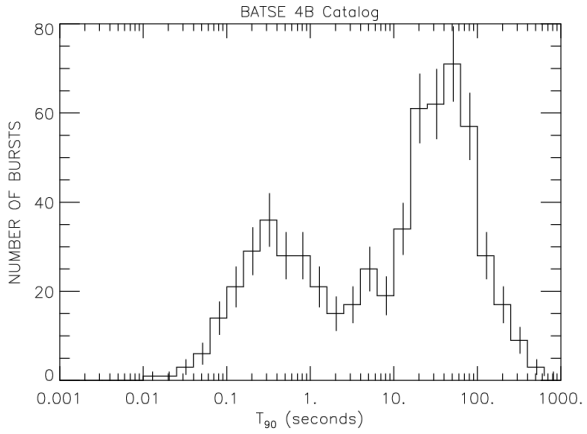


Figure 1. Duration of the bursts detected by BATSE, using a duration parameter $T90$ defined as the time over which a burst emits from 5% of its total measured counts to 95% (Paciesas et al., 1999).

that they take place in galaxies with high stellar formation rates. In addition, $\sim$ 36 of these bursts have been associated with core-collapse supernova, which provides the best evidence that long GRBs are related to the deaths of massive stars (Hjorth & Bloom, 2012).

The first afterglow of a short GRB was detected by Swift in 2005, eight years later than the long counterpart. This is due to short GRB afterglows being fainter than long GRB afterglows, and also because short GRBs account only for about 25% of gamma-ray bursts.

Few host galaxies of short GRBs have been identified, and they are usually found to be elliptical galaxies with low stellar formation rate. There has been no association with supernovae and, consequently, these events are not linked to massive stars. The origin of short GRBs is related to the merger of two compact objects. Using numerical simulations Rezzolla et al. (2011) showed that colliding neutron stars form a rapidly spinning black hole surrounded by a hot and highly magnetized torus.

## 3. Theoretical models

There are at least three basic conditions that any GRB model should fulfill:

- *Energetics*: considering that GRBs occur at cosmological distances, any model should be able to account for an equivalent isotropic energy of $10^{53}$ ergs.

- *Size of the emitting region*: since the temporal scales of variability are very short ($\sim$ 10 ms), then the emitting region should be compact.

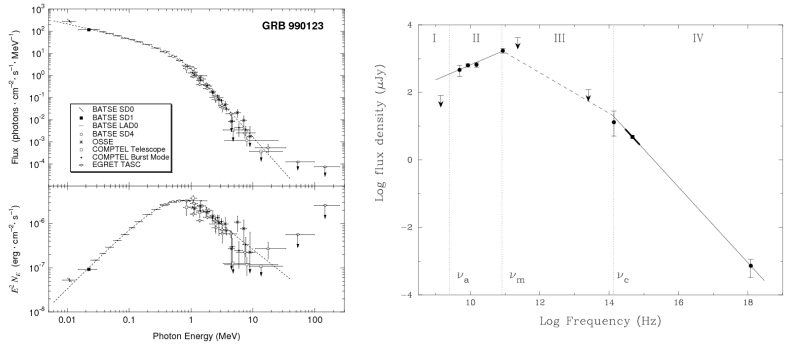


Figure 2. *Left:* Spectrum of the prompt emission of GRB 990123 detected by BATSE (Briggs et al., 1999). *Right:* Spectrum of the afterglow of GRB 970508 (Mészáros, 1999).

- *Radiation mechanism*: the prompt emission as well as the afterglow components are non-thermal (see Fig. 2), implying the presence of relativistic particles. These sources, then, should be able to accelerate particles up to relativistic energies.

These requirements can be achieved by invoking relativistic motions. If the emitting region were static, the gamma-rays should have been attenuated in the source by photo-pair production. This is known as the *compactness problem*. To ease this problem, a first ingredient of theoretical models is that the regions where the prompt and afterglow emission are produced must be moving relativistically in the direction of the observer (see Zhang & Mészáros 2004 for a detailed discussion of the compactness problem).

The typical Lorentz factor required to satisfy the observations is of the order of $\sim 100$. Relativistic jets in AGNs have Lorentz factors $\Gamma \lesssim 30$. GRBs present the fastest known bulk motions in the universe.

One of the most discussed models is the *standard fireball model*, which, until a few years ago, had been very successful describing many characteristic and predicting several features of GRB light curves and spectra. In this model, a central engine powered by accretion -the collapse of the nucleus of a massive star in the case of long GRBs, or the merger of two compact objects for short GRBs- launches a fireball shell. As the fireball propagates, internal shocks are produced by collisions between different shells. In these shocks, particles are accelerated up to relativistic energies in the flow co-moving frame and produce the prompt emission. The fireball shell is eventually decelerated by the interstellar medium, and external shocks are produced. Whereas the broad-band afterglow radiation is usually explained as the result of synchrotron radiation of electrons accelerated in the external shocks, there is still an open debate on what is the mechanism responsible of the non-thermal emission in the prompt phase, i.e., synchrotron or inverse Compton scattering.

With the advent of Swift and Fermi, however, many unexpected properties have been found. Some of these properties, such as afterglow light curves with plateau structure, X-ray flares found at both early and late times, optical flashes too variable or

long lasting prompt emission, cannot be explained by the standard fireball model, and alternative options are being explored.

Among the new models, we can mention models where the jet is magnetically dominated; in this case, the magnetic field is dragged from the highly magnetized central engine to the surface of the progenitor star of long GRBs. Internal shocks cannot be produced in magnetically dominated environments, so, in this context, the particle acceleration may be caused by dissipation of the strong magnetic fields and fast reconnection (Woosley, 1993; Komissarov et al., 2009).

## 4. Neutrino emission

GRBs can also be sources of three important non-electromagnetic signals: gravitational waves, cosmic rays, and neutrinos.

High-energy neutrinos are of particular interest, since the IceCube collaboration has recently reported the observation of 28 events, including the highest energy neutrinos ever observed, with energies in excess of 1 PeV (Aartsen et al., 2013; IceCube Collaboration, 2013). GRBs are among the best candidates to be the sources of them.

GRB models involving shocks as sites to accelerate electrons which produce prompt gamma-rays and long-term afterglows, naturally suggest that baryons should be accelerated by the same shocks as well. These accelerated protons would interact with photons and other baryons to produce high-energy neutrinos that might be detected from Earth.

In a GRB event, there are multiple sites where neutrinos with different energies are generated. There is a large peak in the photo-meson production cross-section at photon energies $E_\gamma \sim 0.35$ MeV in the proton rest frame, due to the $\Delta$-resonance (Stecker, 1973). Most of the contribution to neutrino production comes through this channel. The condition that a proton must fulfill to create pions is (Zhang & Kumar, 2013):

$$E_p E_\gamma \sim 0.147 \text{ GeV}^2 \Big(\frac{\Gamma}{1+z}\Big)^2, \tag{1}$$

where $z$ is the redshift. Neutrinos produced in $p\gamma$ interactions have energies of $E_\nu \simeq 0.05 E_p$.

Several models have been devoted to study the neutrino emission from different regions of the fireball; in what follows, some of them are briefly discussed.

### 4.1. Neutrinos in internal shocks

The photons produced inside the internal shocks within the fireball have typical energies around 1 MeV. For a Lorentz factor of $\Gamma = 100$, the characteristic proton energies for photomeson production are $10^6$ GeV. Then, photomeson interactions in internal shocks result in the production of neutrinos with $E \sim 10^{14}$ eV.

It has been recently shown by Reynoso (2014) that interactions in internal shocks can also lead to the production of PeV neutrinos. They consider a two-zone model (see also Winter et al. 2014), with an acceleration region and a cooling zone. The relation between these regions is quantified as

$$t_{\rm esc}^{-1}(E_i) = \psi_{\rm esc} t_{\rm acc}^{-1}(E_i), \tag{2}$$

where $t_{\rm esc}^{-1}$ and $t_{\rm acc}^{-1}$ are the escape and acceleration rates, respectively. Under this assumption, the value of the parameter $\psi_{\rm esc}$ is related to the energy dependence of the

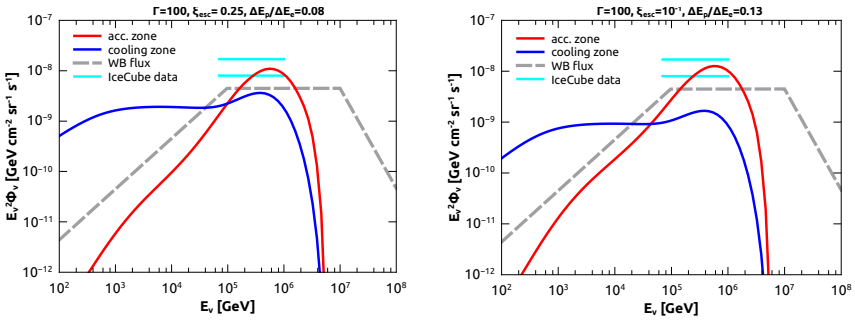


Figure 3. Diffuse flux of muon neutrinos for $\psi_{\rm esc} = 0.25$ and $\psi_{\rm esc} = 0.1$ in the left and right panels, respectively. The contribution from the acceleration zone is marked in red and the one from the cooling zone in blue. From Reynoso (2014).

particle distributions (e.g., Protheroe, 1999). The primary target for $p\gamma$ interactions are the synchrotron photons of the prompt emission. The diffuse neutrino flux is computed, and it is obtained that it can reach the level of the signal recently detected by IceCube (see Fig. 3).

For long GRBs, a different kind of internal shocks are expected in the jet interior, as a result of the propagation of the jet inside the progenitor stars. In these shocks TeV neutrinos can also be produced by photohadronic interactions. The neutrino signal is of significant relevance for the so-called *chocked* GRBs, produced when the jet is unable to break the stellar surface and produced an observable GRB (Mészáros & Waxman, 2001; Horiuchi & Ando, 2008). For these events, the neutrino emission may be the only detectable signal.

### 4.2. Neutrinos in external shocks

External shocks are produced when the fireball of a GRB is decelerated by the surrounding medium: a forward shock propagates over the interstellar medium, and a reverse shock propagates backward, inside the fireball. Photons produced in the GRB afterglow have energies from X-ray to the optical band. Then, photohadronic interactions in the external shocks would result in the production of TeV-PeV-EeV neutrinos (e.g., Waxman & Bahcall, 2000; Dai & Lu, 2001; Razzaque et al., 2004). In particular, in the standard afterglow model the reverse shock emission is thought to be responsible for the optical flash. Since protons can be accelerated up to $\sim 10^{20}$ eV in external shocks (Gallant & Achterberg, 1999), photohadronic interactions of these ultra-high energy protons with optical photons allows PeV-EeV neutrino production.

### 4.3. Neutrinos in different scenarios

Given that the standard internal shock model has been lately under discussion, different scenarios are being explored. In this regard, Gao et al. (2012) studied the neutrino emission in GRBs where the prompt emission is generated in a dissipative jet, instead of being produced in internal shocks. They explored two possibilities, baryonically or magnetically dominated dynamics.

Another example is the work by Gao & Mészáros (2012), in which they estimated the neutrino flux as a result of nuclear collisions in magnetized GRBs. They obtained a significant flux of GeV neutrinos. Murase et al. (2013), on the other hand, studied the production of GeV neutrinos in outflows loaded with neutrons, in which nuclear reactions result in subphotospheric gamma rays that can explain the prompt emission.

A different model has been proposed by Vieyro et al. (2013) in which TeV neutrinos are produced by hadronic interactions in the lateral shocks formed near the stellar surface, when the jet erupts from the star. In this work, they consider the effects of standard neutrino oscillations, and of neutrino spin-flavor precession. The latter is the result of a minimal extension of the Standard Model and was proposed by Akhmedov & Pulido (2002) as a secondary mechanism responsible for the deficit of solar electron neutrinos. The number of muon events estimated for the reverse shock region in this model is comparable with the atmospheric muon events detected by IceCube (Abbasi et al., 2011). Then, a multiyear integration might result in a detectable flux.

### 4.4. Constraining theoretical models

The study of GRBs as sources of high-energy neutrinos can help us to put constrains to the microphysics of GRBs (Zhang & Kumar, 2013). It is worth mentioning, as an example, the work by Gao et al. (2013), in which the implications of the non-detection of neutrinos from the burst GRB 130427A are discussed.

They first use a general model to put constrains on the dissipation radius, the bulk Lorentz factor and the composition of the jet. Figure 4 shows a density plot of the expected number of neutrino events for the burst GRB 130427A. The contours indicates the regions where one event is expected, for different values of the parameters $\epsilon_p$, $\epsilon_e$ and $\epsilon_B$; these quantities represent the fraction of the total energy of the jet that is dissipated and carried by protons, leptons and turbulent magnetic fields, respectively.

They also apply an internal shock model and a baryonic model to this burst, and obtained limits for the relevant parameters of each model. The most strict restrictions are found for the magnetic photospheric model, where a value of $\epsilon_p/\epsilon_e \sim 2$ is obtained, independently of $\Gamma$. The internal shock and the baryonic photosphere models are barely constrained by the absence of neutrino detection.

## 5. Summary and discussion

GRBs are currently regarded by many as the top potential high-energy neutrino sources. Several models of neutrino emission in GRBs predict detectable neutrino levels at different energies.

Current upper limits set by IceCube, however, have already ruled out the validity of some of these models and their predictions (Desiati et al., 2012). The upper limit obtained with the data collected with the 59-string configuration of IceCube is 3.7 times below some theoretical predictions.

This overestimation of the neutrino fluxes may be the result of several simplifications in the treatment of physical processes. On the one hand, many of these works do not consider the energy dependence of particle distribution, but instead only the energy budget is analysed. Hümmer et al. (2010) discussed the importance of considering the energy dependence, and they found that the normalization of the expected neutrino flux is reduced up to one order of magnitude, and the spectrum shifts to higher energies (see also Hümmer et al. 2012).

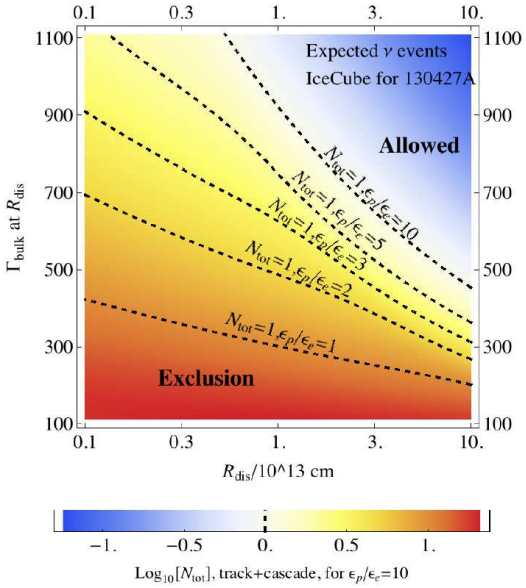


Figure 4. Map of the expected neutrino events in IceCube for GRB 130427A. Here, $\epsilon_e = 0.1$ and $\epsilon_B = 0.01$. From Gao et al. (2013).

On the other hand, the effects of magnetic field on the cooling of secondary particles cannot be neglected, since the GRB environments usually present large magnetic fields, hence synchrotron losses are significant (Li et al., 1996; Reynoso & Romero, 2009; Hümmer et al., 2012).

There are some current studies where the effects mentioned above are considered; these models predict neutrinos fluxes that might be detected by Ice Cube. With the recent completion of IceCube and the increment of the data, the study of neutrino emission might help shed light on some of the most important uncertainties in the study of GRBs, as the role of magnetic fields in the jet dynamic, and the content and composition of the fireball.

Recent works by Mészáros & Rees (2010); Gao et al. (2011); Berezinsky & Blasi (2012); Vieyro et al. (2013) have extended the calculations of neutrino emission to Population III GRBs. These stars are supposed to have been very massive, and accretion onto massive black holes (tenths of solar masses) might lead to a scaled-up collapsar gamma-ray burst (Mészáros & Rees, 2010). These events are of particular cosmological interest, since they are related to the first stars formed in the universe, and they can be used to study the universe in the re-ionization era.

**Acknowledgments.** This work was partially supported by the Argentine agency ANPCyT (PICT 00878).

**References**

Aartsen, M. G., Abbasi, R., Abdou, Y., et al. 2013, Phys. Rev. Lett., 111, 021103

Abbasi, R., Abdou, Y., Abu-Zayyad, T., et al. 2011, Phys. Rev. D, 83, 012001

Akhmedov, E. K. & Pulido, J. 2002, Physics Letters B, 529, 193

Berezinsky, V. & Blasi, P. 2012, Phys. Rev. D, 85, 123003

Briggs, M. S., Band, D. L., Kippen, R. M., et al. 1999, ApJ, 524, 82

Dai, Z. G. & Lu, T. 2001, ApJ, 551, 249

Desiati, P., Abbasi, R., Abdou, Y., et al. 2012, Proceedings for the XIV Vulcano Workshop, Vulcano (ME), Italy

Gallant, Y. A. & Achterberg, A. 1999, MNRAS, 305, L6-L10

Gao, S., Asano, K., & Mészáros, P. 2012, J. of Cosm. and Astrop. Phys., 11, 58

Gao, S., Kashiyama, K., & Meszaros, P. 2013, ApJ, 772, 1, L4

Gao, S. & Mészáros, P. 2012, Phys. Rev. D, 85, 103009

Gao, S., Toma, K., & Mészáros, P. 2011, Phys. Rev. D, 83, 103004

Gehrels, N., Ramirez-Ruiz, E., & Fox, D. B. 2009, ARA&A, 47, 567

Hjorth, J. & Bloom, J. S. 2012, in Gamma-Ray Bursts, C. Kouveliotou, R. A. M. J. Wijers and S. Woosley (eds.), Cambridge Astrophysics Series 51, Cambridge University Press, Cambridge, UK

Horiuchi, S. & Ando, S. 2008, Phys. Rev. D, 77, 063007

Hümmer, S., Baerwald, P., & Winter, W. 2012, Phys. Rev. Lett., 108, 231101

Hümmer, S., Maltoni, M., Winter, W., & Yaguna, C. 2010, Astroparticle Physics, 34, 205

IceCube Collaboration, 2013, Science, 342

Klebesadel, R. W., Strong, I. B., & Olson, R. A. 1973, ApJ, 182, L85

Komissarov, S. S., Vlahakis, N., Königl, A., & Barkov, M. V. 2009, MNRAS, 394, 1182

Li, H., Kusunose, M., & Liang, E. P. 1996, ApJ, 460, L29

Mészáros, P. 1999, A&AS, 138, 533

Mészáros, P. 2002, ARA&A, 40, 137

Mészáros, P. & Rees, M. J. 2010, ApJ, 715, 967

Mészáros, P. & Waxman, E. 2001, Phys. Rev. Lett., 87, 171102

Murase, K., Kashiyama, K., & Mészáros, P. 2013, Phys. Rev. Lett., 111, 131102

Paciesas, W. S., Meegan, C. A., Pendleton, G. N., et al. 1999, ApJS, 122, 465

Piran, T. 2000, Physics Reports, 333, 529

Protheroe, R. J. 1999, in Topics in Cosmic-Ray Astrophysics, M. A. Duvernois (ed.), 247

Razzaque, S., Mészáros, P., & Zhang, B. 2004, ApJ, 613, 1072

Reynoso, M. M. 2014, A&A, 564, A74

Reynoso, M. M. & Romero, G. E. 2009, A&A, 493, 1

Rezzolla, L., Giacomazzo, B., Baiotti, L., et al. 2011, ApJ, 732, L6

Stecker, F. W. 1973, Ap&SS, 20, 47

Vieyro, F. L., Romero, G. E., & Peres, O. L. G. 2013, A&A, 558, A142

von Kienlin, A. 2013, GRB Coordinates Network, 14473, 1

Waxman, E. & Bahcall, J. N. 2000, ApJ, 541, 707

Winter, W., Becker Tjus, J., & Klein, S. R. 2014, A&A, 569, A58

Woosley, S. E. 1993, ApJ, 405, 273

Zhang, B. & Kumar, P. 2013, Phys. Rev. Lett., 110, 121101

Zhang, B. & Mészáros, P. 2004, IJMP A, 19, 2385

Zhang, B. 2014, IJMP D, 1430002, 30002

# Contributed Talks

*Gravitation, Relativistic Astrophysics and Cosmology*
*Second Argentinian-Brazilian Meeting, 2014*
*G. S. Vila, F. L. Vieyro and J. Fabris, eds.*

# Shadow cast by a Kaluza-Klein spinning dilaton black hole

Leonardo Amarilla,[1] and Ernesto F. Eiroa[1,2]

[1]*Departamento de Física, FCEN-UBA, Buenos Aires, Argentina.*
[2]*Instituto de Astronomía y Física del Espacio, Buenos Aires, Argentina*

**Abstract.** We examine the shadow of a rotating Kaluza-Klein black hole in Einstein gravity coupled to a Maxwell field and a dilaton. The size and the shape of the shadow depend on the mass, the charge, and the angular momentum of the compact object. For a given mass, the size increases with the rotation parameter and decreases with the electric charge. The distortion with respect to the non rotating case grows with the charge and the rotation parameter. For fixed values of these parameters, the shadow is slightly larger and less deformed than in the Kerr-Newman case.

## 1. Introduction

The study of gravitational lensing by black holes has received great attention in the last decade, due to the evidence of the presence of supermassive compact objects at the galactic centers. The apparent shapes (or shadows) of non-rotating black holes are circular, but rotating ones present a deformation produced by the spin; topic recently investigated by several researchers, both in Einstein gravity and in modified theories, with the expectation that direct observation of black holes will be possible in the near future. The analysis of the shadows will be a useful tool for obtaining properties of astrophysical black holes and comparing different gravitational theories. Here we consider the shadow cast by a Kerr and by a Kaluza-Klein rotating dilaton black hole with charge, corresponding to a coupling parameter $\gamma = \sqrt{3}$. We pay special attention to the analysis of the shadow of the supermassive black hole in the center of our galaxy.

## 2. The Kerr case

In Boyer-Lindquist coordinates, the Kerr solution has the line element ($G = c = 1$)

$$\begin{aligned} ds^2 &= -(1 - \frac{2Mr}{\Sigma})dt^2 - \frac{4Mar\sin^2\theta}{\Sigma}d\varphi dt + \frac{\Sigma}{\Delta}dr^2 + \Sigma d\theta^2 \\ &\quad + \left[(r^2 + a^2)^2 - \Delta a^2 \sin^2\theta\right]\frac{\sin^2\theta}{\Sigma}d\varphi^2, \end{aligned} \tag{1}$$

where $\Sigma = r^2 + a^2\cos^2\theta$, $\Delta = r^2 - 2Mr + a^2$, and $a = J/M$ is the rotation parameter. The horizons are obtained by solving the equation $\Delta = 0$, which gives $r_\pm = M^2 \pm \sqrt{M^2 - a^2}$, where $r_+$ is the outer (event) horizon and $r_-$ is a Cauchy inner horizon. Kerr spacetime is stationary and axisymmetric. These symmetries have associated Killing vectors, so $p_t = -E$ y $p_\varphi = L_z$ are conserved along the geodesic movement of a particle. There is an additional hidden symmetry associated to a fourth conserved quantity, the

Carter constant (Chandrasekhar 1992). The geodesic structure is determined from the Hamilton-Jacobi equation:

$$\frac{\partial S}{\partial \lambda} = -\frac{1}{2} g^{\sigma\nu} \frac{\partial S}{\partial x^{\sigma}} \frac{\partial S}{\partial x^{\nu}}, \tag{2}$$

where $\lambda$ is an affine parameter along the geodesics, $g_{\sigma\nu}$ is the metric tensor, and $S$ is the Jacobi action. When the problem is *separable*, $S$ can be written in the form

$$S = \frac{1}{2}\mu^2 \lambda - Et + L_z \varphi + S_r(r) + S_\theta(\theta), \tag{3}$$

where $\mu$ is the particle mass. The equations of motion result from $p_\nu = \partial S / \partial x^\nu$. In the case of photons ($\mu = 0$), one can obtain that

$$\Sigma \frac{dt}{d\lambda} = \frac{1}{\Delta}\left[(r^2 + a^2)^2 - \Delta a^2 \sin^2\theta - 2Mar\xi\right], \qquad \Sigma \frac{dr}{d\lambda} = \sqrt{\mathcal{R}},$$

$$\Sigma \frac{d\theta}{d\lambda} = \sqrt{\Theta}, \qquad \Sigma \frac{d\varphi}{d\lambda} = \frac{1}{\Delta}\left[2Mar + (\Sigma - 2Mr)\xi \csc^2\theta\right].$$

with

$$\mathcal{R}(r) = \left[(r^2 + a^2)E - aL_z\right]^2 - \Delta\left[\mathcal{K} + (L_z - aE)^2\right], \tag{4}$$

$$\Theta(\theta) = \mathcal{K} + \cos^2\theta\left[a^2E^2 - L_z^2 \csc^2\theta\right]. \tag{5}$$

The unstable orbits of photons with constant $r$ satisfy the conditions $\mathcal{R} = 0$ and $d\mathcal{R}/dr = 0$. For a Kerr black hole, the radius solution to this system of equations depends on the trajectory of the photon. One can establish a relation between this radius and the conserved quantities, so the system of equations can be solved for the impact parameters $\xi = L_z/E$ y $\eta = \mathcal{K}/E^2$. The physical solution is given by

$$\xi(r) = \frac{(r^2 - a^2)M - \Delta r}{a(r - M)}, \qquad \eta(r) = \frac{r^3\left[4M\Delta - r(r - M)^2\right]}{a^2(r - M)^2}. \tag{6}$$

The parameters $\xi$ and $\eta$ above correspond to the unstable photon orbits. The apparent position of the photon sphere in the sky of a distant observer, generates the contour of the shadow. The "celestial" coordinates of the observer are defined as follows: $\alpha$ is the apparent perpendicular distance of the image as seen from the axis of symmetry, and $\beta$ is the apparent perpendicular distance of the image from its projection on the equatorial plane. For an angle of observation $\theta_0$ with respect to the equatorial plane, they take the form (Vázquez et al. 2004)

$$\alpha = -\xi \csc\theta_0 \quad \text{and} \quad \beta = \pm\sqrt{\eta + a^2\cos^2\theta_0 - \xi^2\cot^2\theta_0}. \tag{7}$$

In the Schwarzschild case ($a = 0$) the apparent shape of the photon sphere is a circle of radius $3\sqrt{3}M$, while for $a \neq 0$ the contour has an asymmetric form because co-rotating photons interact with a more intense potential than counter-rotating ones, producing a closer approach to the black hole in the former case. An observer located in the equatorial plane of the object ($\theta_0 = \pi/2$) is natural when considering the Galactic center supermassive black hole, in this case Eqs. (7) take the form $\alpha = -\xi$ and $\beta = \pm\sqrt{\eta}$. Besides, the effects of rotation are stronger when seen from this plane. For more details, see for example Chandrasekhar (1992).

## 3. Kaluza-Klein rotating black hole

The action corresponding to standard gravity coupled to the Maxwell field $F^{\sigma\nu}$ and the (scalar) dilaton field $\phi$, in units such that $16\pi G = c = 1$, reads

$$\mathcal{S} = \int d^4x\sqrt{-g}\left[-R + 2(\nabla\phi)^2 + e^{-2\gamma\phi}F^2\right], \tag{8}$$

where $R$ is the Ricci scalar. Exact stationary rotating solutions are only known for certain values of the coupling parameter; $\gamma = \sqrt{3}$ leads to the so called Kaluza-Klein rotating black hole, which is obtained by taking the product of the four dimensional Kerr metric, in the Boyer-Lindquist coordinates, with an extra dimension possessing translational symmetry, and then making a boost transformation with velocity $v$ along the fifth dimension. The four dimensional section has the form (Frolov et al. 1987; Horne et al. 1992)

$$\begin{aligned} ds^2 &= -\frac{1-Z}{B}dt^2 - \frac{2aZ\sin^2\theta}{B\sqrt{1-v^2}}dtd\varphi + \frac{B\Sigma}{\Delta_0}dr^2 + B\Sigma d\theta^2 \\ &\quad + \left[B(r^2+a^2) + a^2\frac{Z}{B}\sin^2\theta\right]\sin^2\theta d\varphi^2, \end{aligned} \tag{9}$$

where $\Sigma = r^2 + a^2\cos^2\theta$, $\Delta_0 = r^2 - 2mr + a^2$, $B = \sqrt{1 + Zv^2/(1-v^2)}$, and $Z = 2mr/\Sigma$, with $m$ the mass and $a$ the rotation parameter of the original Kerr solution. The metric (9), along with the electromagnetic vector field $A_t = (1/2)v(1-v^2)^{-1}ZB^{-2}$, and $A_\varphi = -(1/2)av(1-v^2)^{-1/2}ZB^{-2}\sin^2\theta$, and the dilaton field $\phi = -(\sqrt{3}/2)\log B$, is a solution of the equations of motion corresponding to the action (8) for $\gamma = \sqrt{3}$. The geometry (9) is asymptotically flat and represents a black hole with physical mass $M = m\left[1 + (1/2)v^2(1-v^2)^{-1}\right]$, charge $Q = mv(1-v^2)^{-1}$, and angular momentum $J = ma(1-v^2)^{-1/2}$. The physical rotation parameter is defined by $A = J/M$. The sign of the charge $Q$ is determined by the sign of $v$, due to the physical bound $|v| < 1$; if $v = 0$ one recovers the Kerr solution. The roots of $\Sigma$ and $\Delta_0$ are associated to a curvature singularity at $r = 0$ and $\theta = \pi/2$, and to regular horizons, respectively. The event horizon is located at $r_+ = m + \sqrt{m^2 - a^2}$, and exists if $m^2 \geq a^2$. We adopt $M = 1$, which is equivalent to adimensionalize all quantities with $M$.

From the Hamilton-Jacobi equation, for null geodesics ($\mu = 0$) one can obtain the corresponding equations of motion (Amarilla et al. 2013):

$$B\Sigma\frac{dt}{d\lambda} = \frac{2mr}{\Delta_0}\left[(r^2+a^2)\left(\frac{1}{Z} + \frac{v^2}{1-v^2}\right)E + a^2E\sin^2\theta - \frac{aL_z}{\sqrt{1-v^2}}\right],$$

$$B\Sigma\frac{dr}{d\lambda} = \sqrt{\mathcal{R}}, \qquad B\Sigma\frac{d\theta}{d\lambda} = \sqrt{\Theta}, \qquad B\Sigma\frac{d\varphi}{d\lambda} = \frac{2mr}{\Delta_0}\left(\frac{aE}{\sqrt{1-v^2}} - \frac{Z-1}{Z}L_z\csc^2\theta\right),$$

where the function $\mathcal{R}(r)$ has the form

$$\mathcal{R} = \mathcal{R}_{\rm Kerr} + \frac{2r\left\{\left[(aE - L_z)^2 - 2L_z^2 - \mathcal{K} + 2E^2r^2\right]v^2 + 4aL_zE(1-\sqrt{1-v^2})\right\}}{2-v^2}, \tag{10}$$

and $\Theta(\theta)$ is given by Eq. (5). The photon sphere conditions $\mathcal{R}(r) = 0$ and $d\mathcal{R}(r)/dr = 0$ are fulfilled by the impact parameters

$$\begin{aligned}
\xi(r) &= \frac{2(a^2 - r^2)\sqrt{1 - v^2} + \Delta_0\sqrt{\vartheta}}{\zeta}, \\
\eta(r) &= \frac{r^2}{\zeta^2}\left\{4\Delta_0\sqrt{\vartheta}\sqrt{1 - v^2} + 2a^2 r(2 - v^2)^2 + 4a^2 v^2(1 - v^2)\right. \\
&\quad -\frac{r}{2 - v^2}\left[8r(5 + (r - 4)r) + 4(8 - r(31 + 3(r - 6)r))v^2\right. \\
&\quad \left.\left.+2(-32 + r(58 + 3(r - 8)r))v^4 - (r - 4)^2(r - 2)v^6\right]\right\}, \qquad (11)
\end{aligned}$$

where $\vartheta = r[2v^2 + r(2 - v^2)](2 - v^2)$ and $\zeta = a[2(1 - v^2) - r(2 - v^2)]$. The celestial coordinates of the contour of the shadow are determined by replacing these equations in Eqs. (7), which are also valid for this spacetime. For an equatorial observer ($\theta_0 = \pi/2$) these equations simplify to $\alpha = -\xi$ and $\beta = \pm\sqrt{\eta}$.

The shadow can be characterized by using two observables (Hioki et al. 2009). The observable $R_s$ is defined as the radius of a reference circle passing by three points of the shadow: the top position $(\alpha_t, \beta_t)$, the bottom position $(\alpha_b, \beta_b)$, and the point corresponding to the unstable retrograde circular orbit seen by an observer on the equatorial plane $(\alpha_r, 0)$. The distortion parameter $\delta_s$ is defined by the quotient $D/R_s$, where $D$ is the difference between the endpoints of the circle and of the shadow, both of them at the opposite side of the point $(\alpha_r, 0)$. The radius $R_s$ gives the approximate size of the shadow, while $\delta_s$ measures its deformation with respect to the reference circle. If the inclination angle $\theta_0$ is independently known, measurements of $R_s$ and $\delta_s$ could serve to find the physical rotation parameter $A$ and the charge $Q$ (adimensionalized with $M$). These observables are given by $R_s = [(\alpha_t - \alpha_r)^2 + \beta_t^2][2|\alpha_t - \alpha_r|]^{-1}$ and $\delta_s = (\tilde{\alpha}_p - \alpha_p)R_s^{-1}$, where $(\tilde{\alpha}_p, 0)$ and $(\alpha_p, 0)$ are the points where the reference circle and the contour of the shadow cut the horizontal axis at the opposite side of $(\alpha_r, 0)$, respectively.

In Fig. 1, the borders of the shadows of Kaluza-Klein black holes are shown for different values of the physical rotation parameter $A$ and the electric charge $Q$, with $0 \leq |Q| \leq Q_{max}(A)$. The case $A = 0$ is shown in the left plot; the size of the shadow decreases with $Q$, from $R_s = 3\sqrt{3}$ until it shrinks to a point when $Q = Q_{max}(0) = 2$. This is a remarkable feature of this theory, compared with the Reissner-Nordström General Relativity solution for which $R_s = 3\sqrt{3}$ when $Q = 0$, and reaching a minimum size $R_s = 4$ in the extremal case $Q = 1$. The center and right plots show the shadows corresponding respectively to $A = 0.5$ and $A = 0.9$; again, the size of them decreases with $Q$, starting from the same value as for the Kerr solution for fixed $A$ and $Q = 0$, and reaching different extremal sizes for fixed $A$ and $Q = Q_{max}(A)$, when compared with those found for the Kerr-Newman solution. The maximum allowed charge for fixed $A$ is larger than for Kerr-Newman ones, so they can have larger amounts of charge before becoming naked singularities. The shadows of Kaluza-Klein black holes are always bigger than those of Kerr-Newman ones, for the same values of $A$ and $Q$. In Fig. 2 (left), the observable $R_s$ is plotted as a function of $Q$, for several values of $A$: it decreases with $Q$ for all $A$, and the values of $R_s$ are similar for the different values of $A$ considered in the plot; from the frame inside, where the range of $Q$ is smaller, it can be seen that $R_s$ increases with $A$. Each curve ends when the horizon fade out and a naked singularity

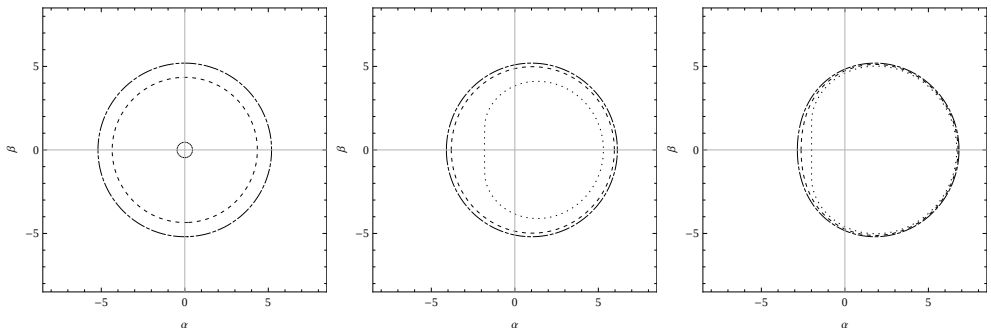


Figure 1. Shadow contours ($\theta_0 = \pi/2$). Left: $A = 0$, $Q = 0$ (dashed-dotted), 0.5 (dashed), and 1.99 (dotted); center: $A = 0.5$, $Q = 0$ (dashed-dotted), 0.5 (dashed), and $Q_{max} = 1.1298$ (dotted); right: $A = 0.9$, $Q = 0$ (dashed-dotted), 0.3 (dashed), and $Q_{max} = 0.4583$ (dotted).

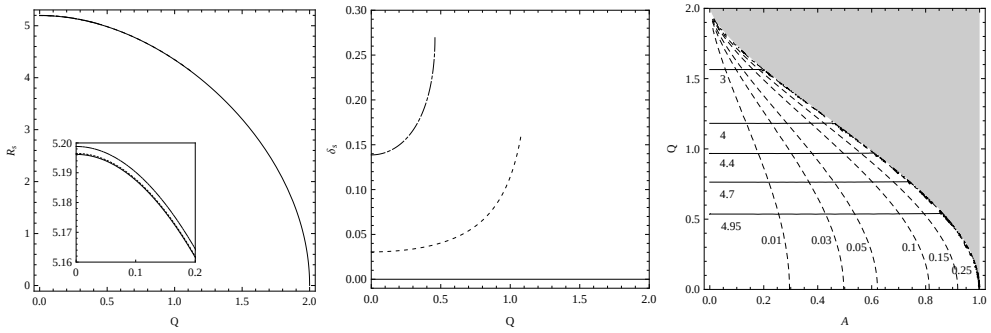


Figure 2. Observables ($\theta_0 = \pi/2$). Left and center: plots of $R_s$ and $\delta_s$ for $A = 0$ (full), $A = 0.5$ (dashed), and $A = 0.9$ (dashed-dotted). Right: contour plots of $R_s$ (full) and $\delta_s$ (dashed).

is formed, for the value $Q_{max}(A)$. In Fig. 2 (center), the observable $\delta_s$ is plotted as a function of $Q$; it increases with the charge until a maximum distortion, obtained when $Q_{max}(A)$. The distortion is an increasing function of $A$ for a fixed value of $Q$. For the same values of $A$ and $Q$, the shadows corresponding to Kaluza-Klein black holes are less distorted than the shadows of Kerr-Newman ones. In Fig. 2 (right), the contour curves with constant $R_s$ and $\delta_s$ are shown in the plane $(A, Q)$; the gray zone representing naked singularities is outside the scope of this work, the boundary corresponds to the curve $Q_{max}(A)$. The values of $A$ and $Q$ an be extracted from the intersection of the curves with constant $R_s$ and $\delta_s$; there is no ambiguity because these curves intersect each other in a unique point.

The angular size of the shadow can be estimated by $\theta_s = R_s/D_o$, with $D_o$ the distance between the black hole and the observer. In the case of the supermassive Galactic black hole Sgr A* (Guillesen et al. 2009), for which $M = 4.3 \times 10^6 M_\odot$ and $D_o = 8.3$ kpc, and taking $\theta_0 = \pi/2$, the results are shown in the following table:

| | $KN$ | | | $KKRD$ | | |
|---|---|---|---|---|---|---|
| $A = 0 \quad \vert \quad Q$ | 0 | 0.25 | 0.5 | 0 | 0.25 | 0.5 |
| $\theta_s(\mu\text{as})$ | 26.5718 | 26.2916 | 25.4047 | 26.5718 | 26.2959 | 25.4763 |
| $\delta_s(\%)$ | 0 | 0 | 0 | 0 | 0 | 0 |
| $A = 0.5 \quad \vert \quad Q$ | 0 | 0.2 | 0.4 | 0 | 0.2 | 0.4 |
| $\theta_s(\mu\text{as})$ | 26.5735 | 26.3951 | 25.8419 | 26.5735 | 26.3968 | 25.8707 |
| $\delta_s(\%)$ | 3.05086 | 3.19113 | 3.69364 | 3.05086 | 3.18884 | 3.64816 |
| $A = 0.9 \quad \vert \quad Q$ | 0 | 0.05 | 0.1 | 0 | 0.05 | 0.1 |
| $\theta_s(\mu\text{as})$ | 26.5855 | 26.5744 | 26.5413 | 26.5855 | 26.5745 | 26.5414 |
| $\delta_s(\%)$ | 13.8666 | 13.9301 | 14.1248 | 13.8666 | 13.9300 | 14.1236 |

From the table one can see that a resolution of the order of 0.01 $\mu$as or better is needed to observe deviations from General Relativity.

## 4. Discussion

We have investigated the shadow due to a spinning charged dilaton black hole, with coupling constant $\gamma = \sqrt{3}$, corresponding to a Kaluza-Klein reduction to four spacetime dimensions. We have obtained that, for fixed rotation parameter, mass, and charge, the presence of the dilaton results in a shadow that is slightly larger and with a reduced deformation, compared with the Kerr-Newman one.

In the next years, direct imaging of black holes will be possible (Johannsen et al. 2012). The Event Horizon Telescope, consisting of radio-telescopes scattered over the Earth, will reach a resolution of 15 $\mu$as at 345 GHz. RadioAstron is a space-based radio telescope launched in 2011, capable of carrying out measurements with 1-10 $\mu$as angular resolution. The space-based Millimetron mission may provide the angular resolution of 0.3 $\mu$as or less at 0.4 mm. The MAXIM project is a space-based X-ray interferometer with an expected angular resolution of about 0.1 $\mu$as. These instruments will be capable of observing the shadow of the supermassive Galactic black hole and those corresponding to nearby galaxies. However, in order to detect the deviations of General Relativity analyzed in this work, more advanced instruments with a better angular resolution is required.

**Acknowledgments.** This work was supported by CONICET and UBA.

## References

Amarilla, L. & Eiroa, E. F. 2013, Phys. Rev. D, 87, 044057

Chandrasekhar, S. 1992, "The mathematical theory of black holes", Oxford U. P.

Frolov, V. P., Zelnikov, A. I. & Bleyer, U. 1987, Ann. Phys. (Berlin), 499, 371

Guillesen et al. 2009, Astrophys. J., 692, 1075

Hioki, K. & Maeda, K. I. 2009, Phys. Rev. D, 80, 024042

Horne, J. H. & Horowitz, G. T. 1992, Phys. Rev. D, 46, 1340

Johannsen, T. et al. 2012, Astrophys. J., 758, 30

Vázquez, S. E. & Esteban, E. P. 2004, Nuovo Cim., 119B, 489

*Gravitation, Relativistic Astrophysics and Cosmology*
*Second Argentinian-Brazilian Meeting, 2014*
*G. S. Vila, F. L. Vieyro and J. Fabris, eds.*

# Constraints on cosmological parameters from Planck and BICEP2 data

Luis A. Anchordoqui

*Department of Physics and Astronomy, Lehman College, City University of New York, Bronx NY 10468, USA*

**Abstract.** We show that the tension introduced by the detection of large amplitude gravitational wave power by the BICEP2 experiment with temperature anisotropy measurements by the Planck mission is alleviated in models where extra light species contribute to the effective number of relativistic degrees of freedom. We also show that inflationary models based on $S$-dual potentials are in agreement with Planck and BICEP2 data.

## 1. Fitting ΛCDM + $r$ to Planck and BICEP2 data

Measurements of the cosmic microwave background (CMB) and large scale structure (LSS) indicate that we live in a spatially-flat, accelerating, infinite universe composed of 4% of baryons ($b$), 26% of (cold) dark matter (CDM), and 70% of dark energy ($\Lambda$). These observations also reveal that the universe has tiny ripples of adiabatic, scale-invariant, Gaussian density perturbations. The favored ΛCDM model implicitly includes the hypothesis of a very early period in which the scale factor of the universe expands exponentially: $a \propto e^{Ht}$, where $H = \dot{a}/a$ is the Hubble parameter (see e.g. Baumann 2009). If the interval of exponential expansion satisfies $\Delta t > N/H$, with $N$ above about 50 to 60, a small casually connected region can grow sufficiently to accommodate the observed homogeneity and isotropy, to dilute any overdensity of magnetic monopoles, and to flatten the spatial hyper-surfaces (i.e., $\Omega \equiv \frac{8\pi\rho}{3M_{\rm Pl}H^2} \to 1$, where $M_{\rm PL} = G^{-1/2}$ is the Planck mass and $\rho$ the energy density; throughout we use natural units, $c = \hbar = 1$). Quantum fluctuations during this inflationary period can explain the observed cosmological perturbations.

Fluctuations are created quantum mechanically on subhorizon scales with a spectrum of wavenumbers $k$. (A mode $k$ is called superhorizon when $k < aH$ and subhorizon when $k > aH$.) While comoving scales, $k^{-1}$, remain constant the comoving Hubble radius, $(aH)^{-1}$, shrinks quasi-exponentially during inflation (driving the universe toward flatness) and the perturbations exit the horizon. Causal physics cannot act on superhorizon perturbations and they freeze until horizon re-entry at late times. A mode exiting the horizon can then be described by a classical probability distribution with variance given by the power spectrum $\mathcal{P}_\chi(k)$. After horizon re-entry the fluctuations evolve into anisotropies in the CMB and perturbations in the LSS. The scale-dependence of the power spectrum is defined by the scalar spectral index, $n_s - 1 \equiv d\ln\mathcal{P}_\chi/d\ln k$, and its running $\alpha_s \equiv dn_s/d\ln k$. The power spectrum is often approximated by a power law form: $\mathcal{P}(k) = A_s(k_*)\,(k/k_*)^{n_s-1+\frac{1}{2}\alpha_s \ln\left(\frac{k}{k_*}\right)+\cdots}$, where $k_*$ is an arbitrary reference that typifies scales probed by the CMB.

The Planck temperature spectrum at high multipoles ($l \gtrsim 40$) describes the standard spatially-flat ΛCDM 6-parameter model $\{\Omega_b h^2, \Omega_{\rm CDB} h^2, \Theta_s, \tau, n_s, A_s\}$ with high precision: *(i)* baryon density, $\Omega_b = 0.02207 \pm 0.00033$; *(ii)* CDM density, $\Omega_{\rm CDM} h^2 = 0.1196 \pm 0.0031$; *(iii)* angular size of the sound horizon at recombination, $\Theta_s = (1.04132 \pm 0.00068) \times 10^{-2}$; *(iv)* Thomson scattering optical depth due to reionization, $\tau = 0.097 \pm 0.038$; *(v)* scalar spectral index, $n_s = 0.9616 \pm 0.0094$; *(vi)* power spectrum amplitude of adiabatic scalar perturbations, $\ln(10^{10} A_s) = 3.103 \pm 0.072$ (Ade et al. 2014b). Planck data also constrain the Hubble constant $h = 0.674 \pm 0.012$ and $\Omega_\Lambda = 0.686 \pm 0.020$. (Herein we adopt the usual convention of writing the Hubble constant at the present day as $H_0 = 100\, h$ km s$^{-1}$ Mpc$^{-1}$.) Note, however, that the data only measure accurately the acoustic scale, and the relation to underlying expansion parameters (e.g., via the angular-diameter distance) depends on the assumed cosmology, including the shape of the primordial fluctuation spectrum. Even small changes in model assumptions can change $h$ noticeably. Unexpectedly, the $H_0$ inference from Planck data deviates by more than $2\sigma$ from the previous result from the maser-cepheid-supernovae distance ladder $h = 0.738 \pm 0.024$ (Riess et al. 2011). The impact of the Planck $h$ estimate is particularly important in the determination of the number of "equivalent" light neutrino species: $N_{\rm eff}$ (Steigman et al. 1977). Combining observations of the CMB with data from baryon acoustic oscillations (BAO), the Planck Collaboration reported $N_{\rm eff} = 3.30 \pm 0.27$ (Ade et al. 2014c). However, if the value of $h$ is not allowed to float in the fit, but instead is frozen to the value determined from the maser-cepheid-supernovae distance ladder the Planck CMB data then gives $N_{\rm eff} = 3.62 \pm 0.25$, which suggests new neutrino-like physics (at around the $2.3\sigma$ level).

Inflation also produces fluctuations in the tensor part of the spatial metric. The gravity-wave fluctuations are also frozen on super-horizon scales and their $B$-mode power spectrum, $\mathcal{P}_h = A_t \left(\frac{k}{k_*}\right)^{n_t + \frac{1}{2}\alpha_t \ln\left(\frac{k}{k_*}\right) + \cdots}$, can be imprinted in the CMB temperature and polarization. We define the tensor-to-scalar amplitude ratio $r = A_t / A_s$ as the free parameter for the ΛCDM + r model.

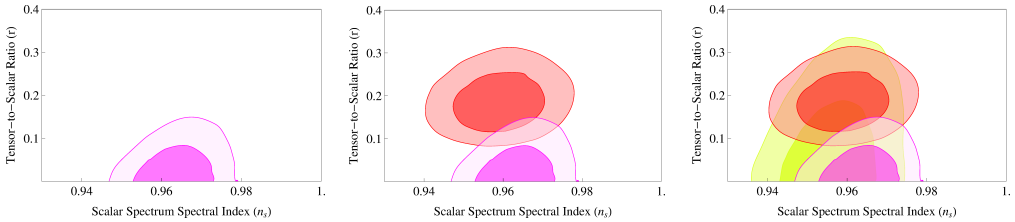


Figure 1. Marginalized joint 68% CL and 95% CL regions for $(r, n_s)$ using Planck + WMAP + BAO data without a running spectral index (left), BICEP2 data with $\alpha_s \neq 0$ (middle), and Planck + WMAP + BAO data with $\alpha_s \neq 0$ (right).

As the BICEP2 Collaboration carefully emphasized (Ade et al. 2014a), the measurement of $r = 0.2^{+0.07}_{-0.05}$ (or $r = 0.16^{+0.06}_{-0.05}$ after foreground subtraction, with $r = 0$ disfavored at $5.9\sigma$) from the B-mode polarization appears to be in tension with the 95% CL upper limits reported by the WMAP ($r < 0.13$, Hinshaw et al. 2009) and Planck ($r < 0.11$, Ade et al. 2014b) collaborations from the large-scale CMB temperature power spectrum. As shown in Fig. 1, extension of the 7-parameter model to include non-zero running of the spectral index ameliorates the tension. However, the

combination of Planck and BICEP2 data favors $\alpha_s < 0$ at almost the $3\sigma$ level, with best fit value around $\alpha_s = -0.028 \pm 0.009$ (68%CL) (Ade et al. 2014a). This is about 100 times larger than single-field ($\phi$) inflation would predict. Such a particular running can be accommodated, however, if $V'''/V$ is roughly 100 times larger than the natural expectation from the size of $V'/V \sim (10M_{\rm Pl})^{-1}$ and $V''/V \sim (10M_{\rm Pl})^{-2}$, where $V(\phi)$ is the inflaton potential (Smith et al. 2014). In Fig. 2 we compare the aftermath of the multiparameter fit of $\{\Omega_b h^2, \Omega_{\rm CDB} h^2, \Theta_s, \tau, n_s, A_s, r, N_{\rm eff}, \sum m_\nu\}$ to the data reported by the Planck and BICEP2 collaborations (Dvorkin et al. 2014; Anchordoqui et al. 2014a). Clearly, a higher effective number of relativistic species can relieve the tension between Planck and BICEP2 results. As shown in Fig. 3, the best multiparameter fit yields $N_{\rm eff} = 0.81 \pm 0.25$ and $h = 0.70 \pm 0.01$, which are consistent with previous measurements.

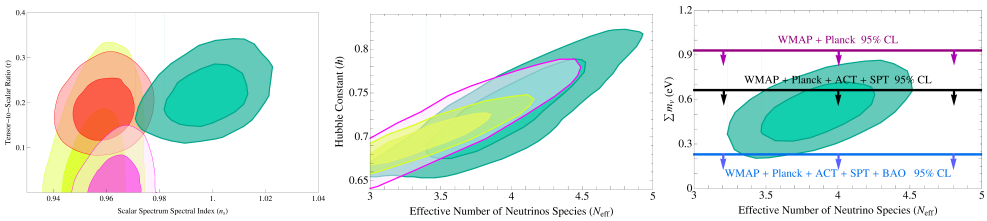


Figure 2. *Left:* Marginalized joint 68% CL and 95% CL regions for $(r, n_s)$ using Planck + WMAP + BAO with and without a running spectral index, BICEP2 data with $\alpha_s \neq 0$ and allowed regions of the 9-parameter fit. *Middle:* 68% and 95% confidence regions for $\Lambda$CDM + $N_{\rm eff}$, using Planck + WMAP (pink) and Planck + WMAP + BAO (yellow) data, together with allowed regions of the 9-parameter fit (green) together . *Right:* 68% and 95% confidence regions of the 9-parameter fit. The horizontal lines indicate the 95% CL upper limits on $\sum m_\nu$.

We end with an observation: that one should keep in mind that there is an on going controversy concerning the effect of background on the BICEP2 result (Liu et al. 2014;

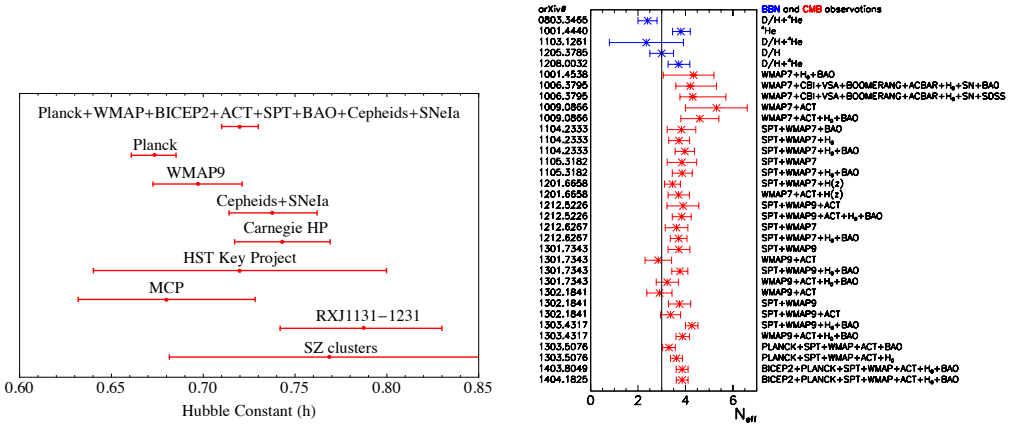


Figure 3. Recent $H_0$ (left) and $N_{\rm eff}$ (right) measurements and the $1\sigma$ confidence intervals from various combinations of models and data sets.

Flauger et al. 2014). In the next section we play devil's advocate and assume that the BICEP2 results are flawed.

## 2. *S*-dual Inflation

Planck data favor standard slow-roll single field inflationary models with plateau-like potentials $V(\phi)$ for which $V'' < 0$, over power-law potentials. However, most of these plateau-like inflaton potentials experience the so-called "unlikeliness problem" (Ijjas et al. 2013). The requirement that $V'' < 0$ in the de Sitter region, and the avoidance of the unlikeliness problem, must now also accommodate (if possible) the tensor-to-scalar ratio detected by BICEP2 data. Finally, a wish rather than a constraint: that the inflaton potential possess some connection to particle physics. To this end, we hypothesize that the potential be invariant under the $S$-duality constraint $g \to 1/g$, or $\phi \to -\phi$, where $\phi$ is the dilaton/inflaton, and $g \sim e^{\phi/M}$.[1] Here $M$ is expected to be within a few orders of magnitude of $M_{\rm Pl}$. This requirement forces the functional form $V(\phi) = f[\cosh(\phi/M)]$ on the potential. In what follows we take for $V$ the $S$ self-dual form $V_1 = V_0\,\mathrm{sech}(\phi/M)$, and $V_2 = V_0\left[\mathrm{sech}(3\phi/M) - \frac{1}{4}\mathrm{sech}^2(\phi/M)\right]$, which solve the unlikeliness problem because they have no power-law wall. For $V_1$, as for power-law inflation (with an exponential potential), inflation does not end. We assume that the dynamics of a second field leads to exit from the inflationary phase into the reheating phase. The requirement that there be 50 to 60 $e$-folds of observable inflation yields $M \gtrsim 1.4 M_{\rm Pl}$, constraining the available region in the $r - n_s$ plane. As can be seen in Fig. 4, the allowed region is consistent with both Planck and BICEP2 data. (Details of the calculation are given in Anchordoqui et al. 2014b). However, as anticipated above, the prediction for $\alpha_s$ is about 100 times smaller than the observed 68% confidence regions, see Fig. 5. For $\alpha_s \neq 0$, agreement with data is only attained at 95% CL.

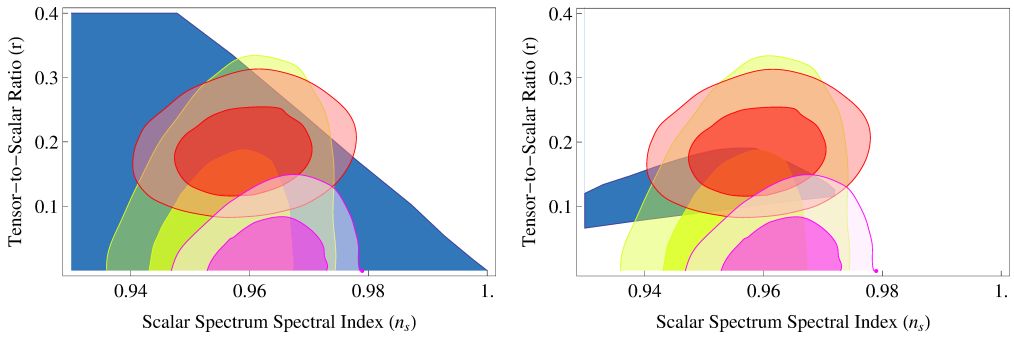


Figure 4. Available parameter space to the potential $V_1$ (left) and $V_2$ (right) together with favored regions by Planck and BICEP2 data (Anchordoqui et al. 2014b). For $V_2$, $N > 60$ corresponds to $r \lesssim 0.1$

[1] String theory exhibits various forms of dualities, i.e. relation between different theories at large and small radii of the compactified manifold (traget space duality, or $T$ duality, Giveon et al. 1994) and at strong and weak coupling ($S$ duality, Font et al. 1990). At the classical level, these dualities appear in equations of motion and in their solutions. Herein we do not attempt a full association with a particular string vacuum, but simply regard the self-dual constraint as a relic of string physics in big bang cosmology.

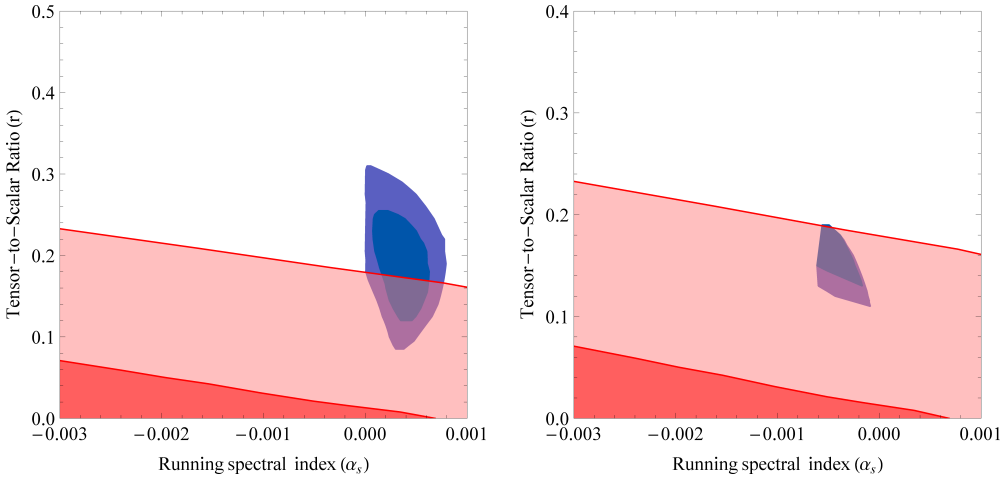


Figure 5. The blue regions show the predictions of $\alpha_2$ for the parameter space available to $V_1$ (left) and $V_2$ (right) after fixing $r$ to be within the 68% and 95% CL regions of BICEP2 measurements. The red areas show the 68% and 95% CL regions favored by a combination of Planck data, WMAP polarization data and small scale CMB data (Ade et al. 2014b).

**Acknowledgments.** I thank my collaborators Vernon Barger, Haim Goldberg, Xing Huang, Danny Marfatia, and Brian Vlcek for their contributions to the work discussed here. This work has been supported by the U.S. NSF CAREER Award PHY-1053663 and by NASA Grant No. NNX13AH52G.

## References

Ade, P. A. R., et al. [BICEP2 Collaboration] 2014a, PhRvL, 112, 241101

Ade, P. A. R., et al. [Planck Collaboration] 2014b, A&A, 571, A22

Ade, P. A. R., et al. [Planck Collaboration] 2014c, A&A, 571, A16

Anchordoqui, L. A., Goldberg, H., Huang, X. & Vlcek B. J. 2014a, JCAP, 1406, 042

Anchordoqui, L. A., Barger, V., Goldberg, H., Huang, X. & Marfatia, D. 2014b, PhLB, 734, 134

Baumann, D. 2009, arXiv:0907.5424.

Dvorkin, C., Wyman, M., Rudd, D. H. & Hu, W. 2014, PRD, 90, 083503

Flauger, R., Hill, J. C. & Spergel, D. N. 2014, JCAP, 8, 39

Font, A., Ibáñez, L. E., Lüst, D. & Quevedo, F. 1990, PhLB, 249, 35

Giveon, A., Porrati, M. & Rabinovici, E. 1994, PhR, 244, 77

Hinshaw, G., et al. [WMAP Collaboration] 2013, ApJS, 208, 19

Ijjas, A., Steinhardt, P. J. & Loeb, A. 2013, PhLB, 723, 261

Liu, H., Mertsch, P. & Sarkar, S. 2014, ApJ, 789, L29

Riess, A. G., et al. 2011, ApJ, 730, 119 [Erratum-ibid. 732, 129, (2011)]

Smith, K. M., Dvorkin, C., Boyle, L., Turok, N., Halpern, M., Hinshaw, G. & Gold, B. 2014, PhRvL, 113, 031301

Steigman, G., Schramm, D. N. & Gunn, J. E. 1977, PhLB, 66, 202

*Gravitation, Relativistic Astrophysics and Cosmology*
*Second Argentinian-Brazilian Meeting, 2014*
*G. S. Vila, F. L. Vieyro and J. Fabris, eds.*

# Collisionless self-gravitating systems in $f(R)$-gravity within Palatini approach and relativistic Boltzmann equation in the Newtonian approach

Raíla André and Gilberto M. Kremer

*Departamento de Física, Universidade Federal do Paraná, Curitiba, Brazil*

**Abstract.** In this work we analyze the dynamics of collisionless self-gravitating systems described by the $f(R)$-gravity and Boltzmann equation in the weak field approximation, focusing on the Jeans instability for theses systems. The field equations in this approximation were obtained within the Palatini formalism. Through the solution of coupled equations we achieved the collapse criterion for infinite homogeneous fluid and stellar systems, which is given by a dispersion relation. This result is compared with the results of the standard case and the case for $f(R)$-gravity in metric formalism, in order to see the difference among them. The limit of instability varies according to which theory of gravity is adopted.

## 1. Introduction

The General Relativity (GR) has emerged as a highly successful theory for cosmological models, surviving various tests. In search of a generalization of GR emerged a theory of gravity known as modified $f(R)$-gravity. An important consequence of this new theory resides in the fact that it is no longer necessary to introduce unknown entities to explain the accelerated expansion of the Universe and the formation of structures. Searching for further generalization, it was introduced also the Palatini formalism where the most fundamental aspect to be noted is the independence, *a priori*, between the metric tensor and affine connection.

In this work, in order to study the formation of structures, we adopt a model described by $f(R)$-gravity from the point of view of the Palatini approach, which is able to describe the dynamics and the collapse of collisionless self-gravitating systems. To investigate this dynamics, it becomes necessary the introduction of the collisionless Boltzmann and Poisson equations for the fields. The Boltzmann equation is an essential tool for the understanding of the processes that occurs in interstellar clouds, as the damping waves perturbations. Here we investigated the Jeans instability for physical systems that exhibit weak gravitational field, with slow variation or static and objects which moves slowly compared to the speed of light. This instability causes the collapse of interstellar gas clouds and hence, the formation of structures. This occurs when the internal pressure of the gas is not enough to prevent gravitational collapse. The aim of this work is to show the difference in the behavior between the solutions obtained from this model and from those obtained by $f(R)$-gravity in the metric formalism in the Newtonian limit (Capozziello et al., 2012) and by Newtonian gravity (see e.g. Binney & Tremaine, 2008). Here we adopt the signature $(-,+,+,+)$ and follow the book (Weinberg, 1972) for the conventions of the Riemann tensor and its contractions.

## 2. Palatini formalism for $f(R)$-gravity in the Newtonian limit

The action which represent the modified gravity theories reads

$$S = \int dx^4 \sqrt{-g}\,[-f(R)/(2\kappa) + \mathcal{L}_m] \tag{1}$$

where $f(R)$ is an analytic function of the Ricci scalar $R$, $\kappa = 8\pi G/c^4$ denotes the gravitational field coupling and $\mathcal{L}_m$ is the Lagrangian density of the matter field.

From the variation of the action (1) according to the Palatini formalism we get the modified Einstein's field equations

$$f'(R)R_{\mu\nu} - \frac{1}{2}g_{\mu\nu}f(R) = -\kappa T_{\mu\nu} = \frac{2\kappa}{\sqrt{-g}}\frac{\delta\left(\mathcal{L}_m\sqrt{-g}\right)}{\delta g^{\mu\nu}}. \tag{2}$$

Above $f' \equiv f'(R) = df(R)/dR$ and $T_{\mu\nu}$ is the energy-momentum tensor of the gravitational sources. The Ricci tensor $R_{\mu\nu}$ and the affine connection $\Gamma^{\alpha}_{\mu\nu}$ are given in terms of the Riemannian Ricci tensor $\widetilde{R}_{\mu\nu}$ and connection $\widetilde{\Gamma}^{\alpha}_{\mu\nu}$ by

$$R_{\mu\nu} = \widetilde{R}_{\mu\nu} - \frac{3}{2f'^2}\partial_\mu f'\partial_\nu f' + \frac{1}{f'}\widetilde{\nabla}_\mu\widetilde{\nabla}_\nu f' + \frac{1}{2f'}\widetilde{\nabla}^\sigma\widetilde{\nabla}_\sigma f' g_{\mu\nu}, \tag{3}$$

$$\Gamma^{\alpha}_{\mu\nu} = \widetilde{\Gamma}^{\alpha}_{\mu\nu} + \frac{1}{2f'}g^{\lambda\alpha}\left[\partial_\mu f' g_{\lambda\nu} + \partial_\nu f' g_{\mu\lambda} - \partial_\lambda f' g_{\mu\nu}\right]. \tag{4}$$

In the Newtonian approach the metric tensor can be written in terms of the Minkowski tensor $\eta_{\mu\nu}$ plus corrections of order $\overline{v}^2 = \overline{M}G/\overline{r}$ (Weinberg, 1972) as $g_{00} = -1 - g^{(2)}_{00}$ and $g_{ij} = \delta_{ij} + g^{(2)}_{ij}$. Up to this order we have

$$\widetilde{R}^{(2)} = -\frac{1}{2}\nabla^2 g^{(2)}_{00} + \frac{1}{2}\nabla^2 g^{(2)}_{ii} = \frac{1}{c^2}\nabla^2(\phi - \varphi), \tag{5}$$

where $\phi$ and $\varphi$ are gravitational potentials associated with $g^{(2)}_{00}$ and $g^{(2)}_{ii}$, respectively.

In this work we consider the following expression for $f(R) = R + f_2R^2$, where $f_2$ is a small quantity. The function proportional to $R^2$ is not able to reproduce an accelerated expansion of the Universe as it is currently observed. However, it should not be a problem, since the formation of structures, which is the focus of this work, occurred at a period much earlier than the current acceleration of the Universe. In this case the trace of (3) in the $\overline{v}^2$ approximation reads

$$\left(1 - 6f_2\nabla^2\right)R^{(2)} = \widetilde{R}^{(2)}, \tag{6}$$

or by considering $\left(1 - 6f_2\nabla^2\right)$ an invertible operator

$$\begin{aligned} R^{(2)} &\approx \left(1 + 6f_2\nabla^2 + 36f_2^2\nabla^4\right)\widetilde{R}^{(2)} \\ &= \frac{1}{c^2}\left[\nabla^2(\phi - \varphi) + 6f_2\nabla^4(\phi - \varphi) + 36f_2^2\nabla^6(\phi - \varphi)\right], \end{aligned} \tag{7}$$

which is an approximation up to the order $f_2^2$. Since

$$\widetilde{R}_{00}^{(2)} = \frac{\nabla^2 g_{00}^{(2)}}{2} = -\frac{\nabla^2\phi}{c^2}, \tag{8}$$

the time component of the Ricci tensor (3) in the $\overline{v}^2$ approximation reduces to

$$R_{00}^{(2)} = \widetilde{R}_{00}^{(2)} - f_2\nabla^2 R^{(2)} \approx -\frac{1}{c^2}\left[\nabla^2\phi + f_2\nabla^4(\phi-\varphi) + 6f_2^2\nabla^6(\phi-\varphi)\right]. \tag{9}$$

The source of the gravitational field is a pressureless fluid where the components of the energy-momentum tensor are given by $T_{\mu\nu} = (\rho c^2, 0, 0, 0)$ with $\rho$ denoting the fluid mass density.

Now the time component and the trace of Einstein's field equations (2) together with (7) and (9) leads to the following system of Poisson equations

$$\nabla^2(\phi+\varphi) - 4f_2\nabla^4(\phi-\varphi) - 24f_2^2\nabla^6(\phi-\varphi) = 16\pi G\rho, \tag{10}$$

$$\nabla^2(\phi-\varphi) + 6f_2\nabla^4(\phi-\varphi) + 36f_2^2\nabla^6(\phi-\varphi) = -8\pi G\rho, \tag{11}$$

respectively. If we sum the above equations and consider $f_2 = 0$, the standard Poisson equation is recovered.

## 3. Jeans instability in the framework of Boltzmann equation

Now the aim is to obtain from the collisionless Boltzmann equation in the Newtonian limit a criterion for the collapse of stellar systems, which is related with a dispersion relation. The collisionless Boltzmann equation has the following form in the Newtonian limit

$$\frac{\partial f}{\partial t} + (\vec{v}\cdot\vec{\nabla}_r)f - (\vec{\nabla}\phi\cdot\vec{\nabla}_v)f = 0, \tag{12}$$

where $f \equiv f(\vec{r},\vec{v},t)$ is the distribution function, which gives the mass density of the stellar system through $\rho(\vec{r},t) = \int f(\vec{r},\vec{v},t)d\vec{v}$.

We consider that the self-gravitating equilibrium system – described by a time-independent distribution function $f_0(\vec{r},\vec{v})$ and potentials $\phi_0(\vec{r})$ and $\varphi_0(\vec{r})$ – is subjected to a small perturbation, namely, $f(\vec{r},\vec{v},t) = f_0(\vec{r},\vec{v}) + \epsilon f_1(\vec{r},\vec{v},t)$, $\phi(\vec{r},t) = \phi_0(\vec{r}) + \epsilon\phi_1(\vec{r},t)$ and $\varphi(\vec{r},t) = \varphi_0(\vec{r}) + \epsilon\varphi_1(\vec{r},t)$, where $\epsilon \ll 1$. The equilibrium for a homogeneous system is achieved by Jeans "swindle" that allows us to make $\phi_0 = 0$ and $\varphi_0 = 0$ without loss of consistency. After these considerations, we linearize the Boltzmann (12) and the field equations (10), (11) through the substitution of the above conditions. Subsequently we write the resulting equations in Fourier space as follows

$$-i\omega\overline{f}_1 + \vec{v}\cdot(i\vec{k}\,\overline{f}_1) - (i\vec{k}\,\overline{\phi}_1)\cdot\frac{\partial\overline{f}_0}{\partial\vec{v}} = 0, \tag{13}$$

$$-k^2(\overline{\phi}_1+\overline{\varphi}_1) - 4f_2k^4(\overline{\phi}_1-\overline{\varphi}_1) + 24f_2^2k^6(\overline{\phi}_1-\overline{\varphi}_1) = 16\pi G\int\overline{f}_1 d\vec{v}, \tag{14}$$

$$k^2(\overline{\phi}_1-\overline{\varphi}_1) - 6f_2k^4(\overline{\phi}_1-\overline{\varphi}_1) + 36f_2^2k^6(\overline{\phi}_1-\overline{\varphi}_1) = 8\pi G\int\overline{f}_1 d\vec{v}, \tag{15}$$

where the overbarred quantities indicate the Fourier transforms in the $(\omega, \vec{k})$ space.

By eliminating the overbarred quantities from the system of equations (13) – (15) it follows the dispersion relation

$$1 + \frac{4\pi G}{k^2}\frac{(1 - 8\,f_2 k^2 + 48\,f_2^2 k^4)}{(1 - 6\,f_2 k^2 + 36\,f_2^2 k^4)}\int\left(\frac{\vec{k}\cdot\frac{\partial f_0}{\partial \vec{v}}}{\vec{v}\cdot\vec{k} - \omega}\right)d\vec{v} = 0. \tag{16}$$

In stellar systems one assumes usually the Maxwell distribution function

$$f_0(\vec{v}) = \frac{\rho_0}{(2\pi\sigma^2)^{\frac{3}{2}}}e^{-\frac{v^2}{2\sigma^2}}, \tag{17}$$

where $\sigma$ is a dispersion velocity and $\rho_0$ a constant mass density.

Without loss of generality we can choose $\vec{k} = (k, 0, 0)$ so that the dispersion relation (16) together with (17) can be integrated with respect to the velocity components $v_y$ and $v_z$, yielding

$$\frac{k^2}{k_J^2} - \frac{(1 - 8\,f_2 k^2 + 48\,f_2^2 k^4)}{(1 - 6\,f_2 k^2 + 36\,f_2^2 k^4)}\frac{2}{\sqrt{\pi}}\int_0^\infty \frac{x^2 e^{-x^2}}{x^2 - \omega^2/(2\sigma^2 k^2)}dx = 0. \tag{18}$$

Here we have introduced the Jeans wavenumber $k_J = \sqrt{4\pi G\rho_0/\sigma^2}$ and the integration variable $x = v_x/(\sqrt{2}\,\sigma)$.

Unstable solutions are such that $\Re(\omega) = 0$ and $\omega_I = \Im(\omega) > 0$ (see Binney & Tremaine, 2008). In this case the integral on the right-hand side of (18) can be evaluated (see eq. 3.466 of Gradshteyn & Ryzhiz, 2007) and the dispersion relation (18) reduces to

$$\frac{\left\langle 9\frac{k^6}{k_J^6}\right\rangle + \left(3\frac{k^4}{k_J^4}\right) + \frac{k^2}{k_J^2}}{\left\langle 12\frac{k^4}{k_J^4}\right\rangle + \left(4\frac{k^2}{k_J^2}\right) + 1} = \left\{1 - \frac{\sqrt{\pi}\omega_I}{\sqrt{8\pi G\rho_0}}\frac{k_J}{k}\,e^{\left(\frac{\omega_I^2}{8\pi G\rho_0}\frac{k_J^2}{k^2}\right)}\mathrm{erfc}\left(\frac{\omega_I}{\sqrt{8\pi G\rho_0}}\frac{k_J}{k}\right)\right\}. \tag{19}$$

Above erfc is the complementary error function and we have introduced the same parametrization for $f_2 = -1/(2k_J^2)$ that was adopted by (Capozziello et al., 2012). The choice of this parameterization was made with the intention of describing a dimensionless ratio and to compare directly with the work done in (Capozziello et al., 2012). Other choices could have been made, but they all culminate in the same result, differing only by constants. Without the terms within the brackets in the numerator and denominator on the left-hand side of (19), it follows the classical dispersion relation for Newtonian gravity. The terms within round brackets refer to the contribution of the $f(R)$ theory in the metric formalism (Capozziello et al., 2012), while the ones within the round and angular brackets correspond to the Palatini formalism.

The solution of (19) for $\omega_I = 0$ furnishes the following limiting values for the wavenumber: (a) $k^2 = 1.3171\,k_J^2$ for the $f(R)$ theory in the Palatini formalism, (b) $k^2 = 1.2638\,k_J^2$ for the $f(R)$ theory in the metric formalism and (c) $k^2 = k_J^2$ in the Newtonian theory. For comparison, the dispersion relation (19) is plotted in Fig. 1 together with the results obtained from the $f(R)$ theory in the metric formalism and from the Newtonian gravity. The gravitational collapse occurs for the unstable wave

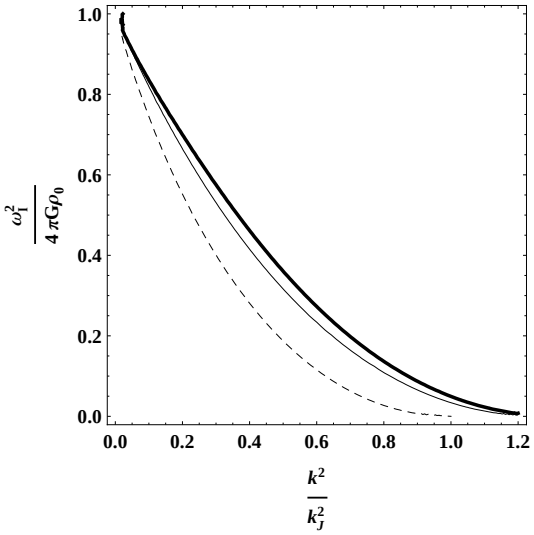


Figure 1. Ratio of wavenumbers $k^2/k_J^2$ versus normalized frequency $\omega_I^2/(4\pi G\rho_0)$ from the dispersion relation (19) for $f(R)$-gravity in Palatini formalism (bold line), for $f(R)$-gravity in metric formalism (thin line) and for Newtonian gravity (dashed line).

solutions where the values of $k^2/k_J^2$ lie below the curves in Fig. 1. Above these values the oscillations remain stable. We infer from this figure that the $f(R)$ theory in the Palatini formalism furnishes a large range of solutions than the metric one, which in its turn is larger than the one of the Newtonian theory.

The stellar system is stable up to a critical mass and if this critical value is exceeded the gravitational collapse occurs. In the Newtonian theory this critical value is the Jeans mass $M_J$, which is defined as the mass within a sphere of diameter $\lambda_J = 2\pi/k_J$, i.e, $M_J = 4\pi\rho_0(\pi/k_J)^3/3$. From the above results one obtain the following ratios: (a) $M/M_J = 0.662$ for the $f(R)$ theory in the Palatini formalism and (b) $M/M_J = 0.704$ for the $f(R)$ theory in the metric formalism. Hence the $f(R)$ theory in the Palatini formalism furnishes the smallest critical mass for the occurrence of the gravitational collapse.

## 4. Conclusions

The dispersion relation is a collapse criterion for infinite homogeneous fluid and stellar systems. Here, this relation is used to study the instability of collisionless systems. Figure 1 shows the behavior of the dispersion relation of the models: Newtonian gravity, $f(R)$-gravity in the metric formulation and this one in the Palatini formalism. It is worth stressing that the characteristic wavenumber is given in terms of the classical one. The model proved to have a higher instability limit when compared to the others. The collapse occurs for higher values of the wavenumber when compared with the Jeans wavenumber, so that critical mass of interstellar clouds decreases, modifying the initial conditions to start the collapse. The dispersion relation obtained via Palatini

formulation differs from that obtained via metric formulation only for terms of order up to $f_2^2$; below this order, no difference was found. The terms of order $f_2^2$ arise only in the Palatini solution, when one writes the generalized Ricci scalar depending on the usual one. Thus, we can conclude that the differences reported here are a direct result of using the Palatini formalism.

The Jeans mass is a criterion for the study of gravitational collapse of interstellar clouds. The cloud is stable for sufficiently small mass (at a given temperature and radius), smaller than the limit established by Jeans mass. If this cloud exceeds this mass limit, it starts a process of contraction until some other force can impede the total collapse. It was shown that the Jeans mass for the systems described by $f(R)$-gravity via Palatini formalism exhibits values smaller than the ones found for the metric case, and especially for Newtonian gravitation. This demonstrates that the limit for initiating the collapse of an interstellar cloud is below the classical limit favoring more the formation of structures. We may interpret this result by saying that the same amount of matter is able to produce a larger curvature, causing a larger acceleration of test particles. Hence the test particles describe a different geodesic than that they would follow in the metric formalism. In this way, we conclude that in the Palatini formalism of $f(R)$ gravity the formation of structures is more efficient than in the metric formalism of $f(R)$ gravity and Newtonian gravity.

**Acknowledgments.** GMK acknowledges the support from the Conselho Nacional de Desenvolvimento Científico e Tecnológico (CNPq), Brazil.

## References

Binney, J. & Tremaine, S. 2008, "Galatic Dynamics", Second Edition, Princeton University Press

Capozziello, S. & De Laurentis, M. 2011, Physics Reports, 509, 167-321

Capozziello, S. et al. 2012, Phys. Rev. D, 85, 044022

Gradshteyn, I. S. & Ryzhiz, I. M. 2007, "Tables of Integrals, Series and Products", Seventh Edition, Academic Press

Weinberg, S. 1972, "Gravitation and Cosmology, principles and applications of the general theory of relativity", John Wiley & Sons

*Gravitation, Relativistic Astrophysics and Cosmology*
*Second Argentinian-Brazilian Meeting, 2014*
*G. S. Vila, F. L. Vieyro and J. Fabris, eds.*

# Averages associated to the energy momentum tensor and study of a two scale system in General Relativity

Ezequiel F. Boero and Osvaldo M. Moreschi

*FaMAF, Universidad Nacional de Córdoba, Ciudad Universitaria, (5000) Córdoba, Argentina*
*Instituto de Física Enrique Gaviola (IFEG), CONICET, Ciudad Universitaria, (5000) Córdoba, Argentina*

**Abstract.** We present a brief study of compound systems of different scales. It is shown that the detailed dynamical studies of massless and massive particles can hardly be associated to standard averaging techniques.

## 1. Introduction

Recently new expressions for the deviation angle and for the optical scalars in the study of weak lensing have been derived in terms of curvature scalar of the lens geometry [GM11]. This formulas, in contrast to standard treatments found in the literature, take into account the spacelike components of the energy-momentum tensor of the lens. One of the advantage of the new expression is that they allow us to model the lens with a broader kind of objects.

In particular, it have been shown the case of a peculiar geometry without mass but with non-vanishing spacelike components [GM12]. This geometry is an exact solution of the Einstein's equations with a non-conventional energy-momentum tensor; despite its bizarre nature it has remarkable features, as we now mention.

It was shown that this geometry can fit the shear profile in studies of weak lensing in Coma's cluster.

A dynamical study of the rotation curves in this geometry shows that if the observations of the tangential velocity, $v_t$, of the rotation curves in this geometry are interpreted with the usual Newtonian relations

$$M_N(r) = \frac{rc^2}{G} v_t^2; \tag{1}$$

it gives the expected linear growth of the deduced Newtonian mass $M_N(r)$ with the radial coordinate. Here $G$ is the gravitational constant and $c$ denotes the speed of light in vacuum.

The radial mass profile of a matter distribution deduced by means of the estimation in the scape velocity of the system can be fitted using the radial scape velocity, $v_e$, in this geometry together with a Newtonian interpretation, this is associating a Newtonian mass $M_N(r)$ given by

$$M_N(r) = \frac{rc^2}{2G} v_e^2. \tag{2}$$

This is pertinent to observations in systems where the issue of the missing mass, or dark matter problem is manifest. This geometry, although a toy model since it has

not mass density, gives account in a very acceptable way some of the features found it in the observations of "dark matter" in astrophysical systems.

This fact rises the question about the possible nature of this peculiar solution and its relation to the dark matter problem and also to the way in which observations are carried out.

The study of phenomenology of dark matter in the new peculiar solutions presented in [GM12] involves the use of two tools: The geodesic equation for massive and massless particles, and the deviation geodesic equation for a congruence of null geodesics.

The former only contains the information that comes from the connection associated to the geometry while the last has information of the curvature (second derivatives) of the geometry.

We want to consider a system composed of small point-like subsystems that contribute to a big complete system.

Each subsystem is considered to have very small velocity with respect to each other so that all of them can be considered as geometric linear stationary contribution over a common flat background.

We employ a generalization of the optical scalars for the case of a such distribution in the approximation of thin lens.

## 2. The system

The distribution of the small constituents of the big system can be described in terms of the stationary distribution function $\mathscr{P}(x^i)$ with $i = 1, 2, 3$ denoting the spacelike coordinates of the flat background. This is a continuous distribution that models the density of the small subsystems.

We work with several pictures in mind: Each subsystem is considered as a vacuum gravitating central object; which therefore is associated to a Schwarzschild geometry. We also consider the case of spherically symmetric geometries with halos which contribute only to their respective $P_r$ component of the microscopic energy-momentum tensor. We consider astrophysical useful distributions to the energy density $\varrho$, as is the isothermal mass distribution.

We are assuming that the nature of the observations is such that one can consider each subsystem and the compound system as stationary; so that we can assume the existence of a global timelike Killing vector field, $\tilde{t}^a$.

### 2.1. Decomposition of the geometry

Let us express the metric $g_{ab}$ of the spacetime in terms of a reference metric $\eta_{ab}$, such that

$$g_{ab} = \eta_{ab} + h_{ab}. \tag{3}$$

Let $\partial_a$ denote the torsion free metric connection of $\eta_{ab}$ and $\nabla_a$ the torsion free metric connection of $g_{ab}$; then one can express the covariant derivative of an arbitrary vector $v^a$ by

$$\nabla_a v^b = \partial_a v^b + \Gamma^{\ b}_{a\ c} v^c; \tag{4}$$

and one can prove that

$$\Gamma^{\ c}_{a\ b} = \frac{1}{2} g^{cd} \left(\partial_a h_{bd} + \partial_b h_{ad} - \partial_d h_{ab}\right) = \Gamma^{\ c}_{b\ a}. \tag{5}$$

Since we are considering contributions of many subsystems $A$'s, the tensor $h_{ab}$ must be the sum of all the contributions, namely

$$h_{ab} = \sum_{(A)} h^{(A)}_{ab}. \tag{6}$$

## 3. Testing a spherically symmetric system with massless particles

In reference [GM11] we have deduced the general equations for the description of weak lensing. We will use here those that are appropriate for the study of spherically symmetric systems.

Let us recall that the lens scalars in the thin lens approximation, in terms of the curvature invariants $\Psi_0$ and $\Phi_{00}$ associated to the Weyl's and Ricci's tensor respectively, are given by

$$\begin{aligned} \kappa =& \frac{d_l d_{ls}}{d_s} \int_{-d_l}^{d_{ls}} \Phi_{00}\, dy, \\ \gamma =& \frac{d_l d_{ls}}{d_s} \int_{-d_l}^{d_{ls}} |\Psi_0|\, dy; \end{aligned} \tag{7}$$

where here $\gamma$ refers to the modulus of the shear.

For thin lenses the bending angle is given by [GM11]

$$\alpha(J) = J\left(\hat{\Phi}_{00}(J) + \hat{\Psi}_0(J)\right); \tag{8}$$

$$\hat{\Phi}_{00} = \int \Phi_{00} d\lambda, \qquad \hat{\Psi}_0 = \int \Psi_0 d\lambda. \tag{9}$$

This expression are valid for each subsystem.

We use $J$ to denote the impact parameter of the null geodesic to center of the lens; $y$ is the Cartesian coordinate along which the photons path, $\lambda$ the affine parameter along the null geodesics and the coordinate $r$ is satisfies $r^2 = J^2 + y^2$.

The above expressions can be put in terms of the total mass, $M(r)$ and the components of the energy-momentum tensor of the lens, using the following relations;

$$\Psi_0 = -3\frac{J^2}{r^2}\tilde{\Psi}_2 e^{2i\vartheta} = -3\frac{J^2}{r^2}\left[\frac{4\pi}{3}\left(\varrho - P_r - P_t\right) - \frac{M}{r^3}\right] e^{2i\vartheta}; \tag{10}$$

where here $\vartheta$ is the angle of polar coordinates in the plane $y = 0$ in a Cartesian coordinate system; and

$$\Phi_{00} = 2\frac{J^2}{r^2}\left(\tilde{\Phi}_{11} - \frac{1}{4}\tilde{\Phi}_{00}\right) + \tilde{\Phi}_{00} = 4\pi\frac{J^2}{r^2}\Big(P_t - P_r\Big) + 4\pi\left(\varrho + P_r\right). \tag{11}$$

In particular, the well known results for a lens with the Schwarzschild geometry

$$\kappa(J) = 0, \tag{12}$$

$$\gamma(J) = \frac{d_l d_{ls}}{d_s}\frac{4M}{J^2}, \tag{13}$$

$$\alpha(J) = \frac{4M}{J}. \tag{14}$$

are obtained by taking $\rho = P_t = P_r = 0$ and M = constant with the integration limits going to infinity.

### 3.1. Treatment of a compound system

When dealing with a compound system, the standard treatment find in textbooks is to consider the situation of a monopole mass (Schwarzschild) and to generalize eq. (14) to a vector equation in the plane of the thin lens.

Here, we generalize the bending angle equation for a an axially symmetric distribution; but before let us recall that given the scalar expression $\alpha(J)$ for bending angle, one can write [GM11] the 2-dimensional equation in terms of the components of $\alpha^i = (\alpha^1, \alpha^2)$ as

$$(\alpha^i) = \alpha(J)(\frac{z_0}{J}, \frac{x_0}{J}); \tag{15}$$

taking into account the appropriate orientation in the two dimensional space of the images.

### 3.2. Generalization for a distribution of spherically symmetric deflectors

It could be convenient to change the notation to a most common one when we consider a distribution of sources. Then, let us denote by $\boldsymbol{\xi}'$ the vector in the plane of the thin lens joining an arbitrary location in the distribution with a given point in the plane of the lens. Then we rewrite equation (15) in the form

$$\hat{\boldsymbol{\alpha}}(\boldsymbol{\xi}) = \alpha(|\boldsymbol{\xi} - \boldsymbol{\xi}'|)\frac{(\boldsymbol{\xi} - \boldsymbol{\xi}')}{|\boldsymbol{\xi} - \boldsymbol{\xi}'|}; \tag{16}$$

which for a macroscopic distribution $\mathscr{P}(\boldsymbol{\xi}', y')$ results in

$$\boldsymbol{\alpha}(\boldsymbol{\xi}) = \int_{\mathbb{R}^2}\int_{-\infty}^{\infty} \mathscr{P}(\boldsymbol{\xi}', y')\alpha(|\boldsymbol{\xi} - \boldsymbol{\xi}'|)\frac{(\boldsymbol{\xi} - \boldsymbol{\xi}')}{|\boldsymbol{\xi} - \boldsymbol{\xi}'|}d^2\xi' dy'; \tag{17}$$

or put it in a compact form we have

$$\boldsymbol{\alpha}(\boldsymbol{\xi}) = \int_{\mathbb{R}^2} \Sigma(\boldsymbol{\xi}, \boldsymbol{\xi}')\frac{(\boldsymbol{\xi} - \boldsymbol{\xi}')}{|\boldsymbol{\xi} - \boldsymbol{\xi}'|^2}d^2\xi'; \tag{18}$$

with

$$\Sigma(\boldsymbol{\xi}, \boldsymbol{\xi}') = \int_{-\infty}^{\infty} \mathscr{P}(\boldsymbol{\xi}', y')\alpha(|\boldsymbol{\xi} - \boldsymbol{\xi}'|)|\boldsymbol{\xi} - \boldsymbol{\xi}'|dy'. \tag{19}$$

In the case of small deflectors of Schwarzschild type, $\alpha(|\boldsymbol{\xi} - \boldsymbol{\xi}'|) = \frac{4m}{|\boldsymbol{\xi} - \boldsymbol{\xi}'|}$; the quantity $\Sigma(\boldsymbol{\xi}, \boldsymbol{\xi}')$ represent the total mass of the distribution projected in the plane of the thin lens. For analogy with this case we will refer to $\Sigma(\boldsymbol{\xi}, \boldsymbol{\xi}')$ in the most general case as the *generalized projected mass*.

## 4. Testing the system with massive particles

### 4.1. The equation of motion

The dynamics of massive particles is determined by the geodesic equation. Let the vector $u^a$ be the four velocity of the particle, then one can express

$$u^a \nabla_a u^b = u^a \partial_a u^b + u^a \Gamma^b_{a\,c} u^c = 0. \tag{20}$$

Since we are assuming small velocities we can express, in first order in the velocities

$$u^a = (1 + \frac{u^2}{2})t^a + v^a + \mathcal{O}(u^3); \tag{21}$$

where

$$\eta_{ab}t^a v^b = 0, \tag{22}$$

$$\eta_{ab}v^a v^b = -u^2. \tag{23}$$

In this way, we see that the equation of motion can be expressed as

$$t^a \partial_a v^b + \Gamma^b_{a\,c} t^a t^c + 2\Gamma^b_{a\,c} t^a v^c = 0; \tag{24}$$

### 4.2. The case of spherical symmetry

A stationary spherically symmetric geometry can be expressed by

$$ds^2 = e^{2\Phi(r)}dt^2 - \frac{dr^2}{1 - \frac{2M(r)}{r}} - r^2\left(d\theta^2 + \sin^2\theta d\phi^2\right); \tag{25}$$

in terms of a standard spherical coordinate system $(t, r, \theta, \phi)$.

For this case one has that the non-vanishing components of the connection tensor are

$$\Gamma^r_{\theta\,\theta} = 2M(r), \tag{26}$$

$$\Gamma^r_{\phi\,\phi} = 2M(r)\sin^2\theta, \tag{27}$$

$$\Gamma^t_{t\,r} = \frac{d\Phi(r)}{dr}, \tag{28}$$

$$\Gamma^r_{t\,t} = \frac{d\Phi(r)}{dr}, \tag{29}$$

$$\Gamma^r_{r\,r} = \frac{d}{dr}\left(\frac{M(r)}{r}\right); \tag{30}$$

where we are considering only linear terms.

Then, considering the non-zero contributions from the connection, one has

$$\frac{dv^r}{dt} = -\frac{d\Phi(r)}{dr}. \tag{31}$$

Therefore, we have only one equation dynamically interesting.

It is important to emphasize that the notion of the $r$ direction is dependent on the system we are considering the interaction with. To carry out the sum over all subsystems $A$ it would be better to introduce a Cartesian description with respect to the background.

When the sum it is carried one obtains the Newton's equation for a particle in a gravitational field. Where the effective potential is given by the sum of the individual contributions of the distribution of the form (31). In particular, when the big scale distribution is spherically symmetric one can use the Newton's theorem on spherical systems to evaluate the effective potential inside of a central sphere of radius $r$ with respect to the origin.

## 5. Summary and perspectives

We have just seen that when studying the dynamics of massive and massless particles, while the first reduces to the simple application of Newtonian techniques, the later is much more complicated, specially when the spacelike components of the energy momentum tensor can not be neglected; as is the case for the geometries that we have presented elsewhere. Therefore, the physical smoothing procedures are not necessarily associated with standard averaging of geometrical quantities as tensors; but come from a detailed study of the particular observation.

**Acknowledgments.** We acknowledge support from CONICET, SeCyT-UNC and Foncyt.

## References

[GM11] Gallo, E. & Moreschi, O. M. 2011, Phys. Rev., D83, 083007
[GM12] Gallo, E. & Moreschi, O. M. 2012, Mod. Phys. Lett., A27, 1250044

*Gravitation, Relativistic Astrophysics and Cosmology*
*Second Argentinian-Brazilian Meeting, 2014*
*G. S. Vila, F. L. Vieyro and J. Fabris, eds.*

# A Rastall scalar-tensor theory

Thiago Caramês,[1] Júlio C. Fabris,[1] Oliver F. Piattella,[1] Vladimir Strokov,[1,†] Mahamadou H. Daouda,[2] and Adriano M. Oliveira[3]

[1]*Departamento de Física - UFES, Vitória, ES, Brazil*
[2]*Département de Physique - Université de Niamey, Niamey, Niger*
[3]*IFES, Guarapari, ES, Brazil*
[†]*On leave from the Lebedev Physical Institute (Moscow, Russia)*

**Abstract.** We formulate a theory combining the principles of a scalar-tensor gravity and the Rastall proposal of a violation of the usual conservation laws. In the resulting Brans-Dicke-Rastall (BDR) theory the only exact, static, spherically symmetric solution is a Robinson-Bertotti type solution besides the trivial Schwarzschild one. The PPN constraints can be completely satisfied for some values of the free parameters.The cosmological solutions display, among others, a decelerate-accelerate transition in the matter dominated phase.

## 1. Introduction

The Brans-Dicke theory, the paradigma of scalar-tensor theories, is considered as an important alternative to the theory of General Relativity (GR) (Brans & Dicke, 1962). In this theory the gravitational coupling $G$ is considered as a dynamical quantity represented by the field $\phi$ which is introduced in the gravitational action through a kinetic term and a non-minimal coupling with the usual Ricci scalar. A new parameter $\omega$ quantifies the interaction of the scalar field and the gravitational term, such that as $\omega \to \infty$ the General Relativity theory is recovered. Recent estimates using the PLANCK data indicates a value $\omega \sim 1000$ (Avilez & Skordis, 2013). In spite of those observational constraints, small – or even negative – values of the parameter $\omega$ may be very interesting. They arise, for example, in the string theories in their low-energy limit (Lidsey et al., 2000). When negative values of $\omega$ are allowed, primordial singularity-free solutions emerge naturally from the Brans-Dicke theory (Gurevich et al., 1973). Late time accelerated solution can also be achieved, but at the price of a negative gravitational coupling (Batista et al., 2001).

Some generalisations of GR evoke the gravitational anomaly effect, viz. Rastall's theory. (Rastall, 1972; 1976) These generalisations touch one of the cornerstones of gravity theories: the conservation laws encoded in the null divergence of the energy-momentum tensor. Since the concept of energy in GR is an object of discussion, the possibility that the energy-momentum tensor has a non-zero divergence should be considered in some situations. The idea of violation of the conventional conservation laws in the context of Brans-Dicke theory has been considered by Smalley (Smalley, 1974). In this approach, the Klein-Gordon type equation for the scalar field was kept as in the Brans-Dicke theory while the Einstein equations were changed accordingly. Here, we would like to revisit this proposal following a different path: we try to write down the field equations in such a way that the Brans-Dicke, GR as well as the ordinary

the Rastall's theory are recovered: we keep the violation of the energy-momentum tensor in a spirit very close to the original formulation of the Rastall's theory, and the Klein-Gordon type equation as well as the Einstein's equations are modified accordingly.

We investigate the resulting theory in two situations: spherically symmetrical and cosmological configuration. In the former case, we obtain that the only non-trivial solution is represented by the Robinson-Bertotti metric (Bertotti, 1959; Robinson, 1959) (its interpretation, however, differs from the conventional one). A solution that represents a star-like configuration is the "trivial" Schwarzschild one. At cosmological level, we show that accelerated solutions are possible in the dust phase of the cosmic evolution without introducing dark energy. We display a particular case where a decelerated/accelerated transition in the recent universe is achieved with a positive effective gravitational coupling.

## 2. The theory

The main idea of Rastall's theory (Rastall, 1972) is the assumption that in curved space-time the usual conservation laws used in GR are violated. Hence, there must be a connection between the divergence of the energy-momentum tensor and the curvature of the space-time. According to this program, the divergence of the energy-momentum tensor may be written as

$$T^{\mu\nu}{}_{;\mu} = \frac{1-\lambda}{16\pi G} R^{,\nu}. \tag{1}$$

In equation (1) $\lambda$ is a free parameter codifying the deviation from the conservation. When $\lambda = 1$ the traditional conservation laws are recovered. Equation (1) is a phenomenological way to implement the gravitational anomaly due to quantum effects.

In the context of the Brans-Dicke theory, we can make the identification $G \propto \frac{1}{\phi}$. Hence,

$$T^{\mu\nu}{}_{;\mu} = \frac{(1-\lambda)\phi}{16\pi} R^{,\nu}. \tag{2}$$

Let us generalize Rastall's version of the field equations to the Brans-Dicke case. Following the original Rastall's formulation in the context of GR, we write,

$$R_{\mu\nu} - \frac{\lambda}{2} g_{\mu\nu} R = \frac{8\pi}{\phi} T_{\mu\nu} + \frac{\omega}{\phi^2}\left\{\phi_{;\mu}\phi_{;\nu} - \frac{1}{2} g_{\mu\nu}\phi_{;\rho}\phi^{;\rho}\right\} + \frac{1}{\phi}\left\{\phi_{;\mu;\nu} - g_{\mu\nu}\Box\phi\right\}. \tag{3}$$

Combining the hypothesis (2) and (3), and using the Bianchi's identities, we obtain that the scalar field $\phi$ must obey the equation:

$$\Box\phi = \frac{8\pi\lambda}{3\lambda - 2(1-2\lambda)\omega} T - \frac{\omega(1-\lambda)}{3\lambda - 2(1-2\lambda)\omega} \frac{\phi^{;\rho}\phi_{;\rho}}{\phi}. \tag{4}$$

Equations (2, 3, 4) form our complete system in this new formulation. When $\lambda = 1$, the usual Brans-Dicke theory is recovered. The effective gravitational coupling today reads:

$$G = \frac{2[2\lambda + (3\lambda - 2)\omega)]}{3\lambda - 2(1-2\lambda)\omega} \frac{1}{\phi}. \tag{5}$$

When $\lambda = 1$ we obtain the corresponding expression for the Brans-Dicke theory.

## 3. Spherically symmetric static vacuum solutions

The classical tests of theory of gravity are based on the motion of test particles in the geometry of a spherically symmetric object like a star or a planet. Hence, to verify the viability of the theory proposed, it is crucial to look for a spherically symmetric solution. As a first step, the (exterior) solution representing the space-time of a star-like object is considered.

In the vacuum case, the equations reduce to

$$R^{,\nu} = 0, \tag{6}$$

$$R_{\mu\nu} - \frac{1}{2}g_{\mu\nu}R = \frac{\omega}{\phi^2}\left\{\phi_{;\mu}\phi_{;\nu} + \frac{\lambda}{2(1-2\lambda)}g_{\mu\nu}\phi_{;\rho}\phi^{;\rho}\right\} + \frac{1}{\phi}\left\{\phi_{;\mu;\nu} + \frac{(1+\lambda)}{2(1-2\lambda)}g_{\mu\nu}\Box\phi\right\}, \tag{7}$$

$$\Box\phi = -\frac{\omega(1-\lambda)}{3\lambda - 2(1-2\lambda)\omega}\frac{\phi^{;\rho}\phi_{;\rho}}{\phi}. \tag{8}$$

The first of these equations leads to $R = R_0 =$ constant. Hence, in vacuum the Ricci scalar is necessarily constant. The case $R_0 = 0$ corresponds to the Schwarzschild solution of GR.

Let us consider a metric in the form:

$$ds^2 = e^{2\gamma}dt^2 - e^{2\alpha}dr^2 - e^{2\beta}(d\theta^2 + \sin^2\theta d\phi^2). \tag{9}$$

The functions $\alpha$, $\beta$ and $\gamma$ depend on the radial coordinate $r$ only. First we find that the constant $R_0$ is given by:

$$R_0 = \omega\left\{\frac{3+2\omega}{3\lambda - 2(1-2\lambda)\omega}\right\}\frac{\phi_{;\rho}\phi^{;\rho}}{\phi^2}. \tag{10}$$

Now, the D'Alambertian reads:

$$\Box\phi = \frac{\left(\sqrt{-g}g^{\mu\nu}\phi_{,\nu}\right)_{,\mu}}{\sqrt{-g}} = -e^{-2\alpha}[\phi'' + (\gamma' + 2\beta' - \alpha')\phi'], \tag{11}$$

where $g \equiv \det g_{\mu\nu}$. Let us choose the radial coordinate such that $\alpha = \gamma + 2\beta$. Writing the Einsteinian equations as

$$R_{\mu\nu} = \frac{\omega}{\phi^2}\left\{\phi_{;\mu}\phi_{;\nu} + \frac{\lambda-1}{2(1-2\lambda)}g_{\mu\nu}\phi_{;\rho}\phi^{;\rho}\right\} + \frac{1}{\phi}\left\{\phi_{;\mu;\nu} + \frac{\lambda-2}{2(1-2\lambda)}g_{\mu\nu}\Box\phi\right\}, \tag{12}$$

we obtain, in the extended form:

$$\gamma'' + \frac{\phi'}{\phi}\gamma' = -\omega\frac{(\lambda-1)}{2(1-2\lambda)}\left(\frac{\phi'}{\phi}\right)^2 - \frac{\lambda-2}{2(1-2\lambda)}\frac{\phi''}{\phi}, \tag{13}$$

$$\gamma'' + 2\beta'' - 2\beta'(\beta' + 2\gamma') - \frac{\phi'}{\phi}(\gamma' + 2\beta') = -\omega\frac{1-3\lambda}{2(1-2\lambda)}\left(\frac{\phi'}{\phi}\right)^2 + \frac{3\lambda}{2(1-2\lambda)}\frac{\phi''}{\phi}, \tag{14}$$

$$\beta'' + \beta'\frac{\phi'}{\phi} - e^{2(\gamma+\beta)} = -\omega\frac{\lambda-1}{2(1-2\lambda)}\left(\frac{\phi'}{\phi}\right)^2 - \frac{\lambda-2}{2(1-2\lambda)}\frac{\phi''}{\phi}. \tag{15}$$

Equations (8, 10) lead to two supplementary equations:

$$R_0 = -\omega\left\{\frac{3+2\omega}{3\lambda-2(1-2\lambda)\omega}\right\}e^{-2\alpha}\left(\frac{\phi'}{\phi}\right)^2, \tag{16}$$

$$\phi'' = -\omega\frac{1-\lambda}{3\lambda-2(1-2\lambda)\omega}\frac{\phi'^2}{\phi}. \tag{17}$$

The only self-consistent solution for the above equations are:

$$\alpha = \alpha_0 - \ln(r/r_0), \tag{18}$$

$$\gamma = \gamma_0 - \ln(r/r_0), \tag{19}$$

$$\beta = \beta_0 = \frac{1}{2}(\alpha_0 - \gamma_0), \tag{20}$$

$$\phi = \phi_0(r/r_0)^{\frac{1}{1-A}}, \quad A = -\omega\frac{1-\lambda}{3\lambda-2(1-2\lambda)\omega}. \tag{21}$$

Hence, the metric is

$$ds^2 = e^{2\alpha_0}\frac{dt^2}{(r/r_0)^2} - e^{2\gamma_0}\frac{dr^2}{(r/r_0)^2} - e^{\alpha_0-\gamma_0}d\Omega^2. \tag{22}$$

If the scale $r_0$ is chosen such that $r_0^2 = e^{\alpha_0-3\gamma_0}$, making redefinitions $t \to e^{-(\gamma_0+\alpha_0)/2}$, $s \to e^{-(\gamma_0-\alpha_0)/2}$, and $r \to rr_0$, we arrive at:

$$ds^2 = \frac{1}{r^2}\left(dt^2 - dr^2 - r^2d\Omega^2\right), \tag{23}$$

which is the so-called Robinson-Bertotti solution that is obtained, in the context of GR, by considering an electromagnetic field. Hence, no black hole solution is possible. This solution appears as the only non-trivial (non-Schwarzschild solution) vacuum solution.

A PPN analysis reveal that the classical tests of a gravitation theory are equally satisfied as in Genera Relativity if $\lambda = 0$ (Caramês et al, 2014). This makes this theory quite competitive.

## 4. Cosmology

Let us consider an isotropic and homogeneous space-time described by the flat Friedmann-Lemaître-Robertson-Walker (FLRW) metric,

$$ds^2 = dt^2 - a(t)^2(dx^2 + dy^2 + dz^2), \tag{24}$$

and an equation of state of the type $p = \alpha\rho$, with $\alpha$ = constant. In this case the equations of motion read:

$$\dot{\rho} + 3\frac{\dot{a}}{a}(1+\alpha)\rho = -\frac{3(1-\lambda)}{8\pi}\phi\left[\frac{\ddot{a}}{a} + \frac{\dot{a}}{a}\frac{\ddot{a}}{a} - 2\left(\frac{\dot{a}}{a}\right)^3\right], \tag{25}$$

$$3\left(\frac{\dot{a}}{a}\right)^2 = \frac{8\pi\rho}{\phi}\left\{\frac{1-3\lambda}{2(1-2\lambda)} + \frac{3(1-\lambda)}{2(1-2\lambda)}\alpha\right\} + \omega\left[\frac{2-3\lambda}{2(1-2\lambda)}\right]\left(\frac{\dot{\phi}}{\phi}\right)^2 + \left[\frac{3(1-\lambda)}{2(1-2\lambda)}\frac{\ddot{\phi}}{\phi} + \frac{3(1+\lambda)}{2(1-2\lambda)}\frac{\dot{a}}{a}\frac{\dot{\phi}}{\phi}\right], \tag{26}$$

$$2\frac{\ddot{a}}{a} + \left(\frac{\dot{a}}{a}\right)^2 = -\frac{8\pi}{\phi}\left\{\frac{1-\lambda-(1+\lambda)\alpha}{2(1-2\lambda)}\right\}\rho + \omega\frac{\lambda}{2(1-2\lambda)}\left(\frac{\dot{\phi}}{\phi}\right)^2 + \frac{1+\lambda}{2(1-2\lambda)}\frac{\ddot{\phi}}{\phi} + \frac{5-\lambda}{2(1-2\lambda)}\frac{\dot{a}}{a}\frac{\dot{\phi}}{\phi}, \tag{27}$$

$$\frac{\ddot{\phi}}{\phi} + 3\frac{\dot{a}}{a}\frac{\dot{\phi}}{\phi} = \frac{8\pi\lambda}{3\lambda - 2(1-2\lambda)\omega}(1-3\alpha)\frac{\rho}{\phi} - \omega\frac{1-\lambda}{3\lambda-2(1-2\lambda)\omega}\left(\frac{\dot{\phi}}{\phi}\right)^2. \tag{28}$$

Equations (25)-(28) form a rich and complex system. In order to get a hint on which kind of solutions they predict, we consider power-law solutions, in the first place. The power-law solutions constitute a very restrictive case, but they can indicate the kind of cosmological solution we can expect from the BDR theory. Hence, suppose the solutions have the form $a = a_0 t^s, \phi = \phi_0 t^p, \rho = \rho_0 t^q$, where $a_0$, $\phi_0$, $\rho_0$, $s$, $p$ and $q$ are constants. This system admits eight pairs of roots for $(s, p)$. For the dust case, $\alpha = 0$, one of the pairs corresponds to the Minkowski case, $p = s = 0$. Another one is $s = p = 1/2$. A third root implies a curious configuration with $s = 0$ and $p = 2$, that is, a static universe, with a varying gravitational coupling. Among the other five pairs, two incorporate an accelerated regime of the expansion while remaining three describe a decelerating universe. The overall situation is described in reference (Caramês et al, 2014), where the meaning of these different results are analysed.

The field equations depends not only on the values of $\lambda$ and $\omega$, but also on the value of the initial conditions. We look for an example of a deceleration/acceleration transition during the matter dominated phase ($\alpha = 0$). Figure 1 shows the behaviour of the Hubble function $H = \frac{\dot{a}}{a}$ and deceleration parameter $q = -1 - \frac{\dot{H}}{H^2}$, for $\omega = 1$ and $\lambda = -1$, undergoing this transition. Note that the effective $G > 0$ stays positive (see (5)).

## 5. Conclusions

In this work we have combined the idea of a scalar-tensor theory of the Brans-Dicke type and Rastall's proposal of a gravitational anomaly encoded in the violation of the conventional conservation law for the energy-momentum tensor. In doing so, we end up with two free parameters: the usual Brans-Dicke parameter $\omega$ and Rastall's parameter $\lambda$, representing a degree of the non-conservation.

We have investigated the BDR theory in two contexts: spherically symmetric static solutions and cosmological regime. In the first case, we found that the only possible non-trivial analytical solution is a Robinson-Bertotti type solution. The only possible

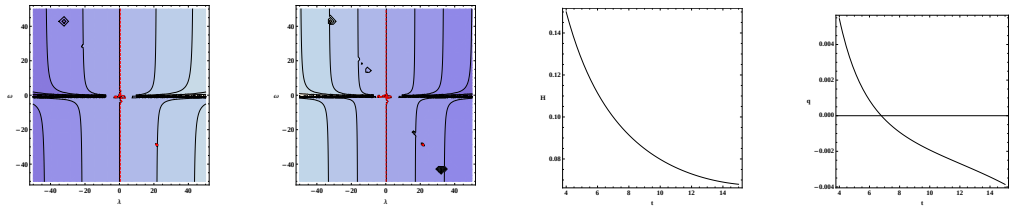

Figure 1. The left panel represents the first root for $s$ displaying acceleration of the scale factor, the red line separating positive (left) and negative (right) values. The left center panel represents the first root for $p$, the red line separating positive (second and fourth quadrants) and negative values (first and third quadrants). The behaviour of the Hubble function $H$ and deceleration parameter $q$ for $\omega = 1$, $\lambda = -1$ and $\alpha = 0$ are displayed in the right center and right panels.

solution in the BDR theory that can represent a star is the usual Schwarzschild solution corresponding to the trivial configuration where the scalar field is constant.

For the cosmological case, we found power law solutions for the matter dominated phase, some of them representing an accelerating expansion, others, decelerating. We have shown that a decelerating/accelerating transition can be achieved in the matter dominated phase in the BDR theory.

**Acknowledgments.** We thank FAPES (Brazil) and CNPq (Brazil) for partial financial support.

## References

Avilez, A. & Skordis, C. 2014, Phys. Rev. Lett., 113, 011101

Batista, A. B., Fabris, J. C., & de Sa Ribeiro, R. 2001, Gen. Rel. Grav., 33, 1237

Bertotti, B. 1959, Phys. Rev., 116, 1331

Bertotti, B. & I. Robinson 1959, Bull. Acad. Pol. Sci., 7, 351

Brans, C. & Dicke, R. H. 1961, Phys. Rev., 124, 925

Caramês, T. R. P. et al. 2014, Eur. Phys. J., C74, 3145

Gurevich, L. E., Finkelstein, A. M. & Ruban, V. A. 1973, Ap&SS, 22, 231

Lidsey, J. E., Wands, D. & Copeland, E. J. 2000, Phys. Rep., 337, 343

Rastall, P. 1976, Phys. Rev., D6, 3357

Rastall, P. 1976, Can. J. Phys., 54, 66

Smalley, L. L. 1974, Phys. Rev., D9, 1635

*Gravitation, Relativistic Astrophysics and Cosmology*
*Second Argentinian-Brazilian Meeting, 2014*
*G. S. Vila, F. L. Vieyro and J. Fabris, eds.*

# Interactions of relativistic particles in stellar winds

Santiago del Palacio,[1] Gustavo E. Romero,[1] and Valentí Bosch-Ramon[2]

[1]*Facultad de Ciencias Astronómicas y Geofísicas de La Plata, Universidad Nacional de La Plata, Argentina.*
[2]*Facultat de Fisica, Universitat de Barcelona, España.*

**Abstract.** Several binary systems hosting a massive star and a companion that is either a similar star or a compact object, present non-thermal emission from radio to $\gamma$-rays. This non-thermal emission is the consequence of the interactions of relativistic particles surrounded by the stellar wind. The main goal of this work is to characterize the high-energy physics of $\gamma$-ray binaries by implementing a general modeling for their most important high-energy processes. To thoroughly investigate the effects of the emitter-star-observer geometry on the resulting radiation, we sistematically applied a non-thermal leptonic model for different locations of the emitter, magnetic fields, and acceleration timescales. The results of this procedure are presented in the form of emissivity maps, which are useful for exploring statistical properties of $\gamma$-ray binaries as well as their expected distribution in the galaxy.

## 1. Introduction

Some of the most luminous galactic sources are high-mass binary systems in which one of the components is a massive star of spectral type OB. This type of binaries present non-thermal emission in the radio and X-ray bands, which suggests the presence of a population of relativistic charged particles (e.g. Mirabel & Rodríguez 1994, Barret 2004). Also, some of these systems have been detected in high energies (HE; $E > 100$ MeV) and/or very high energies (VHE; $E > 100$ GeV) (Dubus 2013, Paredes et al 2013), which shows that they can be efficient accelerators and $\gamma$-ray emitters.

Depending on the nature of the companion (Cn), the systems can be classified as a microquasar, a binary hosting a young pulsar, or a massive star binary. In a microquasar, the Cn is a stellar-mass black hole (BH), or a neutron star (NS) with a weak magnetic field, capable of accreting material coming from the star and generating relativistic jets (Mirabel & Rodríguez 1999); in a binary with pulsar, the Cn is a young NS with a strong magnetic field that powers an intense relativistic wind (Maraschi & Treves 1981); finally, in a massive star binary the Cn is another massive star with a strong stellar wind (e.g. Eichler & Usov 1993, Benaglia & Romero 2003). Note that the high-energy phenomena is similar in all these systems, which in many cases leads to uncertainties in determining the nature of the Cn.

The non-thermal emission from high-mass binaries is generated by ultra-relativistic particles accelerated, generally, in strong shock-waves in plasma flows. The non-thermal energy could be supplied by accretion and transported by jets in microquasars, or carried by supersonic winds of massive stars or the relativistic wind of a pulsar. Most of the accelerated particles cool down locally through interactions with the medium matter,

magnetic and radiation fields. The result at high energies of these interactions depends strongly on the massive star, as it provides targets (mostly ultraviolet photons) for Inverse Compton (IC) scattering, and target atomic nuclei for proton-proton interactions and relativistic Bremmstrahlung, among other radiation processes. Under general conditions within gamma-ray binaries (i.e., magnetic field strengths of the order of 1 G and photon field energy densities of the order of 1 erg/cm$^3$), however, leptons cool down and radiate more efficiently than hadrons. Additionally, the radiation coming from the inner regions of a high-mass binary is likely to undergo absorption due to pair creation in the stellar radiation field (for an assessment of the importance of the different processes, see Bosch-Ramon & Khangulyan 2009).

In this work, we take advantage of the few assumptions required by a simple model, which can be useful to sketch in a generic way the physical properties of these objects. Considering the present and future observational developments, which imply an increase in the quantity of known sources, we apply this model to investigate in detail the physical processes that underlie their high-energy emission.

The structure of this article is as follows: in Section 2, we present the most important aspects of the one-zone model; in Section 3, we apply this tool for different choices of the relevant state parameters; and finally, in Section 4, we discuss our results in the context of the current observational data, and summarize the main conclusions of this work.

## 2. Model

From a generic point of view, high-mass binary systems can be characterized by the presence of a massive star and an accelerator of relativistic particles. We consider both the massive star and the accelerator as point-like objects, and thus homogeneous. In addition, the accelerator and the emitter are assumed steady and co-spatial, as electrons cannot travel long distances while emitting because of the short cooling timescales. This is known as a *one-zone model*, which is the simplest model capable of incorporating the most relevant physical processes of a given system, and of reproducing the main features of its observable quantities.

The injection of relativistic electrons in the emitter is taken to follow an energy distribution $Q(E) \propto E^{-2} \exp(-E/E_{\rm max})$ for energies above 1 GeV up to few $E_{\rm max}$ (the cutoff energy), consistent with a Fermi I acceleration process. The restriction of our analysis to particles with energy above 1 GeV is in order to concentrate on the emission above GeV energies; moreover, the most energetic particles cool down faster and therefore locally, which allows us to neglect the non-radiative losses (i.e., particle escape and adiabatic cooling). Particle maximum energy ($E_{\rm max}$) is obtained by equating their cooling time (taking into account synchrotron and IC losses) to their acceleration time, plus the constraint derived from comparing the accelerator/emitter size ($R$) and the particle gyroradius: $R > r_{\rm g} = E_{\rm max}/qB$. To minimize the number of free parameters, we assumed the characteristic acceleration time to be $t_{\rm acc} = E/(\eta Bcq)$, where $E$, $q$ and $c$ are the particle energy, charge and velocity, respectively; the parameter $\eta$ is the acceleration efficiency, which we assume to be constant. Note that $\eta$ is limited to the range $(0, 1)$, with $\eta = 1$ being the maximum efficiency, which corresponds to assuming Bohm diffusion in the acceleration process.

The relativistic electrons interact with the ambient stellar photon field and with the emitter magnetic field, producing a broad radiation spectrum. The dominant ra-

diative processes are IC scattering and synchrotron, whereas the dominant VHE $\gamma$-ray absorption process is pair production with stellar photons (Gould & Schreder 1967). We have not considered radiation reprocessing, although for weak enough magnetic fields an electromagnetic IC cascade can develop, increasing the transparency to VHE photons, and for stronger fields, the secondary pair radiation can overcome the X-rays from the primary electron distribution in the emitter (e.g. Bosch-Ramon et al. 2008). We have also assumed that the emitting flow is at most mildly relativistic, as it would be the case for a standing shock in a jet or a wind-colliding region, and thus we have not accounted for Doppler boosting, which would increase the model geometrical parameters. Finally, we assumed a distance to the source of $d = 3$ kpc, and a characteristic scale of $a = 3 \times 10^{12}$ cm related to the size of the binary system; for the companion star, we adopted a luminosity of $L_* = 3 \times 10^{38}$ erg/s and an effective temperature of $T_* = 3 \times 10^4$ K; for the accelerator, we assumed an injection luminosity of $L_{\rm inj} = 10^{36}$ erg/s (for comparative purposes, the estimated values of these parameters for the system LS 5039 are $d = 2.9$ kpc, $T_* = 3.9 \times 10^4$ K, $L_* = 7 \times 10^{38}$ erg/s, $a = 2.3 \times 10^{12}$ cm, and $L_{\rm inj} < 10^{37}$ erg/s, while for the system PSR B1259-63 they are $d = 2.3$ kpc, $T_* = 3.4 \times 10^4$ K, $L_* = 3.7 \times 10^{38}$ erg/s, $a = 1.2 \times 10^{14}$ cm, $L_{\rm inj} < 8 \times 10^{35}$ erg/s). As a result, only two free parameters are left in our model: the acceleration efficiency $\eta$, and the ratio of the magnetic field energy density to the radiation field energy density, $\delta = u_{\rm mag}/u_{\rm rad}$. Once these parameters are given certain values, the steady-state electron energy distribution can be computed (see e.g. Khangulyan et al. 2007).

## 3. Results

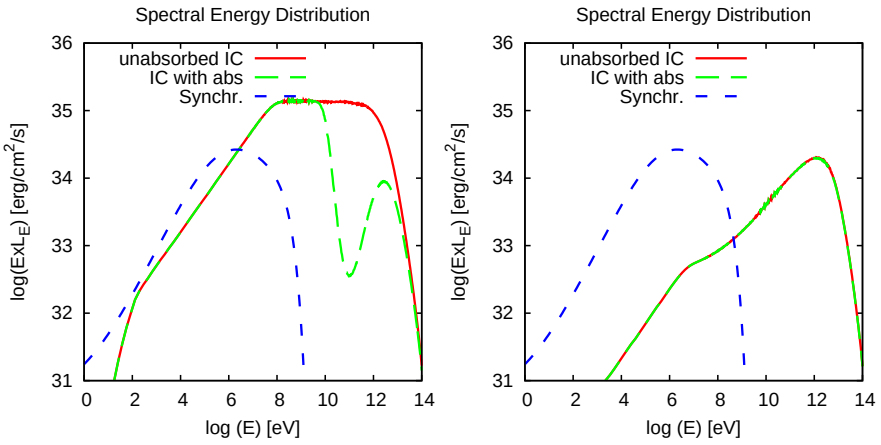


Figure 1. SEDs for a weak magnetic field ($\delta = 10^{-4}$) and a high acceleration efficiency ($\eta = 1$). The left figure was calculated for an emitter behind the star, located at $(-2a, a)$, while the right one was calculated for an emitter in front of the star, located at $(2a, a)$. In both cases the observer is in the direction of the positive $x$-axis and the massive star is at $(0, 0)$.

The spectral energy distribution (SED) is a measure of the amount of energy emitted per time and area units in a certain frequency (or energy). Because the radiative and absorption processes have a strong dependence with the interaction angle, the star-

emitter-observer geometry plays a crucial role in the resulting HE and VHE spectrum. In order to investigate this factor we calculated the SED for different positions of the emitter with respect to the massive star and the observer. In Fig. 1 we present the SEDs for two different positions of the emitter in a case dominated by the radiation field ($\delta = 10^{-4}$) and a highly efficient accelerator ($\eta = 1$). The HE radiation produced by IC scattering in the observer direction is greater if the emitter is behind the massive star; however, the $\gamma$-ray absorption is also enhanced in this configuration, resulting in a diminished VHE flux.

To study the geometrical aspects in which we are interested, and considering that the emitter structure and location within the system is not known, it is useful to display in maps relevant features of the emitter for all the possible locations. To do so, we compute the particle population and the (absorbed) emission from an emitter placed at a specific position in the star-emitter-observer plane, and then we extract any relevant quantity for such a location. This procedure is repeated for every spatial coordinate in the star-emitter-observer plane, and the result is displayed in the form of a two-dimensional map. These maps are studied in the context of physical constraints (related to energy requirements and confinement of the emitter), empirical constraints (scenarios that yield a very intense emission are considered unlikely as there are very few known systems with such characteristics) and instrumental constraints (energy fluxes below the sensitivity of the present instruments cannot be detected).

We focus here on the total energy flux in the ranges: 0.3–10 keV ($F_{\rm X}$), 0.1–10 GeV ($F_{\rm GeV}$) and 0.1–10 TeV ($F_{\rm TeV}$). Furthermore, to probe the validity of the point-like emitter assumption, we estimate the minimum emitter radius considering balance between the ram pressure of the stellar wind and the non-thermal electron pressure, which gives a lower limit for the emitter pressure. We normalize this value to the stellar distance ($r$), and consider the approximation to remain valid as long as $R/r < 0.5$. For illustrative purposes, emissivity maps for a specific case are shown in Fig. 2.

## 4. Discussion

We explored in detail the radiation coming from systems of orbital separation $a > 3 \times 10^{12}$ cm with a *one-zone* leptonic model. This model works well for sources with $L_{\rm inj} < 10^{36}$ erg/s, and it reflects the relevant features of the emission and absorption processes, mainly the geometry role in the detectability of $\gamma$-rays. However, the validity of the approximation is dubious for sources with a high acceleration efficiency, a low magnetic field, and an emitter located at $r > 6a$, as in those regions the value of $R/r$ is highest, with $R/r \sim 0.5$ in such cases.

Some conclusions of our results are:

- In general, sources with low magnetic fields have a higher TeV luminosity, unless the sources host very inefficient accelerators that can hardly reach TeV energies.
- Sources with strong magnetic fields have a higher X-ray luminosity, and in most cases the predicted X-ray luminosity is far above the instrumental sensitivity threshold, which suggests that such sources could be detected even at distances larger than 3 kpc.
- There must be very few powerful sources with a high acceleration efficiency and a weak magnetic field at a distance $\sim$ 3 kpc, as otherwise it would overpredict the

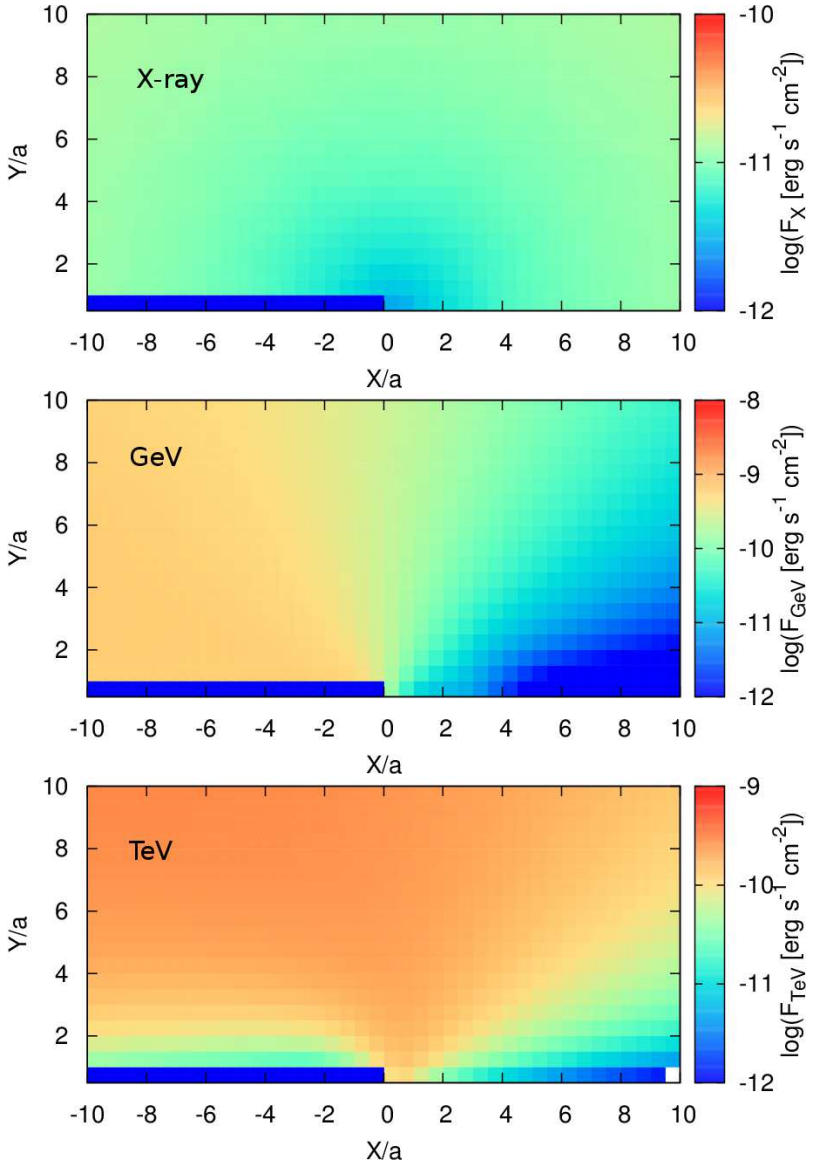


Figure 2. Emission maps in the X-ray, GeV, and TeV bands (top left, top right, and bottom left panels, respectively) for a weak magnetic field ($\delta = 10^{-4}$) and a high acceleration efficiency ($\eta = 1$). In all cases the observer is in the direction of the positive $x$-axis and the massive star is at $(0, 0)$. For a source to be detectable with the current instruments, a lower limit can be set to the energy fluxes: $F_{\rm X} > 10^{-14}$ erg/s/cm$^2$ (*Chandra*, *XMM-Newton*), $F_{\rm GeV} > 10^{-11}$ erg/s/cm$^2$ (*Fermi*) and $F_{\rm TeV} > 10^{-13}$ erg/s/cm$^2$ (MAGIC, HESS, VERITAS). Moreover, in view of the empirical constraints, an upper limit can also be set to the energy fluxes: $F_{\rm X} < 10^{-10}$ erg/s/cm$^2$, $F_{\rm GeV} < 10^{-9}$ erg/s/cm$^2$ and $F_{\rm TeV} < 10^{-11}$ erg/s/cm$^2$.

amount of observed strong $\gamma$-ray emitters. More specifically:

$$\left(\frac{L_{\rm inj}}{10^{36}}\frac{\rm erg}{\rm s}\right)\left(\frac{d}{3\,{\rm kpc}}\right)^{-2} < 0.1 - 1\,.$$

However, there could be more sources with such characteristics if they are weaker and/or at a farther distance (so rather sparse), and they would be observable in the GeV and TeV range in the most favourable orbital phases.

- There could be a considerable number of sources that are currently below the sensitivity of the detectors, as galactic sources with intense magnetic fields are weak $\gamma$-ray emitters, and so they would be hard to detect in gamma rays at a distance $> 3$ kpc.

Adiabatic losses are probably important in the farther regions of the system, so we might have overestimated the emission, specially in the X-ray band. In future works we will explore how the introduction of adiabatic losses affects these results, as well as other effects like the radiation from the secondary pairs and the introduction of a hadronic component. We will also use the emissivity maps as a tool for studying properties such as the $\gamma$-ray luminosity function of high-mass binaries, their lifespan, etc.

**Acknowledgments.** This work is supported by CONICET and by ANPCyT (PICT 2012-00878). V.B-R. acknowledges financial support from MINECO and European Social Funds through a Ramón y Cajal fellowship. This research has been supported by the Marie Curie Career Integration Grant 321520. V.B-R. and G.E.R. acknowledges support by the Spanish Ministerio de Economía y Competitividad (MINECO) under grant AYA2013-47447-C3-1-P.

## References

Barret, D. 2004, AIPC, 703, 238

Benaglia, P. & Romero, G. E. 2003, A&A, 399, 1221

Bosch-Ramon, V., Khangulyan, D. & Aharonian, F. A. 2008, A&A, 482, 397

Bosch-Ramon, V. & Khangulyan D. 2009, IJMPD, 18, 347

Dubus, G. 2013, A&A Rev., 21, 64

Eichler, D. & Usov, V. V. 1993, ApJ, 402, 271.

Gould, R. J. & Schréder, G. P. 1967, Phys. Rev., 155, 1408

Khangulyan, D., Hnatic, S., Aharonian, F. & Bogovalov, S. 2007, MNRAS, 380, 320

Maraschi, L. & Treves, A. 1981, MNRAS, 194, 1

Mirabel, I. F. & Rodríguez, L. F. 1994, Nature, 371,4 6

Mirabel, I. F., & Rodríguez, L. F. 1999, ARA&A, 37, 409

Paredes, J. M., Bednarek, W., Bordas, P. et al. 2013, APh., 43, 301

*Gravitation, Relativistic Astrophysics and Cosmology*
*Second Argentinian-Brazilian Meeting, 2014*
*G. S. Vila, F. L. Vieyro and J. Fabris, eds.*

# Regular phantom black holes as gravitational lenses

Ernesto F. Eiroa[1,2] and Carlos M. Sendra[1,2]

[1]*Instituto de Astronomía y Física del Espacio, Buenos Aires, Argentina*
[2]*Departamento de Física, FCEN-UBA Buenos Aires, Argentina*

**Abstract.** The distortion of the spacetime structure in the surroundings of black holes affects the trajectories of light rays. As a consequence, black holes can act as gravitational lenses. Observations of type Ia supernovas, show that our Universe is in accelerated expansion. The usual explanation is that the Universe is filled with a negative pressure fluid called dark energy, which accounts for 70% of its total density, which can be modeled by a self-interacting scalar field with a potential. We consider a class of spherically symmetric regular phantom black holes as gravitational lenses. We study large deflection angles, using the strong deflection limit, corresponding to an asymptotic logarithmic approximation. In this case, photons passing close to the photon sphere of the black hole experiment several loops around it before they emerge towards the observer, giving place to two infinite sets of relativistic images. Within this limit, we find analytical expressions for the positions and the magnifications of these images. We discuss the results obtained and make a comparison with the Schwarzschild and Brans-Dicke solutions for the case of the galactic center supermassive black hole.

## 1. Introduction

The study of gravitational lensing by black holes has received a boost (Virbhadra et al. 2000) due to the evidence of the presence of supermassive black holes at the center of galaxies, including ours. For these objects, two sets of relativistic images are formed when the light rays pass close to the photon sphere, for which the strong deflection limit is adopted. This approximation was found for any spherically symmetric object with a photon sphere (Bozza 2002). Many works considering strong deflection lenses are found in the literature for different types of black holes. It is thought that observations of the optical effects associated with these objects will be possible in the near future (Eiroa 2013).

The accelerated expansion of the Universe can be explained by the existence of dark energy as the prevailing component (see, for example, Bamba et al. 2012). This can be in the form of phantom energy if $\omega < -1$ in the equation of state $p = \omega\rho$, and can be modeled by a self-interacting scalar field with a potential. Withing this context, regular black hole and wormhole phantom solutions were found (Bronnikov et al. 2006); also phantom dilaton black holes were recently studied as gravitational lenses (Gyulchev et al. 2013; Eiroa et al. 2013).

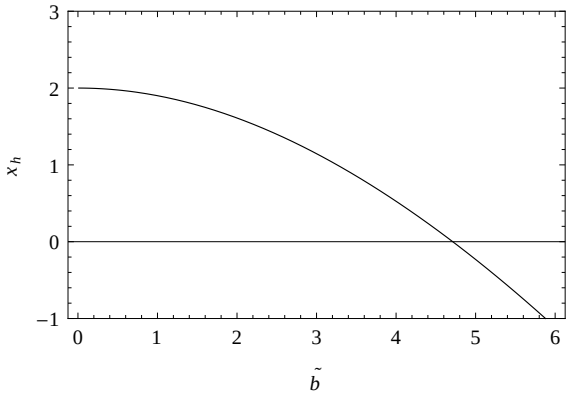


Figure 1. Horizon radius $x_h = r_h/m$ as a function of $\tilde{b} = b/m$.

## 2. Regular phantom black hole

We consider the following spherically symmetric geometry, which is a solution of the Einstein equations with a scalar field possessing a negative kinetic term and a potential (Bronnikov et al. 2006):

$$ds^2 = -A(r)dt^2 + B(r)dr^2 + C(r)d\Omega^2, \tag{1}$$

where

$$A(r) = B(r)^{-1} = 1 + \frac{3mr}{b^2} + (r^2 + b^2)\left[\frac{c}{b^2} + \frac{3m}{b^3}\tan^{-1}\left(\frac{r}{b}\right)\right],$$

$$C(r) = r^2 + b^2, \tag{2}$$

with $c$, $m$, and $b > 0$ constants. The solution is regular everywhere, i.e. free from curvature singularities; $b$ is the scale of the scalar field, and $m$ can be interpreted as the mass. In the particular case that $c = -3m\pi/2b$, the metric becomes asymptotically flat. We have a black hole solution for $m > 0$, with a Killing horizon $r_h$. In this case, the region corresponding $r > r_h$ is asymptotically flat, and the one with $r < r_h$ is asymptotically de Sitter. This solution is stable for $b = 3m\pi/2$, for which $r_h = 0$ (Bronnikov et al. 2012). It is convenient to adimensionalyze the metric with the mass, by defining

$$x = r/m, \quad T = t/m, \quad \tilde{b} = b/m, \tag{3}$$

and adopting the flatness condition, so the black hole solution has the form

$$ds^2 = -A(x)dT^2 + B(x)dx^2 + C(x)(d\theta^2 + \sin^2\theta d\phi^2), \tag{4}$$

$$A(x) = B(x)^{-1} = 1 + \frac{3x}{\tilde{b}^2} + \frac{3}{\tilde{b}}\left(1 + \frac{x^2}{\tilde{b}^2}\right)\left[-\frac{\pi}{2} + \tan^{-1}\left(\frac{x}{\tilde{b}}\right)\right], \tag{5}$$

$$C(x) = x^2 + \tilde{b}^2. \tag{6}$$

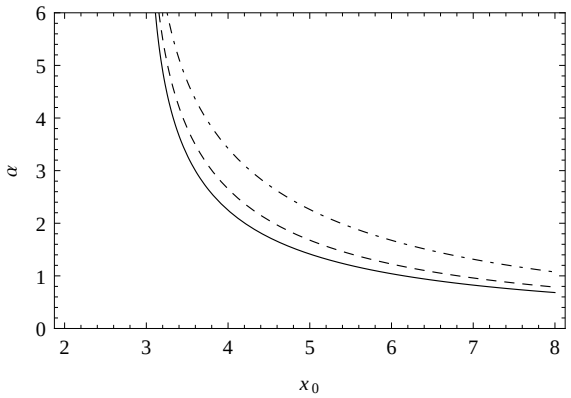


Figure 2. Deflection angle $\alpha$ as a function of the closest approach distance $x_0$ for $\tilde{b} = 1$ (full line), $\tilde{b} = 3$ (dashed line), and $\tilde{b} = 6$ (dashed-dotted line).

The adimensionalyzed radius of the horizon $x_h$, corresponding to the root of $A(x)$, is a decreasing function of $\tilde{b}$, shown in Fig. 1. The radius of the photon sphere $x_{ps}$ is given by the largest positive solution of the equation

$$A'(x)C(x) = C'(x)A(x), \tag{7}$$

where the prime represents the derivative with respect to $x$. For the phantom black hole, corresponds to the constant value $x_{ps} = 3$.

## 3. Strong deflection limit

The deflection angle for a photon coming from infinity, as a function of the closest approach distance $x_0$, is given by (Virbhadra et al. 1998)

$$\alpha(x_0) = I(x_0) - \pi, \tag{8}$$

where

$$I(x_0) = \int_{x_0}^{\infty} \frac{2\sqrt{B(x)}dx}{\sqrt{C(x)}\sqrt{\frac{C(x)}{C(x_0)}\frac{A(x_0)}{A(x)} - 1}}. \tag{9}$$

The deflection angle is a monotonic decreasing function of $x_0$, as can be seen in Fig. 2. It diverges when $x_0$ approaches to the radius of the photon sphere $x_{ps} = 3$, and goes to zero for large $x_0$. When $x_0$ is close enough to $x_{ps}$, the deflection angle is greater than $2\pi$, which means that the photons perform one or more turns around the black hole before emerging towards the observer. This results in two infinite sets of relativistic images, one on each side or the black hole (i.e. at the same side and at the opposite side of the source). To study the situation where the photons pass close to the photon sphere, we adopt the so-called strong deflection limit (Bozza 2002). The integral (9) can be split into two parts

$$I(x_0) = I_D(x_0) + I_R(x_0), \tag{10}$$

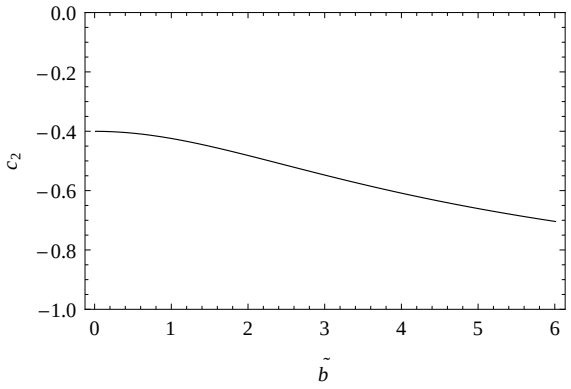


Figure 3. Strong deflection limit coefficient $c_2$ as a function of $\tilde{b}$.

where $I_D$ yields the leading order term in the divergence of the deflection angle, which is logarithmic; $I_R$ is regular for all values of $x_0$ and can be easily evaluated. It can be shown that in this limit, the deflection angle can be approximated by the simple general form (Bozza 2002)

$$\alpha(u) = -c_1 \ln\left(\frac{u}{u_{ps}} - 1\right) + c_2 + O(u - u_{ps}), \tag{11}$$

with $u = [C(x_0)A^{-1}(x_0)]^{1/2}$ the impact parameter, and $u_{ps} = u(x_{ps})$. The quantities $c_1$ and $c_2$ are the strong deflection limit coefficients, which depend only on the metric functions. Performing the calculations for the regular phantom black hole, we have that $c_1 = 1$ is a constant, and $c_2$ results (Eiroa et al. 2013)

$$c_2 = -\pi + c_R + \ln \frac{\tilde{b}^3\left[-6\tilde{b} + 9\pi + \tilde{b}^2\pi - 2(9+\tilde{b}^2)\tan^{-1}\left(\frac{3}{\tilde{b}}\right)\right]^2}{(9+\tilde{b}^2)^2\left[2\tilde{b} - 3\pi + 6\tan^{-1}\left(\frac{3}{\tilde{b}}\right)\right]^3}, \tag{12}$$

where $c_R = I_R(x_{ps})$ is obtained numerically for each value of the parameter $\tilde{b}$. The coefficient $c_2$ is a decreasing function of $\tilde{b}$, as shown in Fig. 3.

Adopting a configuration where the black hole ($l$) is situated between the source ($s$) and the observer ($o$), both located in the (asymptotically) flat region, at distances $x \gg x_h$, the lens equation is given by (Bozza 2008)

$$\tan\beta = \frac{d_{ol}\sin\theta - d_{ls}\sin(\alpha-\theta)}{d_{os}\cos(\alpha-\theta)}, \tag{13}$$

where $d_{os}$, $d_{ol}$ and $d_{ls}$, are the observer-source, observer-lens, and lens-source angular diameter distances, respectively; $\beta$ is the angular position of the source, and $\theta$ is the angular position of the image. For highly aligned objects, i.e. $\beta$ and $\theta$ small, the lensing effects are more significant, and the deflection angle, for each set of relativistic images, is close to an even multiple of $\pi$:

$$\alpha = \pm 2n\pi \pm \Delta\alpha_n, \tag{14}$$

where $n \in \mathbb{N}$, and $0 < \Delta\alpha_n \ll 1$. Then, the lens equation takes the simplified form

$$\beta = \theta \mp \frac{d_{ls}}{d_{os}}\Delta\alpha_n. \tag{15}$$

From the lens geometry, we have that $u = d_{ol}\sin\theta \approx d_{ol}\theta$. Replacing this relation in Eq. (11), and using the lens equation (15), it is not difficult to see that the angular position of the $n$-th relativistic image results (Bozza 2002)

$$\theta_n = \pm\theta_n^0 + \frac{\xi_n d_{os}}{d_{ls}}(\beta \mp \theta_n^0), \tag{16}$$

where

$$\theta_n^0 = \frac{u_{ps}}{d_{ol}}\left[1 + e^{(c_2 - 2n\pi))/c_1}\right], \tag{17}$$

and

$$\xi_n = \frac{u_{ps}}{c_1 d_{ol}} e^{(c_2-2n\pi)/c_1}. \tag{18}$$

The magnification of the $n$-th image $\mu_n$ is given by the quotient between the angle subtented by the image and the source:

$$\mu_n = \left|\frac{\beta}{\theta_n}\frac{d\beta}{d\theta_n}\right|^{-1}. \tag{19}$$

Replacing Eq. (16) in expression (19), within the approximations adopted above, the magnification of each relativistic image takes the form

$$\mu_n = \frac{1}{\beta}\frac{\theta_n^0 \xi_n d_{os}}{d_{ls}}. \tag{20}$$

The magnifications decrease exponentially with $n$, so the first relativistic image is the brighest one, as can be seen by replacing expressions (17) and (18) in (20). These magnitudes can be related with observations by defining the observables:

$$s = \theta_1 - \theta_\infty \tag{21}$$

and

$$r = \frac{\mu_1}{\sum_{n=2}^{\infty}\mu_n}. \tag{22}$$

The angular position $\theta_\infty$ is the limiting value where the images approach as $n \to \infty$, which is an increasing function of $\tilde{b}$ for a given value of $d_{ol}$. The first relativistic image is expected to be resolved from the others since it is the outermost and brightest one. Then, the observable $s$ is defined as the angular separation between the first relativistic image and the others, which are packed together at the limiting value $\theta_\infty$. The observable $r$ is the quotient between the flux of the first relativistic image and the flux coming from all the others. In the strong deflection limit, and for high alignment, we obtain that

$$s = \theta_\infty e^{(c_2-2\pi)/c_1} = \theta_\infty e^{c_2-2\pi} \tag{23}$$

and

$$r = e^{2\pi/c_1} = e^{2\pi}, \tag{24}$$

which are functions of $c_1$ and $c_2$. For the phantom black hole, $c_1 = 1$, so $r$ is a constant. The quotient $s/\theta_\infty$ is plotted as a function of $\tilde{b}$ in Fig. 4.

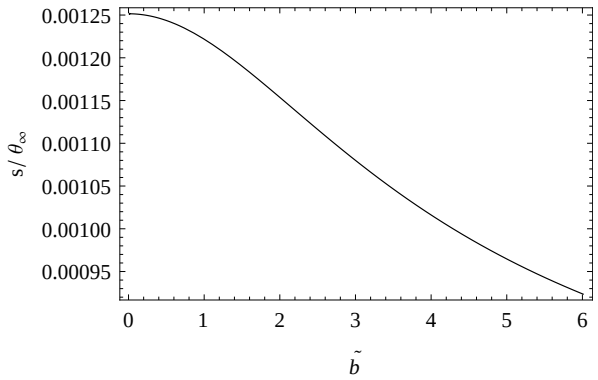


Figure 4. Observable $s/\theta_\infty$ as a function of $\tilde{b}$.

## 4. Summary and discussion

In this work, uncharged regular phantom black holes, obtained from a scalar field possessing a negative kinetic term and a potential, were studied as gravitational lenses. The strong deflection limit coefficients $c_1$ and $c_2$ were calculated, which allowed us to obtain analytical expressions for the positions and the magnifications of the relativistic images, and the observables $\theta_\infty$, $r$ and $s$. The first relativistic image is the outer one, which is also the brightest, and the others are packed together at the limiting value $\theta_\infty$. If the strong deflection limit coefficients can be obtained from observational data, the phantom black holes studied here can be clearly distinguished from the Schwarzschild and vacuum Brans-Dicke solutions, because the values of $c_2$ are different (Bozza 2002; Sarkar et al. 2006).

**Acknowledgments.** This work has been supported by CONICET and UBA.

## References

Bamba, K., Capozziello, S., Nojiri, S., Odintsov, S. D. 2012, Astroph. Space Sci., 342, 155

Bozza, V. 2002, Phys. Rev. D, 66, 103001

Bozza, V. 2008, Phys. Rev. D, 78, 103005

Bronnikov, K. A., Fabris, J. C. 2006, Phys. Rev. Lett., 96, 251101

Bronnikov, K. A., Konoplya, R. A, Zhidenko, A. 2012, Phys. Rev. D, 86, 024028

Eiroa, E. F. 2013, in "Gravitation, Relativistic Astrophysics and Cosmology, Proceedings of the First Argentinian-Brazilian Meeting", Livraria da Fisica, São Paulo

Eiroa, E. F., Sendra, C. M. 2013, Phys. Rev. D, 88, 103007

Gyulchev, G. N., Stefanov, I. Z. 2013, Phys. Rev. D, 87, 063005

Sarkar, K., Bhadra, A. 2006, Class. Quant. Grav., 23, 6101

Virbhadra, K. S., Narasimha, D., Chitre, S. M. 1998, Astron. Astroph., 337, 1

Virbhadra, K. S., Ellis, G. F. R. 2000, Phys. Rev. D, 62, 084003

*Gravitation, Relativistic Astrophysics and Cosmology*
*Second Argentinian-Brazilian Meeting, 2014*
*G. S. Vila, F. L. Vieyro and J. Fabris, eds.*

# Hamiltonian formalism for modified teleparallel gravity

Rafael Ferraro[1,2] and María José Guzmán[1]

[1]*Instituto de Astronomía y Física del Espacio (IAFE, CONICET-UBA), Casilla de Correo 67, Sucursal 28, (1428) Buenos Aires, Argentina*
[2]*Departamento de Física, Facultad de Ciencias Exactas y Naturales, Universidad de Buenos Aires, Ciudad Universitaria, Pabellón I, (1428) Buenos Aires, Argentina*

**Abstract.** Starting from the canonical formalism for constrained Hamiltonian systems, we develop a second order approach to tackle the issue of the number of degrees of freedom in teleparallel theories of gravity.

## 1. Introduction to teleparallel gravity

The teleparallel equivalent of general relativity (TEGR) is an alternative geometrical reformulation of general relativity. This theory was originally developed by Einstein in an attempt of unifying gravity and electromagnetism (Einstein 1930, 1939). In this formulation, the field of tetrads is taken as the dynamical variable instead of the metric tensor. The tetrad is a basis $e_a(x)$, $a = 0, 1, 2, 3$, of vectors in the spacetime. Each vector $e_a$ can be decomposed in a coordinate basis with components $e^\mu{}_a$, such that the orthonormality condition reads $\eta_{ab} = g_{\mu\nu} e^\mu{}_a e^\nu{}_b$, where $\eta_{ab} = \text{diag}\,(1, -1, -1, -1)$ is the Minkowski metric. This relation allows to obtain the metric starting from the tetrad, with the aid of the co-basis $\mathbf{e}^a(x)$, since $g_{\mu\nu} = \eta_{ab} e^a{}_\mu e^b{}_\nu$ (matrices $e^\nu{}_b$ and $e^a{}_\mu$ are inverse each other). Thus, the determinant of the metric is written as $\sqrt{-g} = det[e^a{}_\mu] = e$.

An important feature of the TEGR Lagrangian is that it does not contain second derivatives of the tetrad, because it is quadratic in the tensor

$$T^\mu{}_{\nu\rho} = e^\mu{}_a (\partial_\nu e^a{}_\rho - \partial_\rho e^a{}_\nu), \tag{1}$$

which resembles the electromagnetic field tensor. This can be regarded as the torsion of the Weitzenböck connection $\Gamma^\mu{}_{\rho\nu} = e^\mu{}_a \partial_\nu e^a{}_\rho = -e^a{}_\rho \partial_\nu e^\mu{}_a$, which differs from Levi-Civita connection in the contorsion tensor $K^\mu{}_{\rho\nu} = \frac{1}{2}\left(T_\rho{}^{\mu\nu} - T^{\mu\nu}{}_\rho + T^{\nu\mu}{}_\rho\right)$. Weitzenböck connection has torsion but not curvature.

The TEGR action is written in terms of the torsion scalar $\mathcal{T}$, which is defined as $\mathcal{T} = S_\rho{}^{\mu\nu} T^\rho{}_{\mu\nu}$, where the tensor $S_\rho{}^{\mu\nu}$ reads

$$S_\rho{}^{\mu\nu} \equiv \frac{1}{2}\left(K^{\mu\nu}{}_\rho + T_\lambda{}^{\lambda\mu}\,\delta^\nu_\rho - T_\lambda{}^{\lambda\nu}\,\delta^\mu_\rho\right). \tag{2}$$

The TEGR action is

$$S_{\text{TEGR}} = \frac{1}{2\kappa}\int d^4x\; e\; \mathcal{T}. \tag{3}$$

The equivalence between general relativity and the TEGR is based on the fact that the TEGR Lagrangian is equal to the Einstein-Hilbert Lagrangian up to a four-divergence that is integrated out in the action: the relation between the (Levi-Civita) Ricci scalar and the torsion scalar is

$$\mathcal{T} = -R - 2\nabla_\rho(T_\mu{}^{\mu\rho}). \tag{4}$$

## 2. Modified teleparallel gravity

In the spirit of $f(R)$ gravity, we can define $f(\mathcal{T})$ gravity, an appealing modified gravity theory that deformates the teleparallel action by means of an arbitrary function $f$ (Ferraro et al. 2007, 2008). Its action is

$$S_T[e^a] = \frac{1}{2\kappa}\int d^4x\; e\; f(\mathcal{T}). \tag{5}$$

Varying with respect to the tetrad, the field equations for this theory are

$$\begin{aligned} 4\left(\frac{1}{e}\partial_\mu(e\, S_a{}^{\mu\nu}) + e^\lambda_{\ a}\, T^\rho_{\ \mu\lambda} S_\rho{}^{\mu\nu}\right)\, f'(\mathcal{T}) \quad & + \\ 4S_a{}^{\mu\nu}\partial_\mu(\mathcal{T})\; f''(\mathcal{T}) - e^\nu_{\ a}\; f(\mathcal{T}) \quad &= \quad -2\kappa\, e^\lambda_{\ a}\, T^\nu_{\ \lambda}, \end{aligned} \tag{6}$$

where $T^\nu_{\ \lambda}$ is the energy-momentum tensor. Unlike $f(R)$ theories, the dynamical equations in $f(\mathcal{T})$ theories are always second order, since the Lagrangian does not contain second derivatives of the tetrad field. A distinctive feature of these equations is the loss of local Lorentz invariance: if $e^a(x)$ is a solution then the transformed tetrad $e^{b'} = \Lambda^{b'}_{\ a}(x)\, e^a$ is not, in general, a solution of the field equations. In fact the divergence in equation (4) is not invariant under local Lorentz transformations. This fact is harmless when $f(\mathcal{T}) = \mathcal{T}$, since the divergence is integrated out in the action, but it is crucial in a non-trivial $f(\mathcal{T})$ theory because the divergence remains encapsulated in the argument of $f$. This feature means that the theory possesses degrees of freedom that do not lie in the metric tensor, since $g_{\mu\nu}$ is unable to distinguish among locally Lorentz-related tetrads. The nature of the extra degrees of freedom is an open issue.

## 3. Hamiltonian formalism

In general relativity and gauge theories there are constraints among the canonical momenta. Therefore, the initial values of the canonical momenta cannot be freely chosen, but they have to accomplish the constraint relations. Moreover, the evolution of the system has to preserve the constraints; this consistency requirement can lead to more constraints. At the end of the day, one gets a set of $f$ first class (on-shell commuting) constraints and $s$ second class (forming canonical pairs) constraints (see, for instance, Sundermeyer 1982). For a system of $n$ pairs of canonical variables $(q,\ p)$ the number of physical degrees of freedom $\#d.o.f$ is

$$\#d.o.f. = n - f - \frac{s}{2}. \tag{7}$$

The knowledge of the algebra of constraints is fundamental for the quantization of the theory, so being a strong motivation for considering the Hamiltonian formalism of this kind of theories. For the moment, we are interested in getting the number of physical degrees of freedom of TEGR and $f(\mathcal{T})$ theories.

### 3.1. Teleparallel gravity

We will recall the approach of Maluf et al. (2001) for the Hamiltonian formalism of the TEGR (see also Maluf et al. 2011, Maluf 2013). This is done through a first order formulation of the Lagrangian density, in an analogous way to the first order formulation of electromagnetism, in which $A_\mu$ and $F_{\mu\nu}$ are considered independent fields (for different approaches see Blagojevic et al. 2000 and Okolów 2013).

The first order formulation of the TEGR is written in terms of the torsion tensor $T_{abc} = e^\lambda_{\ a}\ e^\mu_{\ b}\ e^\nu_{\ c}\ T_{\lambda\mu\nu}$, and also an auxiliary field quantity $\phi_{abc} = -\phi_{acb}$. Then the Lagrangian will be

$$L(e,\phi) = k\ e\ \Lambda^{abc}(\phi_{abc} - T_{abc}), \tag{8}$$

where $\Lambda^{abc}$ is defined by

$$\Lambda^{abc} = \frac{1}{4}(\phi^{abc} + \phi^{bac} - \phi^{cab}) + \frac{1}{2}(\eta^{ac}\phi^b - \eta^{ab}\phi^c), \tag{9}$$

and $\phi_b = \phi^a_{\ ab}$. Indices $a$, $b$, $c$ are lowered and raised by means of $\eta_{ab}$ and $\eta^{ab}$. The variation of the Lagrangian with respect to $\phi^{abc}$ led to the result $\phi_{abc} = T_{abc}$, while the variation with respect to the tetrad yields the standard equations of motion of the TEGR. So the Lagrangian $L(e,\phi)$ is equivalent to the teleparallel gravity Lagrangian.

The momentum canonically conjugated to $e_{ak}$ is $\Pi^{ak} = -4k\ e\ \Lambda^{a0k}$. Here the relation between $\Pi^{ak}$ and the velocity $\dot{e}_{ak}$ is non trivially encoded in the torsion through the tensor $\Lambda^{a0k}$. From this definition, four primary constraints $\Pi^{a0} = 0$ appears, due to the antisymmetries of the Lagrangian.

After obtaining the primary Hamiltonian $H_0 = \Pi^{ai}\ \dot{e}_{ai} - L(e,\phi)$, the momentum $\Pi^{ak}$ is decomposed into irreducible components, by writing the momenta into symmetric and antisymmetric parts,

$$\Pi^{ak} = e^a_i\ \Pi^{(ik)} + e^a_i\ \Pi^{[ik]} + e^a_0\ \Pi^{0k}. \tag{10}$$

Through this procedure, the authors find more primary constraints based on the fact that only the symmetrical components $\Pi^{(ik)}$ depends on the velocities. This leads to the primary constraints $\Gamma^{ab} = -\Gamma^{ba} = \Pi^{[ab]} + 4k\ e\ (\Sigma^{a0b} - \Sigma^{b0a}) = 0$. Secondary constraints $C^a = 0$ arise from the requirement that the primary constraints do not evolve in time. These are given by $C^a = e^{a0}\ H_0 + e^{ai}\ H_i$, where $H_i = -e_{ai}\ \partial_k \Pi^{ak} - \Pi^{ak}\ T_{aki}$.

With all of this, the full Hamiltonian density, including Lagrange multipliers, can be written as

$$H(e_{a\mu}, \Pi^{a\mu}, \lambda_{ab}, \lambda_a) = e_{a0}\ C^a + \lambda_{ab}\ \Gamma^{ab} + \lambda_a\ \Pi^{a0}. \tag{11}$$

The complete set of constraints is separated in first and second class constraints through the calculation of the Poisson brackets.

From this analysis, it is obtained that $C^a$, $\Gamma^{ab}$ and $\Pi^{a0}$ are a set of first class constraints. With this information we can count the physical degrees of freedom of the TEGR theory: the dynamical field quantities $(e_{ai}, \Pi^{ai})$ display $n = 12$ pairs of canonical variables. There are $4 + 6 = 10$ first class constraints $(C^a, \Gamma^{ab})$ that generate symmetries of the action. Then,

$$\#d.o.f._{TEGR} = 12 - 10 = 2, \tag{12}$$

as it was expected, since the theory is equivalent to general relativity.

### 3.2. Modified teleparallel gravity

Li et al. (2011) analyze the structure of constraints of $f(\mathcal{T})$ by rewriting the Lagrangian density in an equivalent form

$$L = -e[\phi\mathcal{T} - V(\phi)]. \tag{13}$$

In fact, by varying with respect to the scalar field $\phi$ one gets $\mathcal{T} = V'(\phi)$, which implies that the Lagrangian contains the Legendre transformation of $V(\phi)$. Therefore the scalar Lagrangian is just a function of $\mathcal{T}$:

$$f(\mathcal{T}) = \phi\mathcal{T} - V(\phi). \tag{14}$$

By anti-transforming one gets

$$\phi = f'(\mathcal{T}), \tag{15}$$

which allows to fix the potential $V$ to be used for each function $f$. This form of the Lagrangian adds an extra primary constraint $\pi = \partial L/\partial(\dot{\phi}) \equiv 0$. However, the appearance of $V(\phi)$ in the Hamiltonian modifies the structure of the Poisson brackets, which become hard to calculate. After some simplifications, the authors find eight first class constraints and eight second class constraints. Since the configuration space harbors 17 variables, they get

$$\#d.o.f._{f(T)} = 17 - 8 - \frac{8}{2} = 5. \tag{16}$$

Therefore, $f(\mathcal{T})$ gravity would have 3 extra degrees of freedom compared with teleparallel gravity. The authors suggest that the extra degrees of freedom could imply a massive vector field or a massless vector field plus a scalar field.

## 4. Another procedure for the Hamiltonian formalism

In order to develop a second order formalism for TEGR and modified teleparallelism, we start with the torsion scalar $\mathcal{T}$ written in the following way:

$$\mathcal{T} = \frac{1}{4}T^{\rho}{}_{\mu\nu}T_{\rho}{}^{\mu\nu} - \frac{1}{2}T^{\rho}{}_{\mu\nu}T^{\mu\nu}{}_{\rho} - T^{\rho}{}_{\mu\rho}T^{\rho\mu}{}_{\rho}. \tag{17}$$

All the terms are quadratic in the the product $\partial_{[\mu}e^{a}{}_{\nu]}\,\partial_{[\rho}e^{b}{}_{\lambda]}$. So we can reorganize them to eventually get the Lagrangian in a proper form:

$$L = e\,\mathcal{T} = e\,\frac{1}{2}\,\partial_{[\mu}e^{a}{}_{\nu]}\,\partial_{[\rho}e^{b}{}_{\lambda]}\,e^{\mu}_{c}\,e^{\nu}_{e}\,e^{\rho}_{d}\,e^{\lambda}_{f}\,N_{ab}{}^{cedf}, \tag{18}$$

where the object playing the role of a *supermetric* is

$$N_{ab}{}^{cedf} \doteq 2\,\eta_{ab}\,\eta^{d[c}\eta^{e]f} - 4\,\delta^{[f}_{a}\,\eta^{d][c}\,\delta^{e]}_{b}. \tag{19}$$

Then, the canonical momenta are given by

$$\Pi^{\nu}_{a} \doteq \frac{\delta L}{\delta\dot{e}^{a}_{\nu}} = e\,\partial_{[\rho}e^{b}{}_{\lambda]}\,e^{0}_{c}\,e^{\nu}_{e}\,e^{\rho}_{d}\,e^{\lambda}_{f}\,N_{ab}{}^{cedf}. \tag{20}$$

In this result we recognize the constraints $\Pi^0_a = 0$ ($e^0_c e^0_e$ is symmetric but $N_{ab}{}^{cedf}$ is antisymmetric in $c, e$), that resemble the primary electromagnetic constraint. They were expectable, due to the electromagnetic flavor of the TEGR Lagrangian. This means the evolution of $e^a_{\ 0}$ is not completely determined by the Lagrangian and the initial conditions; as a consequence, $g_{0\nu}$ involve some gauge freedom. This gauge freedom also affects the tensor density $\det(g_{\mu\nu})\ g^{ij}$ $(i, j = 1, 2, ...)$). This means that the gauge freedom in $e^a_{\ 0}$ is also contained in $e\ e^i_{\ a}$ . Instead, it is easy to prove that no trace of $e^a_{\ 0}$ is left in $e\ e^0_{\ a}$; then, it is $\{\Pi^0_a, e\, e^0_{\ a}\} = 0$. The relation between the rest of canonical momenta and velocities is

$$e\ e^e_k\ \Pi^k_a = e\ e^e_\nu\ \Pi^\nu_a = (\dot{e}^b_{\ j} - \partial_j e^b_{\ 0})\ e^j_{\ f}\ C_{ab}{}^{ef} + \ P_a{}^e\ , \tag{21}$$

where the following definitions hold

$$C_{ab}{}^{ef} \doteq e^2\ e^0_{\ d}\ e^0_{\ c}\ N_{ab}{}^{cedf}, \quad P_a{}^e \doteq e^2\ e^0_{\ c}\ (\partial_j e^b_{\ k})\ e^j_{\ d}\ e^k_{\ f}\ N_{ab}{}^{cedf} \tag{22}$$

(it is $C_{ab}{}^{ef} = C_{ba}{}^{fe}$ and $\{\Pi^0_a\ ,\ C_{ab}{}^{ef}\} = 0$). We will get more primary constraints whenever the equation (21) cannot be solved for all the canonical velocities $\dot{e}^b_{\ j}$. Then we have to focus on the rank of the tensor $C_{ab}{}^{ef}$. It is easy to verify that the supermetric $N_{ab}{}^{cedf}$ cancels out in $D = 1 + 1$ dimensions, so meaning that all the canonical momenta are constrained to vanish and no physical degrees of freedom are left. In higher dimensions we should examine how many null eigenvalues has the matrix $C_{ab}{}^{ef}$. We can define the superindex $A \doteq (a, e)$ to write $C_{ab}{}^{ef}$ as a symmetric $D^2 \times D^2$ matrix $C_{AB}$ and the equation (21) as the linear set

$$e\ (\Pi_A - P_A) = C_{AB}\ E^B, \tag{23}$$

where $\Pi_A \doteq e^e_k\ \Pi^k_a$, $E^B \doteq (\dot{e}^b_{\ j} - \partial_j e^b_{\ 0})\ e^j_{\ f}$. Each eigenvector $V^A$ of $C_{AB}$ having a vanishing eigenvalue leads to an additional primary constraint

$$G_{(V)} \doteq (\Pi_A - P_A)\, V^A = 0. \tag{24}$$

The algebra of primary constraints is not trivial. Although $\{\Pi^0_a\ , C_{AB}\} = 0$ means that $\{\Pi^0_a\ , V^A\} = 0$, $P_A$ still contains traces of $e^a_{\ 0}$ hidden in $e^j_{\ d}\ e^\lambda_{\ f}$. Therefore

$$\{\Pi^0_a, \Pi^0_b\} = 0, \qquad \{\Pi^0_a\ , G_{(V)}\} = -\{\Pi^0_a\ , P_A\} V^A \neq 0. \tag{25}$$

Neither $\{G_{(V)}, G_{(W)}\}$ is trivial because there are traces of $e^a_{\ j}$ in $\Pi_A$, $P_A$ and $V^A$. Just to exemplify, let us consider the case $D = 3$. It is easy to verify that one of the six null eigenvectors of $C_{AB}$ is $V^A = (0, 1, 0, 1, 0, 0, 0, 0, 0)$, where $A = (a, e)$ is given by $3(a-1)+e$. Then, the $P_A$'s enter the respective constraint $G_{(V)}$ through the combination

$$P_A V^A \ \ = \ \ P^1_0 + P^0_1 = 2\ e^2\ (\partial_1 e^2_{\ 2} - \partial_2 e^2_{\ 1}). \tag{26}$$

The complete structure of the algebra of constraints will be analyzed in a forthcoming work.

## 5. Summary and perspectives

We reviewed the first order approach of Maluf et al. (2001) for counting physical degrees of freedom in teleparallel gravity. Thus, one can show that TEGR contains the same number of degrees of freedom than general relativity. Based on this procedure, Li et al. (2011) concluded that $f(\mathcal{T})$ gravity has three degrees of freedom more than general relativity. We have shown the treatment of the primary constraints in the framework of a second order procedure, which could facilitate the identification of the physical degrees of freedom when $f(\mathcal{T})$ gravity is tackled through the method depicted in Section 3.2.

**Acknowledgments.** The authors thank N. Deruelle for helpful discussions. This work was supported by Consejo Nacional de Investigaciones Científicas y Técnicas (CONICET) and Universidad de Buenos Aires.

## References

Einstein, A. 1928, Sitzungsber. Preuss. Akad. Wiss., 217

Einstein, A. 1930, Math. Annal., 102, 685

Einstein, A. 1939, Sitzungsber. Preuss. Akad. Wiss., 401

Blagojevic, M. & Nikolic, I. A. 2000, Phys. Rev. D,62, 024021

da Rocha-Neto, J. F., Maluf, J. W. & Ulhoa, S. C. 2010, Phys. Rev. D, 82, 124035

Ferraro, R. & Fiorini, F. 2007, Phys. Rev. D, 75, 084031

Ferraro, R. & Fiorini, F. 2008, Phys. Rev. D, 78, 124019

Li, M., Miao, R. X. & Miao, Y. G. 2011, JHEP, 1107, 108

Maluf, J. W. & da Rocha-Neto, J. F. 2001, Phys. Rev. D, 64, 084014

Maluf, J. W. 2013, Annalen Phys., 525, 339

Okolów, A. 2013, Gen. Rel. Grav., 45, 2569

Sundermeyer, K. 1982, "Lecture Notes in Physics", Vol. 169, Springer-Verlag

*Gravitation, Relativistic Astrophysics and Cosmology*
*Second Argentinian-Brazilian Meeting, 2014*
*G. S. Vila, F. L. Vieyro and J. Fabris, eds.*

# Primordial magnetic helicity

Alejandra Kandus

*Laboratorio de Astrofísica Teórica e Observacional*
*DCET - Universidade Estadual de Santa Cruz*
*Rod. Ilhéus-Itabuna km 16, CEP:45662-900, Ilhéus-BA, Brazil*

**Abstract.** It is investigated if magnetic fields generated during reheating after inflation posses magnetic helicity, $H^M$. This quantity is a measure of the number of twists and links of magnetic lines and is generated at the birth of the fields. This topological property is of fundamental importance in determining the evolution of the magnetic fields in the primordial plasma and the operation of dynamos. The magnetic fields we consider are induced by stochastic electric currents of scalar charges, cosmologically generated at the transition between inflation and reheating. We compute the rms value of the fields and of $H^M$ finding non-zero in both cases. The main result is that the fields generated by the mentioned mechanism have maximal magnetic helicity.

## 1. Introduction

Magnetic fields are widespread in the Universe, independently of the redshift: From our own Milky Way up to high redshift galaxies, magnetic fields regular over the size of the structure are observed, with intensities $B_G \sim \mu$G. The observations just mentioned challenge the accepted paradigm for magnetogenesis, namely a seed field amplified by a dynamo operating since the creation of the structure, and point to a possible cosmological, not in-situ, origin of the magnetic fields. Viable cosmological magnetogenesis scenarios are based on the breaking of conformal invariance of the magnetic field, i.e. the magnetic field must evolve in a way such that $B(\eta) \neq B_0/a^2(\eta)$, where $B_0$ is an initial value and $a(\eta)$ is the scale factor of a flat Friedmann Robertson Walker (FRW) universe and $\eta$ the conformal time. Due to the lack of success in finding a primordial magnetogenesis mechanism that explains both the intensity and the geometry of the observed fields, research began toward magnetohydrodynamical processes that could amplify the primordially generated seeds during the radiation dominated epoch of the universe, prior to structure formation. During that period, decaying turbulence might have been operative, it having been triggered by reheating and/or electroweak and QCD phase transitions. The topology of the initial magnetic field plays a crucial rôle in determining the evolution of the field in a turbulent scenario. It is described by the magnetic helicity which is defined as $H^M = \int_V \bar{B} \cdot \bar{A}$. In the absence of ohmic dissipation it is a conserved quantity in MHD, and is interpreted as the number of twists and links of the field lines. The distinctive feature of $H^M$ is that it performs an *inverse cascade*, i.e. it evolves from small scales toward large scales, thus coherently reorganizing the field on large scales.

## 2. Magnetic helicity of stochastic magnetic fields

We consider the magnetogenesis mechanism developed in 1998 by Calzetta et al., based on a charged scalar field minimally coupled to gravity in a FRW universe, described by the Lagrangian $\mathcal{L} = \sqrt{-g}\left[g^{\mu\nu}D_\mu\Phi D_\nu^\dagger\Phi^\dagger + m^2\Phi\Phi^\dagger + (1/4)\,F^{\mu\nu}F_{\mu\nu}\right]$. When the transition from inflation to reheating unfolds, the scale factor of the FRW universe changes as $a_I(t) \propto \exp(Ht) \rightarrow a_R(t) \propto t^{2/3}$ and as a consequence the scalar field vacuum state turns into particle state, i.e. $\phi_I(\kappa,\eta) = \alpha_\kappa\phi_R(\kappa,\eta) + \beta_\kappa\phi_I^*(\kappa,\eta)$ where $\beta_\kappa$ accounts for particle creation. As a consequence a stochastic electric current develops: its mean value is zero but not its rms value, which is the source of a stochastic magnetic field. For sub-horizon modes we have $\beta_p \sim i/\left(16\tau_0 p^5\right)$, $p \geq 1$, while for super-horizon modes $\beta_p \simeq -i\sqrt{9H/16m}\,p^{-3/2}$ for $p < m/H$ and $\beta_p \simeq -i\,(3/8)\,e^{-ip}\,p^{-3}$ for $m/H < p < 1$. We see that the contribution of sub-horizon modes is suppressed relative to the super-horizon ones. However the former are responsible for a mildly turbulent flow on scales of the order of the horizon size, with Reynolds numbers $R_e \simeq 100$. As the induced fields are random, all mean values are zero, and the rms values must be estimated through the calculation of two-point correlation functions. For the magnetic helicity, the detailed calculation of those function was done by Calzetta & Kandus in 2014, who expressed it as the sum of four Feynmann graphs shown in figures 1 and 2. In them, full lines represent the charged scalar fields, dotted lines the vector potential $A^i$ while dashed lines the magnetic field $B^i$. The prefactor of the mean helicity graph is null as expected. The dimensionless relevant parameters for numerical evaluation are $m/H \simeq 10^{-11} - 10^{-9}$, $\kappa_G \simeq 10^{-51} - 10^{49}$ and $\frac{\sigma_0}{H} \simeq 10^{-7/2} - 10^{-3/2}$, where $H$ is the Hubble constant during inflation, $m$ the mass of the scalar field, $\kappa_G = k_G/H$ the dimensionless galactic scale and $\sigma_0$ the electric conductivity at the onset of radiation dominance.

### 2.1. Magnetic helicity and magnetic fields on galactic scales

The magnetic helicity on galactic scales due to mean and fluctuating fields on that scale is

$$\mathcal{H}_M(\kappa) \equiv \Xi^{1/2}(\kappa) \sim \left(\frac{H}{\sigma_0}\right)^2\left(\frac{m}{H}\right)^{11/6}\frac{102}{\left(\pi^4 e\right)^{2/3}}\kappa^{-1/2} \tag{1}$$

with fractal dimension $D = 1/2$. The important quantity for dynamo action however, is the field intensity due to fields that are regular on the considered scale. This is obtained by filtering out the fluctuating fields, obtaining that the magnetic helicity reads

$$\mathcal{H}_M(\kappa_\lambda) \sim e^{-2/3}\left(\frac{m}{H}\right)^{4/3}\left(\frac{H}{\sigma_0}\right)^2 \tag{2}$$

with fractal dimension $D = 0$. Comparing with the previous dimension, we see that the variation of the number of magnetic links with the scale is due to fluctuating fields. Smooth fields also have non-trivial topology, the associated number of defects is scale invariant. The associated magnetic field can be estimated as

$$B(\kappa_G) \sim H_M^{1/2}\kappa_G^2 \sim e^{-1/3}\left(\frac{m}{H}\right)^{2/3}\left(\frac{H}{\sigma_0}\right)\kappa_G^2 \tag{3}$$

and replacing the figures we obtain a present value of $B_G^{hel} \sim 10^{-61}$ G, which is too small to seed the galactic dynamo, even the field having non-trivial topology.

The scale we considered to evaluate the fields in this section re-entered the particle horizon by the end of radiation dominance, i.e. it was frozen-out during that period and consequently no causal processes could affect it. One such process is the above mentioned inverse cascade of magnetic helicity, and is the subject of the following section.

### 2.2. Magnetic helicity at small scales: causal evolution inside particle horizon

In this section we consider the evolution of the fields generated inside the particle horizon at the beginning of radiation dominance. Now the field evolves in a causally connected domain and hence the kinematical effects of the conservation of helicity can be taken into account. The hypotheses we make are that decaying turbulence is operative during all radiation dominance and that the scale of the horizon has the same value that at the end of inflation, which in dimensionless variables means $\kappa_H \simeq 1$. We also assume that magnetic helicity is perfectly conserved, a fact that leads to a comoving coherence scale growth of the form $\lambda(\eta) \propto \lambda_0 \eta^{2/3}$, and a field decay law $B(\eta) \propto B_0 \eta^{-1/3}$, where $\eta$ is the dimensionless conformal time and $\lambda_0$ and $B_0$ are initial values for the comoving scale and field respectively. On a scale $\kappa^{-1} \sim 1$ at the beginning of radiation dominance magnetic helicity is $\mathcal{H}_M \sim \pi^{-4/3} e^{-10/3} (H/m) \kappa^{-2}$, and considering the evolution described just above, we obtain a magnetic field interval

$$\mathcal{B}_{eq} \sim \frac{1}{\pi^{2/3} e^{5/3}} \left(\frac{H}{m}\right)^{1/2} \left(\frac{h_{eq}}{h_{rh}}\right)^{-1/6} \sim 10^{-9}\mathrm{G} - 10^{-5}\mathrm{G} \tag{4}$$

with coherence length values

$$\ell_{eq} \sim H^{-1} \left(h_{eq}/h_{rh}\right)^{1/3} \sim 10^{-3}\mathrm{pc} - 10^{-1}\mathrm{pc}. \tag{5}$$

According to the literature, the obtained range of magnetic field intensities is very high and the coherence scales are of astrophysical importance.

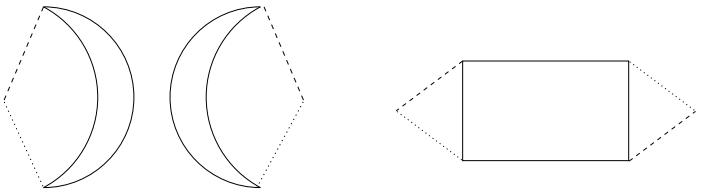

Figure 1. *Left:* Mean Helicity graph (multiplicity 1). *Right:* Square graph (Multiplicity 4).

## 3. Summary and perspectives

In this work we have studied if magnetic field induced by stochastic currents existing during reheating have non-trivial topology. We found that this is indeed the case and estimated the associated field intensities in two important scales. The first one was the

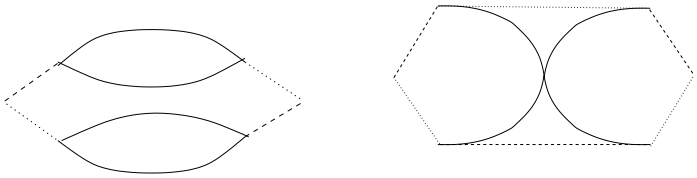

Figure 2. *Left:* Two Bubbles graph (Multiplicity 2). *Right*: Cross graph (Multiplicity 2).

galactic scale, where the contributing fields did not evolved causally. We found that although the topology is non-trivial the field intensity is too weak to feed the galactic dynamo. The second scale was the horizon scale at the end of reheating, where the field could experienced inverse cascade of magnetic helicity. Assuming a very simple, optimistic model for the evolution, we obtain very high intensities over astrophysical interesting scales. These facts open the door to consider more realistic environments and mechanisms in the early universe to address the evolution of primordial magnetic fields.

**Acknowledgments.** This work has been developed in collaboration with Esteban Calzetta (FCEyN - UBA and IFIBA - CONICET), and was partially supported by CNPq/CAPES PROCAD project 552236/2011-0.

## References

Berger, M. A. & Field, G. B. 1984, J. Fluid Mech., 147, 133

Bernet, M. L. et al. 2008, Nature, 454, 302

Calzetta, E. et al. 1998 , Phys. Rev. D, 57, 7139

Calzetta, E. & Kandus, A. 2010, JCAP, 08, 007

Calzetta, E. & Kandus, A. 2014, Phys. Rev. D, 89, 083012

Han, J. L. et al. 2006, Astrophys. J., 642, 868

Kahniashvili, T. et al., 2013, Phys. Rev. D, 87, 083007

Kandus, A. et al. 2000, Phys. Lett. B, 472, 287

Kandus, A. et al. 2011, Phys. Rept., 505, 1

Moffatt, H. K. 1978, "Magnetic Field Generation in Electrically Conducting Fluids", Cambridge Univ. Press, Cambridge

Pouquet, A. et al. 1976, J. Fluid Mech., 77, 321

Zel'dovich, Y. B. et al. 1983, "Magnetic Fields in Astrophysics", Gordon & Breach, New York

*Gravitation, Relativistic Astrophysics and Cosmology*
*Second Argentinian-Brazilian Meeting, 2014*
*G. S. Vila, F. L. Vieyro and J. Fabris, eds.*

# Statistical aspects of the quantum origin of the primordial cosmic seeds

Gabriel León,[1] Susana J. Landau,[1] and Daniel Sudarsky[2]

[1]*Departamento de Física, Facultad de Ciencias Exactas y Naturales, Universidad de Buenos Aires and IFIBA, CONICET, Ciudad Universitaria - Pab. I, (1428) Buenos Aires, Argentina*
[2]*Instituto de Ciencias Nucleares, Universidad Nacional Autónoma de México, México D.F. 04510, México*

**Abstract.** The explanation of the origin of cosmic structure, provided by the inflationary paradigm, is not completely satisfactory as all of the scenarios, based on the conventional approach to the so-called "quantum-to-classical transition", lack the ability to point out the physical mechanism responsible for generating the inhomogeneity and anisotropy of our Universe starting from and exactly homogeneous and isotropic vacuum state associated with the early inflationary regime. The "collapse proposal" considers the spontaneous collapse of the wave function as a possible solution to that problem. In this letter, we present the answers provided by the above proposal and explore their relevance to the investigations concerning the characterization of the observational quantities and other statistical aspects of the cosmic microwave background.

## 1. Introduction

One of the cornerstones of the $\Lambda$-Cold Dark Matter cosmological model is the inflationary paradigm. The modern standard inflationary scenario states that all cosmic structure was originated from quantum fluctuations of the vacuum state of the inflaton field. The general setting is that the perturbations evolved in a Friedmann-Robertson-Walker (FRW) background space-time with a nearly exponential expansion. Once the physical wavelength associated with these fluctuations becomes larger than the Hubble radius, they are identically associated with classical density perturbations. When the Universe becomes matter dominated, primeval density inhomogeneities are amplified by gravity and grow into the structure we see today. The photon density perturbations left a particular imprint in the Cosmic Microwave Background (CMB), which is associated with fluctuations in the photons temperature. The signature left by the photons in the CMB is one of the most important predictions of the inflationary paradigm and indeed is confirmed by recent observational data.

Nevertheless, when examining the above picture in more detail, one finds important issues regarding the "quantum-to-classical" transition of the primordial perturbations. In fact, the problem lies in the so-called quantum measurement problem. Quantum decoherence has been a constant reference in the attempts to deal with this issue (Adler, 2003). In a nutshell, decoherence is the process by which a system that is not isolated, but in interaction with an environment, "loses" coherence into the degrees of freedom of such environment. It is a well studied effect that follows rather than supersedes the laws of quantum physics. Its main achievement is to allow for the study of the conditions in

which the quantum interferences expected from the idealized consideration of a system as being isolated, become observationally suppressed as the result of the system's interaction with the environment. Nevertheless, as stated explicitly in (Joos, 1999), decoherence does not solve the measurement problem, what decoherence tell us is that certain objects appear classical when observed; clearly this raises a question: what is an observation? and to answer it, at some stage we still have to apply the usual probability rules of Quantum Theory.

On the other hand, there is a widespread view in the cosmological community that decoherence addresses the quantum-to-classical issue[1] when applied to the inflationary Universe. In fact, there has been numerous works dedicated to implement the decoherence program, and different variations of the same, to the early Universe, e.g. decoherence as a result of quantum Brownian motion of the wave function of the inflaton (Lombardo, 2005), decoherence without decoherence (Kiefer, 2009), etc. Nevertheless, as we will argue next, decoherence does not solve the aforementioned problem in a full and satisfactory manner. The precise formulation of the problem can be stated in the following manner (Perez, 2006):

According to the inflationary paradigm, the accelerated inflationary scenario is described by a homogeneous and isotropic space-time (i.e. by a spatially flat FRW metric) characterizing the Universe, this is, the space-time does not contain any perturbations at all. Moreover, the quantum fields are all characterized by their vacuum state $|0\rangle$, usually such vacuum state corresponds to the so-called Bunch-Davies vacuum. In Appendix A of Landau (2013) is shown that the Bunch-Davies vacuum is homogeneous and isotropic. Additionally, the dynamics of the space-time are provided by Einstein's equations, this is, if the space-time is originally homogeneous and isotropic and Einstein's equations cannot break such symmetry, then the resulting space-time is still homogeneous and isotropic. Moreover, as we have mentioned, the vacuum state characterizing the quantum fields is also homogeneous and isotropic, but the dynamics of the quantum state is governed by Schroedinger's equation, which does not break translational and rotational invariance; thus, the initial quantum state cannot be evolved into a final state lacking such symmetries. Then the issue is: How did the primordial perturbations are born given that the equations governing the dynamics are symmetry preserving? In other words, it is not clear how out of an initial condition which is homogeneous and isotropic both in the background space-time and in the quantum state that describes the "fluctuations," and based on a dynamics that supposedly preserves those symmetries, one ends up with a non-homogeneous and non-isotropic state characterizing the late actual Universe.

Concerning decoherence and its implementation to solve the aforementioned problem, we can quote first a popular textook on the subject (Mukhanov, 2005): "*However decoherence is not enough to explain the breakdown of translational invariance*". Furhtermore, the application of decoherence to the early Universe faces the following issues: (i) requires identification of certain degrees of freedom to be taken as an "environment." That would entail using our on limitations to measure things, as part of the argument. (ii) decoherence relies on the diagonalization, after a suitable time-average,

[1] As a matter of fact, we find a bit misleading the term "quantum-to-classical transition." Most people would agree that there are no classical or quantum regimes. The fundamental description ought to be always a quantum description. However, there exist regimes in which certain quantities can be described to a sufficient accuracy by their classical counterparts represented by the corresponding expectation values. All this depends, of course, on the physical state, the underlying dynamics, the quantity of interest, and the context in which we might want to use it.

of the density matrix. However, decoherence does not tell us that the situation is now described by one element of the diagonal density matrix, but by all, and as such the situation is still symmetric.

In a recent series of works (Perez, 2006; Sudarsky, 2011), the said problem has been analyzed in detail; the solution, according to those works, is to invoke a *collapse of the wave function*, i.e. a spontaneous change from the original quantum state associated to the inflaton field into a new quantum state lacking the symmetries of the initial state. This collapse acts on each mode characterizing the quantum state of the inflaton field. The inhomogeneities of the field (described by the post-collapse state) are related to the (classical) perturbations in the metric by the Einstein's semiclassical equations. The result of the evolution of such perturbations is related to the actual anisotropies and inhomogeneities observed in the CMB. It is evident that the mechanism (that breaks the symmetries) should be a physical process independent of external entities (i.e. "observers," "measurement devices" or "an environment") as by definition the Universe contains everything.

In the following we will focus on the manner in which the consideration of statistical aspects of the CMB should be modified when taking into account the modifications needed to explain the emergence of inhomogeneities and anisotropies in terms of theories incorporating something like the spontaneous collapse of the wave function.

## 2. Issues regarding the statistical aspects of the standard inflationary paradigm

Here, we will present a brief summary of what we consider to be the main issues regarding the statistical aspects that afflicts the traditional inflationary scenario. The detailed discussion can be consulted in Ref. (Landau, 2013).

Let us start by reminding the reader that in the standard approach, the study of the statistical nature of the problem is based on the study of the statistical $n$-point functions of the Newtonian potential (which is equivalent to the curvature perturbation in the longitudinal gauge) $\overline{\Psi(x_1)\dots\Psi(x_n)}$, with the overline denoting the average over an ensemble of Universes. However, we have no access to such ensamble, therefore one has the challenge to relate such ensemble average with the quantities that we actually measure; furthermore, one needs to consider how these quantities are connected with the quantum $n$-point functions. The traditional approach relies on the identification

$$\overline{\Psi(x_1)\dots\Psi(x_n)} = \langle\hat{\Psi}(x_1)\dots\hat{\Psi}(x_n)\rangle, \tag{1}$$

with $\langle\hat{\Psi}(x_1)\dots\hat{\Psi}(x_n)\rangle$ the standard quantum mechanical $n$-point function for the quantum field operators.

We remark that the left hand side of Eq. (1) is associated with an ensemble of Universes, all of which, even if real, are unaccessible to us. The usual line of argument continues by invoking ergodic arguments, to make a further connection between ensemble averages and time averages, with other vague arguments indicating one might replace the latter with spatial averages and often turning, in practice, to orientation averages.

There are three major issues that arise here:

(i) How do we go from the arguments supporting ergodicity in time averages to the corresponding arguments for spatial averages? In fact, regarding this point

we note that there are intrinsic problems in considering ergodicity of processes within a two-sphere.

(ii) Regarding the CMB, we, in fact, do not have access to the spatial sections that would allow us to investigate the space averages. We only have access to the particular intersection of our past light come with the 3D hypersurface of decoupling. That is, to a two-sphere that we see as the source of the CMB photons that reach us today: the surface of last scattering. How do we go from spatial averages to averages over that two-sphere?

(iii) The identification of the classical ensemble average with the quantum correlation functions should be justified more accurately. In particular, if we take the identification as presented in Eq. (1) a problem arises in the case of the 1-point function: The physical observable corresponds to the temperature anisotropies in the CMB, which we denote by $\Theta(\varphi,\theta)$, and that can be expanded in spherical harmonics as $\Theta(\varphi,\theta) = \sum_{lm} a_{lm} Y_{lm}(\varphi,\theta)$. A well-known result is that for large scales, the temperature anisotropies are directly related to the Newtonian potential $\Theta \simeq \Psi$ (known as the Sachs-Wolfe effect). Therefore, the coefficients $a_{lm}$ can be expressed as: $a_{lm} = \int d\Omega Y_{lm}(\varphi,\theta)\Psi(\varphi,\theta)$; consequently, if one follows the standard prescription given by Eq. (1), then $\Psi = \langle 0|\hat{\Psi}|0\rangle = 0$, thus, $a_{lm} = 0$. Advocates of the standard approach would indicate that $\langle a_{lm}\rangle = 0$ is not to be taken as "the prediction of the model" regarding our Universe and that this would only hold for an ensemble of Universes. The issue, of course, is what precise interpretative posture regarding the theory can be used to justify this, while at the same time justifying the positions taken *vis-à-vis* the other quantities that emerge from the theory (such as the higher $n$-point functions).

## 3. Inflation and the collapse of the wave function

We will introduce a new ingredient to the inflationary paradigm: the *self-induced collapse hypothesis*: a phenomenological model incorporating the description of the effects of a dynamical collapse of the wave function of the inflaton on the subsequent cosmological evolution. The induced collapse operates in close analogy with a "measurement" in the quantum-mechanical sense, but evidently without any observer or external apparatus that could be considered to perform a measurement. That is, one assumes that at a certain time $\eta^c_{\vec{k}}$, the state of the field, which was initially the vacuum state, changes spontaneously into another state that could in principle be a non-symmetrical state. This proposal is inspired by the ideas of Penrose and Diósi, i.e. that gravity could be responsible for the collapse of the wave function.

We start with the action of a scalar field minimally coupled to gravity. We next separate the field into an homogeneous and isotropic background plus small fluctuations: $\phi(\vec{x},\eta) = \phi_0(\eta) + \delta\phi(x,\eta)$. The field perturbations induce perturbations in the background ($K = 0$ Robertson-Walker) metric: $ds^2 = a(\eta)^2[-(1+2\Psi)d\eta^2 + (1-2\Psi)\delta_{ij}dx^i dx^j]$. Our quantum field is $\hat{y} = a\hat{\delta\phi}$; and the canonical conjugate momentum is $\hat{\pi}_y = a\hat{\delta\phi}' = \hat{y}' - \hat{y}a'/a$ (The prime denotes derivative with respect to $\eta$).

Expanding the metric perturbation in Fourier modes, $\Psi_{\vec{k}}$, and using Einstein semiclassical equations, $G_{ab} = 8\pi G\langle\hat{T}_{ab}\rangle$, we obtain

$$\Psi_{\vec{k}}(\eta) = -\sqrt{\frac{\epsilon}{2}}\frac{H}{M_P k^2}\Big[\Big(\cos(k\eta - k\eta^c_{\vec{k}}) + \frac{\sin(k\eta - k\eta^c_{\vec{k}})}{k\eta^c_{\vec{k}}}\Big)\langle\hat{\pi}_{\vec{k}}(\eta^c_{\vec{k}})\rangle - k\sin(k\eta - k\eta^c_{\vec{k}})\langle\hat{y}_{\vec{k}}(\eta^c_{\vec{k}})\rangle\Big], \quad (2)$$

with $H$ the Hubble factor, which during inflation is nearly constant, $\epsilon$ is the slow-roll parameter, and $M_P$ the reduced Planck's mass. One can check that, before the collapse, the quantum state corresponds to $|0\rangle$, therefore, $\langle\hat{\pi}_{\vec{k}}(\eta^c_{\vec{k}})\rangle = \langle\hat{y}_{\vec{k}}(\eta^c_{\vec{k}})\rangle = 0$, thus $\Psi_k = 0$ and the space-time is completely homogeneous and isotropic. It is only after the collapse that generically $\langle\hat{\pi}_{\vec{k}}(\eta^c_{\vec{k}})\rangle \neq 0, \langle\hat{y}_{\vec{k}}(\eta^c_{\vec{k}})\rangle \neq 0$ and, consequently, $\Psi_k \neq 0$.

The collapse proposal is based on the hypothesis that each mode would jump to a new state where the expectation value would be determined by both, the scale of the uncertainties and some random variable. That is, $\langle\hat{y}^{R,I}_{\vec{k}}(\eta^c_k)\rangle_\Theta = x^{R,I}_{\vec{k},y}\sqrt{(\Delta\hat{y}^{R,I}_{\vec{k}})^2_0}$, $\langle\hat{\pi}^{R,I}_{\vec{k}}(\eta^c_k)\rangle_\Theta = x^{R,I}_{\vec{k},\pi}\sqrt{(\Delta\hat{\pi}^{R,I}_{\vec{k}})^2_0}$, where $R, I$ denotes the real and imaginary parts of the field, respectively; $\eta^c_k$ is the conformal time of collapse; $(\Delta\hat{y}^{R,I}_{\vec{k}})^2_0$, $(\Delta\hat{\pi}^{R,I}_{\vec{k}})^2_0$ are the uncertainties of each mode of the field momentum operators in the vacuum state; and $x^{R,I}_{\vec{k},y}$, $x^{R,I}_{\vec{k},\pi}$ are random variables with a Gaussian distribution centered at zero with spread one.

Given the previous prescription, it is clear that, the Newtonian potential $\Psi$, after the collapse, is characterized in in terms of the random variables that determine the post-colapse state. One of the advantages of our approach is that the nature of the randomness, which one usually attributes to quantum theory, becomes transparent and specific: the variables $x^{R,I}_{\vec{k},y}$, $x^{R,I}_{\vec{k},\pi}$ characterize, once and for all, every kind of stochasticity involved.

As mentioned previously, the curvature perturbation $\Psi$ is closely related with the observational quantities, i.e. the temperature anisotropies. Therefore, the value of all the $\{x^{R,I}_{\vec{k},y}, x^{R,I}_{\vec{k},\pi}\}$ corresponding to our Universe, fixes the value of the observed temperature anisotropies. Naturally, we cannot give a definite prediction for those values, however, as will be argued next, the fact that a large number of modes $\vec{k}$ contribute to the observed temperatures anisotropies, justifies a statistical analysis that leads to a theoretical estimate for the observational quantities.

## 4. Connection to observations

In the collapse proposal, the coefficients $a_{lm}$ are related to the random variables directly as

$$a_{lm} \simeq \frac{H}{\sqrt{\epsilon}M_P}\int\frac{d^3k}{k^{3/2}}j_l(kR_D)T(k)Y^\star_{lm}(\hat{k})\Big[\Big(\cos z_k - \frac{\sin z_k}{z_k}\Big)(x^R_{\vec{k},\pi} + ix^I_{\vec{k},\pi}) + \sin z_k\Big(1 + \frac{1}{z_k^2}\Big)^{1/2}(x^R_{\vec{k},y} + ix^I_{\vec{k},y})\Big], \quad (3)$$

with $R_D$ the radius of the last scattering surface; $T(k)$ the transfer function, which represents the evolution of the curvature perturbation from the end of inflation to the time of decoupling; $j_l$ is the spherical Bessel function of order $l$, and we have defined $z_k \equiv k\eta^c_{\vec{k}}$.

Equation (3) shows how the random numbers $x^{R,I}_{\vec{k},y}$, $x^{R,I}_{\vec{k},\pi}$, associated with the collapse of the wave function, determine the coefficients $a_{lm}$. Let us remark that Eq. (3) cannot be used to make a definite prediction as it involves the random numbers. However, we can regard the integral appearing in Eq. (3), as a sum of complex numbers representing a kind of two-dimensional random walk. As in any case for a random walk, one might estimate the most likely value of the magnitude of the total displacement. Thus, we focus primarily on the most likely value of $|a_{lm}|^2$ (denoted by $|a_{lm}|^2_{ML}$). We evaluate that quantity using a fiducial ensemble of realizations of the random walk and take it approximately equal to the ensemble average value over of the total displacement, i.e. $|a_{lm}|_{ML} \simeq \overline{|a_{lm}|}$. The overline appearing denotes average over the fiducial ensemble of realizations. Explicitly our model predicts

$$|a_{lm}|^2 = \int \frac{d^3k}{k^3} \frac{H^2}{M_P^2 \epsilon 400\pi^4} j_l(kR_D)^2 |Y_{lm}(\hat{k})|^2 T(k) C(z_k), \tag{4}$$

where

$$C(z_k) = \left(1 + \frac{1}{z_k^2}\right) \sin^2 z_k + \left(\cos z_k - \frac{\sin z_k}{z_k}\right)^2. \tag{5}$$

The information regarding that a collapse has occurred is entirely contained in the function $C(z_k)$. As we have noted in previous works, this quantity becomes a simple constant if the collapse time happens to follow a particular pattern in which the time of collapse of the mode $\vec{k}$ is given by $\eta^c_k = Z/k$ with $Z$ as a constant. In fact, the standard answer would correspond to $C(k)$ = constant (which can be thought as an equivalent "nearly scale-invariant power spectrum"). Thus, the result obtained for the relation between the time of collapse and the mode's frequency, i.e. $\eta^c_{\vec{k}} k$= constant is a rather strong conclusion that could represent relevant information about whatever the mechanism of collapse is.

## 5. Conclusions

The treatment of the statistical aspects in the collapse proposal is quite different from the standard inflationary paradigm: In the standard accounts, one is going from quantum correlation functions to classical $n$-point functions averaged over an ensemble of Universes; then, one goes to $n$-point correlation functions averaged over different regions of our own Universe, and, finally, one relates this last quantity with the observable $|a_{lm}|^2$. These series of steps are not at all direct and they involve a lot of subtle issues that the standard picture does not provide in a transparent way. On the other hand, within the collapse approach to the subject, the observable $|a_{lm}|^2$ is related to the random variables, $x^{R,I}_{\vec{k},y}$, $x^{R,I}_{\vec{k},\pi}$, which are associated to the quantum collapse. Therefore, in our model, all stochasticity involved is naturally inherited by having introduced the collapse hypothesis. This makes the treatment more transparent when dealing with the statistical aspects of the problem.

**Acknowledgments.** The work of G. L. and D. S. is supported by CONACyT Grant No. 101712 and PAPIIT Project No. IN107412-3. G. L. acknowledges financial support by a CONICET postdoctoral grant. S. L. acknowledges support for this work provided by PIP 0152/10 CONICET.

## References

Adler, S. L. 2003, Studies in History and Philosophy of Modern Physics, 34, 135

Joos, E. 1999, "Elements of Environmental Decoherence, proceedings of the conference Decoherence Theoretical, Experimental and Conceptual Problems", P. Blanchard et al. (eds.), Springer

Kiefer, C. & Polarski, D. 2009, Advanced Science Letters, 2, 164

Landau, S., León, G. & Sudarsky, D. 2013, Physical Review D, 88, 023526

Lombardo, F. C. 2005, Brazilian Journal of Physics, 35, 391

Perez, A. , Sahlmann, H. & Sudarsky, D. 2006, Classical and Quantum Gravity, 23, 2317

Mukhanov, V. F. 2005, "Physical Foundations of Cosmology," Cambridge University Press, Cambridge, UK

Sudarsky, D. 2011, IJMP D, 20, 509

*Gravitation, Relativistic Astrophysics and Cosmology*
*Second Argentinian-Brazilian Meeting, 2014*
*G. S. Vila, F. L. Vieyro and J. Fabris, eds.*

# Analysing the potential of OLIMPO's spectroscopic and photometric measurements in estimating cluster parameters

Camila Paiva Novaes,[1] Paolo de Bernardis,[2] and Silvia Masi[2]

[1]*Divisão de Astrofísica, Instituto Nacional de Pesquisas Espaciais, 1758 Av. dos Astronautas, São José dos Campos, São Paulo, Brazil*
[2]*Dipartimento di Fisica, Università di Roma La Sapienza, 2 P.le A. Moro, Roma, Lazio, Italy*

**Abstract.** The Sunyaev-Zeldovich (SZ) effect is one of the most important secondary anisotropy of the Cosmic Microwave Background (CMB) Radiation. The OLIMPO experiment, a mm-wave balloon-born telescope, is aimed to measure this effect in a set of a carefully selected clusters. OLIMPO was developed to cover a wide range of frequencies and with a high angular resolution. These features make it a promising instrument to measure CMB anisotropies at high multipoles and the SZ effect caused by galaxy clusters. We performed simulations of the OLIMPO spectroscopic and photometric measures of the line-of-sight trough one of the galaxy clusters chosen to be observed by the instrument. Using each kind of simulations individually and combined in order to fit a theoretical curve, we find out that, as expected, spectroscopic simulations have a superior performance, allowing the estimative of a larger set of cluster parameters, and being more accurate in estimating some of them. Moreover, a combination of spectroscopic and photometric simulations can even improve some parameter estimates and reduce the bias inherent to them.

## 1. Introduction

The SZ effect is the most important secondary CMB anisotropy, dominant at $l \gtrsim 2000$, and is caused by the inverse Compton scattering by hot electrons inside galaxy clusters. One out of 100 electrons that cross the core of a galaxy cluster is scattered, gaining energy and thus distorting the CMB blackbody spectrum, with a decrement below $\approx 220$ GHz and an increment above that (Sunyaev & Zel'dovich 1969). Since the scattering depends only upon the electron density and temperature, the thermal SZ effect is independent of the cluster distance and can be used to study the mass distribution in high redshifts. The kinetic SZ effect, about an order of magnitude weaker than the thermal component, is a second order effect caused by the cluster drift across the line-of-sight (LOS). The total distortion of the CMB signal can be expressed by (Birkinshaw 1999)

$$\frac{\Delta T_{SZ}}{T_{CMB}} = f(x)y - \tau_e\left(\frac{v_{pec}}{c}\right), \tag{1}$$

where the first therm is related to the thermal effect, with the comptonization parameter given by $y = \int (4k_B T_e/m_e c^2)\sigma_T n_e d\ell$, and the second therm corresponds to the kinetic effect, related to the peculiar velocity $v_{pec}$ of the cluster.

The SZ distinctive spectral signature can be used to independently identify high-redshift clusters, whose optical or X-ray observations are hard to detect. Combined

with observations in other wavelengths, it can be used to study the baryon mass fraction in clusters (indirectly estimating the $\Omega_b$ parameter), to determine $H_0$ (jointly to X-ray measures), to estimate clusters peculiar velocities and, using the number counts of clusters, to probe the growth of structures (and the energy density of the Universe).

A a large amount of SZ measurements have been performed in the last few years. Some instruments, besides the Planck satellite (Planck Collaboration 2015), which produced an all-sky catalogue of galaxy clusters detected via SZ effect, are, e.g., the South Pole Telescope - SPT (Carlstrom et al. 2011), Sunyaev Zel'dovich Array - SZA (Sharp et al. 2010), Atacama Cosmology Telescope - ACT (Hincks et al. 2010) and OLIMPO (Masi et al. 2008, 2010).

## 2. The OLIMPO mission

OLIMPO is a mm-wave balloon-born experiment which is a combination of: a 2.6 m diameter Cassegrain telescope with pointing and scanning capabilities, four multi-frequency arrays of advanced bolometers and a long duration $^3He$ cryostat. The instrument is designed to perform a long duration (10-15 days) balloon flight along the circumpolar region, departing from Svalbard islands in 2015. It will produce a set of sensitive maps covering a wide range of frequencies and with high angular resolution (Table 1). Details about the telescope can be found in Masi et al. (2005, 2008 and 2010).

Table 1. Characteristics of the OLIMPO instruments (Conversi et al. 2010).

| | | | | |
|---|---|---|---|---|
| Frequency (GHz) | 143 | 217 | 353 | 450 |
| Bandwidth (GHz FWHM) | 40 | 61 | 98 | 126 |
| FWHM (arcmin) | 5.2 | 3.7 | 2.3 | 1.9 |
| # of detectors | 19 | 19 | 24 | 24 |
| NEP ($\mu K/Hz^{1/2}$) | 145 | 275 | 430 | 4300 |

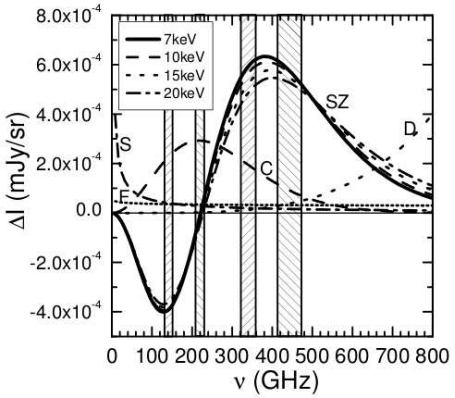


Figure 1. Spectrum of SZ effect for different energy of the ionized intracluster gas. The vertical bands refer to the frequency bands of OLIMPO experiment (Masi et al. 2008).

The high angular resolution and the wide range of frequencies make OLIMPO a promising instrument to measure CMB anisotropies at high multipoles, study the far infrared background due to unresolved galaxies at high redshift and measure the SZ effect caused by galaxy clusters. The Figure 1 shows the spectrum of SZ effect and the frequency bands covered by OLIMPO, optimally located in order to sample both, the negative, the null and the positive SZ effects.

The OLIMPO observation strategy is to point to a given target, taken from a carefully selected list of clusters, and explore the properties of the object with a good signal-to-noise ratio (namely, to spend several hours on the same object). This is a good approach for studying cluster properties and also a good follow-up for Planck observations. With an angular resolution ranging from $1.9'$ to $5.2'$, it is possible to track (in the better resolution) the cluster profile with steps just slightly larger than the typical core radius: $\sim 2'$.

## 3. Simulations

The SZ signal from galaxy clusters are contaminated by several astrophysical components along the LOS. This leads to the need for multi-frequency measurements in order to be possible to separate the contribution of each one, as well as to analyse its SZ spectrum. However, each astrophysical signal theoretically depends of a set of parameters, and consequently it is necessary a large number of parameter to describe the total measured signal. For this reason, only photometric measures in few frequency bands are not enough to estimate all these parameters, even knowing some of them quite well and neglecting others.

Providing further information for this type of analysis, OLIMPO will also perform spectroscopic measurements, besides the multi-band photometry, achieved through the addition of a Differential Fourier Transform Spectrometer (DFTS) in front of the same photometer (for details see Schillaci et al. 2014). As presented in de Bernardis et al. (2012), the low resolution spectroscopic measurements of the SZ effect are quite promising in estimating parameters describing clusters and signals along the LOS. For this reason, the analyses presented here is aimed to evaluate the potential of OLIMPO in estimating these parameters.

Since OLIMPO measurements will integrate the signal along the LOS, the simulations of the total signal have to include several components. The astrophysical components chosen to integrate the simulations, and related parameters, are summarized below, considering an observation of the LOS towards ABELL2219, a very bright cluster.

**Thermal SZ effect ($\Delta I_t$):** from Eq. 1, and neglecting relativistic corrections, the thermal SZ can be described by: the electron temperature $kTe$ and the optical depth $\tau_t = \int_{LOS} n_e \sigma_T dl$.

**CMB anisotropies ($\Delta I_{CMBi}$) and kinetic SZ effect ($\Delta I_v$):** since the CMB radiation and kinetic SZ effect have the same spectrum, we can describe them as: $\Delta I_{CMB} = \Delta I_{CMBi} + \Delta I_v$. This way it is possible to consider only one parameter to describe both signals, namely, $\Delta I_{CMB}$.

**Non-thermal effect ($\Delta I_{nt}$):** a non-thermal population of electrons can also cause the scattering of the CMB photons, allowing the production of SZ effect depending of the quantity of electrons, which can be produced by, for example, Active Galactic

Nuclei (AGN) and relativistic plasma in cluster cavity (Colafrancesco 2010, Birkinshaw 1999, de Bernardis et al. 2012). The parameters describing this effect are: the optical depth of the non-thermal component $\tau_{nt}$ ($\sim \tau_t/50$) and the minimum momentum $p$ of the electrons.

**Dust emission ($\Delta I_d$):** this Galactic emission can be described by a modified black body (MBB) model (Planck Collaboration 2014) written as $I_\nu = AB_\nu(T)\nu_D^\beta = B_\nu(T)\tau_D$. $A$ is the amplitude of the MBB, $B_\nu(T)$ is the Planck function for an equilibrium temperature $T$, and $\beta_D$ is the dust spectral index. Then, this foreground component can be characterized by the parameter $\tau_D$, the dust optical depth.

Synchrotron and free-free Galactic emissions are not considered in our analysis, since they are negligible with respect to dust in the frequency range OLIMPO operates. We have also verified the contribution of CO rotational transition line emission in the position of ABELL2219. Using the CO map released by Planck Collaboration in 2013,[1] we confirmed the negligibility of this signal for OLIMPO on the cluster region. Finally, we can write the total power on the detector, as function of the frequency $\nu$, as (see de Bernardis et al. 2012):

$$S(\nu) = A\Omega E(\nu)(1 - \epsilon_m(\nu))[\Delta I_t + \Delta I_{CMB} + \Delta I_{nt} + \Delta I_d], \tag{2}$$

where $A$ is the collecting area (200 cm), $\Omega$ is the solid angle subtended by the detector (Table 1), $E(\nu)$ is the efficiency of the detection system, and $\epsilon_m(\nu)$ is the total emissivity of the optical system and atmosphere.

The errors for photometric and spectroscopic measurements are estimated, respectively, as

$$\sigma_{phot} = \left[\frac{\int_{BW} NEP_f^2 d\nu}{2t}\right]^{1/2}, \quad \sigma_{spec} = 0.61\, c\, \frac{\sqrt{\int_{BW} NEP_f^2 d\nu}}{\Delta\nu\sqrt{t}}, \tag{3}$$

where $t$ is the integration time, $NEP_f$ is the noise equivalent power (photon noise) produced by the instrument and atmosphere, with integration performed on the bandwidth (BW), and $\Delta\nu$ is the spectral resolution.

The spectroscopic and photometric simulations are repeated 1000 times, adding errors estimated from a Gaussian distribution with zero mean and standard deviation given by the Eqs. 3. We fit each simulated measurement using Eq. 2, and the best-fit is obtained according to the minimum $\chi^2$. Figure 2 presents an example of both types of simulations and the corresponding error bars. The integration time is 4 hours for each type of measurements, and $\Delta\nu = 6$ GHz.

## 4. Results

### 4.1. Bandwidth analysis

Equations 3 show that wider bands, despite the larger number of measurements, increase the error, compared to narrower bands. Therefore, to verify the best configuration in the case of OLIMPO, we performed tests using two types of simulations as those described

[1] http://pla.esac.esa.int/pla/aio/planckProducts.html

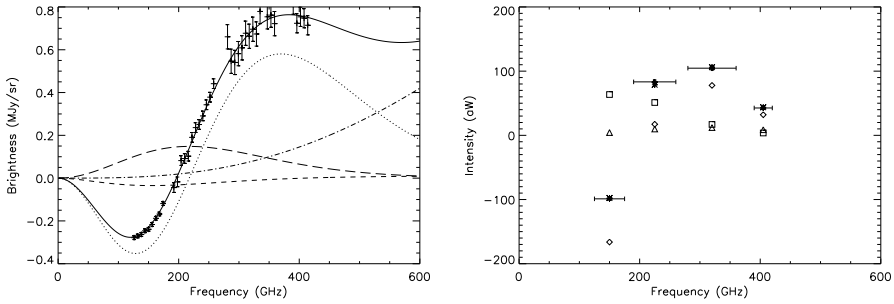


Figure 2. Simulated spectroscopic (4 hours, left) and photometric (4 hours, right) measurements of the SZE towards ABELL2219 (see Table 2 for the input cluster parameters), with the respective vertical error bars (the horizontal bars correspond to the BW FWHM). The continuous line (asterisk) is the best-fit line for the spectroscopic (photometric) measures. The dotted (diamond), dot-dashed (triangle), long dashed (square) and dashed lines are the thermal SZ, dust, CMB + kinetic SZ and non-thermal SZ anisotropies, respectively (Schillaci et al. 2014).

above, but using different BW configurations: Narrow bands (see values on Table 1), and Wide bands (width of 50, 125, 35 and 30 GHz, for the bands of 143, 217, 353 and 450 GHz, respectively). For simplicity, this test is performed considering just two signals: thermal SZ and Dust, fitting just two free parameters, $\tau_t$ and $\tau_D$ (see Table 2 for input values).

The best-fit of the simulated measurements provides the estimative of the free parameters, obtaining smaller errors in the case of Narrow bands. It confirms Narrow bands configuration to be better then the Wide bands.

### 4.2. Spectroscopy and photometry combination

In section 3 we discussed about the large number of independent parameters needed to describe the cluster and foreground components along the LOS. This is the reason why few-bands photometry is not enough to constrain all of them, or even to separate the thermal SZ contribution from the others. However, a low-resolution spectroscopy of SZ effect can provide a sufficient number of degrees of freedom (DOF) to fit several of these parameters.

Aiming to investigate the performance of OLIMPO telescope as a spectrometer ($\Delta\nu$ = 6 GHz) and as a photometer combined to a spectrometer in estimating these parameters, we used a set of simulations as described in section 3. Results of estimating 5 and 6 free parameters are summarized in Table 2, where are also available the input values. These results confirm the good performance of the simulated spectroscopic measurements, and the improvement of the estimates when combining them with the photometric measurements.

## 5. Concluding remarks

The work presented here demonstrates the potential of the OLIMPO measurements on estimating parameters describing galaxy clusters and foreground components. The analysis confirm that the instrument as a photometer alone cannot measure more than

Table 2. Cluster and foreground parameters estimated from simulated observations of the SZE along a line of sight towards a cluster of galaxies. S refers to spectroscopic observations (4 hours), S+P refers to spectroscopic observations for 4 hours, and photometric observations for 4 additional hours. The BW are those presented on Table 1 (Schillaci et al. 2014).

| | | 5 parameters | | 6 parameters | |
|---|---|---|---|---|---|
| Parameters | input | best-fit (S) | best-fit (S+P) | best-fit (S) | best-fit (S+P) |
| $100\tau_T$ | 1.70 | 1.76 ± 0.32 | 1.76 ± 0.29 | 1.78 ± 0.42 | 1.74 ± 0.29 |
| $kT_e$ (keV) | 9.5 | 9.5 ± 1.7 | 9.6 ± 1.7 | 9.6 ± 1.8 | 9.6 ± 1.6 |
| $10^6\tau_D$ | 1.85 | 1.85 ± 0.22 | 1.85 ± 0.17 | 1.94 ± 0.13 | 1.82 ± 0.23 |
| $10^4\Delta T_{CMB}$ | 3.1 | 3.04 ± 1.26 | 3.07 ± 0.11 | 3.07 ± 1.54 | 3.05 ± 0.11 |
| $10^4\tau_{nt}$ | 1.0 | 0.95 ± 2.13 | 1.00 ± 0.11 | 0.38 ± 6.07 | 0.88 ± 0.86 |
| $p$ | 1.0 | - | - | 5 ± 26 | 3.2 ± 6.1 |
| $\chi^2/DOF$ | - | 35.8/36 | 39.4/40 | 35.8/35 | 42.1/39 |

four parameters, while as a spectrometer it can measure five or six parameters, and even improve these estimates combining photometric and spectroscopic measurements. Our results indicate how promising is the low resolution spectroscopy of the SZ effect with OLIMPO telescope.

**Acknowledgments.** C. P. Novaes acknowledges the CNPq [237059/2012-6] fellowship, and Dr. Luca Lamagna for helpful discussions.

## References

Birkinshaw, M. 1999, Phys. Rep., 310, 97

Carlstrom, J. E. et al. 2011, Astronomical Society of the Pacific, 903, 568

Colafrancesco, S. 2010, AIP Conf. Proc., 1206, 5

Conversi, L. et al. 2010, A&A, 524, A7

de Bernardis, P. et al. 2012, A&A, 538, A86

Hincks, A. D. et al. 2010, Astrophys. J. Supp., 191, 423

Masi, S. et al. 2005, Proceedings ESA SP-590

Masi, S. et al. 2008, Mem. of S. A. It., 79, 887

Masi, S. et al. 2010, ASI Proposal

Planck Collaboration 2015, ArXiv 1502.01598

Planck Collaboration 2014, A&A, 571, A11

Sharp, M. K. et al. 2010, Astrophys. J., 713, 82

Schillaci, A. et al. 2014, A&A, 565, A125

Sunyaev, R. A. and Zel'dovich, Y. B. 1969, Astrophys. Space Sci. 4, 301

*Gravitation, Relativistic Astrophysics and Cosmology*
*Second Argentinian-Brazilian Meeting, 2014*
*G. S. Vila, F. L. Vieyro and J. Fabris, eds.*

# Gamma-ray induced cascades in cosmic environments

L. J. Pellizza,[1,3] M. Orellana,[2,3] M. C. Medina,[1,3] S. E. Pedrosa,[3,4]
G. E. Romero,[1,3] and M. Tueros[1,3]

[1]*Instituto Argentino de Radioastronomía (CONICET / CCT La Plata), Argentina*
[2]*Sede Andina de la Universidad Nacional de Río Negro, Argentina*
[3]*Consejo Nacional de Investigaciones Científicas y Técnicas, Argentina*
[4]*Instituto de Astronomía y Física del Espacio (CONICET / UBA), Argentina*

**Abstract.** The new generation of gamma-ray telescopes has revealed a rich sky at very high photon energies. The unveiling of the nature of these sources and the understanding of the physical processes that give rise to the gamma-ray emission are among the most important present challenges of high-energy astrophysics. To investigate these issues, the propagation and interaction of the emitted electromagnetic radiation, both within the source and during its journey to the observer, must be understood. In this work we describe the development of a tool to provide an accurate, *ab-initio* description of the propagation of gamma rays in astrophysical environments. We expect this tool to contribute to the understanding of the physics of cosmic gamma-ray emitters.

## 1. Introduction

During the last decades, the development of new instruments to collect radiation at very high photon energies (MeV–TeV) has provided a wealth of information on sources emitting in this spectral range (e.g., Hartman et al. 1999; Cheng & Romero 2004; Abdo et al. 2009, Aharonian et al. 2009). Many sources were identified with objects detected at lower energies, while many others remain still unidentified. To unveil the nature of these emitters, their gamma-ray spectrum must be modeled to determine the physical processes that produce the observed photon distribution. However, the observed spectrum differs from the primary one emitted by the source, due to the interaction of gamma-ray photons with electromagnetic and matter fields present either within the source or between it and the observer. These fields modify the primary radiation, changing the spectrum and introducing temporal and spatial variations in it. A precise description of the modification is then crucial for a good comparison of the emission models with observations.

Tools for radiation modification calculation have been developed since long time ago, either using semi-analytical or numerical techniques (e.g., Protheroe 1986; Bednarek 2000; Aharonian et al. 2006; Bednarek 2007; Orellana et al. 2007; Khangulyan et al. 2008; Sierpowska & Bednarek 2005; Cerrutti et al. 2009; Kachelrieß et al. 2012). Numerical techniques based on Monte Carlo schemes are especially well suited for scenarios in which the optical depth of the intervening medium to the VHE radiation is large. In this case simple absorption calculations are inadequate, because the secondary particles produced by the interaction of primaries with background fields carry a large

fraction of the energy, strongly modifying the spectrum. These particles continue to interact with background fields, developing cascades in which the spectrum is modified in several stages.

In spite of their increasing complexity, numerical Monte Carlo techniques are confronted with a series of common problems, among them the computation of photon cross sections, the computation of interaction products, or the treatment of charged particle deflections in magnetic fields. These problems were usually solved by simplifying assumptions such as the one-dimensional treatment of cascades (e.g., Protheroe 1986; Bednarek 2000), probably with semi-analytical corrections for the lateral development (Kachelrieß et al. 2012), the use of background field symmetries to simplify cross section computations, or the isotropization of charged-particle motion in magnetic fields (Sierpowska & Bednarek 2005). These simplifications prevent the use of these tools to investigate complex systems with non-symmetric background fields, magnetic fields not strong enough to fulfill the isotropization condition, or phenomena with short scale spatial or temporal variations.

In this paper we present an overview of an ongoing project by our group (Pellizza et al. 2010; Pellizza et al. 2015), whose purpose is to overcome the aforementioned problems and simplifications of numerical techniques. We aim at developing a high-performance, *ab initio* simulation tool for radiation modification computation with arbitrary sources and background fields. This tool, named PRINCE (PRopagation and INteraction in Cosmic Environments), is described in Sect. 2.. Sect. 3. shows some preliminary results, and Sect. 4. discusses some of our prospects to apply PRINCE to astrophysical problems.

## 2. The PRINCE project

The main goal of the PRINCE project is to create a tool versatile enough to describe the spectrum modification in almost any arbitrary environment. We focused in solving the main shortcomings of previous approaches. As nearly all numerical codes devised for this problem, PRINCE uses a Monte Carlo scheme to sample photons from the primary source spectrum, and computes their propagation through the background fields. The propagation of each particle is described as a set of continuous trajectories interspersed by interactions between the travelling particle and a background one. The interactions destroy the incoming particles, creating new ones. The propagation of the new particles is then computed in the same way as that of primaries, until they reach the observer or their energy falls below a specified threshold.

In the already mentioned previous works, the occurrence of an interaction of a particle is determined by Monte Carlo sampling of its free path, given the background density, the interaction cross section and the particle velocity. This scheme assumes that the background field is homogeneous and stationary, which is an important limitation for many astrophysical systems. To overcome this difficulty, we adopted a different scheme. Following techniques developed for other astrophysical areas, such as N-body gravitational codes, we compute the trajectories of the particles by dividing them into small timesteps. The integration is trivial within each timestep, and the ocurrence of an interaction can be Monte Carlo sampled from its probability, which is still related to the same properties of particles and background. Using individual and adaptive timesteps for each particle allows our code to adapt the interaction sampling to spatial and temporal variations of the background density.

The calculation of interaction probabilities (or mean free paths in previous works) leads to the problem of computing total cross sections. In previous works usually this computation is done in an analytical way, using different assumptions such as the isotropy of background fields (e.g., Protheroe 1986; Bednarek 2000). Once again, this prevents the use of these schemes for systems in which the assumptions are not fulfilled, such as highly anisotropic photon fields near the companion of compact objects in binary systems. To avoid this limitation, PRINCE computes the total cross sections through numerical integration, allowing the use of any well behaved background field, without any assumption at all. The sampling of the interaction products is also done numerically through a third Monte Carlo algorithm, and requiring strict momentum and energy conservation.

The trajectories themselves are easy to integrate. For neutral particles they are straight lines traversed at constant velocity, while for charged particles only magnetic fields (if present) are important to deflect them. As the code uses timesteps adapted to the field variations (either temporal or spatial), the evolution of the particles within each timestep can be assumed as occurring in a constant field, and the trajectories have analytical solutions. The energy loss by synchrotron emission of charged particles in magnetic fields is also computed.

The time variations of the spectra have never been computed self-consistently, the only attempts were done assuming that this variation has a timescale much greater than that of the cascade, and hence independent computations at different times were used (e.g., Cerrutti et al. 2009). The spatial (or angular, in the plane of the sky) dependence has been approached semianalytically for non-magnetic simulations, or through simplifying hypotheses when magnetic fields are present, such as the isotropization of lepton directions in strong magnetic fields (Khangulyan et al. 2008; Kachelrieß et al. 2012). This assumptions still leave many realistic astropysical scenarios unexplored. With the PRINCE scheme, the effects of magnetic fields are computed in a self-consistent way.

The PRINCE code implements the aforementioned physics, together with several administrative routines that allow the user to set up and run simulations of the cascades induced by VHE radiation in a large variety of astrophysical systems. The code is written in the C programming language and parallelized using both MPI and OpenMP to produce a high-performance tool. This tool is complemented with post-processing routines that allow the users to obtain observables from the simulation results.

## 3. Preliminary results

In this section we present a set of two preliminary results to show the sort of problems that can be explored with PRINCE. First, we simulated the electromagnetic cascade produced by a monoenergetic point source of 10 PeV photons against the Cosmic Microwave Background (CMB), and within a uniform magnetic field of intensity $B = 10^{-15}$ G. Fig. 1 depicts the trajectories of the cascading particles, showing the deflection from a straight line. This deflection is larger for lower energy particles. As a result, an extended source is observed, with a spectrum that varies with position in the plane of the sky (Fig. 2).

The second, more realistic simulation involves the cascade produced by gamma-ray photons from an extragalactic TeV source by two photon fields, the CMB and the Extragalactic Background Light (EBL), and a randomly oriented intergalactic magnetic field with a correlation length of 1 Mpc (Neronov et al. 2013). The CMB was modeled

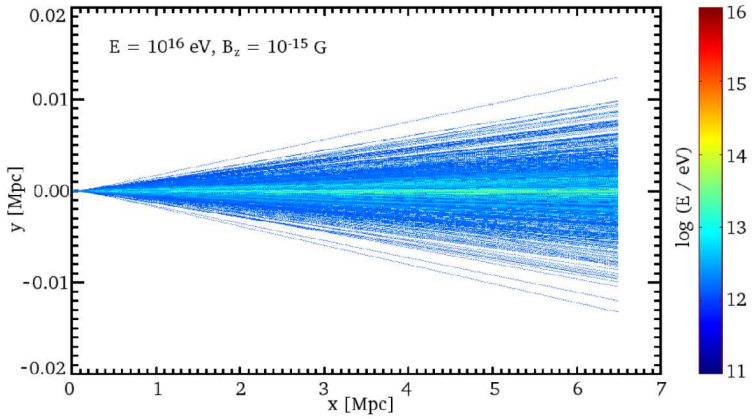


Figure 1. Electromagnetic cascade produced by a monoenergetic point source of 10 PeV photons against the CMB, in a uniform magnetic field with an intensity of $10^{-15}$ G. The trajectories of the particles involved in the cascade are shown; low energy particles suffer larger deflections from the primary motion direction than high energy ones.

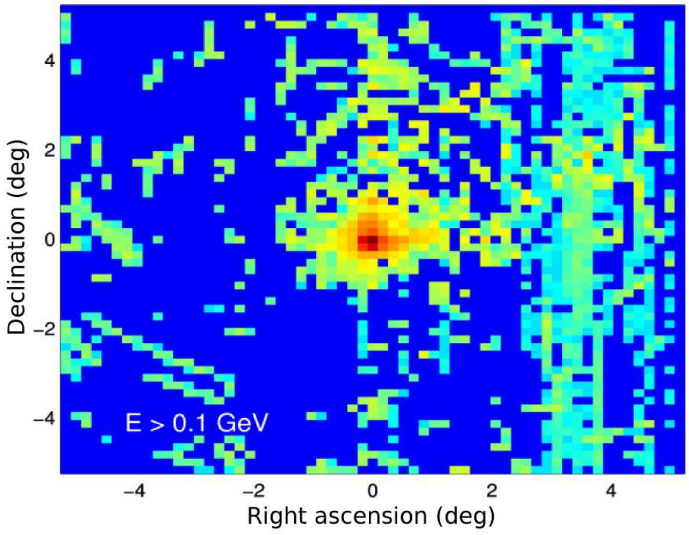


Figure 2. Electromagnetic cascade produced by a monoenergetic point source of 10 PeV photons against the CMB, in a uniform magnetic field with an intensity of $10^{-15}$ G. This simulated image of the source presents an angular extension in the plane of the sky that depends on energy.

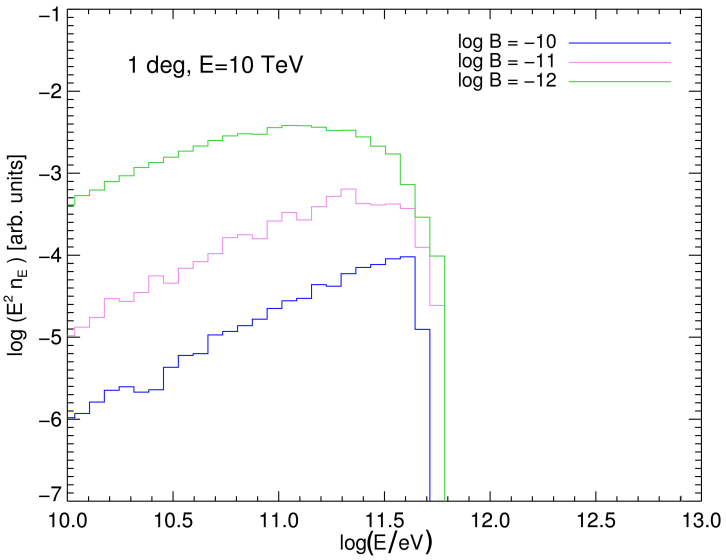


Figure 3. Spectra of a 10 TeV jet with an opening angle of 1 deg, after traversing 600 Mpc of intergalactic medium, for different values of the magnetic field strength. The magnetic field coherence length is fixed at 1 Mpc.

as a 2.73 K blackbody, while for the EBL we used the model of Finke et al. (2010). The source is a monoenergetic ($E = 10\,\mathrm{TeV}$) jet spreading with an opening angle of 1 deg, located at 600 Mpc from the observer. Fig. 3 shows the spectrum of the source as a function of the intensity of the intergalactic magnetic field. The absorption of TeV photons is due mainly to the EBL. The absorbed radiation is converted into lower energy (10–100 GeV) photons through leptons produced by pair creation, giving rise to the bump seen at these energies. The cooling of leptons through synchrotron radiation is responsible for the variation of the spectral intensity at GeV energies with the magnetic field intensity.

## 4. Discussion

PRINCE is an ongoing project devoted to the development of a high-performance computing tool for the investigation of VHE radiation cascades. The tool allows the simulation of the spectrum of gamma-ray sources in arbitrary environments, using *ab initio* computations of the physical processes involved in radiation modification, and eliminating as many simplifying assumptions as possible. The basis of the tool is a computing code that uses three Monte Carlo schemes to solve the propagation of individual photons emitted by the source through background electromagnetic and matter fields, until it reaches the observer.

PRINCE has been successfully tested in simple astrophysical situations, such as the cascades produced by TeV–PeV gamma-ray photons against extragalactic photon fields, and with ambient magnetic fields. In the future, we plan to use this tool to

simulate different astrophysical sources, including microquasars, active galactic nuclei, and dark-matter annihilation signals. We expect that the comparison of our numerical experiments with observations will allow us to provide clues to answer relevant astrophysical questions, such as the nature of dark matter or the intensity and origin of intergalactic magnetic fields.

**Acknowledgments.** L. J. Pellizza acknowledges support from ANPCyT through project PICT 2011-0959.

## References

Abdo, A. A. et al. 2009, ApJ Suppl., 183, 46

Aharonian, F. et al. 2006, J. Phys. Conf. Ser., 39, 408

Aharonian, F. et al. 2009, ApJ Lett., 695, L40

Bednarek, W. 2000, A&A, 362, 646

Bednarek, W. 2007, A&A, 464, 259

Cerutti, B. et al. 2009, A&A, 507, 1217

Cheng, K. S. & Romero, G. E. 2004, "Cosmic Gamma-Ray Sources", Kluwer Academic Publishers, The Netherlands

Finke, J. D. et al. 2010, ApJ, 712, 238

Hartman R. C., et al. 1999, ApJ Suppl., 123, 79

Kachelrieß, M. et al. 2012, CoPhC, 183, 1036

Khangulyan, D. et al. 2008, MNRAS, 383, 467

Neronov, A. et al. 2013, A&A, 554, A31

Orellana, M. et al. 2007, A&A, 465, 703

Pellizza, L. J. et al. 2010, IJMPD, 19, 671

Pellizza, L. J. et al. 2015, in prep.

Protheroe, R. J. 1986, MNRAS, 221, 769

Sierpowska A. & Bednarek, W. 2005, MNRAS, 356, 711

*Gravitation, Relativistic Astrophysics and Cosmology*
*Second Argentinian-Brazilian Meeting, 2014*
*G. S. Vila, F. L. Vieyro and J. Fabris, eds.*

# The black hole mass function of Type 1 AGN

Eduardo S. Pereira and Oswaldo D. Miranda
*Divisão de Astrofísica, Instituto Nacional de Pesquisas Espaciais, SP 12227-010, Brazil*

**Abstract.** An important question in the modern astrophysics is related to the origin and evolution of the supermassive black holes (SMBH) ubiquitous in the galaxy nucleus. In this work is shown a robust method to determine the estimator of the binned mass function of SMBH, $n_{est}$, hosted by type I AGN. The advantage of the method presented here is that the flux-limited of the survey was taken into account in a more accurate way. For this work it was considered data from Sloan Digital Sky Survey Data Release 7. We observed that the $n_{est}$ was obtained with relative low bias and error. Also, it was noted that the BHMF declines at high redshifts and peaks in the range of $10^{8.6}$M$_\odot$-$10^{9.3}$M$_\odot$ shifting in the direction of high masses when $z$ increases.

## 1. Introduction

In a recent work we have developed a new data mining process to obtain a statistical representative subsample of supermassive black holes (Pereira & Miranda, 2014). The advantage of our method with respect to previous works in the literature is that the flux-limited of the catalog was taken into account in a more accurate way. The basic key of the method is in the fact that we combine robust statistical methods: The Freedman-Diaconis rule (Freedman Diaconis 1980) to calculate the width of the bin used to obtain the probability density function of the bolometric quasar luminosity (PDFL); and non-parametric Monte Carlo bootstrap resample with replacement method (henceforward just bootstrap) to estimate the bias and error of the derived data. The advantage of this method is that no prior knowledge about the data distribution is necessary.

In that previous work we studied the mean Eddington ratio (MER) which is associated with both the dynamic of accretion as with the balance between the gravitational force and the radiation pressure of the accretion disk. We have shown that the MER was related to the mean bolometric luminosity and with the available gas to the growth of supermassive black holes. This last fact could be measured by the evolution history of the mean accretion rate. Thus, we could present for the first time a clear physical meaning for the MER.

Our intention is to study the connection between the Duty Cycle of type I AGN with the cosmic star formation rate. The Duty Cycle function is defined as the ratio between active and total supermassive black holes. For this propose, we have as a first step to understand how is the distribution of the population of the active black holes hosted by type I AGN. In this work we extend the method presented by Pereira & Miranda (2014) in order to calculate the estimator of the mass function of supermassive black holes.

In this work we use as data sample the Sloan Digital Sky Survey Data Release 7 (SSDS DR7) Quasar Catalog (Schneider, 2010), that contains 105,783 type 1 AGN (quasars) with luminosity greater than $M_i = -22.0$. In particular, we consider the

catalog provided by Shen et al. (2011) - the SSDS DR7 Catalog of Quasar Properties. This catalog contains supplementary information like: the *full-width-at-half-maximum* (FWHM) of broad lines; central black hole masses (estimated using the FWHM); luminosity of broad lines as well as the bolometric luminosity of the quasars. Our final subsample contains 57, 496 objects with redshift from 0.03 up to 4.5.

This work is organized as follows: In the section 2. an improved method to obtain the estimator of supermassive black hole mass function is presented. Our final remarks are presented in the section 3.. We consider standard cosmological model ($\Lambda$CDM) with $\Omega_b = 0.04$, $\Omega_m = 0.24$, $\Omega_\Lambda = 0.76$, $h = 0.73$.

## 2. The supermassive black hole mass function

Page & Carrera (2000) presented an improved method, when compared with the traditional $1/V_a$, to construct binned luminosity functions. The great contribution of that work was the better way to take into account the survey flux limit. If we apply the same considerations of Page & Carrera (2000) to obtain the supermassive Black Hole Mass Function (BHMF), then it is possible to write:

$$n_{bh}^{est}(z, m_{bh}) = \frac{N_{AGN}}{\int_{m_{bh,min}}^{m_{bh,max}} \int_{z_{min}}^{z_{max}} \frac{dV}{dz} dz dm_{bh}}, \tag{1}$$

where $n_{bh}^{est}$ is the binned estimate of the BHMF, $N_{AGN}$ is the number of objects found in the bin $\Delta m_{bh}$ and $\Delta z$. Note that, because the subsamples are constructed considering the probability density function of the bolometric quasar luminosity (PDFL) (see Pereira & Miranda, 2014), the $z_{max}$ that appears in Eq. (1) is just the maximum redshift of an object into the bin, e.i., the $z_{max}$ is determined by the flux-limit of the survey in a given bin.

The error in $n_{bh}^{est}(z, m_{bh})$ can be obtained by:

$$\delta n_{bh}^{est}(z, m_{bh}) = \frac{\delta N_{AGN}}{\int_{m_{bh,min}}^{m_{bh,max}} \int_{z_{min}}^{z_{max}} \frac{dV}{dz} dz dm_{bh}}, \tag{2}$$

where $\delta N_{AGN}$ can be given by the Poisson error. We also compute the error given by Eq. (2) using the Bootstrap method (for details see the appendix of the work of Pereira & Miranda, 2014). We observe that this method provides, with high accuracy, the same $\delta n_{bh}^{est}$ given by the Poisson error. This imply that the Bootstrap is well calibrated as an error and bias estimator.

It is important to stress that the found bias is lower than a few percents of the value of the $n_{bh}^{est}$. Here we consider a double power law to fit the $n_{bh}^{est}$ in the following form:

$$n_{bh} = n_{bh}^{*} \left[ \left( \frac{m_*}{m_{bh}} \right)^{\gamma_1} + \left( \frac{m_{bh}}{m_*} \right)^{\gamma_2} \right], \tag{3}$$

where $\gamma_1$, $\gamma_2$, $n_{bh}^{*}$ and $m_*$ are free parameters.

In Figure 1 are presented the BHMF for the redshift range $[0.3, 2.1]$. In general, we observe that the BHMF declines for high redshifts and that the BHMF peaks in the

range of $10^{8.6}$M$_\odot$-$10^{9.3}$M$\odot$ shifting for the direction of higher masses when $z$ increases. An important point is that our results are in accordance with the works of Vestergaard et al. (2008), who obtained the BHMF considering the traditional $1/V_a$, and Wang et al. (2006). In Table 1 we present the best fit data parameters in the redshift range of $z = [0.3, 2.1]$.

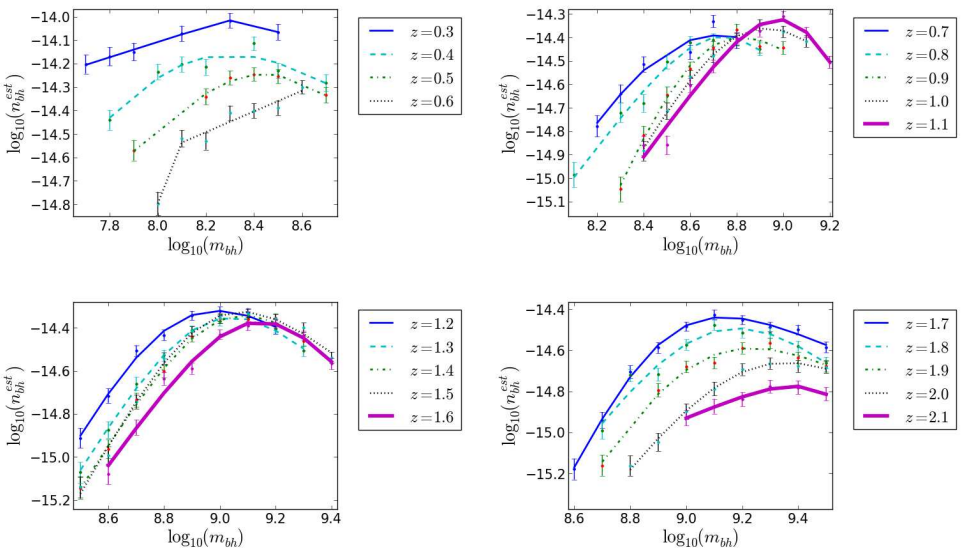


Figure 1. Binned Mass Function of supermassive black holes for redshifts $[0.3, 2.1]$.

## 3. Summary and perspectives

In this work is presented a new method to obtain the mass function of supermassive black holes. The difference of the method presented here, in relation to other methods described in literature, is that we employ a new data mining process in order to construct a representative subsample of the SMBHs. The major advantage of this method is the possibility of taking into account the catalog flux limit. This occurs because we consider the behaviors of the probability density function of the bolometric quasar luminosity distribution for each bin of mass, of the central black hole, and redshift. However, only a fraction of the original sample can be used to construct the final subsample.

In order to evaluate our method, it was considered the non-parametric Monte Carlo bootstrap resample with replacement (see Pereira & Miranda 2014 for details). From this method was calculated the bias of the obtained BHMF. We verify that the bias is lower than 4 percent of the final value of the BHMF estimators. This means that is possible to have a binning method to construct the BHMF with very low bias.

The BHMF declines at high redshifts and peaks in the range of $10^{8.6}$M$_\odot$-$10^{9.3}$M$_\odot$ shifting in the direction of higher masses when $z$ increases.

The next step of our work will be calculate the mass function of the total supermassive black holes in order to obtain the Duty Cycle of quasar. Also we will present a

Table 1. Best fit parameters of BHMF at different redshifts

| z | $n^*_{bh}$ ($\times 10^{-15}$) | $m_*$ ($\times 10^9$) | $\gamma_1$ | $\gamma_2$ |
|---|---|---|---|---|
| 0.3 | 12.00 | 0.37 | −6.41 | −0.33 |
| 0.4 | 13.00 | 0.14 | −0.66 | −1.34 |
| 0.5 | 11.40 | 0.30 | 1.05 | 1.23 |
| 0.6 | 2.60 | 0.10 | 0.44 | −80.03 |
| 0.7 | 7.60 | 0.38 | −0.73 | −1.56 |
| 0.8 | 8.00 | 0.60 | −1.65 | −1.32 |
| 0.9 | 7.09 | 0.47 | −0.81 | −2.28 |
| 1.0 | 8.46 | 0.71 | −1.05 | −1.73 |
| 1.1 | 9.15 | 1.11 | −2.34 | −1.35 |
| 1.2 | 8.57 | 0.71 | −0.85 | −2.27 |
| 1.3 | 8.56 | 0.93 | 2.10 | 1.19 |
| 1.4 | 8.87 | 1.05 | 2.08 | 1.27 |
| 1.5 | 8.8 | 0.94 | 2.32 | 1.04 |
| 1.6 | 8.48 | 1.36 | 1.81 | 1.63 |
| 1.7 | 5.82 | 0.86 | 2.71 | 0.59 |
| 1.8 | 6.23 | 1.27 | −1.07 | −1.78 |
| 1.9 | 4.43 | 1.12 | 2.14 | 0.65 |
| 2.0 | 4.10 | 1.70 | −0.83 | −1.76 |
| 2.1 | 2.51 | 3.79 | 0.57 | 3.53 |

robust model to connect the Cosmic Star Formation rate with the evolutionary history of supermassive black holes hosted by type I AGN.

**Acknowledgments.** ESP would like to thank the Brazilian Agency FAPESP (grant 2012/21877-5) for support. ODM would like to thank the Brazilian Agency CNPq for partial financial support (grant 304654/2012-4).

## References

Page, M. J. & Carrera, F. J. 2000, MNRAS, 311, 433

Pereira, E. S. & Miranda, O. D. 2014, Ap&SS, 352, 801-807

Schneider, D. et al. 2010, AJ, 139, 6, 2360

Shen, Y. et al. 2011, ApJ Supplement Series, 194, 45

Vestergaard, M. et al. 2008, ApJ, 674, L1

Wang, J., Chen, Y. & Zhang, F. 2006, ApJ, 647, L17

*Gravitation, Relativistic Astrophysics and Cosmology*
*Second Argentinian-Brazilian Meeting, 2014*
*G. S. Vila, F. L. Vieyro and J. Fabris, eds.*

# Gravitational entropy of a Kerr black hole

Daniela Pérez[1] and Gustavo E. Romero[1,2]

[1]*Instituto Argentino de Radioastronomía, C.C.5, (1894) Villa Elisa, Bs. As., Argentina*
[2]*Facultad de Ciencias Astronómicas y Geofísicas, UNLP, Paseo del Bosque s/n, (1900) La Plata, Bs. As., Argentina*

**Abstract.** The gravitational entropy of a Kerr black hole is calculated using a classical estimator based on the Bel-Robinson tensor, which has been recently proposed by Clifton, Ellis, and Tavakol. We prove that, in the frame we consider, Clifton et al.'s estimator does not reproduce the Bekenstein-Hawking entropy of a Kerr black hole.

## 1. Introduction

Black holes are among the simplest objects of the universe. They can be fully described by a small number of parameters: mass ($M$), angular momentum ($J$), and electric charge ($Q$). Wheeler seems to have been the first to notice that, if we are not to abandon the Second Law of Thermodynamics, material accreted by a black hole should not only transfer to the hole its mass, angular momentum, and electric charge, but its entropy as well. Bekenstein (1972, 1973) noticed that the properties of the area of the event horizon of a black hole resemble those of entropy and proposed the following relation:

$$S_{\rm BH} = \frac{A}{4\, l_{\rm P}^2}. \tag{1}$$

Here, $S_{\rm BH}$ is the entropy of the black hole, $A$ is the area of the event horizon, and $l_{\rm Pl} = \sqrt{G\hbar c^{-3}}$ is the Planck length. A generalized second law of black hole thermodynamics was also derived by Bekenstein (1974). Bardeen, Carter, and Hawking (1973) formulated the four laws of black hole physics, which are similar to the four laws of thermodynamics.

Since black holes can be fully described in terms of the gravitational field, it seems reasonable to associate an entropy with the gravitational field itself. In absence of a theory of quantum gravity, a statistical measure of the gravitational entropy is not possible. Instead, approximations might be obtained using classical invariants of General Relativity, as first suggested by Penrose (1979).

Several authors have tried to implement Penrose's proposal. Recently, Clifton, Ellis and Tavakol (2013) offered a novel definition for the entropy of the gravitational field based on integrals over quantities constructed from the pure Weyl form of the Bel-Robinson tensor. In particular, they calculated the gravitational entropy for a Schwarzschild black hole, for a spatially flat Robertson-Walker geometry with scalar perturbations, and for the inhomogeneous Lemaître-Tolman-Bondi solution.

The main goal of the present work is to calculate the gravitational entropy of a Kerr black hole using Clifton et al.'s proposal, and test whether such estimator still reproduces the Benkenstein-Hawking entropy of a Kerr black hole.

Throughout this paper we use geometrized units $G = c = 1$.

## 2. Bel-Robinson estimator

Clifton, Ellis, and Tavakol (2013) defined the entropy of the gravitational field $S_{\rm grav}$ following these five requirements: 1) $S_{\rm grav} \geq 0$, 2) $S_{\rm grav} = 0 \Leftrightarrow C_{\rm abcd} = 0$, where $C_{\rm abcd}$ is the Weyl tensor, 3) $S_{\rm grav}$ gives a measure of the local anisotropy of the free gravitational field, 4) $S_{\rm grav}$ should be equal to the Bekenstein-Hawking entropy on the event horizon of a black hole, 5) $S_{\rm grav}$ should increase monotonically as structure forms in the universe.

In particular, Clifton and coworkers constructed a definition of $S_{\rm grav}$ in analogy with the fundamental law of thermodynamics:

$$T_{\rm grav} dS_{\rm grav} = dU_{\rm grav} + p_{\rm grav} dV. \tag{2}$$

Here, $T_{\rm grav}$, $S_{\rm grav}$, $U_{\rm grav}$ and $p_{\rm grav}$ stand for the effective temperature, entropy, internal energy, and isotropic pressure of the free gravitational field respectively, whereas $V$ is the spatial volume. Expressions for the effective energy density $\rho_{\rm grav}$ and pressure $p_{\rm grav}$ are derived from the Bel-Robinson tensor, which for Coulomb-like gravitational fields, such as black hole spacetimes, take the form:

$$8\pi\rho_{\rm grav} = 2\alpha\sqrt{\frac{2\mathcal{W}}{3}}, \tag{3}$$

$$p_{\rm grav} = 0, \tag{4}$$

where $\alpha$ is a constant and $\mathcal{W} = 1/4\left(E_a{}^b E^a{}_b + H_a{}^b H^a{}_b\right)$ is the "super-energy density", and $E_{ab}$ and $H_{ab}$ denote the electric and magnetic part of the Weyl tensor, respectively.

The temperature of the gravitational field is defined as a local quantity that reproduces the Hawking (1974, 1975), Unruh (1976), and de Sitter temperatures (Gibbons and Hawking, 1977) in the appropriate limits (Clifton at al., 2013). It has the following expression:

$$T_{\rm grav} = \frac{\left|\dot{u}_a z^a + H + \sigma_{ab} z^a z^b\right|}{2\pi}. \tag{5}$$

Here $u_a$ is a timelike unit vector, $z^a$ is a spacelike unit vector aligned with the Weyl principal tetrad, $H = \Theta/3$ being $\Theta = \nabla_a u^a$ the expansion scalar and $\sigma_{ab} = \nabla_{(a} u_{b)} + a_{(a} u_{b)} - 1/3\ \Theta h_{ab}$ is the shear tensor; $h_{ab}$ is the projection tensor $h_{ab} = g_{ab} - (u_c u^c)\, u_a u_b$.

Clifton and coworkers calculated the gravitational entropy of a Schwarzschild black hole, recovering the Bekenstein-Hawking entropy on the event horizon of the hole. In the following section we extend their calculations to a Kerr black hole and analyze whether such estimator still represents a good classical measure of the entropy of the gravitational field.

## 3. Bel-Robinson estimator for Kerr black holes

The line element of the Kerr spacetime in oblate spheroidal coordinates $(t, r, \theta, \phi)$ takes the form (Doran, 2000):

$$\begin{aligned} d\tau^2 &= -\left(1 - \frac{2Mr}{\rho^2}\right) dt^2 + \frac{\rho^2}{r^2 + a^2} dr^2 - 2\sqrt{\frac{2Mr}{r^2 + a^2}} dt\, dr - 4aMr \frac{\sin^2\theta}{\rho^2} dt\, d\phi \\ &+ 2a\sqrt{\frac{2Mr}{r^2 + a^2}} \sin^2\theta d\phi dr + \rho^2 d\theta^2 + \left[\left(r^2 + a^2\right) + 2Mra^2 \frac{\sin^2\theta}{\rho^2}\right] \sin\theta^2 d\phi^2, \end{aligned}$$

where $\rho^2 = r^2 + a^2\cos^2\theta$. The constant $M$ represents the mass of the black hole and $a$ its angular momentum.

Clifton et al.'s proposal is frame-dependent. We make the simplest choice for a Kerr spacetime (see below). Specifically, we adopt the following unit vectors[1] $u^a$ and $z^a$:

$$u^a = \left(\frac{r^2 + a^2}{\sqrt{-\Delta}\,\sqrt{r^2 + u^2}}, 0, 0, \frac{a}{\sqrt{r^2 + u^2}\,\sqrt{-\Delta}}\right), \tag{6}$$

$$z^a = \left(\frac{\sqrt{r^2 + a^2}\,\sqrt{2Mr}}{\sqrt{-\Delta}\,\sqrt{r^2 + u^2}}, \frac{\sqrt{-\Delta}}{\sqrt{r^2 + u^2}}, 0, \frac{a\,\sqrt{2Mr}}{\sqrt{-\Delta}\,\sqrt{r^2 + u^2}\,\sqrt{r^2 + a^2}}\right), \tag{7}$$

where $u = a\cos\theta$ and $\Delta = r^2 + a^2 - 2Mr$. In the region interior to the outer event horizon $u^a u_a = 1$ and $z^a z_a = -1$. The vector $z^a$ is chosen to be orthogonal to the hypersurfaces of constant time $t$. Because of the four-fold coordinate degrees of freedom inherent to General Relativity, there is not a unique foliation of spacetime into a family of nonintersecting spacelike 3-surfaces $\Sigma$. For the Kerr spacetime metric given by Eq. (6), we have checked that the unit vectors $u^a$ and $z^a$ satisfy all conditions for the calculation of the gravitational entropy as stated by Clifton et al. (2013).

We now proceed to the calculation of the gravitational energy density and temperature according to Eqs. (3) and (5), respectively.

The gravitational energy density takes the form:

$$\rho_{\text{grav}} = \frac{\alpha}{4\pi} \frac{M}{\left(r^2 + u^2\right)^{3/2}}. \tag{8}$$

In Figures 1 and 2,we show plots of $\rho_{\text{grav}}$ as a function of the radial coordinate for $\theta = \pi/2$ and $\theta = \pi/4$, respectively. The gravitational energy density is everywhere well-defined and positive, except towards the ring singularity, as expected.

We obtain the following expression for the temperature of the gravitational field:

$$T_{\text{grav}} = \frac{\left|-ra^2 - Mu^2 + ru^2 + Mr^2\right|}{2\pi\ \left(r^2 + u^2\right)^{3/2}\sqrt{-\Delta}}, \tag{9}$$

[1] This calculation extends that presented in Pérez & Romero (2014), by choosing principal null tetrads. The results, notwithstanding, remain the same.

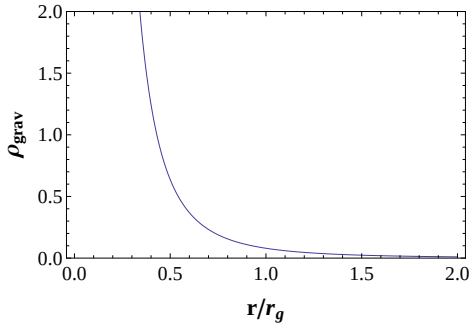


Figure 1. Plot of $\rho_{\rm grav}$ as a function of the radial coordinate for $a = 0.8$ and $\theta = \pi/2$.

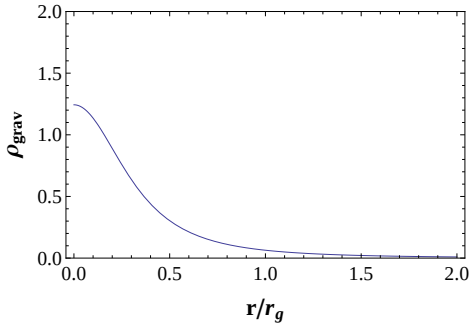


Figure 2. Plot of $\rho_{\rm grav}$ as a function of the radial coordinate for $a = 0.8$ and $\theta = \pi/4$.

where the absolute value brackets were added to avoid negative or complex values. A 3-dimensional plot of $T_{\rm grav}$ as a function of the radial and angular coordinate for $a = 0.8$ is shown in Figure 3. We see that $T_{\rm grav}$ is everywhere well-defined except towards the inner and outer horizons.

As explained by Clifton et al. (2013), a small change in the gravitational entropy density of a black hole occurs when a small amount of mass is added:

$$\delta s_{\rm grav} = \frac{\delta\left(\rho_{\rm grav} v\right)}{T_{\rm grav}}. \tag{10}$$

In the expression above the element of volume is $v = z^a \eta_{abcd} dx^b dx^c dx^d$, where $\eta_{abcd} = \eta_{[abcd]}$, $\eta_{0123} = \sqrt{|g_{ab}|}$. For the our particular coordinate choice:

$$v = \frac{\sqrt{2Mr}\left(r^2 + a^2\right)^{1/2}\left(r^2 + u^2\right)^{1/2}}{a\sqrt{-\Delta}} d\phi\, du\, dr. \tag{11}$$

We now proceed to calculate the gravitational entropy $S_{\rm grav}$ by performing the integration of Eq. (10) over the volume $V$ enclosed by the outer event horizon on a hypersurface of constant $t$, for a fixed value of $a$:

$$S_{\rm grav} = \int_{\rm V} \frac{\rho_{\rm grav} v}{T_{\rm grav}}, \tag{12}$$

in order to test whether the Bel-Robinson proposal in the choosen frame reproduces the Bekenstein-Hawking entropy of a Kerr black hole. We notice, however, that independently of the coordinate choice, the region inside the inner horizon is not time-orientable since the region is chronology-violating (Visser, 1996). The contribution to the gravitational entropy should come from the region between the inner and outer horizons.

Integral (12) can explicitly be written as:

$$S_{\rm grav} = \beta \int_{r_-}^{r_+} \int_0^{\pi} \frac{r^{1/2}\ \left(r^2 + a^2\right)^{1/2}\ \left(r^2 + a^2 \cos^2\theta\right)^{1/2} \sin\theta\, d\theta\, dr}{|f(r,\theta)|},$$

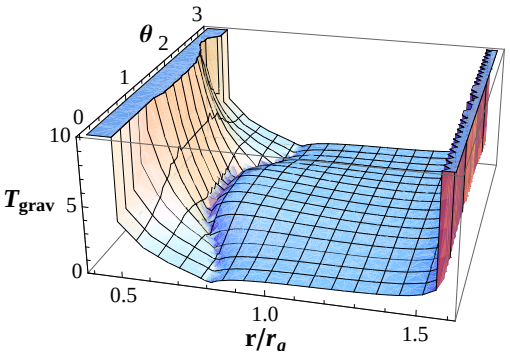


Figure 3. Plot of $T_{\rm grav}$ as a function of the coordinates $r$ and $\theta$ for $a = 0.8$.

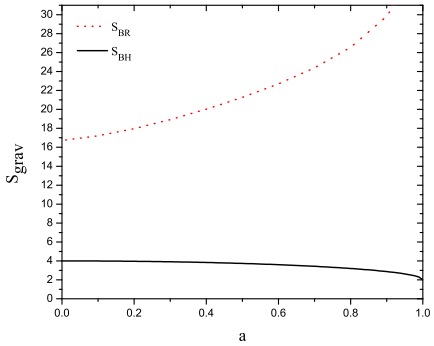


Figure 4. Plot of $S_{\rm BR}$ and $S_{\rm BH}$ as a function of the angular momentum $a$.

where $\beta = 2^{1/2}\pi\alpha\ M^{3/2}$. In the latter equation we have already integrated over the azimuthal coordinate $\phi$. The function $f(r,\theta)$ is defined as $f(r,\theta) \equiv -ra^2 + Mr^2 + a^2\cos^2\theta\,(-M+r)$. The domain of integration of Eq. (13) is:

$$T = \left\{(r,\theta) \in \Re^2 / \ r_- \leq r \leq r_+ \ \wedge \ 0 \leq \theta \leq \pi\right\}. \tag{13}$$

We divide $T$ into two subregions denoted $D$ and $G$ respectively, such that $T = D \cup G$,

$$D = \left\{(r,\theta) \in \Re^2 / \ r_- \leq r \leq r_* \ \wedge \ 0 \leq \theta \leq \pi\right\}, \tag{14}$$

where $r_*$ is the solution of the equation $f(r_*,0) = 0$, and $G = T - D$.

Given the definitions above, Eq. (13) can be written as $S_{\rm grav} = \beta\left(S^{\rm D}_{\rm grav} + S^{\rm G}_{\rm grav}\right)$ where,

$$S^{\rm D}_{\rm grav} = \int\int_D \frac{r^{1/2}\left(r^2+a^2\right)^{1/2}\left(r^2+a^2\cos^2\theta\right)^{1/2}\sin\theta\ d\theta\ dr}{|f(r,\theta)|}, \tag{15}$$

$$S^{\rm G}_{\rm grav} = \int\int_G \frac{r^{1/2}\left(r^2+a^2\right)^{1/2}\left(r^2+a^2\cos^2\theta\right)^{1/2}\sin\theta\ d\theta\ dr}{|f(r,\theta)|}. \tag{16}$$

The integral given by Eq. (15) is an improper divergent integral; in particular it tends to infinity for those values of $r$ and $\theta$ such that $f(r,\theta) = 0$. Conversely, integral (16) is well defined for $a \in (0,1)$, and can be integrated numerically.

We show in Figure 4 the result of the numerical integration of $S^{\rm G}_{\rm grav}$ (see Eq. 16). We also plot the Bekenstein-Hawking entropy, denoted $S_{\rm BH}$, as a function of the angular momentum of the hole. It is clear that $S_{\rm BR}$ does not reproduce the Bekenstein-Hawking entropy of a black hole. We conclude that even in the domain of integration $G$ where the entropy is well defined, it is not a good approximation to the Bekenstein-Hawking entropy, at least for the current coordinate choice. We do not discard that for a different choice of vectors $u^a$ and $z^a$, the Bel-Robinson proposal may coincide with Bekenstein-Hawking result. However, the fact that the innermost region of the Kerr spacetime is not folliable and time-orientable suggests that our result might be general.

## 4. Final remarks

We have computed the gravitational energy density, temperature, and gravitational entropy of a Kerr black hole according to the Bel-Robinson estimator. The calculations were performed using a pair of vectors $u_a$ and $z^a$ spacelike and timelike, respectively, that determine a Weyl principal tetrad. The choice of such vectors, however, is not unique, thus being $\rho_{\rm grav}$ and $T_{\rm grav}$ frame dependent quantities. Under the simplest coordinate choice, we proved that the gravitational entropy is not well defined.

The first requirement that a reliable classical estimator of the gravitational entropy needs to fulfill is that it should be well-behaved in all types of horizons where quantum field calculations can be used as an independent probe of the entropy. Only when a complete match be obtained, the classical estimators can be used to evaluate other families of spacetimes with some confidence.

**Acknowledgments.** This work is supported by PICT 2012-00878, Préstamo BID (ANPCyT). We are grateful for the valuable comments of an anonymous referee. We also thank Santiago E. Perez Bergliaffa for useful advice.

## References

Bardeen, J. M., Carter, B. & Hawking, S. W. 1973, Commun. Math. Phys. 31, 161-170

Bekenstein, J. D. 1972, Lett. Nuovo Cim. 4, 737-740

Bekenstein, J. D. 1973, Phys. Rev. D 7, 2333-2346

Bekenstein, J. D. 1974, Phys. Rev. D 9, 3292-3300

Clifton, T., Ellis, G. F. R. & Tavakol, R. 2013, Class. Quant. Grav., 30, 125009

Doran, C. 2000, Phys. Rev. D 61, 067503

Gibbons, G. W. & Hawking, S. W. 1977, Phys. Rev. D 15, 2738-2751

Hawking, S. W. 1974, Nature 248, 30-31

Hawking, S. W. 1975, Commun. Math. Phys. 43, 199-220

Penrose, R. 1979, "General Relativity, an Einstein Centenary Survey", in Singularity and Time-Asymmetry, S. W. Hawking and W. Israel (eds.), pp. 581-638, Cambridge Univ. Press, Cambridge

Pérez, D. & Romero, G. E. 2014, Gen. Rel. Grav. 46, 9, 1774

Unruh, W. G. 1976, Phys. Rev. D 14, 870-892

Visser, M. 1996, "Lorentzian wormholes: from Einstein to Hawking", AIP Series in Computational and Applied Mathematical Physics, Springer-Verlag, New York

*Gravitation, Relativistic Astrophysics and Cosmology*
*Second Argentinian-Brazilian Meeting, 2014*
*G. S. Vila, F. L. Vieyro and J. Fabris, eds.*

# Towards a proof of the equivalence between FRW background expansion and statistical isotropy

Yeinzon Rodríguez,[1,2] L. Gabriel Gómez,[1] and Carlos M. Nieto[2]

[1]*Centro de Investigaciones en Ciencias Básicas y Aplicadas, Universidad Antonio Nariño, Cra 3 Este # 47A - 15, Bogotá D.C. 110231, Colombia*
[2]*Escuela de Física, Universidad Industrial de Santander, Ciudad Universitaria, Bucaramanga 680002, Colombia*

**Abstract.** We will expose in this paper our advances towards a proof of the equivalence between FRW background expansion, during some period of time that contains primordial inflation, and the statistical isotropy of the primordial curvature perturbation $\zeta$ at the end of this period of time. Our motivation rests on the growing interest in the existence of a preferred direction in the Universe hinted by the continuous presence of anomalies in the CMB data.

## 1. Introduction

Cosmology is based on a, once believed, sacred principle: the homogeneity and isotropy at large scales. The actual meaning of this statement is that perturbations in the energy density distribution at large scales, and in the CMB temperature, are statistically homogeneous and isotropic, i.e., their $n$-point correlators in real space are invariant under spatial translations and spatial rotations. However, the CMB data releases have consistently presented a possible indication of the existence of a preferred direction in the Universe in relation with the different anomalies in the data (Ade et. al., 2014; Bennett et. al., 2013). Names as "the axis of evil" employed to describe some of the anomalies are evidence of both the idea of a preferred direction and the position of the cosmologists community about the violation of the sacred principle. There are two ways of thinking of a preferred direction in the Universe, one at the background level and the other at the perturbative level: at the background level we can have non-FRW expansion which can be associated, for instance, to the presence of a shear in the metric or an anisotropic curvature; whereas at the perturbative level we can have statistical anisotropy in the perturbations, especially in the primordial curvature perturbation $\zeta$. It is quite reasonable to think that a non-FRW background expansion always feeds the statistical anisotropy; moreover, sometimes a FRW background expansion is assumed in the analysis of the statistical anisotropy. Notwithstanding, there is no any proof yet regarding the actual relation between these two characteristics. It is our mission in this paper to expose our advances towards such a kind of proof. We will sketch the main argument of a proof of the equivalence between FRW background expansion, during some period of time that contains primordial inflation, and the statistical isotropy of the primordial curvature perturbation $\zeta$ at the end of this period of time, at the level of the power spectrum, leaving the most delicate points for a deeper analysis and discussion in a future publication.

## 2. Statistical homogeneity and isotropy

Quantum mechanics only allows us to predict probabilities of different outcomes after an experiment in an ensemble of systems, in contrast to classical mechanics which does allow us to predict the exact outcome after an experiment in just one element of the ensemble. Since the underlying physical mechanism in the generation of cosmological perturbations is of quantum nature, the cosmologists are more interested in studying the statistical properties of a perturbation map, say the CMB map or the galaxy distribution map. The way of doing this is via the $n$-point correlators of the perturbations in real space. Let's define a scalar cosmological perturbation $\beta(\mathbf{x})$ in real space and make a Fourier integral expansion

$$\beta(\mathbf{x}) \equiv \int \frac{d^3k}{(2\pi)^3} e^{i\mathbf{k}\cdot\mathbf{x}} \beta(\mathbf{k}), \tag{1}$$

where $\beta(\mathbf{k})$ is the Fourier mode function of $\beta(\mathbf{x})$. The $n$-point correlators of $\beta(\mathbf{x})$ are averages over the ensemble of the products $\beta(\mathbf{x}_1)\beta(\mathbf{x}_2)...\beta(\mathbf{x}_n)$ where $\mathbf{x}_1$, $\mathbf{x}_2$, ..., $\mathbf{x}_n$ represent different points in space[1]:

$$\langle \beta(\mathbf{x}_1)\beta(\mathbf{x}_2)...\beta(\mathbf{x}_n)\rangle \equiv \int \frac{d^3k_1}{(2\pi)^3}\frac{d^3k_2}{(2\pi)^3}...\frac{d^3k_n}{(2\pi)^3} \quad e^{i(\mathbf{k}_1\cdot\mathbf{x}_1+\mathbf{k}_2\cdot\mathbf{x}_2+...+\mathbf{k}_n\cdot\mathbf{x}_n)} \times \\ \times\langle \beta(\mathbf{k}_1)\beta(\mathbf{k}_2)...\beta(\mathbf{k}_n)\rangle\,. \tag{2}$$

Thus, the correlation functions in real space may be studied via the correlation functions in momentum space. Let's see now the meaning of statistical homogeneity and statistical isotropy.

**Statistical homogeneity:** of course the perturbation map is not homogeneous (i.e., it is not invariant under spatial translations), but it may be that the probability distribution function governing $\beta(\mathbf{x})$ is, which is called statistical homogeneity. This means that the $n$-point correlators in real space are invariant under translations in space, i.e.

$$\langle \beta(\mathbf{x}_1+\mathbf{d})\beta(\mathbf{x}_2+\mathbf{d})...\beta(\mathbf{x}_n+\mathbf{d})\rangle = \langle \beta(\mathbf{x}_1)\beta(\mathbf{x}_2)...\beta(\mathbf{x}_n)\rangle, \tag{3}$$

where $\mathbf{d}$ is some vector in real space establishing the amount of spatial translation. The only way of achieving this, in view of Eq. (2), is expressing the argument in the exponential function inside the integral as the addition of several terms of the form $f(\mathbf{x}_i - \mathbf{x}_j)$, which in turn is possible (but it is not the only possibility) if the $n$-point correlators in momentum space are proportional to a Dirac delta function:

$$\langle \beta(\mathbf{k}_1)\beta(\mathbf{k}_2)...\beta(\mathbf{k}_n)\rangle \equiv (2\pi)^3\delta^3(\mathbf{k}_{12...n}) M_\beta(\mathbf{k}_1,\mathbf{k}_2,...,\mathbf{k}_n)\,. \tag{4}$$

In the previous expression, $\mathbf{k}_{12...n}$ means $\mathbf{k}_1+\mathbf{k}_2+...+\mathbf{k}_n$, and the function $M_\beta(\mathbf{k}_1,\mathbf{k}_2,...,\mathbf{k}_n)$ is called the $(n-1)$-spectrum.

**Statistical isotropy:** once statistical homogeneity has been secured, in the form of Eq. (4), we ask about the invariance under spatial rotations (i.e. isotropy). Of course again,

[1]The ensemble average inside the integral is over the Fourier mode functions only since they are the stochastic variables.

the perturbation map is not isotropic, but it may be that the probability distribution function governing $\beta(\mathbf{x})$ is, which is called statistical isotropy. This means that the $n$-point correlators in real space are invariant under rotations in space, i.e.

$$\langle\beta(\tilde{\mathbf{x}}_1)\beta(\tilde{\mathbf{x}}_2)...\beta(\tilde{\mathbf{x}}_n)\rangle = \langle\beta(\mathbf{x}_1)\beta(\mathbf{x}_2)...\beta(\mathbf{x}_n)\rangle\,, \tag{5}$$

where $\tilde{\mathbf{x}}_i = \mathcal{R}\ \mathbf{x}_i$, $\mathcal{R}$ being a rotation operator. To satisfy the above requirement, the $(n-1)$-spectrum must satisfy the condition

$$M_\beta(\tilde{\mathbf{k}}_1, \tilde{\mathbf{k}}_2, ..., \tilde{\mathbf{k}}_n) = M_\beta(\mathbf{k}_1, \mathbf{k}_2, ..., \mathbf{k}_n)\,, \tag{6}$$

where the tildes over the momenta represent as well a spatial rotation, parameterized by $\mathcal{R}$, in momentum space. This condition has more explicit consequences in the spectrum (1-spectrum) and the bispectrum (2-spectrum):

$$M_\beta(\mathbf{k}_1, \mathbf{k}_2) \equiv P_\beta(\mathbf{k}_1, \mathbf{k}_2) = P_\beta(k)\,, \tag{7}$$

$$M_\beta(\mathbf{k}_1, \mathbf{k}_2, \mathbf{k}_3) \equiv B_\beta(\mathbf{k}_1, \mathbf{k}_2, \mathbf{k}_3) = B_\beta(k_1, k_2, k_3)\,, \tag{8}$$

where in the first line $k = |\mathbf{k}_1| = |\mathbf{k}_2|$, and in the second line $k_i = |\mathbf{k}_i|$. Starting from the trispectrum (3-spectrum), the condition in Eq. (6) about statistical isotropy in all the higher-order $(n-1)$-spectra cannot be reduced to similar conditions to the ones in Eqs. (7) and (8), so that the minimal way of parameterizing the $(n-1)$-spectra (with $n \geq 4$) will always be in terms of all the $n$ wavevectors. The scalar nature of $\beta(\mathbf{x})$ is very important since, if it were a vector or a tensor, there would not be a way to make the $n$-point correlators in real space invariant under spatial rotations. In those cases, we relax the meaning of statistical isotropy and establish that it is present if the $(n-1)$-spectra of the scalar pertubations that multiply the respective polarization vectors or tensors satisfy Eq. (6).

## 3. The separate universe assumption and the $\delta N$ formalism

**The separate universe assumption:** this assumption refers to the behaviour of the Universe after smoothing on a specified comoving scale $k^{-1}$, during the super horizon era $k \ll aH$. It states that the spatial gradients, at most of order $k/a$, are negligible, which actually means that the Universe at each comoving location behaves as if it were homogeneous (Lyth & Liddle, 2009). Each smoothed region about each comoving location is then regarded as a separate homogeneous universe. By virtue of this, the form of the equations for the dynamical quantities in each separate universe is the same as for the unperturbed quantities. The separate universe assumption is a powerful tool for dealing with perturbations in the very early Universe and has become one of the most employed methodologies as alternative to the standard cosmological perturbation theory.

**The $\delta N$ formalism:** the $\delta N$ formalism (Dimopoulos et. al., 2009; Lyth & Liddle, 2009) provides a powerful method to evaluate the primordial curvature perturbation $\zeta(\mathbf{x}, t)$ in terms of the perturbations of the fields a few Hubble times after horizon crossing $t_*$ (corresponding to a flat slicing), and the derivatives of the unperturbed number of $e$-foldings $N(t, t_*) = \int_{t_*}^{t} H(t')dt'$ with respect to the unperturbed fields evaluated at $t_*$. According to this formalism, once the separate universe approach has been invoked, and

a comoving threading has been established, the value of $\zeta$ in a uniform energy density hypersurface at the final time $t$ is given by the perturbation in the time integral of the local volume expansion rate $\theta$ along a curve starting at an initial flat hypersurface at the time $t_i$:

$$\zeta(\mathbf{x}, t) \equiv \delta N(\mathbf{x}, t, t_i) - \langle \delta N(\mathbf{x}, t, t_i) \rangle \,. \tag{9}$$

Here, the bracket notation means a ensemble average (which corresponds to a spatial average if there is statistical homogeneity). In many inflationary scenarios, the number $N$ of $e$-foldings depends only on the values of the fields at $t_*$ so we can write the curvature perturbation as an expansion in the perturbations of the fields at this time. Assuming the presence of just one scalar field and one vector field (the generalization to more fields is straightforward), we have:

$$\begin{aligned} \zeta(\mathbf{x}, t) \equiv \delta N(\phi(\mathbf{x}), A_i(\mathbf{x}), t) \quad &= \quad N_\phi \delta\phi + N_i \delta A_i + \frac{1}{2} N_{\phi\phi} (\delta\phi)^2 + N_{\phi i} \delta\phi \delta A_i + \\ &\quad + \frac{1}{2} N_{ij} \delta A_i \delta A_j + \ldots \,, \end{aligned} \tag{10}$$

where

$$N_\phi \equiv \frac{\partial N}{\partial \phi} \,, \quad N_{\phi\phi} \equiv \frac{\partial^2 N}{\partial \phi^2} \,, \qquad N_{\phi i} \equiv \frac{\partial^2 N}{\partial A_i \partial \phi} \,, \quad \text{etc.} \,, \tag{11}$$

are the derivatives with respect to the scalar $\phi$ and the spatial components of the vector field $\mathbf{A}$.

## 4. FRW background expansion implies statistical isotropy

We will make the following assumptions:

1. The action is such that the FRW metric is an attractor in the background.
2. The fields involved are just scalar and/or vector fields.
3. The background expansion is FRW type during the whole time spanning from the beginning of inflation to the time when the curvature perturbation $\zeta$ is evaluated.

By invoking the separate universe assumption, the form of the equations for the dynamical quantities at each comoving location is the same as for the unperturbed quantities. Thus, the field perturbation equations in momentum space do not depend explicitly on $\mathbf{k}$. They depend on time, thus on $k_*$, but do not depend on the direction of $\mathbf{k}$. Their solutions are, therefore, independent of the direction of $\mathbf{k}$ except for the set of initial conditions $\{\alpha^n_{\mathbf{k}}\}$. However, the field perturbations are evaluated in the flat slicing, so, taking into account the assumption 3, the whole perturbed metric in this slicing is actually FRW which is conformally equivalent to Minkowski. This has as a consequence that the set of initial conditions, when quantizing, can be written as $\{\hat{\alpha}^n_{\mathbf{k}} = \alpha^n_k \hat{a}^n_{\mathbf{k}}\}$ where $\hat{a}^n_{\mathbf{k}}$ is the respective annihilation operator. Following the usual procedure to calculate the power spectrum of the field perturbations, this implies that the latter are statistically isotropic (and statistically homogeneous) at the level of the power spectrum (since the $\alpha^n_k$ do not depend on the direction of $\mathbf{k}$). This is valid for all the relevant cosmological

scales since the time of horizon exit for each of them is contained in the period of time defined in the assumption 3.

Now, if the background expansion is FRW type, the fluid that fills the universe is perfect; therefore, by invoking assumption 2, the field configuration must be given by any number of scalar fields and/or multiple randomly oriented copies (just one is enough) of a triad of mutually orthogonal vector fields with the same norm. This must be accomplished during the whole period of time defined in assumption 3.[2] Thus, by employing the $\delta N$ formalism, we obtain (Gómez & Rodríguez, 2013)

$$P_\zeta(\mathbf{k}_1) = P_\zeta^{iso}(k_1)[1 + g_\zeta^1(\hat{\mathbf{k}}_1 \cdot \hat{\mathbf{N}}_1)^2 + g_\zeta^2(\hat{\mathbf{k}}_1 \cdot \hat{\mathbf{N}}_2)^2 + g_\zeta^3(\hat{\mathbf{k}}_1 \cdot \hat{\mathbf{N}}_3)^2], \tag{12}$$

where

$$P_\zeta^{iso}(k_1) = (N_\phi)^2 P_{\delta\phi}(k_1) + (N_i^1)^2 P_+^1(k_1) + (N_i^2)^2 P_+^2(k_1) + (N_i^3)^2 P_+^3(k_1), \tag{13}$$

and

$$g_\zeta^n = \frac{(N_i^n)^2[P_{long}^n(k_1) - P_+^n(k_1)]}{P_\zeta^{iso}(k_1)}, \tag{14}$$

$P_+^n(k)$ being the parity even spectrum of the $n$-th vector field, $P_{long}^n(k)$ being the longitudinal spectrum of the $n$-th vector field, and

$$\hat{\mathbf{N}}_n = \frac{\mathbf{N}_n}{|\mathbf{N}_n|}, \tag{15}$$

where $\mathbf{N}_n$ is the vector formed by the derivatives of $N$ with respect to the each spatial component of the $n$-th vector field. However, because of the symmetries of the field configuration, we have

$$\hat{\mathbf{N}}_1 = \pm\hat{\mathbf{i}}, \tag{16}$$
$$\hat{\mathbf{N}}_2 = \pm\hat{\mathbf{j}}, \tag{17}$$
$$\hat{\mathbf{N}}_3 = \pm\hat{\mathbf{z}}, \tag{18}$$
$$(N_i^1)^2 = (N_i^2)^2 = (N_i^3)^2, \tag{19}$$
$$P_+^1 = P_+^2 = P_+^3, \tag{20}$$
$$P_{long}^1 = P_{long}^2 = P_{long}^3, \tag{21}$$

and, therefore,

$$g_\zeta^1 = g_\zeta^2 = g_\zeta^3 = g_\zeta\,. \tag{22}$$

Thus,

$$P_\zeta(\mathbf{k}_1) = P_\zeta^{iso}(k_1)[1 + g_\zeta[(\hat{\mathbf{k}}_1 \cdot \hat{\mathbf{i}})^2 + (\hat{\mathbf{k}}_1 \cdot \hat{\mathbf{j}})^2 + (\hat{\mathbf{k}}_1 \cdot \hat{\mathbf{z}})^2]], \tag{23}$$
$$= P_\zeta^{iso}(k_1)[1 + g_\zeta], \tag{24}$$

where the last step is valid because of the director cosines property of a unit vector. We conclude then that the power spectrum of $\zeta$ is actually independent of the direction of $\mathbf{k}_1$, rendering the two-point correlator of $\zeta$ in real space statistically isotropic.

[2]This has as a consequence that the action must be consistent with the isotropy during the referred period of time, e.g., the masses for the members of each triad must be equal (although not necessarily the same masses among triads).

## 5. Non-FRW background expansion implies statistical anisotropy

If the background metric is not FRW at some time, then the background metric is not FRW at $t_*$ because of assumption 1. Thus (Gómez & Rodríguez, 2013),

$$\begin{aligned} P_\zeta(\mathbf{k}_1) &= P_\zeta^{iso}(k_1)[1 + \tilde{g}_{\delta\phi}(\hat{\mathbf{k}}_1 \cdot \hat{\mathbf{d}}_{\delta\phi})^2 + \tilde{g}_+^1(\hat{\mathbf{k}}_1 \cdot \hat{\mathbf{d}}_+^1)^2 + \tilde{g}_+^2(\hat{\mathbf{k}}_1 \cdot \hat{\mathbf{d}}_+^2)^2 + \\ &\quad + \tilde{g}_+^3(\hat{\mathbf{k}}_1 \cdot \hat{\mathbf{d}}_+^3)^2 + \tilde{g}_N^1(\hat{\mathbf{k}}_1 \cdot \hat{\mathbf{N}}_1)^2 + \tilde{g}_N^2(\hat{\mathbf{k}}_1 \cdot \hat{\mathbf{N}}_2)^2 + \tilde{g}_N^3(\hat{\mathbf{k}}_1 \cdot \hat{\mathbf{N}}_3)^2], \end{aligned} \tag{25}$$

where none of the $\tilde{g}$, except perhaps for the $\tilde{g}_N$ (if the background metric is again FRW at the time when $\zeta$ is evaluated), are the same, and, in contrast, all the $\hat{\mathbf{d}}$ directions are the same and equal to the preferred direction at $t_*$. We conclude then that the power spectrum of $\zeta$ does depend in this case on the direction of $\mathbf{k}_1$, rendering the two-point correlator of $\zeta$ in real space statistically anisotropic.

## 6. Conclusions

When we take Sections 4 and 5 together, they show that, under the established assumptions, the FRW background expansion is equivalent to the statistical isotropy of $\zeta$ in connection with its two-point correlator in real space during some period of time that contains primordial inflation.

**Acknowledgments.** This work was supported by COLCIENCIAS grant number 110656933958 RC 0384-2013 and by COLCIENCIAS - ECOS-NORD grant number RC 0899-2012. Y.R. acknowledges VIE (UIS) for the financial support through its mobility programme.

## References

Ade, P. A. R. et. al. 2014, Astron. Astrophys., 571, A23

Bennett, C. L. et. al. 2013, Astrophys. J. Suppl. Ser., 208, 20

Dimopoulos, K. et. al. 2009, JCAP, 0905, 013

Gómez, L. G. & Rodríguez, Y. 2013, AIP Conf. Proc., 1548, 270

Lyth, D. H. & Liddle, A. R. 2009, "The primordial density perturbation", Cambridge University Press, Cambridge, UK

*Gravitation, Relativistic Astrophysics and Cosmology*
*Second Argentinian-Brazilian Meeting, 2014*
*G. S. Vila, F. L. Vieyro and J. Fabris, eds.*

# Charge–size inequality in General Relativity

Marcelo E. Rubio[1] and Sergio Dain[1,2]

[1]*Facultad de Matemática, Astronomía y Física, Universidad Nacional de Córdoba, Argentina*
[2]*CONICET*

**Abstract.** We present a new inequality[1] between electric charge and some measure of size for ordinary objects in General Relativity. A universal area–charge inequality for arbitrary dynamical black holes was recently proved (Dain et al. 2012). Our purpose is to generalize this result for ordinary bodies, or look for a counterexample. Mainly, we discuss the spherical case in which there are at least two intuitive notions of size, and finally we prove the inequality inside a sphere with constant conformal electric charge density.

## 1. Introduction

Consider a static body with total electric charge $Q$. Let $\mathcal{R}$ be some measure of it size, with units of lenght. We want to study if is there a universal relation between $Q$ and $\mathcal{R}$. Of course, we should define precisely what do we understand about size. For instance, $\mathcal{R}$ could be the area radius if it is the case of a spherical symmetric body (in general, the area radius is well defined for any smooth 2–surface, but without spherical symmetry we expect that it will be not a good measure of size).

We conjecture the following statement: *Let $\Omega$ be a 3–dimensional region that has total electric charge $Q(\Omega)$ and let $\mathcal{R}(\Omega)$ be a measure of the size of $\Omega$. Then, it holds the inequality*

$$Q(\Omega)^2 \leq \frac{c^4}{G}\mathcal{R}(\Omega)^2. \tag{1}$$

The physical motivation of the above inequality is the following: a charged body has a minimum size given by the total amount of electric charge inside it.

To define a quantity that tell us information about the size of any region of space is a non trivial task, and it has several subtleties. There is often the case in which the notion of size is related to the notion of geometric quantities like area or volume; however, it is not difficult to realize that there is not true in general: just imagine two bodies with equal surface area and equal volume but with arbitrary different shape. A precise discussion of measures of size is present in Galloway et al. (2008), O'Murchadha (1986) and Schoen et al. (1983). Likewise, there are cases in which the desired definition is clear and unambiguous, such as a sphere.

We will take geometric units, such that $G = c = 1$, where $G$ is Newton's constant of gravity and $c$ the speed of light in vacuum.

[1]This project is part of Marcelo Rubio's final work (Rubio, M. E. 2014) to obtain a degree in Physics.

## 2. Size in spherical symmetry

It is natural to begin studying the conjecture in spherical symmetry; that is, $\Omega$ is a sphere of area radius $r$; and take this quantity as a measure of the size of $\Omega$. Of course, this is not the most general measure one can choose.

In geometric terms, let $\Omega$ be a spherical surface with smooth boundary inside an asymptotically flat initial data $(\Sigma, h_{ij}, K_{ij})$ of field equations. The surface area of the sphere depends on the induced metric $h$, so we expect that $r$ is a monotonic function of $\ell$, the *proper distance* of the sphere (in particular, this function is the identity in case of flat geometry).

More precisely, the above conjecture in case of spherical symmetry can be enunciated as follows:

**Conjecture 2.1.** *Let $\Omega$ be a sphere contained in an asymptotically flat initial data of field equations that satisfies the dominant energy condition, with electric charge $Q$, and whose proper length is $\ell$. Then, the inequality*

$$Q^2 \leq \ell^2 \tag{2}$$

*holds.*

We will take as initial data an asymptotically flat spatial hypersurface $\Sigma$ with the topology of $\mathbb{R}^3$, induced metric $h_{ij}$ and no extrinsic curvature; that is $K_{ij} = 0$. Thus, if no matter density is present on $\Sigma$, the constraints are

$$\mathcal{R} = 2\mathcal{E}^i\mathcal{E}_i; \quad \mathcal{D}_i\mathcal{E}^i = 4\pi\rho, \tag{3}$$

where $\mathcal{R}$ is the 3–curvature scalar of $h$, $\mathcal{E}^i$ the electric field 3–vector and $\rho$ the electric charge density. The symbol $\mathcal{D}_c$ denotes the Levi-Civitta covariant derivative on $\Sigma$ with respect to $h$.

We impose spherical symmetry taking *plane–conformal coordinates* $(r, \theta, \varphi)$ such that the line element is

$$dh^2 = \Phi^4(r)\left[dr^2 + r^2\left(d\theta^2 + \sin^2(\theta)d\varphi^2\right)\right], \tag{4}$$

where $\Phi^4$ is any conformal factor with $\Delta\Phi \leq 0$, by virtue of the first constraint equation ($\Delta$ is the *flat* laplacian operator). Note that the area radius of a $r = r_0$ surface is not $r_0$. The proper distance is

$$\ell(r) = \int_0^r \Phi^2(s)ds, \tag{5}$$

and the area radius of a 2–surface $r = r_0$ is

$$r_0^{(A)} = \Phi^2(r_0)r_0. \tag{6}$$

An integration by parts of (5) shows that $\ell \geq r^{(A)}$.

In terms of $\Phi$, let's define new *conformal quantities*

$$\tilde{\mathcal{E}}^i(\hat{r}) := \Phi^6\mathcal{E}^i(\hat{r}), \quad \tilde{\rho}(\hat{r}) := \Phi^6\rho(\hat{r}), \tag{7}$$

such that equations (3) become

$$\tilde{\mathcal{D}}_i\tilde{\mathcal{E}}^i = 4\pi\tilde{\rho}, \tag{8}$$

$$\Delta\Phi = -\frac{\tilde{\mathcal{E}}^2}{4\Phi^3}, \tag{9}$$

where $\tilde{\mathcal{D}}_c$ is the Levi-Civitta covariant derivative with respect to the *euclidean* 3–metric, and $\Delta$ is the *flat* laplacian operator. Note that $Q$ is *conformally invariant* under the transformation (7).

## 3. Main result

Let $(\Sigma, h_{ij}, K_{ij} = 0)$ be initial data that contains a sphere with plane radius $r = R$ and *constant conformal density* $\tilde{\rho}$. We want to solve equations (8) and (9) for $\Phi(r)$, with asymptotically flat condition at infinity, namely

$$\lim_{r\to\infty} \Phi(r) = 1. \tag{10}$$

Since equation (9) is non linear, it is almost impossible to find a general solution thereof. However, the manifestly elliptic character of this equation allows one to estimate the exact solution, bounding it by functions that satisfy *linear* problems. All it is possible because of the following powerful result (for more details, see Evans, 2010):

**Theorem 3.1.** *Let $\Omega$ be a bounded region and consider the problem*

$$\Delta u = f(u), \quad u|_{\partial\Omega} = g, \tag{11}$$

*where $u : \Omega \to \mathbb{R}$. Let $u_+$ be a solution of*

$$\Delta u_+ \leq f(u_+), \quad u_+|_{\partial\Omega} = g, \tag{12}$$

*and $u_-$ a solution of*

$$\Delta u_- \geq f(u_-), \quad u_-|_{\partial\Omega} = g. \tag{13}$$

*Then, there exists solution to (11) and moreover,*

$$u_- \leq u \leq u_+ \tag{14}$$

*in $\Omega$.*

The functions $u_-$ and $u_+$ are called, respectively, *subsolution* and *supersolution* of $u$.

Let $u$ be a function such that

$$\Phi = 1 + u. \tag{15}$$

Equation (9) implies that $u$ satisfies the equation

$$\Delta u = -\frac{\tilde{\mathcal{E}}^2}{4(1+u)^3}. \tag{16}$$

The conformal electric field can be computed by virtue of equation (8):

$$\tilde{\mathcal{E}}(r) = \begin{cases} \frac{4\pi\tilde{\rho}}{3} r, \ r \leq R \\ \\ \frac{4\pi\tilde{\rho}R^3}{3r^2}, \ r > R. \end{cases} \tag{17}$$

The following first result will be crucial to prove the inequality.

**Lemma 3.2.** *The function $u_-$ that satisfies the problem*

$$\Delta u_- = -\frac{\tilde{\mathcal{E}}^2}{\left(1+\frac{\pi^2}{3}\tilde{\rho}^2R^4\right)^3}, \quad \lim_{r\to\infty} u_- = 0, \tag{18}$$

*is a subsolution of $u$.*

*Proof:* Note that (18) is a *linear* problem on $u_-$. The unique smooth solution of (18) can be computed explicitly; in fact,

$$u_-(r) = \begin{cases} \frac{2\pi^2\tilde{\rho}^2}{9\left(1+\frac{\pi^2}{3}\tilde{\rho}^2R^4\right)^3}\left(\frac{3}{2}R^4 - \frac{1}{10}r^4\right), & r \le R \\ \\ \frac{16\pi^2\tilde{\rho}^2R^5}{9\left(1+\frac{\pi^2}{3}\tilde{\rho}^2R^4\right)^3 r}\left(\frac{3}{10} - \frac{R}{8r}\right), & r > R. \end{cases} \tag{19}$$

This function is monotonically decreasing and therefore

$$u_-(r) \le u_-(0) = \frac{\pi^2\tilde{\rho}^2R^4}{3\left(1+\frac{\pi^2}{3}\tilde{\rho}^2R^4\right)^3} \le \frac{\pi^2}{3}\tilde{\rho}^2R^4, \tag{20}$$

which implies that

$$\Delta u_- = -\frac{\tilde{\mathcal{E}}^2}{(1+\frac{\pi^2}{3}\tilde{\rho}^2R^4)^3} \ge -\frac{\tilde{\mathcal{E}}^2}{(1+u_-)^3}, \tag{21}$$

and finally $u_- \le u$. □

From this subsolution, we can construct explicitly a lower bound $r_-^{(A)}$ for the area radius $r^{(A)}$. In fact, defining $\Phi_- := 1 + u_-$, we have

$$r_-^{(A)} := r\Phi_-(r)^2 \le r\Phi(r)^2 = r^{(A)}. \tag{22}$$

The electric charge for $r \le R$ is $Q(r) = \frac{4}{3}\pi\tilde{\rho}r^3$. Taking the difference between $r_-^{(A)}$ and $Q$ for any $r \le R$, we obtain

$$\frac{r_-^{(A)} - Q}{r} = \frac{1}{256\left(1+\frac{3\Lambda}{16}\right)^6}\left(\frac{x^2}{5} - 3\Lambda\right)^2 + \frac{15\Lambda - x^2}{40\left(1+\frac{3\Lambda}{16}\right)^3} - x + 1, \tag{23}$$

where

$$x := \frac{4}{3}\pi\tilde{\rho}r^2, \quad \Lambda := \frac{16\pi^2}{9}\tilde{\rho}^2R^4. \tag{24}$$

Thus, that difference is a fourth order polynomial in $x$, $P_\Lambda(x) := (r_-^{(A)} - Q)/r$. Since $r \ge R$, $x$ varies from 0 to $\sqrt{\Lambda}$, implying that

$$P_\Lambda(x) \ge \frac{7\Lambda}{20\left(1+\frac{3\Lambda}{16}\right)^3} - \sqrt{\Lambda} + 1 \ge -\sqrt{\Lambda} + 1, \tag{25}$$

which is positive for all $0 \leq x \leq \sqrt{\Lambda}$ if $\sqrt{\Lambda} \leq 1$; that is, if

$$Q \leq R. \tag{26}$$

We have proved the main result of this work, enunciated in the following

**Theorem 3.3.** *Let* $(\Sigma, h_{ij})$ *be a time symmetric asymptotically flat initial data that satisfies the dominant energy condition and contains a sphere of plane radius* $R$ *with constant conformal density and total electric charge* $Q$*, such that*

$$R \geq Q. \tag{27}$$

*Then it holds the following inequality*

$$r^{(A)}(r) \geq Q(r) \tag{28}$$

*for all* $r \leq R$*.*

## 4. Comments and perspectives

We have found a relevant evidence of the validity of a universal inequality between charge and size for bodies. Remembering that $\ell \geq r^{(A)}$ and by virtue of Theorem 3.3, it also holds the inequality with the proper lenght. Since $r^{(A)} \geq r$, the hypothesis of the Theorem implies that inequality (27) holds in the boundary of the sphere. However, it is not possible to change that hypothesis; the condition $r^{(A)}(R) \geq Q(R)$ is weaker than $R \geq Q(R)$.

From this work it is possible to continue the research in order to prove the inequality in spherical symmetry, approaching both analytically and numerically.

## References

Dain, S. Jaramillo, J. & Reiris, M. 2012, Class. Quant. Grav., 29, 035013

Evans, L. 2010, "Partial Differential Equations", Graduate Students in Mathematics, Vol. 19, Second Edition, American Mathematical Society

Galloway, G. & O' Murchadha, N. 2008, Class. Quant. Grav., 25, 105009

O'Murchadha, N. 1986, Phys. Rev. Letters, 57, 19

Rubio, M. E. 2014, "Desigualdad entre carga y tamaño en Relatividad General", Facultad de Matemática, Astronomía y Física, Universidad Nacional de Córdoba

Schoen, R. & Yau, S. 1983, Commun. Math., 90, 575-579

*Gravitation, Relativistic Astrophysics and Cosmology*
*Second Argentinian-Brazilian Meeting, 2014*
*G. S. Vila, F. L. Vieyro and J. Fabris, eds.*

# Charged compact stars

Yara de Souza, Maurício O. Calvão, Beatriz B. Siffert, and Carlos Zarro

*Instituto de Física, Universidade Federal de Rio de Janeiro,*
*Caixa Postal 21945, Rio de Janeiro, Brasil*

**Abstract.** We study the equilibrium and stability of charged compact stars. In order to do so, we choose to solve numerically a system of differential equations describing the structure of charged compact objects, including the generalization of the Tolman-Oppenheimer-Volkoff equation for this class of objects. We assume a polytropic equation of state for the fluid, and for the relation between charge density and the fluid's energy density, we have assumed a more realistic relation than the linear relation usually used in the literature and compared the results with this case.

## 1. Introduction

Compact stars are the fate that awaits many stars after their lifetime. During the luminous life of the star, part of the original Hydrogen is converted in fusion reactions to heavier element. When a sufficient quantity of heavy elements is produced in the core of the star, it can collapse, and an enormous energy will be released in the explosion of the star.

The cessation of the fusion marks the end of the luminous life of the star, its duration and the final stage of the star depends on its mass. Neutron stars and black holes are the destiny of massive stars ($> 8M_\odot$) in which nuclear fusion reached the iron end point - the end point of exothermic fusion. During the collapse, high densities are attained ad the neutralization process (electron capture by protons, producing neutrons and neutrinos) is favored. Therefore neutron stars are formed mainly by degenerated neutrons, which counterbalance the gravitational inward force. They are extremely dense stars having 1 or $2M_\odot$ inside a 10 km radius [1].

For stars up to a few solar masses, nuclear fusion does not proceed all the way through iron, stopping at the CNO chain. At this stage the core will collapse, although not reaching densities high enough to initiate the neutralization reaction. The remain star will be a white dwarf, typically of 1 $M_\odot$ and radios of $\sim$ 5000 km [1]. Matter inside the white dwarf is ionized and further collapse is prevented due to degenerate electron's pressure.

In general relativity, the equations describing hydrostatic equilibrium of compact stars are known as the Tolman-Oppenheimer and Volkoff equations. A feature of these equations is that pressure appears at the same foot as energy density, so at the same time it will contribute to prevent gravitational collapse, it will also contribute to the energy density, which causes the gravitational collapse [2]. White dwarfs become unstable above the critical mass of 1.4 $M_\odot$, known as the Chandrasekhar mass, which is the limit mass for an object supported by the pressure of relativistic degenerated electrons. Meanwhile, modeling neutron stars as an ideal gas of degenerate neutrons, Oppenheimer and Volkoff found a mass limit of 0.7 $M_\odot$, which yields the maximum mass that can

be sustained against gravitational compression by the pressure of degenerated neutrons and their repulsive interaction. More realistic models can increase this limit up to $\sim 4$ $M_\odot$ [2].

The possibility that stars could actually contain a non-vanishing net charge was first pointed out by Rosseland in 1924 [3]. He modeled stars as an ideal gas of positive ions and electrons initially electrically neutral and concluded that, due to their greater thermal energy, the electrons tend to escape the star more often than the ions, and thus induce a positive charge on the star. The process will be carried on until the inward force on a free electron is equal to the inward force on a positive ion.

Rosseland [3] also showed that in a Newtonian star charge density should be proportional to mass density. In the following years this relation remained used, even for compact stars, for which general relativity should be used, see [4], [5], [6] and [7], among others.

In this work we study the equilibrium and stability of charged compact stars using a more realistic relation between the charge and energy densities than the linear relation usually assumed in the literature in order to determine if such charged objects could really exist in a stable condition in nature.

## 2. The structure of charged compact stars

### 2.1. Tolman-Oppenheimer-Volkoff equations

We follow the steps performed in [8], whose results we wanted to reproduce first. We take the line element for a spherically symmetric and static star:

$$ds^2 = e^{\nu}c^2dt^2 - e^{\lambda}dr^2 - r^2(d\theta^2 + sin^2\theta d\phi^2), \tag{1}$$

and model the matter inside as a perfect fluid plus an electromagnetic field:

$$T^{\mu}_{\nu} = (P + \varepsilon)u^{\mu}u_{\nu} - P\delta^{\mu}_{\nu} + \frac{1}{4\pi}\left(F^{\mu\alpha}F_{\alpha\mu} - \frac{1}{4}\delta^{\mu}_{\nu}F_{\alpha\beta}F^{\alpha\beta}\right), \tag{2}$$

where $P$ is the pressure, $\varepsilon$ is the energy density of the fluid.

A spherical surface of radius $r$, within the star, presents an electric field $E$:

$$E(r) = \frac{1}{\varepsilon_0 r^2}\int_0^r r'^2\rho_{ch}(r)e^{\lambda/2}dr', \tag{3}$$

and encloses an electric charge $Q$:

$$Q(r) = \int_0^r r'^2\rho_{ch}(r)e^{\lambda/2}dr', \tag{4}$$

where $\rho_{ch}$ is the star's charge density.

The star's mass inside a spherical shell of radius $r$ is then:

$$M(r) = \frac{4\pi}{c^2}\int_0^r r'^2\left(\varepsilon + \frac{\varepsilon_0 E^2}{2}\right)dr'. \tag{5}$$

Using the (00) component of Einstein's equation:

$$\frac{e^{-\lambda}}{r^2}\left(r\frac{d\lambda}{dr}-1\right)+\frac{1}{r^2}=\frac{8\pi G}{c^4}\left(\varepsilon+\frac{\varepsilon_0 E^2}{2}\right), \tag{6}$$

the four equations which describe the equilibrium of charged stars [9] turn out to be the generalized Tolman-Oppenheimer-Volkoff equation:

$$\frac{dP}{dr}=-\frac{G\left[4\pi r^3\left(\frac{P}{c^2}-\frac{\varepsilon_0 E^2}{2c^2}\right)\right](\varepsilon+P)}{c^2r^2\left(1-\frac{2GM}{c^2r}\right)}+\rho_{ch}Ee^{\lambda/2}, \tag{7}$$

and

$$\frac{dE}{dr}=-\frac{2E}{r}+\frac{\rho_{ch}e^{\lambda/2}}{\varepsilon_0}, \tag{8}$$

$$\frac{dM}{dr}=4\pi r^2\left(\frac{\varepsilon}{c^2}+\frac{\varepsilon_0 E^2}{2c^2}\right), \tag{9}$$

$$\frac{d\lambda}{dr}=\frac{8\pi G}{c^4}re^{-\lambda}\left(\frac{\varepsilon}{c^2}+\frac{\varepsilon_0 E^2}{2c^2}\right)-\left(\frac{e^{\lambda}-1}{r}\right). \tag{10}$$

Since we have 6 variables, $P, E, M, \lambda, \rho_{ch}$ and $\varepsilon$, and only 4 equations, we need two other equations in order to solve the system of eqs. (7)-(10). One of them is the relation between the charge density $\rho_{ch}$ and the fluid energy density $\varepsilon$ and comes from the hypothesis that the star is more sorely charged in its exterior shells than in its center:

$$\rho_{ch}=f/\varepsilon, \qquad f=\text{const.} \tag{11}$$

Following the steps of [8], we see that the effects in the structure of the star due to the presence of charge begin to be notable for $f\sim 3\times 10^{-4}$ $(\text{MeV/fm}^3)^{1/2}$/km. We use this value, which was calculated for the linear case, also for the inverse relation so we can compare them.

The other missing equation will be a polytropic equation of state, that is, a simple equation of state such as $p=K\varepsilon^{\Gamma}$. A star having such equation of state is called a polytrope.

### 2.2. Matter inside the star

We model the interior of the neutron star as a non relativistic degenerate ideal Fermi gas of nuclei and electrons.

The assumption of degeneracy (all quantum states up to a given energy occupied) is valid for low temperatures $T$ - much less than the Fermi energy $E_F$.

$$T\ll E_F=\sqrt{k_F^2+m_e^2}, \tag{12}$$

where we have set $\hbar=1=c$, then $k_F$ is the Fermi momentum and $m_e$ is the electron mass.

To obtain the equation of state we need an expression for the pressure $p$ (in SI units),

$$p(k_F) = \frac{8\pi}{3c(2\pi\hbar)^3}\int_0^{k_F}(k^2c^2+m_e^2c^4)^{-1/2}k^4dk. \quad (13)$$

Considering the non relativistic limit, where $k_F \ll m_e$:

$$\begin{aligned} p(k_F) &= \frac{m_e^4c^5}{3\pi^2\hbar^3}\int_0^{k_F/m_ec} u^4du \\ &= \frac{m_e^4c^5}{15\pi^2\hbar^3}(k_F/m_ec)^5 \\ &= \frac{\hbar^2}{15\pi^2m_e}\left(\frac{3\pi^2Z\rho}{Am_N}\right)^{5/3}. \end{aligned}$$

Thus, using Einstein's equation from special relativity $\varepsilon(r) = \rho(r)c^2$ , the pressure yields:

$$p(k_F) \approx K_{nonrel}\varepsilon^{5/3}, \quad (14)$$

where:

$$K_{nonrel} = \frac{\hbar^2}{15\pi^2m_e}\left(\frac{3\pi^2Z}{Am_Nc^2}\right)^{5/3}. \quad (15)$$

We see that the non relativistic Fermi gas gives a polytropic equation of state with $\Gamma = 5/3$ [10].

The value of the constant $K_{nonrel}$ depends on the type of ions of which the star is formed. We follow the steps of [9] and choose $K_{nonrel} = 0.05$ fm$^{8/3}$ ($c = 1 = \hbar$).

Equation (14) is the second missing equation, now we can proceed to solve numerically the system of eqs. (7)-(10), (11) and (14).

## 3. Results

We solve this system with the following boundary conditions:

$$\begin{aligned} E(r=0) &= 0, \qquad M(r=0) = 0, \\ \lambda(r=0) &= 0, \qquad P(r=0) = P_c. \end{aligned} \quad (16)$$

The equations are to be integrated from the center of the star, $r = 0$, to the point where $P = 0$. Zero pressure can support no overlying material against the gravitational attraction exerted on it from the mass within and so marks the edge of the star. The point $R$ where the pressure vanishes is therefore the radius of the star and $M(R)$ its gravitational mass.

Figures 1 and 2 show the total mass against the radius obtained for stars with both cases of charge distribution studied and a fixed value for $f$. It can be observed that in both cases there is a maximum mass as expected and both are $\sim 1.4M_\odot$.

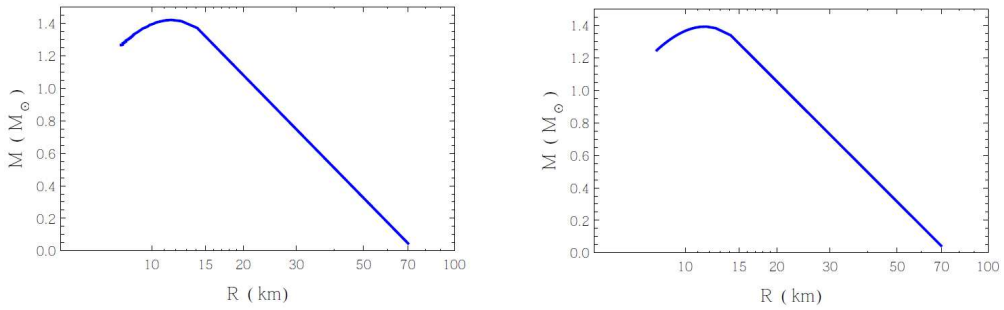


Figure 1. Total mass × total radius for stars with a linear relation (left) and a more realistic relation (right) between charge density and energy density, such as: $\rho_{ch} = f\varepsilon$ (left) and $\rho_{ch} = f/\varepsilon$ (right).

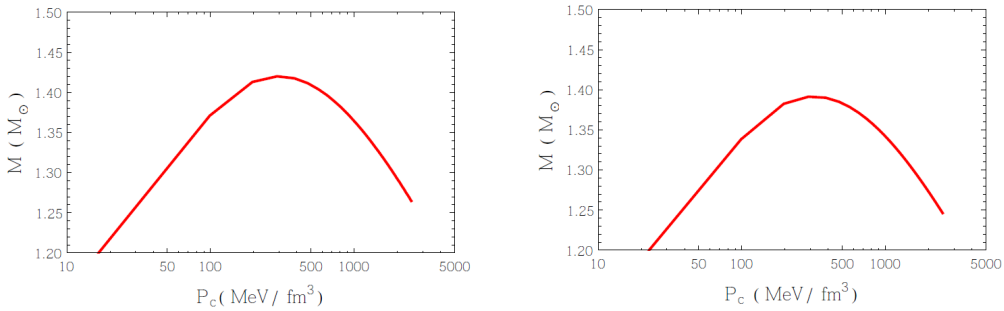


Figure 2. Total mass ×central pressure for stars with a linear relation (left) and a more realistic relation (right) between charge density and energy density, such as: $\rho_{ch} = f\varepsilon$ (left) and $\rho_{ch} = f/\varepsilon$ (right).

The solutions of eqs. (7)-(10) are configurations in hydrostatic equilibrium however equilibrium does not assure stability. A necessary condition for stability is that the central density of the star must increase along with its mass, thus:

$$\frac{\partial M(\varepsilon_c, f)}{\partial \varepsilon_c} > 0 \tag{17}$$

Figures 3 and 4 show the total mass of stars as a function of their central pressure for both cases of charged distribution. As well as in Figures 1 and 2, there is a maximum value for the mass of the star above which there are no stable configurations, thus the stable region ends at the mass limit.

## 4. Conclusions

We verified the existence of an upper mass limit for hydrostatic equilibrium, and little dependence of the total mass achieved with the charge distribution of the star for Figures

1 and 2 and Figures 3 and 4 are extremely similar, the only substantial difference being that stars with a linear relation between charge density and energy density achieve a slightly greater mass. We also showed it is possible to obtain stable configurations using the inverse relation between the charge density and the energy density of the star.

We want to investigate the stability and equilibrium conditions for more realistic models for distributions of charge inside compact stars.

## References

[1] Glendenning, N. K. 2000, "Compact Stars: Nuclear Physics, Particle Physics and General Relativity, 2nd ed.", Springer Verlag, New York, USA

[2] Bekenstein, J. D. 1971, Phys. Rev. D, 4

[3] Rosseland, S. 1924, MNRAS, 84, 720

[4] Zhang, J. L., Chau, W. Y. & Deng, T.Y. 1982, Ap&SS, 88, 81-88

[5] Cabanell, I. 1983, Ap&SS, 94

[6] Ghezzi, C. R. 2005, Phys. Rev. D, 72

[7] Mirza, B. 2008, IJMPD, 17

[8] Siffert, B. B., de Mello Neto, J. R. T. & Calvão, M. O. 2007, Braz. J. Phys., 37, 609

[9] Ray, S., Espíndola, A. L., Malheiro, M., Lemos, J. P. S. & Zanchin, V. T. 2003, Phys. Rev. D, 68, 084004

[10] Silbar, R. R. & Reddy, S. 2004, Am. J. Phys., 72, 892

[11] Bazin, M., Schiffer, M. & Adler, R. 1965, "Introduction to General Relativity", McGraw-Hill

*Gravitation, Relativistic Astrophysics and Cosmology*
*Second Argentinian-Brazilian Meeting, 2014*
*G. S. Vila, F. L. Vieyro and J. Fabris, eds.*

# Galaxy evolution studies from space and ground based large IR/sub-mm surveys

Luigi Spinoglio

*Istituto di Astrofisica e Planetologia Spaziali, INAF, Via Fosso del Cavaliere 100, 00133 Roma, Italy*

**Abstract.** Large spectroscopic surveys in the IR and submillimeter are crucial to study large scale processes such as the evolution of galaxies through the coevolution of the processes of star formation in the host galaxies and black hole accretion in active galactic nuclei. The mid-to-far-IR is where most energy is emitted by the dust obscured processes of star formation and black hole accretion. To unravel such processes along the history of galaxies and establish their role along evolution, rest frame mid-to-far IR spectroscopy is needed, because at these frequencies dust extinction is at its minimum and a variety of atomic and molecular transitions, tracing most astrophysical domains, occur. Future IR space telescopes, such as the SPace Infrared telescope for Cosmology and Astrophysics (SPICA), and ground-based large submillimeter telescopes, such as the Cerro Chajnantor Atacama Telescope (CCAT), will be able to perform such surveys in a synergic way.

## 1. Introduction

The strong correlation in the local Universe between central black hole mass and stellar velocity dispersion of the galactic bulge (the "Magorrian Plot", Magorrian et al. 1998; Ferrarese & Merrit, 2000) implies a strong physical relation between black hole accretion in Active Galactic Nuclei (AGN) and star formation (SF). On a cosmic scale, the evolution of supermassive black holes (SMBHs) appears tied to the evolution of the star-formation rate (SFR) (Marconi et al. 2004; Merloni 2004). In Fig.1 it is shown that the shape of the star formation rate density as a function of redshift (e.g. Burgarella et al. 2013) is similar to the shape of the black hole accretion density (e.g. Delvecchio et al. 2014). Heckman et al. (2004) made a study of 23,000 low-redshift narrow emission-line AGNs of the Sloan Survey, suggesting that the growth of black holes through *accretion* and the growth of bulges through *star formation* are related at the present time in the same way that they have been related, on average, throughout cosmic history.

One of the major goals of the cosmological studies of galaxy evolution is to understand the full cosmic history of energy generation by stars (through fusion processes) and black holes (through accretion of matter). This history is traced not only by high luminosity objects, i.e. the quasars, but mainly by low to intermediate luminosity galaxies, such as those objects corresponding to Seyfert galaxies in the local Universe, which dominate at the "knee" of the Luminosity Function. The importance of measuring these energy production rates lies also in the fact that they provide a measure of the built up of the mass of the central black hole, on one side, and of galactic stars, on the other side, and their integral over cosmic times must —ultimately— be consistent with the observed galaxy and black hole masses. This will lead us to understand the inter-relation

of quasar activity and star formation, and ultimately the key processes responsible for shaping the mass and luminosity functions of galaxies.

Optical continuum measurements alone are completely inadequate to obtain these data and even optical spectroscopy on a massive scale cannot yield definitive answers because dust reddening may block our view at short wavelengths. What is needed therefore is spectroscopy at longer rest wavelengths to uncover how much of this emission is partly or heavily extinguished.

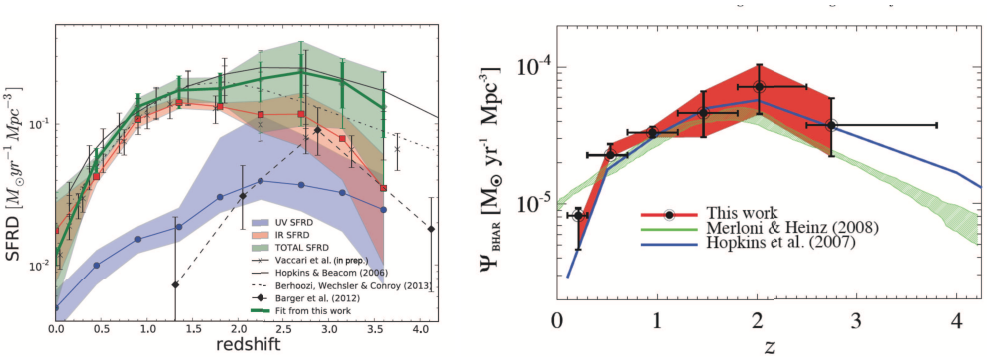


Figure 1. *Left: (a)* Star Formation Rate Density (SFRD) from IR and UV observations (Bulgarella et al. 2013). The UV determination of the SFRD is about a factor ten lower than the IR SFRD, demonstrating that IR observations are essential in the redshift range $0 < z < 3$. *Right: (b)* Black Hole Accretion Rate Density (Delvecchio et al. 2014)

## 2. Rest-frame mid-IR spectroscopy to study galaxy evolution

### 2.1. Comparing different techniques and regimes for separating AGN and SF

We want to compare in this section the various techniques to detect and separate the AGN and SF component in galaxies. There are many different criteria that can be used to distinguish AGN and SF, but there are limits and potentialities of the different observational techniques:

- UV/Optical (consider, e.g. the "BTP" classification based on optical spectra, proposed by Baldwin, Phillips & Terlevich, 1981) and even near-IR observations are able to measure the galaxy morphology and the spectra, however they seriously suffer from dust obscuration. As an example, Fig.1(a) shows that the UV measurements of the star formation rate density (SFRD) as a function of redshift is missing 90% of the SFRD observed in the IR.

- X-ray observations are good tracers of AGN, however only weak X-ray emission can be detected from star formation and, even more importantly, heavily-obscured AGN (Compton-thick) are completely lost.

- Radio observations (with planned facilities like EVLA,[1] SKA[2]) can detect AGN and SF to large redshift and can see through gas and dust, they can measure morphology and spectral energy distributions (SED), detect polarization and variability, which are signatures of AGN, however not always redshifts can be measured. At its highest frequencies, SKA could be able to measure redshifted molecular lines in the ISM of galaxies.

- mm/submm observations (e.g. ALMA,[3] CCAT[4]) will provide information on SF from spectral features (redshifted CO, [CII], etc.), however no clear AGN tracers are available at the longest far-IR/submillimeter wavelengths. From the results of recent *Herschel* observations, it has been shown that the high-J CO lines spectral line energy distributions (SLED) could in principle distinguish between photodissociation regions, originated in SF environments, and X-ray Dominated Regions (XDR), excited by AGN. However, the presence of shocks and mechanical energy originated by supernovae makes the interpretation of the CO SLED uncertain (see, e.g. van der Werf et al. 2010, Rangwala et al. 2011, Spinoglio et al. 2012a, Meijerink et al. 2013).

- Rest-frame mid-IR/far-IR imaging spectroscopy can provide a complete view of galaxy evolution by measuring the role of AGN and SF because (provided that large field of view and high sensitivity can be reached) it can trace simultaneously both SF and AGN, measure redshifts and see through large amounts of dust. It seems therefore to be the most promising technique.

### 2.2. The power of infrared spectroscopy

Figure 2(a) shows how well the IR fine structure lines cover the density-ionisation parameter space which characterises the photoionised and photon dissociated gas (Spinoglio & Malkan 1992). A combination of these lines and line ratios can trace both star formation and black hole accretion. The long wavelengths of these lines, ranging from the far-IR for the photodissociation and HII region lines through the mid-IR for the AGN lines, to the near-IR for the coronal lines, ensure that we can observe these different tracers by minimising the effect of dust extinction.

The rich rest-frame mid-IR spectra, that have been observed in active and starburst galaxies in the local Universe with the mid-IR spectrometer *IRS* (Houck et al. 2004) onboard the *Spitzer* satellite (Werner et al. 2004) can be observed in the far-IR in the redshift range of $0.4 < z < 3.0$. Figure 2(b) shows the average *Spitzer IRS* high-resolution mid-IR spectra (Tommasin et al. 2010) of subclasses of Seyfert galaxies from the 12$\mu$m Seyfert galaxy sample of Rush, Malkan & Spinoglio (1993). For comparison, we also show the average spectrum of starburst galaxies (Bernard-Salas et al. 2009). The quality of the data is very high and shows the many features that can distinguish between AGN and star formation processes, such as the high-ionisation lines from [NeV] at 14.3$\mu$m and 24.3$\mu$m, originated exclusively from AGN, or the 11.2$\mu$m PAH feature

[1]EVLA is the Expanded Very Large Array radio telescope: http://www.aoc.nrao.edu/evla/

[2]SKA is the Square Kilometre Array radio telescope: https://www.skatelescope.org/

[3]ALMA is the Atacama Large Millimeter/submillimeter Array: www.almaobservatory.org/

[4]CCAT is the Cerro Chajnantor Atacama Telescope: www.ccatobservatory.org/

and the low ionisation lines from [NeII] and [SIII], typical of HII and star forming regions. Mid-/far-IR imaging spectroscopy is therefore able to trace galaxy evolution throughout cosmic times in an unbiased way by minimising dust extinction.

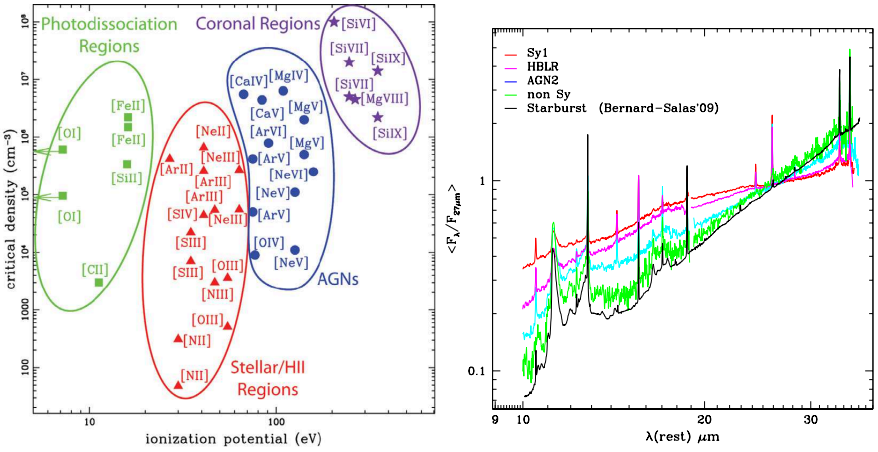


Figure 2. *Left: (a)* The IR fine-structure lines cover a large volume of the physical parameters characterising the gas: critical density of each transition as a function of its ionisation potential (Spinoglio & Malkan 1992) *Right: (b)* Mid-IR spectra of active and starburst galaxies from the *Spitzer* Space Telescope (Tommasin et al. 2010).

## 3. Spectroscopic cosmological surveys in the rest-frame infrared

Due both to the atmospheric absorption, which leaves open only a few sparse windows in the near- and mid-IR, and to the high thermal background at room temperature at IR wavelengths, it has soon been realised that, to be successful, infrared astronomy had to be done from space telescopes, as it was demonstrated by the success of the various space missions, from *IRAS* (Neugebauer et al. 1984) to *Herschel* (Pilbratt et al. 2010). However, the poor sensitivity and multiplexing power of the spectrographs of these spacecrafts have limited the observations to only a few samples of distant galaxies (e.g., Yan et al. 2007; Menéndez-Delmestre et al. 2009; Sturm et al. 2010). Substantial progress in studying galaxy evolution therefore can only be achieved by using direct mid- to far-IR spectroscopic surveys, which will provide measured (rather than estimated) redshifts and also unambiguously characterise the detected sources, by measuring the AGN and starburst contributions to their bolometric luminosities over a wide range of cosmological epochs, through their spectroscopic signatures.

SPICA (Nakagawa et al. 2011) will be the next-generation, space infrared observatory, which, for the first time, will contain a large (3.2-meter) actively cooled telescope (down to 6K), providing an extremely low background environment. With its instrument suite, SPICA will provide not only high spatial resolution and unprecedented sensitivity in mid- and far-infrared imaging, but especially large field medium spectral resolution imaging spectroscopy. These characteristics put SPICA among the best planned facilities to perform spectroscopic cosmological surveys in the mid- to

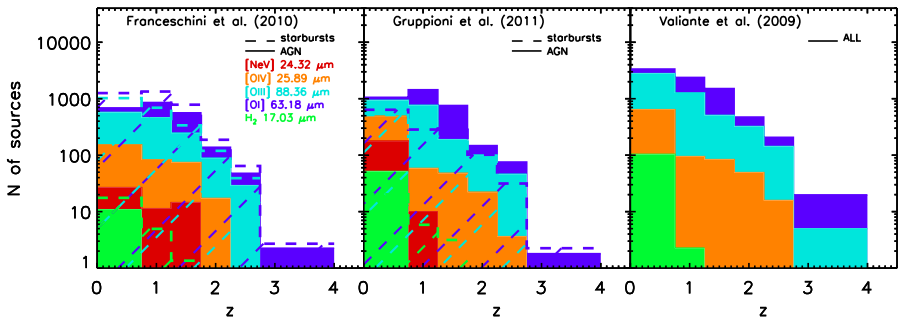


Figure 3. Predictions of starburst galaxies and AGN detections as a function of redshift, per spectral line and object type. AGN are shown as continuum lines, starburst galaxies as dashed lines. The survey covers 0.5 deg$^2$ of sky, requesting 450 hours of total time with SAFARI-SPICA (Spinoglio et al. 2012b).

far-IR. Using theoretical models for galaxy formation and evolution constrained by the luminosity functions observed with both *Spitzer* and *Herschel* and the relations between line and continuum far-IR luminosity, as measured in the local Universe for active and starburst galaxies, Spinoglio et al. (2012b) have predicted the intensities of key lines able to trace AGN and star formation activity as a function of redshift.

Figure 3 compares three models showing the number of galaxies that can be detected by the far-IR spectrometer SAFARI (Roelfsema et al. 2012) an FTS with a $2' \times 2'$ field of view, planned to be onboard of SPICA, in each spectral line for the two different populations of AGN- and starburst-dominated galaxies. The total numbers of detectable objects agree, taking the different models, to within a factor of 2-3 for most lines and z ranges. At least a thousand galaxies will be simultaneously detected in four lines at $5\sigma$ over a half square degree. A survey of the given assumptions will lead to the detection of bright lines (e.g., [O I] and [O III]) and PAH features in about one thousand of galaxies at $z > 1$. About one hundred of $z > 1$ AGN will be detected in the [O IV] line, and about ten of $z > 1$ sources will be detected in [Ne V] and $H_2$.

On the other hand, the Cerro Chajnantor Atacama Telescope (CCAT) (Sebring et al. 2010) will be complementary to SPICA, being able to observe the [OIII]88$\mu$m line at $z > 1.3$, where this line leaves the SAFARI spectral range. CCAT will be very efficient for studies of [CII], an important coolant of the interstellar medium, at all $z < 5$. Just within the range $3 < z < 4$, it will detect more than 300 galaxies at $5\sigma$ level in a 0.5 deg$^2$ survey (Spinoglio et al. 2012b).

## 4. Conclusions

We summarise this work with these points:

- After many decades of efforts, we are close to having reliable measures of SF rate and AGN accretion power, through MIR/FIR spectroscopic surveys, unaffected by dust.

- Accurately measuring the star formation rate and the AGN accretion power is the first step towards understanding galaxy evolution over cosmic history.
- FIR spectroscopic surveys with SPICA will physically measure galaxy evolution.
- Given the expected sensitivity of SAFARI ~$2.5\times10^{-19}$ W/m$^2$ ($5\sigma$,1 hr.) thousands of sources will be detected in more than 4 lines in typical 0.5 deg$^2$ surveys (t=450 h).
- Complementary to SAFARI, CCAT will detect several hundreds of galaxies at R~1000 in a 0.5 deg$^2$ survey in 4.5 hours in [OIII]88$\mu$m and thousands of galaxies in [CII]158$\mu$m.
- These surveys will clarify the inter-relation between quasar activity and star formation, which of the two processes influence the other and ultimately will test the processes able to shape the mass and luminosity functions of galaxies.

## References

Baldwin, J. D., Phillips, M. M. & Terlevich, R. 1981, PASP, 93, 5
Bernard-Salas, J. et al. 2009, ApJS, 184, 230
Burgarella, D. et al. 2013, A&A, 554, A70
Delvecchio, I. et al. 2014, MNRAS, 439, 2736
Ferrarese, L. & Merrit, D. 2000, ApJ, 539 L9
Heckman, T. M. et al. 2004, ApJ, 613, 109
Houck, J. R. et al. 2004, ApJS, 154, 18
Magorrian, J. et al. 1998, AJ, 115, 2285
Marconi, A. et al. 2004, MNRAS, 351, 169
Meijerink, R. et al. 2013, ApJ, 762, L16
Menéndez-Delmestre, K. et al. 2009, ApJ 699, 667
Merloni, A. 2004, MNRAS, 353, 1035
Nakagawa, T. et al. 2011, SPIE, 8442, 84420O
Neugebauer, G. et al. 1984, ApJ, 278, L1
Pilbratt, G. L. 2010, A&A, 518, L1
Rangwala, N. et al. 2011, ApJ, 743, 94
Roelfsema, P. et al. 2012, SPIE, 8442, 84420R
Rush, B., Malkan M. A. & Spinoglio, L. 1993, ApJS, 89, 1
Sebring, T. et al. 2010, SPIE, 7733, 77331X
Spinoglio, L. & Malkan, M.A. 1992, ApJ, 399, 504
Spinoglio, L. et al. 2012a, ApJ, 758, 108
Spinoglio, L. et al. 2012b, ApJ, 745, 171
Sturm, E. et al. 2010, A&A, 518, L36
Tommasin, S. et al. 2010, ApJ, 709, 1257
van der Werf, P. P. et al. 2010, A&A, 518, L42

Werner, M. W. et al. 2004, ApJS, 154, 1
Yan, L. et al. 2007, ApJ, 658, 778

*Gravitation, Relativistic Astrophysics and Cosmology*
*Second Argentinian-Brazilian Meeting, 2014*
*G. S. Vila, F. L. Vieyro and J. Fabris, eds.*

# Cosmological application of the geometric scalar theory of gravity

J. D. Toniato,[1] M. Novello,[1] E. Bittencourt,[2] and U. Moschella[3]

[1]*Centro Brasileiro de Pesquisas FÃŋsicas, Rio de Janeiro, Brazil*
[2]*UniversitÃă di Roma La Sapienza, Rome, Italy*
[3]*UniversitÃă degli Studi dell'Insubria, Como, Italy*

**Abstract.** We present the main properties of the behaviour of the universe in the framework of the recent proposal of a geometric theory of gravity (GSG) based on a single scalar field. Interesting distinctions from general relativity (GR) appear when developing cosmological models in this new theory. In GSG, flatness, accelerated expansion and the initial singularity of the universe, three important issues surrounding the current standard cosmology, are overcome without making use of any exotic fluid.

## 1. Introduction

Throughout the last century General Relativity has become the paradigmatic scheme for the study and the description of gravitational phenomena. Although its success has been very impressive, many alternative proposals have been set forward in recent years that try to modify GR in several respects, in particular to get around the need of introducing dark matter and dark energy which represent substances unknown at the laboratory scale. Most of the proposed modifications occur in the realm of cosmology where the intensity of the gravitational field is strong enough to excite new phenomena not contemplated by GR. However because of the highly paradigmatic status of GR only a narrow set of possible modifications of this theory has been discussed up to date. A typical example consists in replacing the scalar curvature $R$ in the Einstein-Hilbert action with a somehow arbitrary function $F(R)$.

This is not the road that one should follow according to Mach's epistemological critique. Following Mach, the natural way to undertake a deep modification of a paradigmatic theory is to return to the main ideas of its primordial phase, re-examine its foundations and its evolutionary way to become paradigmatic in a historical context. Although this does not guarantee success to the new proposal, this thinking can lead us to find a really alternative physical description to the previous model. GR itself arose from deep conceptual changes existing in Newton's universal gravitation and it represented a revolution in theoretical physics.

After the advent of special relativity it was thought that the incorporation of the gravitation to the relativistic concept would naturally occur by substituting the Newtonian three-dimensional potential by a scalar function defined in the Minkowski spacetime. However, the proposals by Nordström, Einstein, Grossmann and others, along this line, were not successful. The previous scalar theories showed to be problematic for two main properties that they own, the source of the gravitational potential is the trace of the energy-momentum tensor and the gravitational metric is conformally flat.

This scenario changed when it was shown that is possible to establish a geometrical description of the gravitational phenomena, as in GR, from a single scalar field. The so called Geometric Scalar Gravity (GSG) follows the main idea of general relativity and assume as an *a priori* that gravity is described by a Lorentzian geometry. In general relativity the ten components of the metric tensor are the basic variables of the theory (up to diffeomorphism invariance). Here the metric tensor is determined by the derivatives of a fundamental independent physical quantity represented by the scalar field $\Phi$. This means that although we make use of a scalar field to represent all gravitational processes we do not follow the previous examples of scalar gravity.

GSG is not only in complete agreement with the solar system observations (see references) but also provides a new theoretical tool to inquiry of gravitational systems that will enable us to have a different look to unanswered questions in the area. In this study, in particular, we develop a cosmological model in accordance what we know about the universe today. We will see how GSG naturally overcomes some main existing difficulties in the standard cosmology: flatness, accelerated expansion and initial singularity.

## 2. Geometric Scalar Gravity: a short summary

The main difference between GSG and the ancient scalar theories is that the gravitational potential $\Phi$ only interacts with all kind of matter and energy trough the metric structure,

$$q^{\mu\nu} = \alpha\, \eta^{\mu\nu} + \frac{\beta}{w}\, \partial^{\mu}\Phi\, \partial^{\nu}\Phi, \tag{1}$$

where $\partial_{\mu} \equiv \partial/\partial x^{\mu}$ , $w = \eta^{\mu\nu}\partial_{\mu}\Phi\, \partial_{\nu}\Phi$ and the coefficients $\alpha$ and $\beta$ are fixed as

$$\alpha = e^{-2\Phi}, \qquad \beta = \frac{(\alpha-1)(\alpha-9)}{4}. \tag{2}$$

In GSG the metric is not a fundamental independent quantity but a function of the scalar field $\Phi$. The latter is assumed to satisfy the following equation,

$$\sqrt{V}\, \Box\Phi = \kappa\, \chi, \tag{3}$$

with,

$$V = \alpha + \beta = \frac{(3-\alpha)^2}{4\alpha^3}, \tag{4}$$

and the $\Box$ is the d'Alembert operator construct with the gravitational metric of Eq. (1). The source of the gravitational field, at the r.h.s. of the dynamical equation, is constructed out of the following expressions:

$$E = \frac{1}{\Omega}\, T^{\mu\nu}\, \partial_{\mu}\Phi\, \partial_{\nu}\Phi \tag{5}$$

$$C^{\lambda} = \frac{\beta}{\alpha\Omega}\left(T^{\lambda\mu} - E q^{\lambda\mu}\right) \partial_{\mu}\Phi \tag{6}$$

$$\chi = \frac{1}{2}\,(E - T) - \frac{\alpha}{\alpha - 3}\, E - \frac{1}{2} C^{\lambda}{}_{;\lambda} \tag{7}$$

where $T = q^{\mu\nu}T_{\mu\nu}$ and $\Omega = q^{\mu\nu}\partial_{\mu}\Phi\, \partial_{\nu}\Phi$. For more details about this formulation we strongly suggest to read the original paper indicated in the references.

## 3. Cosmology

To construct a homogeneous and isotropic geometry for the universe we impose the scalar field will have temporal dependence only,

$$\Phi = \Phi(T)\,, \tag{8}$$

in the coordinate system $x^\mu = (T, x, y, z)$ , where the auxiliary Minkowski metric has its diagonal form $\eta_{\mu\nu} = \mathrm{diag}(1, -1, -1, -1)$ . The non-null coefficients of the gravitational metric are

$$q^{00} = \alpha + \beta, \qquad q^{11} = q^{22} = q^{33} = -\alpha, \tag{9}$$

where $\alpha = \alpha(T)$ and $\beta = \beta(T)$. Then the line element takes the form

$$ds^2 = \frac{1}{\alpha+\beta}\,dT^2 - \frac{1}{\alpha}\,(dx^2 + dy^2 + dz^2), \tag{10}$$

that can be written as,

$$ds^2 = dt^2 - a(t)^2\,(dx^2 + dy^2 + dz^2), \tag{11}$$

with $\alpha \equiv 1/a^2$ and $dt = dT/\sqrt{\alpha+\beta}$. This line element characterizes a geometry that is spatially homogeneous and isotropic. As occurs in GR, $t$ is the cosmological time and the function $a(t)$ is the scale factor of the universe. Note that homogeneity of the scalar field imposes isotropy in the metric which has a non curve spatial section. Therefore, the flatness problem does not even exist in the cosmology of GSG.

Using this configuration, the left-hand side of the dynamical equation (3) for the gravitational field becomes

$$\sqrt{V}\,\Box\Phi = \pm\,\frac{a}{2}\,(3a^2 - 1)\left(\frac{\ddot{a}}{a} + 2\,\frac{\dot{a}^2}{a^2}\right), \tag{12}$$

where $\dot{X} = dX/dt$. The $\pm$ sign appears in order to maintain the positivity of the $\sqrt{V}$ function, which is directly related to the determinant of the metric $q_{\mu\nu}$, namely,

$$\sqrt{-q} = \frac{\sqrt{-\eta}}{\alpha^3\,\sqrt{V}}\,, \tag{13}$$

Thus, the cosmological model of GSG provides two distinct solutions to describe the evolution of the universe. When $0 \le 3a^2 < 1$ we consider the negative sign in the Eq. (12) and, when $3a^2 > 1$ , we consider the positive sign. Since the first one seems to be a not very probable scenario (limited scale factor), we will explore here only the second solution.

The r.h.s. of the dynamical equation concerns the quantity $\chi$ which is determined by the definitions made in the previous section,

$$\chi = -\frac{1}{2}\left[T + \left(\frac{1+3a^2}{1-3a^2}\right)E + C^{\lambda}{}_{;\lambda}\right]. \tag{14}$$

Since $\partial_\mu\Phi = \sqrt{\Omega}\;\delta^0_\mu$ it follows that $E = T^{00}$ and therefore

$$C^{0} = 0\,, \qquad C^{i} = \frac{\beta}{\alpha\sqrt{\Omega}}\,T^{i0}\,. \tag{15}$$

Because the gravitational field depends only on $t$, it is natural to expect that all the relevant quantities have only temporal dependence too. In principle it could be possible that some quantities like the heat flux depend also on the spatial coordinates provided that $C^{i}_{\ ;i}$ is function of $t$ alone. For the sake of simplicity we proceed here with the hypothesis that the components of the energy-momentum tensor depends only on time. The divergence of $C^{\lambda}$ vanishes and equation (3) reads

$$a(3a^2-1)\left(\frac{\ddot{a}}{a}+2\frac{\dot{a}^2}{a^2}\right)=\kappa\left[3p+\left(\frac{2\rho}{3a^2-1}\right)\right]. \tag{16}$$

For a barotropic perfect fluid $p=\lambda\,\rho$, with $\lambda$ being a constant, and the conservation of the energy-momentum tensor implies

$$\rho=\rho_0\,a^{-3(1+\lambda)}, \qquad \rho_0\equiv\text{constant}. \tag{17}$$

Thus, the cosmological equation becomes

$$a\left(\frac{\ddot{a}}{a}+2\,\frac{\dot{a}^2}{a^2}\right)=\kappa\,\rho_0\,\frac{(2-3\lambda+9\lambda\,a^2)}{a^{3(3+\lambda)}(3a^2-1)^2} \tag{18}$$

always with the condition $3a^{-2}>1$. This expression can be readily integrated yielding

$$\dot{a}^2=\frac{M}{a^4}-2\kappa\rho_0\,\frac{a^{-2-3\lambda}}{(3\,a^2-1)}, \tag{19}$$

where $M$ is an integration constant. As it should be expected, the above expressions are singular at $3a^2=1$. However this value is unattainable because the square of the velocity becomes zero at a minimal value $a_m$ strictly grater than $1/\sqrt{3}$. At that point the universe bounces.

The possibility of having a bouncing for standard fluids is quite remarkable. In FLRW cosmology the bouncing is possible either by non-minimal coupling with matter fields or by negative pressures. In GSG the situation is different: the universe always bounces.

### 3.1. Pressureless matter

Let us discuss the case of dust ($\lambda=0$) in some detail. First, the constant $M$ has to satisfy the bound $M>2\kappa\rho_0/3$ for the universe to exist ($\dot{a}^2>0$). As said before, it is easily verified that the universe bounces at the point,

$$a_m=\sqrt{\frac{1}{3}\left(1-\frac{2\kappa\rho_0}{3M}\right)^{-1}}, \qquad \dot{a}_m=0, \ \text{ and } \ \ddot{a}_m>0\,. \tag{20}$$

It is possible to construct a phase diagram that shows the behaviour of the universe. Rewriting the dynamical equation considering two independent variables, the Hubble parameter $=\dot{a}/a$ and the scale factor, we set the system of differential equations,

$$\dot{a}=H(t)\,a(t)\,, \tag{21}$$

$$\dot{H}=-3\,H(t)^2+\tfrac{2}{a(t)^4(3\,a(t)^2-1)^2}\,. \tag{22}$$

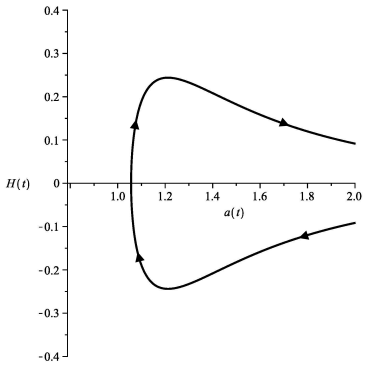


Figure 1. Phase diagram for an universe filled with pressureless matter. We consider $M = 0.9\kappa\rho_0$ .

Figure 1 shows that the universe starts collapsing from the infinity, reach the minimum value of the scale factor and expands to the infinity again. Since $a_m$ represents a minimum for the scale factor, we see that dust generates an regime of accelerated expansion for the universe.

Fluids with positive $\lambda$ (including radiation) have a similar behaviour. They all have a bounce, followed by an early accelerated phase and a final decelerated phase. The expansion last forever. At late times, they all share the same behaviour with

$$a(t) \sim t^{1/3} \tag{23}$$

irrespective of the value of $\lambda$.

### 3.2. Negative pressure

When the pressure is negative, i.e. for $\lambda < 0$, there exist static cosmological solutions of Eq. (18):

$$a_0 = \sqrt{\frac{1}{3} - \frac{2}{9\lambda}} > \frac{1}{\sqrt{3}} \tag{24}$$

so that

$$M_\lambda = 3|\lambda|\kappa\rho_0 \left(\frac{1}{3} + \frac{2}{9|\lambda|}\right)^{1+\frac{3}{2|\lambda|}} \tag{25}$$

Note that this is the minimal possible value of the constant $M$ relative to the equation of state $\lambda$ (below this value $\dot{a}^2$ would be negative for all $a$). For any choice $M > M_\lambda$ there are two values where $\dot{a} = 0$. Since the acceleration is positive for $a = a_{min}$ and negative for $a = a_{max}$ the latter are inversion points and the universe eternally oscillates between a minimal and a maximal value of the cosmic scale factor $a_{min} \leq a \leq a_{max}$ .

## 4. Conclusions

We develop a cosmological model using the new born geometric scalar theory of gravity. Initially the theory forecasts two solutions for its dynamical equation due to the shape

of the $V$ function. These solutions are unconnected, in other words, one must work with only one of them in order to describe the universe. In this sense, the non limited solution ($3a^2 > 1$) is the one which is more realistic and it was explored in this work.

The first results highlight several distinct behaviours of the standard FLRW cosmology, among which stands out the fact that the scale factor is not singular and has an accelerated expansion phase for usual fluids like radiation or non relativistic matter.

Important to recall that GSG is newly born and its properties and solutions are largely yet unknown. For instance, we still did not analyze completely the problem of structures formation observed in the universe. Any alternative theory of gravity should be able to enclose an explanation for that phenomenon. We hope that this work can at least stimulate a regain of interest and thinking about scalar theories of gravity.

## References

Norton, J. D. 1992, Archive for History of Exact Science, 45, 17-94

Novello, M., Bittencourt, E., Moschella, U., Goulart, E., Salim, J. M. & Toniato, J. D. 2013, J. Cosmol. Astropart. Phys., 06, 014

Renn, J. & Sauer, T. 2007, "Pathways out of classical physics - Einstein's double strategy in his search for the gravitational field equations", in The genesis of General Relativity, J. Renn (ed.), Vol 1, Springer, Dordrecht, http://www.hss.caltech.edu/ tilman/Pathways.pdf

Ryden, B. 2003, "Introduction to Cosmology", Addison-Wesley, San Francisco

*Gravitation, Relativistic Astrophysics and Cosmology*
*Second Argentinian-Brazilian Meeting, 2014*
*G. S. Vila, F. L. Vieyro and J. Fabris, eds.*

# Exploring non-linear cosmological matter diffusion coefficients

Hermano Velten[1] and Simone Calogero[2]

[1]*Departamento de Física, Universidade Federal do Espírito Santo (UFES), Av. Fernando Ferrari, Campus Goiabeiras, Vitória, Brazil*
[2]*Mathematical Sciences, Chalmers University of Technology, Gothenburg University, S-412 96 Gothenburg*

**Abstract.** Since microscopic velocity diffusion can be incorporated into general relativity in a consistent way, we study cosmological background solutions when the diffusion phenomena takes place in an expanding universe. Our focus here relies on the nature of the diffusion coefficient $\sigma$ which measures the magnitude of such transport phenomena. We test dynamics where $\sigma$ has a phenomenological dependence on the scale factor, the matter density, the dark energy and the expansion rate.

## 1. Introduction

For most of the universe lifetime its dynamics can be fairly approximated by a homogeneous, isotropic and expanding sphere whose energy content is dominated by pressureless matter. The hot radiative (Big Bang) primordial universe cools down quickly until the radiation energy drops to the same level as the matter energy density. This happens very soon, when the universe is only $\sim 50$ kyrs old. During the following 10 Gyrs the total universe cosmic energy budget is well approximated by a pressureless matter fluid. This is the matter dominated epoch where most of the main astrophysical effects take place, such as the formation of stars, galaxies and clusters of galaxies. The matter component can be divided into two distinct contributions: the first one is the expected baryonic sector which contains the known heavy particles of the standard particle model. The second contribution comes from an unknown component called dark matter which is at least five times more abundant than the baryonic matter and is the building block of any successful cosmological theory. The matter domination era is a necessary stage for the formation of structures, but it ends when the universe is $\sim 10$ Gyrs old. From this moment on, another form of energy, called dark energy, accelerates the background expansion slowing down the agglomeration rate. The nature of the dark energy is also still unknown. The simplest explanation for this effect relies on the existence of a cosmological constant $\Lambda$. However, one could admit different descriptions for the dark energy phenomena, like scalar fields, which may (Amendola 2000; Zimdahl et al. 2003; Dalal et al. 2011; Castro et al. 2012) or may not interact with the other cosmic components.

In the standard model described above the matter dynamics is therefore described by the relativistic Euler equation $\nabla^\mu T_{\mu\nu} = 0$ on the the matter fluid energy-momentum tensor. In particular, the fluid feels only indirectly (via the gravitational potential) the presence of other components, e.g., photons, neutrinos and dark energy.

If we assume fluid particles undergoing velocity diffusion in a background medium, it was shown in Calogero (2011, 2012) that the matter dynamics can be described by the equations

$$\nabla_\mu J^\mu = 0, \quad \nabla_\mu T^{\mu\nu} = \sigma J^\nu. \tag{1}$$

The first equation guarantees the standard conservation law for the particles current density $J^\mu$. This is a remarkable fact concerning the inclusion of the diffusion mechanism into the general relativistic context. Indeed, this is also the case in the usual Fokker-Planck equation which describes the evolution of the probability density function of the velocity of the particles rather than their creation/annihilation rates. The quantity $\sigma$ in the second equation is the (positive) diffusion coefficient, which measures the energy transferred to the fluid particles by the diffusion forces per unit of time.[1] So far only the case of a constant $\sigma$ has been considered in the literature, see e.g. Calogero & Velten (2013) and Shogin et al. (2013), but here the possibility that $\sigma$ varies through space-time will be considered.

Since the second relation in (1) states that, in the presence of diffusion, the matter energy-momentum tensor is not a divergence free quantity, and having in mind Bianchi's identities, it is clear that the space-time geometry cannot be determined by the standard Einstein field equations of general relativity. The inconsistency with the Bianchi identities can be circumvented by adding a cosmological scalar field $\phi$ to the Einstein equation, which thereby becomes

$$R_{\mu\nu} - \frac{1}{2} g_{\mu\nu} R + \phi g_{\mu\nu} = T_{\mu\nu}, \tag{2}$$

where we use physical units such that $8\pi G = c = 1$. The scalar field $\phi$ plays the role of the background medium in which diffusion takes place. Taking the divergence $\nabla^\mu$ of both sides of eq. (2), we obtain that $\phi$ obeys

$$\nabla_\mu \phi = \sigma J_\mu. \tag{3}$$

In the next section we will show that after assuming a FLRW metric the resulting cosmology is equivalent to GR having two interacting fluids. This corroborates our claim that the diffusion mechanism can be seem as a possible physical origin for energy exchange between cosmological fluids.

In order to avoid the need to introduce a new evolution equation for $\sigma$, and at the same time to ensure that the value of $\sigma$ is coordinates-independent, we assume that $\sigma = f(s)$, where $s$ is a scalar invariant quantity constructed from $\phi, g_{\mu\nu}, J^\mu$ and $T_{\mu\nu}$. The simplest choices for the scalar invariant $s$ are

$$s_1 = -J^\mu J_\mu, \quad s_2 = g^{\mu\nu} T_{\mu\nu}, \quad s_3 = \phi. \tag{4}$$

In the next section we present the basic equations for a viable cosmological model based on the diffusion theory outlined above. This model extends the one studied in Calogero & Velten (2013) by considering a time dependent diffusion coefficient $\sigma$.

[1] We take the opportunity to point out a little misprint in our article (Calogero & Velten, 2013). In the paragraph after eq. (2.3), the sentence "The value $3\sigma$ measures the energy..." should read "The value $\sigma$ measures the energy...".

## 2. Cosmological model with variable matter diffusion

A viable cosmological model in which dark matter undergoes microscopic velocity diffusion into a dark energy solvent field $\phi$ has been developed in Calogero (2012) and Calogero & Velten (2013). This model is obtained from the general diffusion theory described in the Introduction under the following assumptions: (i) the matter content is described by a pressureless fluid, i.e., the energy-momentum tensor $T_{\mu\nu}$ and the current density $J^\mu$ are given by $T_{\mu\nu} = \rho u_\mu u_\nu$ and $J^\mu = nu^\mu$, where $\rho$ is the energy density, $n$ the particles number density and $u^\mu$ the four-velocity field of the dust fluid; (ii) the universe is spatially homogeneous, isotropic and flat and so in particular the space-time metric can be written in the form

$$ds^2 = -dt^2 + a(t)^2(dx^2 + dy^2 + dz^2), \quad a_0 = 1,$$

where a subscript 0 indicates the evaluation at time $t = 0$; (iii) the diffusion coefficient $\sigma$ is a positive constant. The resulting cosmological model has been called $\phi$CDM model in Calogero & Velten (2013) and is described by the following system on the standard normalized energy densities

$$\frac{d\Omega_m(z)}{dz} - \frac{3\Omega_m(z)}{1+z} = -\tilde{\sigma}\frac{(1+z)^2}{E(z)}, \tag{5}$$

$$\frac{d\Omega_\phi(z)}{dz} = \tilde{\sigma}\frac{(1+z)^2}{E(z)}, \tag{6}$$

$$\frac{H(z)}{H_0} = E(z) = \sqrt{\Omega_m(z) + \Omega_\phi(z)}, \tag{7}$$

with $z = a^{-1} - 1$ and $\tilde{\sigma} = \frac{\sigma n_0}{3H_0^3}$.

For $\tilde{\sigma} = 0$ the $\phi$ field remains constant in time and the solution is given by the $\Lambda$CDM model:

$$\Omega_m^{(0)}(z) = \Omega_{m0}^{(0)}(1+z)^3, \quad \Omega_\phi^{(0)}(z) = \Omega_{\phi 0}^{(0)} = 1 - \Omega_{m0}^{(0)}.$$

Equations (5) and (6) denote a coupled system where energy flows from the matter to the dark energy field. The direction of the flux is due to the fact that $\tilde{\sigma} > 0$. Interacting models play an important role to alleviate the cosmic coincidence problem, i.e., the fact that only today the dark matter and dark energy densities are of the same order of magnitude. Usually the interaction term in the right hand side of equations (5) and (6) is incorporated in a *ad hoc* way. Therefore, the diffusion mechanism appears as a genuine physical mechanism responsible for the interaction on the dark sector.

In the rest of the paper we assume that $\tilde{\sigma}$ in the equations above is time-dependent. We will employ the following phenomenological choices

$$\tilde{\sigma}_{(n)} \equiv \tilde{\sigma}_0 a^k, \quad \tilde{\sigma}_{(\rho)} \equiv \tilde{\sigma}_0 \left(\frac{\Omega_m}{\Omega_{m0}}\right)^\lambda, \quad \tilde{\sigma}_{(\phi)} \equiv \tilde{\sigma}_0 \left(\frac{\Omega_\phi}{\Omega_{\phi 0}}\right)^\delta, \quad \tilde{\sigma}_{(H)} \equiv \tilde{\sigma}_0 \left(\frac{H}{H_0}\right)^h.$$

We remark that, since for the model under discussion the scalar invariants $s_1, s_2$ in (4) are given by $s_1 = n_0(1+z)^3$, and $s_2 = -\rho = H_0\Omega_m(z)$, the choices $\tilde{\sigma}_{(n)}$, $\tilde{\sigma}_{(\rho)}$ and $\tilde{\sigma}_{(\phi)}$ correspond respectively to a diffusion coefficient that is a power of the scalar invariants $s_1 = n^2$, $s_2 = -\rho$, $s_3 = \phi$ to which (4) reduce in the dust fluid case.

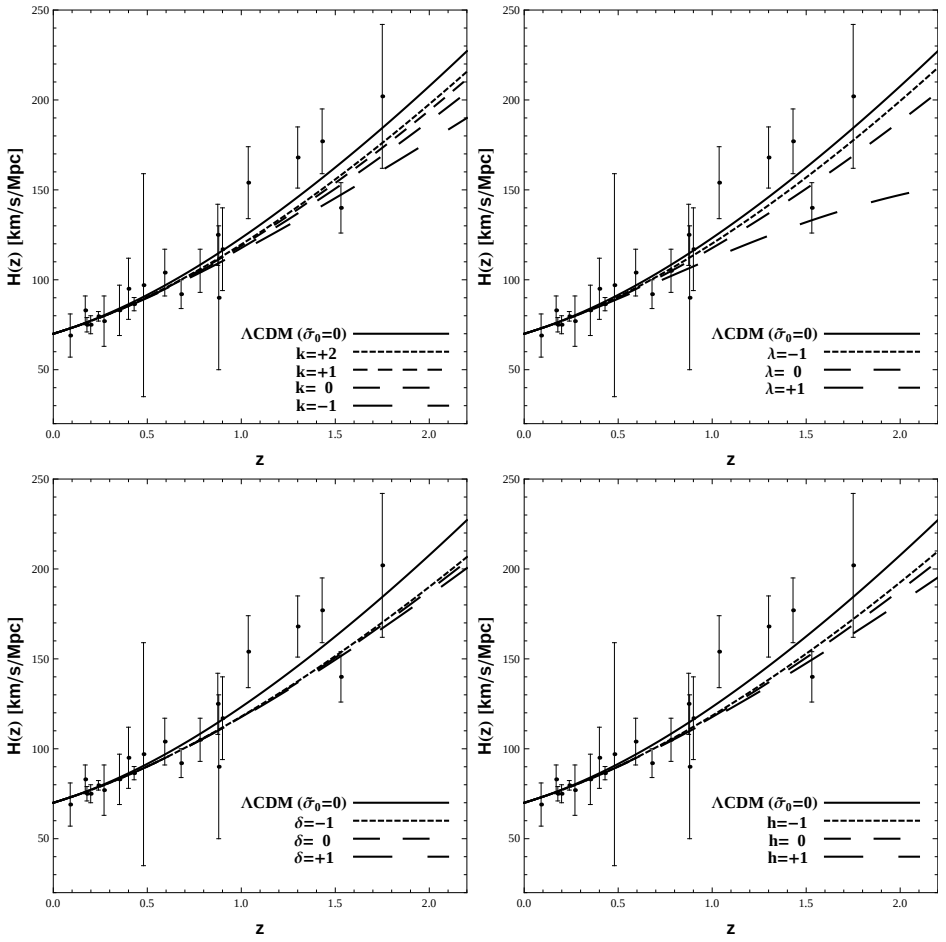


Figure 1. Evolution of the Hubble expansion -H(z)- for the different choices of time dependent diffusion coefficient. The four panels represent the cases: Top left ($\tilde{\sigma}_{(n)}$), top right ($\tilde{\sigma}_{(\rho)}$, bottom left ($\tilde{\sigma}_{(\phi)}$) and bottom right ($\tilde{\sigma}_{(H)}$).

## 3. Cosmological background dynamics

Let us investigate now how the different options for the coefficient $\sigma$ affect the background dynamics of the cosmological model.

In our analysis we will fix the reference values $\Omega_{m0} = 0.3$ ($\Omega_\Lambda = \Omega_{\phi 0} = 0.7$) and $H_0 = 70\,\mathrm{km/s^{-1}Mpc^{-1}}$. Moreover the today magnitude of the diffusion coefficient will be fixed at $\tilde{\sigma}_0 = 0.1$. Although background observational data can be described by this value, the structure formation process is severely affected by the diffusion mechanism. The analysis using the matter power spectrum data imposes the upper bound $\tilde{\sigma}_0 < 0.01$ (Calogero & Velten, 2013). However, we will keep the reference value $\tilde{\sigma}_0 = 0.1$ as a guide since here we are mostly concerned with the background expansion. Indeed, depending on the value of $k$, $\lambda$, $\delta$ and $h$, the resulting diffusive dynamics becomes closer to the ΛCDM model, thus allowing for larger values of $\tilde{\sigma}_0$.

The results of our analysis are contained in Figs. 1 and 2, where we plot respectively the Hubble function and the fractionary densities corresponding to the different choices of the time dependent diffusion coefficient $\sigma$. In each plot the dynamical quantities for the ΛCDM model are shown with solid lines. The case of a constant $\tilde{\sigma} = \tilde{\sigma}_0$ has been already shown in Calogero & Velten (2013). The observational data points displayed in Fig. 1 are based on a technique which uses the differential age of old red galaxies. They were compiled in Farooq et al. (2013). The main conclusion that can be drawn from the pictures is that the diffusion dynamics can be made arbitrarily close to those of the ΛCDM model by choosing the exponent $k$ positive and large, or the exponents $\lambda, \delta, h$ negative and with large absolute value.

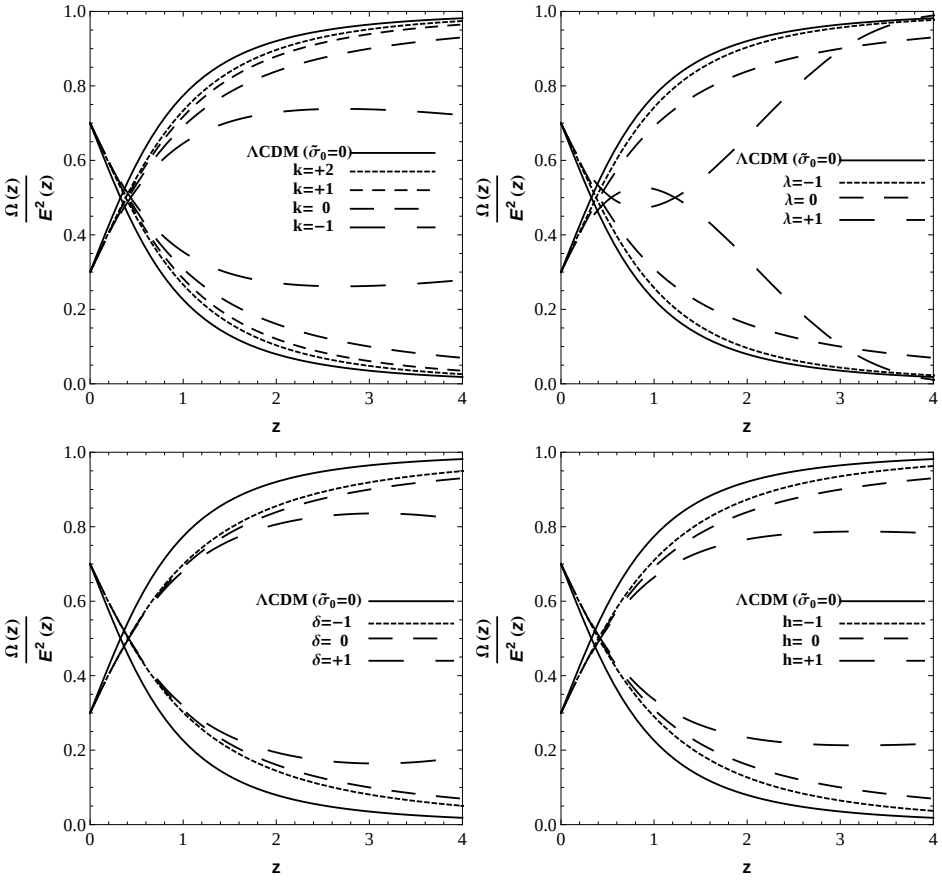


Figure 2. Evolution of the fractionary density parameters for the different choices of time dependent diffusion coefficient. The four panels represent the cases: Top left ($\tilde{\sigma}_{(n)}$), top right ($\tilde{\sigma}_{(\rho)}$, bottom left ($\tilde{\sigma}_{(\phi)}$) and bottom right ($\tilde{\sigma}_{(H)}$).

## 4. Conclusions

We have investigated the background evolution for a cosmological model where the matter component undergoes microscopic velocity diffusion into the dark energy field, which acts as the diffusion solvent. Previously, the case of a constant diffusion coefficient $\sigma$ = const was studied (Calogero & Velten, 2013). In this contribution we consider different temporal dependences for the diffusion coefficient, which derive by postulating a power-law dependence of $\sigma$ on the other dynamical variables of the model.

Our main result can be stated in the following way: by a proper choice of the exponent in the power-law, the dynamics of the diffusion model can be made arbitrarily close to those of the ΛCDM expansion. In some sense, this means that even for "high" values for the magnitude of the today's diffusion coefficient $\tilde{\sigma}_0$, such as $\tilde{\sigma}_0 = 0.1$, an appropriate time dependence can alleviate the diffusion effects on the cosmic background dynamics. In any case, following the results of Calogero & Velten (2013), it is mandatory a study making use of the cosmological perturbation theory. The cosmic matter diffusion is very sensitive to this analysis and the most strong constraints come from the structure formation process. We hope to deal with this issue in a future communication.

**Acknowledgments.** HV thanks CNPq (Brazil) for partial financial support and the organizers of the II GRACO held in Buenos Aires.

## References

Amendola, L. 2000, Phys. Rev., D62, 043511

Calogero, S. 2011, JCAP, 11, 016

Calogero, S. 2012, J. Geom. Phys., 62, 2208

Calogero, S. & Velten, H. 2013, JCAP, 11, 025

Castro D. R., Velten, H. & Zimdahl, W. 2012, JCAP, 06, 024

Dalal N., Abazajian, K., Jenkins, E. & Manohar, A. V. 2011, Phys. Rev. Lett., 86, 1939

Farooq. O., Mania. D. & Ratra, B. 2013, Astrop. J., 764, 138

Shogin, D. & Hervik, S. 2013, JCAP, 10, 005

Zimdahl, W. & Pavón, D. 2003, Gen. Rel. Grav., 35, 413

*Gravitation, Relativistic Astrophysics and Cosmology*
*Second Argentinian-Brazilian Meeting, 2014*
*G. S. Vila, F. L. Vieyro and J. Fabris, eds.*

# Proton loading of jets and other consequences of the injection of neutrons in accretion flows

Gabriela S. Vila,[1] Florencia L. Vieyro,[1] and Gustavo E. Romero[1,2]

[1]*Instituto Argentino de Radioastronomía, C.C. 5, (1894) Villa Elisa, Buenos Aires, Argentina*
[2]*Facultad de Cs. Astronómicas y Geofísicas, Universidad Nacional de La Plata, Paseo del Bosque S/N, (1900) La Plata, Buenos Aires, Argentina*

**Abstract.** Relativistic neutrons are injected in the corona surrounding an accreting black hole through hadronic interactions of locally accelerated protons. If the source is a microquasar, a fraction of these neutrons may escape and penetrate the base of the jet. The neutrons will decay into protons inside the outflow, this being then a possible mechanism for loading Poynting-dominated jets with baryons. We study the characteristics of the proton distribution injected in this way and the consequences on the high-energy radiative spectrum of the jet. We also investigate the fate of those neutrons that escape the corona into the external medium.

## 1. Introduction

The composition of relativistic jets is an open issue. All relativistic jets emit synchrotron radiation at radio wavelengths. The characteristics of the radio spectrum give very strong evidence in favour of the presence of accelerated electrons (or electron-positron pairs) with a non-thermal distribution. The radiative output from protons may be largely unimportant unless they are accelerated to very high energies and find suitable targets to interact, such as a dense matter field or an intense magnetic field.[1] Currently, observational evidence of a baryonic component exists only for two accreting black holes: the galactic microquasars SS 433 and 4U1630-47 (Migliari et al. 2002, Díaz Trigo et al. 2013). The X-ray spectra of these objects show blueshifted iron lines. The inferred velocity of the iron nuclei ($\sim 0.3 - 0.4c$) is consistent with the interpretation that they are traveling with the jets.

The question of composition is relevant because it is expected to be related to the launching mechanism of the outflows. Jets launched through the Blandford-Znajek process (e.g. Blandford & Znajek 1977) or similar (i.e. powered by the rotational energy of the black hole) are basically a Poynting flux plus electron-positron pairs created in situ. If, on the other hand, the outflows are launched and fed with matter from the accretion disk as a collimated wind (e.g. Blandford & Payne 1982), they should contain as well protons and other nuclei.

The launching mechanism, however, is definitively not the only factor that determines the composition of jets. Black hole-driven jets may get loaded with baryons by

[1]See for example Romero et al. (2003) and Vila et al. (2012) for models of hadronic emission of jets in microquasars.

entrainment with the matter in the medium they traverse – the outflows from the outer accretion disk or the wind of a companion star in a high-mass microquasar, for example.

In low-luminosity active galactic nuclei (AGN) and X-ray binaries (XRBs), observations support the existence of an advection-dominated and radiatively inefficient hot cloud of plasma around the compact object. This "corona" is usually modeled as a two-temperature ion-electron thermal plasma, sometimes with the addition of a population of non-thermal electrons or electron-positron pairs, see e.g. Vurm & Poutanen (2009). Compton up-scattering of disk photons by the electrons in the corona is the classical explanation for the origin of the power-law hard X-ray spectrum observed during the low-hard state of XRBs.[2] Recently, Romero et al. (2010), Vieyro et al. (2012) and Vieyro & Romero (2012) developed a radiative model for magnetized coronae in black hole XRBs that includes relativistic protons. They applied the model to Cygnus X-1, successfully reproducing the MeV emission detected by COMPTEL and *INTEGRAL* (McConnell et al. 2000, Cadolle Bell et al. 2006, Jourdain et al. 2012).

Relativistic protons in the corona produce gamma rays through the decay of neutral pions created in inelastic collisions with thermal protons. In about a half of the $pp$ collisions the proton turns into a neutron. The conditions in the corona are such that the neutrons escape virtually without interacting and propagate for long distances until they decay. A fraction of these neutrons will enter the jets (if they exist) and decay there, injecting a proton and an electron that will get trapped by the local magnetic field and advected with the outflows. This is, then, another possible mechanism to load jets with protons.

The production and escape of neutrons from the central regions in AGN has been studied before by several authors, see e.g. Sikora et al. (1989), Bednarek (1992), Atoyan & Dermer (2003), and Toma & Takahara (2012). Here, we study the injection of neutrons in the magnetized corona of a microquasar through interactions of non-thermal protons with matter and radiation. We show that the neutrons escape the corona almost freely, and calculate their distribution in energy and space outside the source. We also compute the local spectrum of the protons and electrons injected where the neutrons decay. For those protons injected inside the jets, we estimate their high-energy emission by the interaction with a dense clump in the wind of the companion star. Finally, we discuss the characteristics of the radiation from the electrons injected far from the corona.

## 2. Corona model

We apply the corona model developed by Romero et al. (2010), Vieyro et al. (2012) and Vieyro & Romero (2012). The reader is referred to those works for a detailed description of the model, here we only comment briefly on its most important aspects.

We assume the corona to be homogeneous and spherical, with a radius of $R_c = 35R_{grav}$ (the mass of the black hole is $15M_\odot$, as in Cygnus X-1). The bolometric luminosity of the corona is $L_c = 0.01L_{Edd} \approx 10^{37}$ erg s$^{-1}$. The mean number density of thermal protons and electrons in the corona is $n_{p,e} \approx 10^{13}$ cm$^{-3}$. The hypothesis of

[2]This emission may as well be synchrotron radiation from electrons in the jets, see Vila & Romero (2009) and Vila et al. (2012).

equipartition between the energy density of thermal particles and the magnetic energy density, yields a mean magnetic field strength $B_c \approx 10^5$ G.

Relativistic protons are injected in the corona with a power-law energy spectrum $Q_p \propto E_p^{-2.2}$ [erg$^{-1}$ cm$^{-3}$]. This is consistent with a diffusive acceleration mechanism, that in the corona may operate at sites of fast magnetic reconnection (de Gouveia dal Pino & Lazarian 2005, but see also Drury 2012). The steady-state distribution of relativistic protons $N_p(E_p)$ [erg$^{-1}$ cm$^{-3}$] is calculated solving a system of kinetic equations that couple the behaviour of protons, electrons, and photons in the corona. The equation for each particle species includes terms that account for injection, energy losses, and escape.

The relativistic protons in the corona cool as they interact with the thermal protons, the non-thermal radiation emitted by the relativistic electrons, the blackbody photons from the accretion disk, and the Comptonized disk photons. The latter is the most relevant radiation field, that we parametrize as a power-law with a cutoff of the form $n_{\rm ph} \propto E_{\rm ph}^{-\beta} \exp\left(-E_{\rm ph}/E_0\right)$ with $\beta = 1.6$ and $E_0 = 150$ keV.

The main channels of proton-proton ($pp$) and proton-photon ($p\gamma$) collisions that produce neutrons are

$$\begin{aligned} p + p &\rightarrow p + n + \pi^+ + a\pi^0 + b(\pi^+ + \pi)\,, \\ p + p &\rightarrow n + n + 2\pi^+ + a\pi^0 + b(\pi^+ + \pi)\,, \\ p + \gamma &\rightarrow n + \pi^+ + a\pi^0 + b(\pi^+ + \pi), \end{aligned} \tag{1}$$

where the integers $a, b$ are the pion multiplicities. To calculate the neutron injection functions we adopt the parameterizations given by Sikora (1989), Atoyan (1992), and Atoyan & Dermer (2003).

## 3. Results

The left panel of Figure 1 shows the injection rates of neutrons created in $pp$ and $p\gamma$ interactions, as a function of energy. The total power injected in neutrons inside the corona is $L_n \approx 6 \times 10^{35}$ erg s$^{-1}$. The cooling rates for neutrons by collisions with protons and photons, the decay rate, and the inverse of the corona crossing time are plotted in the right panel of Figure 1. The escape time is the shortest for all energies considered, so we make the approximation that all neutrons leave the corona before decaying without losing energy.

The steady-state distribution of neutrons in energy and space outside the corona, may be written as $N_n(E_n, r) \propto r^{-2} \exp\left(-r/r_\tau\right)$, where $\tau(E_n)$ and $v_n(E_n)$ are the mean lifetime and the velocity of the neutrons, respectively, and $r_\tau = \tau_n v_n$. The coordinate $r$ is the radial distance to the center of the corona. Each neutron injects a proton, an electron, and an electron antineutrino at decay, $n \rightarrow p + e^- + \bar{\nu}_e$. The proton carries $\sim 99.9\%$ of the energy of the neutron, so the proton injection function is well approximated as $Q_p^{n\rightarrow p}(E_p, r) \approx N_n(E_n, r)/\tau(E_n)$ with $E_p = 0.999 E_n$. To calculate the injection rate of electrons we followed Abraham et al. (1966). The results are shown in Figure 2. The total power injected in protons is $\sim 10^{35}$ erg s$^{-1}$ whereas the power in electrons is $\sim 10^{30}$ erg s$^{-1}$. Most of these particles are created within $r \approx 10^{12-13}$ cm, a region whose size is of the order of the size of the binary system.

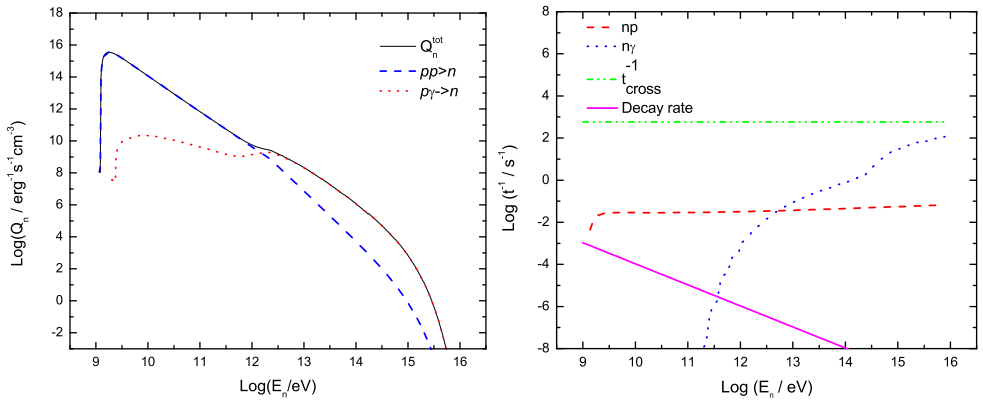


Figure 1. Left: injection rate of neutrons as a function on energy inside. Right: cooling, escape, and decay rates of neutrons in the corona.

To estimate the fraction of neutrons that decay inside the jets, we assumed that these are launched at a distance $50R_{\rm grav}$ from the black hole, and that they are conical with a half opening angle $\sim 6°$. For this choice of geometry, the decay of neutrons along the jets (up to $r \sim 10^{12}$ cm) injects a total power $\sim 10^{34}$ erg s$^{-1}$ in protons. Notice that these protons are non-thermal: their energy distribution mimics that of the parent neutrons, that in turn depends on that of the relativistic protons in the corona.

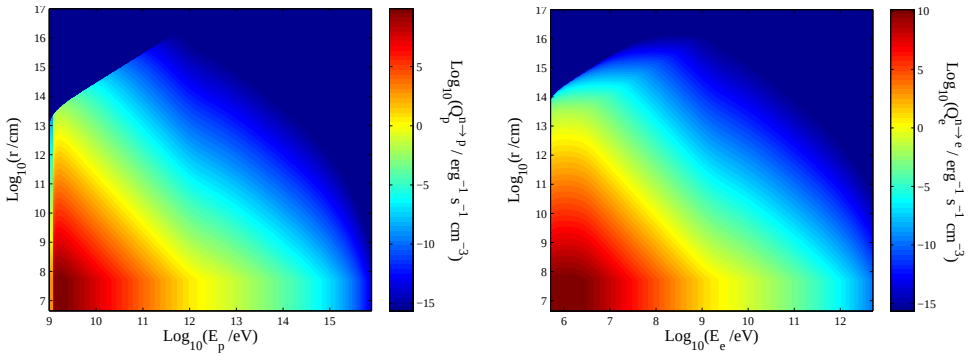


Figure 2. Left: injection spectrum of protons by decay of neutrons as a function of energy and distance to the black hole. Right: the same but for electrons.

If the companion star is a massive, young star with strong winds, the clumps in the wind may penetrate the jet. These clumps are dense and therefore suitable targets for the relativistic protons in the jets, producing gamma rays by decay of neutral pions decays from *pp* collisions (Araudo et al. 2009). Applying the model of Romero & Vila (2008) and Vila et al. (2012) to characterize the jets, we estimate the gamma-ray spectrum for different combinations of size, density, and location of the clump. The results are shown in Fig. 3.

Much less power is injected in electrons than in protons. Electrons, however, cool very efficiently. Those injected within the binary system will interact with the magnetic field and the radiation field of the companion star. For a massive star, typical values

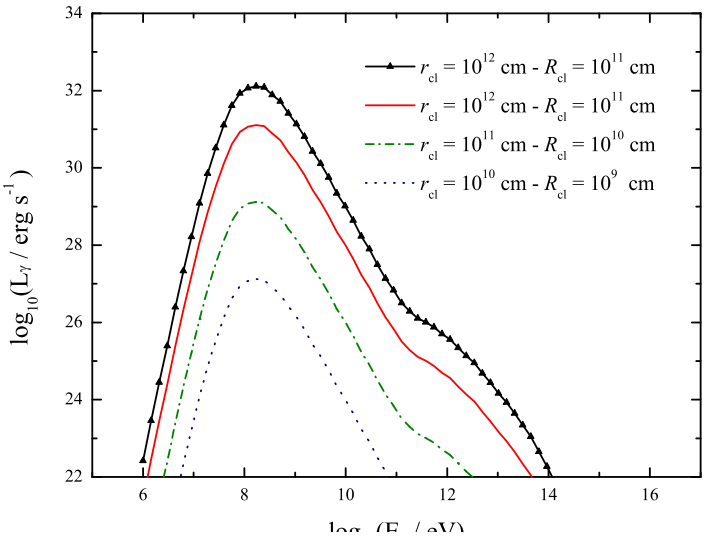


Figure 3. Gamma-ray emission from *pp* collisions in a jet-clump interaction, for different values of the clump radius $R_{\rm cl}$ and distance to the black hole $r_{\rm cl}$. The density of the clump is $n_{\rm cl} = 10^{12}$ cm$^{-3}$, except for the black symbol-line curve where $n_{\rm cl} = 10^{13}$ cm$^{-3}$.

of magnetic field and temperature at the surface are $B_\star \sim 100$ G and $T_* \sim 10^4$ K. Under these conditions the cooling times of electrons are very long, so they will diffuse far from their injection site before losing an appreciable fraction of their energy. The calculation of the radiative spectrum of the electrons and of the morphology of the emission region must be carried out accounting for propagation effects as in Bosch-Ramon & Khangulyan (2011). For the electron energies and magnetic fields considered here, the formation of a radio synchrotron nebula at ~GHz frequencies may be expected. If electrons cool predominantly through this channel, the nebula should be detectable at the level of the mJy at 1 GHz for a source at $\sim 2$ kpc.

## 4. Summary and perspectives

We have studied the production of neutrons in the corona of an accreting stellar-mass black hole. The decay of these neutrons inside the jets - if present - is a way of loading them with baryons irrespective of the launching mechanism. These protons are energetic and have a non-thermal distribution; they may produce gamma rays by interaction with a dense matter target such as a clump from the wind of the companion star. Although according to our results the power in protons is low, the added contribution of several quasi-simultaneous jet-clump interactions may give rise to weak flaring emission at GeV energies, such as that recently observed in Cygnus X-1 by Bodaghee et al. (2013). The cooling of electrons injected outside the corona should create a detectable radio nebula at scales of the size of the binary system. The detailed structure of the nebula will be addressed elsewhere.

**Acknowledgments.** This research was supported by grants PIP 0078/2010 and PICT 2012-00878 Préstamo BID.

**References**

Abraham, P. B., Brunstein, K. A. & Cline, T. L. 1966, Phys. Rev., 150, 1088
Araudo, A. T., Bosch-Ramon, V. & Romero, G. E. 2009, A&A, 503, 673
Atoyan, A. 1992, A&A, 257, 465
Bednarek, W. 1992, A&A, 264, 331
Blandford, R. D. & Payne, D. G. 1982, MNRAS, 199, 883
Blandford, R. D. & Znajek, R. L. 1977, MNRAS, 179, 433
Bodaghee, A. et al. 2013, ApJ, 775, id.98
Cadolle Bel, M. et al. 2006, A&A, 446, 591
de Gouveia dal Pino, E. M. & Lazarian, A. 2005, A&A, 441, 845
Díaz-Trigo, R., Miller-Jones, J. C. A., Migliari, S. et al. 2013, Nature, 504, 260
Drury, L. O'C. 2012, MNRAS, 422, 2474
Jourdain, E., Roques, J. P. & Malzac, J. 2012, ApJ, 744, id.64
McConnell, M. L. et al. 2000, ApJ, 543, 928
Migliari, S., Fender, R. & Méndez, M. 2002, Science, 297, 1673
Romero, G. E., Vieyro, F. L. & Vila, G. S. 2010, A&A, 519, id.A109
Romero, G. E. & Vila, G. S. 2008, A&A, 485, 623
Romero, G. E. et al. 2003, A&A, 410, L1
Sikora, M., Begelman, M. & Rudak, B. 1989, ApJ, 341, L33
Toma, K. & Takahara, F. 2012, ApJ, 754, 148
Vieyro, F. L. & Romero, G. E. 2012, A&A, 542, id.A7
Vieyro, F. L. et al. 2012, A&A, 546, id.A46
Vila, G. S. & Romero, G. E. 2010, MNRAS, 403, 1457
Vila, G. S., Romero, G. E. & Casco, N. A. 2012, A&A, 538, id.A97
Vurm, I. & Poutanen, J. 2009, ApJ, 698, 29

# Posters

*Gravitation, Relativistic Astrophysics and Cosmology*
*Second Argentinian-Brazilian Meeting, 2014*
*G. S. Vila, F. L. Vieyro and J. Fabris, eds.*

# Kerr geometry in modified teleparallel gravity

Cecilia Bejarano,[1] Rafael Ferraro,[1,2] and María José Guzmán[1]

[1]*Instituto de Astronomía y Física del Espacio (IAFE, CONICET-UBA), Argentina*
[2]*Departamento de Física, Facultad de Ciencias Exactas y Naturales, Universidad de Buenos Aires, Argentina*

**Abstract.** We show that Kerr geometry admits a tetrad where the scalar torsion vanishes. This result implies that Kerr spacetime is also a solution for a wide family of $f(T)$ theories.

## 1. Introduction

Many models of modified gravity have been proposed in order to tackle the shortcomings of general relativity (Capozziello & Faraoni, 2011). Firstly, deformations at large scales could provide a geometric explanation to the phenomena (hypothetically) caused by dark matter and dark energy. Secondly, deformations at small scales could smooth or avoid the undesired singularities either at the primordial era or inside black holes. Thirdly, the elusive question about the theory of quantum gravity could be enlightening by a new perspective of gravity. Recently, a different approach to modified gravity was introduced in the framework of the teleparallelism (see Ferraro & Fiorini 2007 as seminal paper and Ferraro 2012 as a compact review).

### 1.1. Teleparallel theory

Gravity can be studied in the framework of teleparallelism (Einstein, 1928, 1930a, 1930b), where the dynamical variable is not the metric tensor but the tetrad or *vierbein* $\{\mathbf{e}_a(x)\}$ (a field of bases in the tangent space). The tetrad is linked to the metric by means of the condition of orthonormality $\eta_{ab} = \mathbf{e}_a \cdot \mathbf{e}_b$ ($\eta_{ab}$ is the Minkowski metric):

$$\eta_{ab} = g_{\mu\nu}\, e_a^\mu\, e_b^\nu \qquad \text{or} \qquad \eta^{ab} = g^{\mu\nu}\, e_\mu^a\, e_\nu^b, \tag{1}$$

where $e_a^\mu$ and $e_\mu^a$ are the components of the tetrad and the dual basis, respectively. The teleparallel equivalent of general relativity (TEGR) is governed by the action (Hayashi & Shirafuji (1979), Arcos & Pereira (2004))

$$S = \frac{1}{2\kappa}\int d^4x\; e\, T, \tag{2}$$

where $\kappa = 8\pi G$, $e = \det[e_\mu^a] = \sqrt{-g}$ and $T$ is the so-called scalar torsion, an invariant which is quadratic in the Weitzenböck torsion $T^\mu{}_{\nu\rho} = e_a^\mu\,(\partial_\nu e_\rho^a - \partial_\rho e_\nu^a)$. The equivalence between this theory and general relativity comes from the fact that $T$ relates to the Levi-Civita scalar curvature $R$ through a 4-divergence:

$$T = -R + 2\, e^{-1}\, \partial_\rho (e\, T_\mu^{\mu\rho}). \tag{3}$$

### 1.2. Modified teleparallel gravity

A $f(T)$ theory is a deformation of the TEGR where the Lagrangian $e\,T$ is replaced for $e\,f(T)$ (Ferraro & Fiorini, 2007). This procedure mimics the one of $f(R)$ theories for modified general relativity (Buchdahl, 1970). The dynamical equations of a $f(T)$ theory are

$$-2\,\kappa\,e_a^\lambda\,\mathcal{T}_\lambda^\nu \;=\; 4\,e^{-1}\,\partial_\mu[e\;f'(T)\;S_a^{\mu\nu}] + 4\;f'(T)\;e_a^\lambda\;T^\rho_{\mu\lambda}\;S_\rho^{\mu\nu} - f(T)\;e_a^\nu\,, \qquad (4)$$

where $\mathcal{T}_\lambda^\nu$ is the energy-momentum tensor (assuming that matter is coupled to the metric in the usual way) and

$$2\;S_\rho^{\mu\nu} \;=\; \frac{1}{2}\,(T_\rho^{\mu\nu} - T^{\mu\nu}_{\ \ \rho} + T^{\nu\mu}_{\ \ \rho}) + T_\lambda^{\ \lambda\mu}\,\delta_\rho^\nu - T_\lambda^{\ \lambda\nu}\,\delta_\rho^\mu \;=\; 2\,e_\rho^a\;S_a^{\mu\nu}, \qquad (5)$$

being $T = S_\rho^{\mu\nu}T^\rho_{\ \mu\nu}$ the Weitzenböck scalar torsion.

A remarkable advantage of $f(T)$ theories over $f(R)$ theories and other modified theories of gravity is the fact that the dynamical equations remain second order. For instance, $f(R)$ theories display fourth order equations, which can be converted to second order by introducing an auxiliar scalar field carrying the information of a new degree of freedom not contained in general relativity. $f(T)$ theories come also with new degrees of freedom because the tetrad involves more dynamical variables than the metric. At the level of the teleparallel equivalent, the excess of variables is compensated by an excess of local symmetry: the TEGR action is not only invariant under general changes of coordinates but under local Lorentz transformations of tetrads. This extra local Lorentz invariance in the tangent space means that the tetrad contains no more information than the metric. In fact, the metric $g_{\mu\nu} = \eta_{ab}\,e_\mu^a\,e_\nu^b$ does not change under local Lorentz transformations of tetrads. This extra local Lorentz invariance is not inherited by $f(T)$ theories, given that the variation of $T$ under local Lorentz transformations is a 4-divergence. This is a harmless boundary term in the TEGR, but it is a relevant change in $f(T)$ gravity because it remains encapsulated inside the argument of the function $f$, so spoiling the local Lorentz invariance. As a consequence, $f(T)$ theories have extra degrees of freedom. This was also shown in Li et al. (2011) through a Hamiltonian formalism.

## 2. TEGR vacuum solutions remaining valid in $f(T)$ theories

Since modified teleparallel theories of gravity are non-local Lorentz invariant, finding the appropriate tetrad solution could be a very complicated task, even for highly symmetric geometries. A naively chosen tetrad for the searched symmetry could fail to be the solution of equation (4) because it is separated from the real solution by a local Lorentz transformation dictated by the symmetry itself. In some cases it can be proved that a given geometry that solves Einstein equations remains as a solution for $f(T)$ theories for a proper (non-naive) tetrad. In Ferraro & Fiorini (2011) it was shown that this is the case for Schwarzschild geometry. The argument is actually very simple: any vacuum TEGR solution with vanishing $T$ also solves the equations of motion of $f(T)$ gravity with $f$ sufficiently smooth. In fact, equation (4) becomes

$$0 = 4\,e^{-1}\partial_\mu(e\;S_a^{\mu\nu}) + 4\;e_a^\lambda\;T^\rho_{\mu\lambda}\;S_\rho^{\mu\nu} - e_a^\nu\;\frac{f(0)}{f'(0)}, \qquad (6)$$

which is a TEGR vacuum equation with cosmological constant $2\Lambda = f(0)/f'(0)$. In this section we will exploit this result to prove that Kerr geometry remains as a vacuum solution for $f(T)$ theories of gravity.

### 2.1. Null tetrads approach

A given metric can be written with the help of a null tetrad as

$$\mathbf{g} = \mathbf{n}\otimes\mathbf{l} + \mathbf{l}\otimes\mathbf{n} - \mathbf{m}\otimes\overline{\mathbf{m}} - \overline{\mathbf{m}}\otimes\mathbf{m}, \tag{7}$$

where $\{\mathbf{n}^a\} = \{\mathbf{l}, \mathbf{n}, \mathbf{m}, \overline{\mathbf{m}}\}$ is a field of bases in the co-tangent space satisfying

$$\begin{aligned} \mathbf{l}\cdot\mathbf{l} = 0 &= \mathbf{n}\cdot\mathbf{n}, & \mathbf{m}\cdot\mathbf{m} &= 0 = \overline{\mathbf{m}}\cdot\overline{\mathbf{m}} \\ \mathbf{l}\cdot\mathbf{n} = 1 &= -\mathbf{m}\cdot\overline{\mathbf{m}}, & \mathbf{l}\cdot\mathbf{m} &= 0 = \mathbf{n}\cdot\mathbf{m}\,. \end{aligned} \tag{8}$$

Notice that these relations do not completely define the null tetrad since $\mathbf{l}$ and $\mathbf{n}$ can be replaced for

$$\mathbf{l} \longrightarrow e^{\lambda(x)}\,\mathbf{l}\,, \qquad \mathbf{n} \longrightarrow e^{-\lambda(x)}\,\mathbf{n}\,. \tag{9}$$

Moreover, any null tetrad can be associated with an orthonormal tetrad,

$$\mathbf{e}^0 = \frac{\mathbf{l}+\mathbf{n}}{\sqrt{2}}\,, \quad \mathbf{e}^1 = \frac{\mathbf{l}-\mathbf{n}}{\sqrt{2}}\,, \quad \mathbf{e}^2 = \frac{\mathbf{m}+\overline{\mathbf{m}}}{i\sqrt{2}}\,, \quad \mathbf{e}^3 = \frac{\mathbf{m}-\overline{\mathbf{m}}}{i\sqrt{2}}\,, \tag{10}$$

and vice-versa. The transformation (9) is equivalent to a Lorentz transformation of tetrad (10) with parameter $\gamma(x) = \cosh\lambda(x)$.

Now, we state the strategy we will follow: given a tetrad coming from a TEGR vacuum solution, we will apply the transformation (9) to look for a new tetrad having $T = 0$ (the geometry is kept unchanged!). Provided such a new tetrad exists, then we will assert that this tetrad is a solution even for $f(T)$ theories with $f$ sufficiently well behaved. Remarkably, Weitzenböck torsion $T^{\mu}{}_{\nu\rho}$ remains unchanged under *global* linear transformations of the tetrad; therefore, we can directly use the null tetrad in the computation.

### 2.2. Kerr geometry

Kerr geometry can be expressed in the way given by equation (7) with the help of the null tetrad

$$n^b{}_{\mu} = \frac{1}{\sqrt{2}}\begin{pmatrix} 1-\frac{2Mr}{r^2+a^2c^2\theta} & 1+\frac{2Mr}{r^2+a^2c^2\theta} & 0 & a\,s^2\theta\left(1+\frac{2Mr}{r^2+a^2c^2\theta}\right) \\ 1 & -1 & 0 & -a\,s^2\theta \\ 0 & 0 & r+ia\,c\theta & i\,s\theta(r+ia\,c\theta) \\ 0 & 0 & r-ia\,c\theta & -i\,s\theta(r-ia\,c\theta) \end{pmatrix}, \tag{11}$$

where $a$ is the angular momentum per unit of mass. Notice that $c\theta$ and $s\theta$ are shorthands for $\cos\theta$ and $\sin\theta$. Coordinates $x^\mu = (t, r, \theta, \phi)$ in equation (11) are not the familiar Boyer-Lindquist coordinates $x^\mu = (\widetilde{t}, r, \theta, \varphi)$ but they relate in a simple way:

$$d\varphi = d\phi + \frac{a}{r^2+a^2-2Mr}\,dr\,, \qquad d\widetilde{t} = dt + \frac{2Mr}{r^2+a^2-2Mr}\,dr\,. \tag{12}$$

Matrix (11) contains the covector $\mathbf{l}$ in the first row, $\mathbf{n}$ in the second row, etc. So, we perform the transformation (9) by multiplying and dividing the first and second rows,

respectively, by the factor $e^{\lambda(x)}$. Then, we search for a function $\lambda(t, r, \theta)$ making zero the scalar torsion; we obtain

$$\lambda(t, r, \theta) = \frac{t + r}{2} \left( \frac{r - \frac{3\, a^2\, \cos^2\theta}{r} - \frac{4\, a^2 M\, \cos^2\theta}{r^2 + a^2\, \cos^2\theta}}{r^2 + a^2\, \cos^2\theta} \right). \tag{13}$$

According to the previous argument, the null tetrad already found and its associated orthonormal tetrad, solve the dynamics of any $f(T)$ theory, provided that $f(0) = 0$, $f'(0) \neq 0$.

## 3. Summary

Although theories of modified gravity are expected to remove or smooth singularities, we show that Kerr geometry is not deformable by a $f(T)$ theory having $f(0) = 0$, $f'(0) \neq 0$. We have achieved this goal by showing that the TEGR admits a solution for Kerr geometry with vanishing scalar torsion $T$. This property implies that such a tetrad remains a solution for a family of smooth deformations of the TEGR, typically those theories like $f(T) = T + O(T^2)$.

**Acknowledgments.** This work has been supported by Universidad de Buenos Aires and CONICET.

## References

Arcos, H. I. & Pereira, J. G. 2004, Int. J. Mod. Phys. D, 13, 2193

Buchdahl, H. A. 1970, Mon. Not. R. Astron. Soc., 150, 1

Capozziello, S. & Faraoni, V. 2011, "Beyond Einstein gravity: A survey of gravitational theories for cosmology and astrophysics", Fundamental Theories of Physics 170, Springer, New York

Einstein, A. 1928, Sitzungsber. Preuss. Akad. Wiss. Phys. Math. Kl. 217; 1930a, Sitzungsber. Preuss. Akad. Wiss. Phys. Math. Kl. 401; 1930b, Math. Ann. 102, 685

Ferraro, R. & Fiorini, F. 2007, Phys. Rev. D, 75, 084031

Ferraro, R. & Fiorini, F. 2011, Phys. Rev. D, 84, 083518

Ferraro, R. 2012, AIP Conf. Proc., 1471, 103

Hayashi, K. & Shirafuji, T. 1979, Phys. Rev. D, 19, 3524

Li, M., Miao, R. X. & Miao, Y. G. 2011, JHEP, 07, 108

*Gravitation, Relativistic Astrophysics and Cosmology*
*Second Argentinian-Brazilian Meeting, 2014*
*G. S. Vila, F. L. Vieyro and J. Fabris, eds.*

# Emissivity of neutrinos by the direct Urca process and cooling of neutron stars in the presence of a strong magnetic field

Eduardo Lenho Coelho,[1] Marcelo Chiapparini,[1] and Rodrigo P. Negreiros[2]

[1]*524 São Francisco Xavier St., Rio de Janeiro, Rio de Janeiro, Brazil*
[2]*Gal. Milton Tavares de Souza, Niterói, Rio de Janeiro, Brazil*

**Abstract.** Strong magnetic fields of magnitudes up to $10^{14}$ G are suppose to exists at the surface of pulsars, which are highly magnetized neutron stars. The strength of magnetic field in the center of a neutron star remains unknown. According to the scalar virial theorem, magnetic field in the core could be as large as $10^{18}$ G. Direct Urca process is an extremely efficient mechanism for cooling a proton neutron star after its formation. In this work we study the influence of strong magnetic fields on the cooling of neutron stars coming from direct Urca process. We calculate numerically the emissivity of neutrinos and the cooling for different magnetic fields due to the direct Urca process, and compare the results for the case without magnetic field.

## 1. Introduction

The matter at high densities is described using a relativistic mean field (MF) theory and the Lagrangian that describes this model, with a uniform magnetic field $B$ along the $z$ axis, is given by (Glendenning 1997)

$$\begin{aligned}\mathcal{L} &= \sum_b \bar{\psi}_b[i\gamma_\mu D^\mu - m_b + g_{\sigma b}\sigma - g_{\omega b}\gamma_\mu\omega^\mu - \frac{1}{2}g_{\rho b}\gamma_\mu\boldsymbol{\tau}\cdot\boldsymbol{\rho}^\mu]\psi_b + \frac{1}{2}\partial_\mu\sigma\partial^\mu\sigma \\ &- \frac{1}{2}m_\sigma^2\sigma^2 - U(\sigma) - \frac{1}{4}\omega_{\mu\nu}\omega^{\mu\nu} + \frac{1}{2}m_\omega^2\omega_\mu\omega^\mu - \frac{1}{4}\boldsymbol{\rho_{\mu\nu}}\cdot\boldsymbol{\rho^{\mu\nu}} + \frac{1}{2}m_\rho^2\boldsymbol{\rho_\mu}\cdot\boldsymbol{\rho^\mu} \\ &+ \sum_{l=e^-,\,\mu^-}\bar{\psi}_l[i\gamma_\mu(\partial^\mu + iq_lA^\mu) - m_l]\psi_l - \frac{1}{4}F_{\mu\nu}F^{\mu\nu}, \end{aligned} \quad (1)$$

where $D^\mu = \partial^\mu + iq_bA^\mu$, $A^0 = 0$, $\vec{A} = (0, xB, 0)$, $q_b$ and $q_l$ are the electric charge of baryons and leptons, $\psi_b$ is the Dirac spinor for baryon $b$ in the octet $\{n, p, \Lambda, \Sigma, \Xi\}$ with mass $m_b$; $m_\sigma$, $m_\omega$, $m_\rho$ and $g_{\sigma b}$, $g_{\omega b}$, $g_{\rho b}$ are the masses and coupling constants of mesons $\sigma, \omega, \rho$ respectively. The mesonic and electromagnetic field strength tensors are $\omega_{\mu\nu} = \partial_\mu\omega_\nu - \partial_\nu\omega_\mu$, $\rho_{\mu\nu} = \partial_\mu\rho_\nu - \partial_\nu\rho_\mu$ and $F_{\mu\nu} = \partial_\mu A_\nu - \partial_\nu A_\mu$. The Lagrangian of leptons (electrons and muons) is written in the third line while the scalar self-interactions term is $U(\sigma) = \frac{1}{3}b\,m_n(g_{\sigma n}\sigma)^3 + \frac{1}{4}c(g_{\sigma n}\sigma)^4$, where $b$ and $c$ are constants. The dynamic equations of nucleon and mesons are obtained from the Euler-Lagrange equations $\frac{\partial\mathcal{L}}{\partial\phi(x)} - \partial_\mu\frac{\partial\mathcal{L}}{\partial(\partial_\mu\phi)} = 0$, where $\phi(x)$ is the corresponding field. The resulting

equations of motion in the mean field approximation are given by

$$g_{\omega n}\omega_0 = \left(\frac{g_{\omega n}}{m_\omega}\right)^2 \sum_b \chi_{\omega b}\rho_b, \quad g_{\rho n}\rho_{03} = \left(\frac{g_{\rho n}}{m_\rho}\right)^2 \sum_b \chi_{\rho b} I_{3b}\rho_b, \tag{2}$$

$$m_n^* = m_n + \left(\frac{g_{\sigma n}}{m_{\sigma n}}\right)^2 [b\, m_n\,(m_n - m_n^*)^2 + c(m_n - m_n^*)^3 - \sum_b \chi_{\sigma b} n_s], \tag{3}$$

where $I_{3b}$ is the 3-component of the isospin of the baryon $b$, $m_n^* = m_n - \chi_{\sigma b} g_{\sigma n}\sigma$, $\chi_{\sigma b} = g_{\sigma b}/g_{\sigma n}$, $\chi_{\omega b} = g_{\omega b}/g_{\omega n}$, $\chi_{\rho b} = g_{\rho b}/g_{\rho n}$; the scalar density is $n_s = n_s^{q_b=0} + n_s^{q_b\neq 0}$, with

$$n_s^{q_b=0} = \frac{m_b^*}{2\pi^2}\left[\mu_b^* k_b - m_b^{*2}\ln\left(\frac{\mu_b^* + k_b}{m_b^*}\right)\right], n_s^{q_b\neq 0} = \frac{m_b^* |q_b| B}{2\pi^2}\sum_{\nu=0}^{\nu_{\max(b)}} g_\nu \ln\left[\frac{\mu_b^* + k_{b,\nu_b}}{m_{b,\nu_b}^*}\right] \tag{4}$$

where $m_{b,\nu_b}^{*2} = m_b^{*2} + 2\nu_b|q_b|B$, $\nu$ is the Landau principal quantum number and the Landau level degeneracy $g_\nu$ is 1 for $\nu = 0$ and 2 for $\nu > 0$. The effective chemical potentials of baryons are $\mu_b^* = \mu_b - \chi_{\omega b} g_{\omega n}\omega_0 - \chi_{\rho b} g_{\rho n} I_{3b}\rho_{03}$. They are constrained due to the $\beta$-equilibrium condition, which reads $\mu_b = \mu_n - q_b\mu_{e^-}$, $\mu_{e^-} = \mu_{\mu^-}$, where $\mu_n$, $\mu_{e^-}$ and $\mu_{\mu^-}$ are the chemical potentials of neutron, electron and muon respectively. The number density of baryons and leptons is $\rho_b^{q_b=0} = \frac{k_b^3}{3\pi^2}$, $\rho_b^{q_b\neq 0} = \frac{|q_b|B}{2\pi^2}\sum_{\nu=0}^{\nu_{\max(b)}} g_\nu k_{b,\nu_b}$, $\rho_l = \frac{|q_l|B}{2\pi^2}\sum_{\nu=0}^{\nu_{\max(l)}} g_\nu k_{l,\nu_l}$, where $k_b$ and $k_{b,\nu_b} = (\mu_b^{*2} - m_b^{*2} - 2\nu_b|q_b|B)^{1/2}$ are the Fermi momentum of neutral and charge baryons respectively, $k_{l,\nu_l} = (u_l^2 - m_l^2 - 2\nu_l|q_l|B)^{1/2}$ is the Fermi momentum of leptons. The upper limits $\nu_{\max(b)}$ and $\nu_{\max(l)}$ are defined by the conditions $k_{b,\nu_b}^2 \geq 0$ and $k_{l,\nu_l}^2 \geq 0$. Neutron star matter satisfies the constraints of conservation of baryon number and neutrality of electric charge, which reads

$$\rho = \sum_b \rho_b, \quad 0 = \sum_b q_b\rho_b + \sum_{l=e^-,\,\mu^-} q_l\rho_l. \tag{5}$$

The energy density due to the matter is given by (Chakrabarty, Bandyopadhyay & Pal 1997)

$$\begin{aligned}
\varepsilon_m &= \frac{1}{3}b\, m_n(g_{\sigma n}\sigma)^3 + \frac{1}{4}c\,(g_{\sigma n}\sigma)^4 + \frac{1}{2}\left(\frac{m_{\sigma n}}{g_{\sigma n}}\right)^2 (g_{\sigma n}\sigma)^2 + \frac{1}{2}\left(\frac{m_{\omega n}}{g_{\omega n}}\right)^2 (g_{\omega n}\omega_0)^2 \\
&+ \frac{1}{2}\left(\frac{m_{\rho n}}{g_{\rho n}}\right)^2 (g_{\rho_n}\rho_{03})^2 + \sum_{b(q=0)} \frac{1}{8\pi^2}[2\mu_b^{*\,3}k_b - m_b^{*\,2}\mu_b^* k_b - m_b^{*\,4} \\
&\times \ln\left\{\frac{\mu_b^* + k_b}{m_b^*}\right\}] + \frac{|q|B}{4\pi^2}\sum_{b(q\neq 0)}\sum_{\nu_b=0}^{\nu_{\max(b)}} g_\nu[\mu_b^* k_{b,\nu_b} + m_{b,\nu_b}^{*2} \ln\left\{\frac{\mu_b^* + k_{b,\nu_b}}{m_{b,\nu_b}^*}\right\}] \\
&+ \frac{|q|B}{4\pi^2}\sum_{l=e^-,\,\mu^-}\sum_{\nu_l=0}^{\nu_{\max(l)}} g_\nu[\mu_l\, k_{l,\nu_l} + m_{l,\nu_l}^2 \ln\left\{\frac{\mu_l + k_{l,\nu_l}}{m_{l,\nu_l}}\right\}],
\end{aligned} \tag{6}$$

where $m_{l,\nu_l}^2 = m_l^2 + 2\nu_l|q_l|B$. The matter pressure is given by $P_m = \mu_n\rho_b - \varepsilon_m$. Next, we add to these the contribution from electromagnetic field tensor, obtaining the total energy density and pressure as $\varepsilon = \varepsilon_m + B^2/2$, $P = P_m + B^2/2$.

The system of coupled nonlinear equations (2-3) with constraints (5) is solved numerically by iteration. The coupling constants are given in Chiapparini et al. (2009). Figure 1 shows relative population of each specie of particles as a function of the baryon density for the cases without and with a strong magnetic field ($1.0 \times 10^{19}$ G for illustration). It can be seen that the incorporation of strong magnetic field increases the proton and electron fraction.

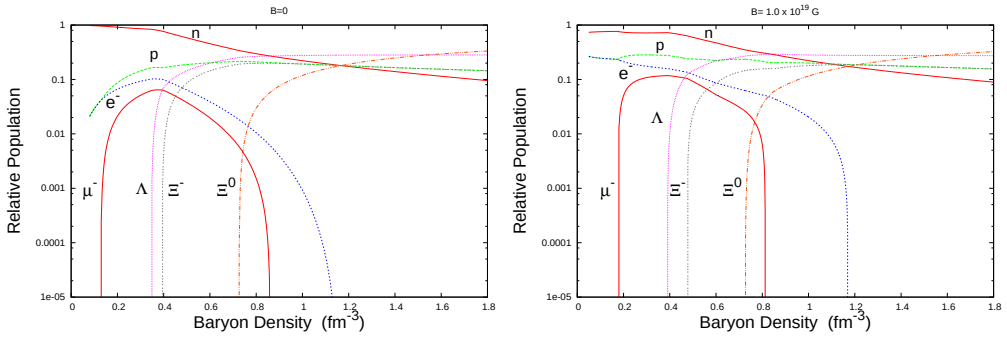


Figure 1. The particle fractions in cold $\beta$-equilibrated neutron star without and with magnetic field.

The direct Urca process is the most powerful mechanism of neutrino emission in the core of neutron stars. The reaction is given by $n \rightarrow p + e^- + \bar{\nu}_{e^-}$, $p + e^- \rightarrow n + \nu_{e^-}$. This process may occur if the proton fraction is large enough ($k_{Fn} \leq k_{Fp} + k_{Fe}$, where $k_{F\alpha} = (3\pi^2\rho_\alpha)^{1/3}$), in order to conserve momentum in the reaction. The emissivity due to the antineutrino emission process in the presence of a uniform magnetic field $B$ strong enough that only the ground Landau level is occupied is (Bandyopadhyay et al. 1998)

$$\begin{aligned}\epsilon_\nu &= 2\int \frac{Vd^3k_1}{(2\pi)^3}\int \frac{Vd^3k_2}{(2\pi)^3}\int_{-qBL_x/2}^{qBL_x/2}\frac{L_y dk_{3y}}{2\pi}\int \frac{L_z dk_{3z}}{2\pi}\int_{-qBL_x/2}^{qBL_x/2}\frac{L_y dk_{4y}}{2\pi} \\ &\times \int \frac{L_z dk_{4z}}{2\pi} E_2 W_{fi}\, f_1\,[1-f_3][1-f_4], \end{aligned} \tag{7}$$

where the pre-factor 2 takes into account the neutron spin degeneracy and the $f_i$'s are the Fermi-Dirac distribution functions. By the Fermi's golden rule, the transition rate per unity volume is $W_{fi} = \langle|M_{fi}|^2\rangle/tV$, where $t$ is the time, $V = V_xV_yV_z$ is the normalization volume and the matrix element for the V-A interaction is $M_{fi} = \frac{G_F}{\sqrt{2}}\int d^4X\bar{\psi}_1(X)\gamma^\mu(g_V - g_A\gamma_5)\psi_3(X)\bar{\psi}_2(X)\gamma_\mu(1-\gamma_5)\psi_4(X)$, where $\langle . \rangle$ denotes an averaging over the initial spin of $n$ and a sum over spins of final particles ($p$, $e^-$); $g_V$ and $g_A$ are vector and axial-vector coupling constants and the indices $i = 1-4$ refer to the $n$, $\nu_{e^-}$, $p$ and $e^-$, respectively. The wave functions for neutron and neutrino are plane wave functions and the wave functions for both protons and electron are given by Kobayashi & Sakamoto (1983). Then, the emissivity is

$$\epsilon_\nu = \frac{457\pi}{5040}G_F^2\cos^2\theta_c(q_bB)\left[(g_V+g_A)^2\left(1-\frac{k_{F_3}}{\mu_3^*}\right)+(g_V-g_A)^2\left(1-\frac{k_{F_1}}{\mu_n^*}\cos\theta_{14}\right)\right.$$

$$-(g_V^2 - g_A^2)\frac{m^{*2}}{\mu_3^*\mu_1^*}\Bigg]\exp\left[\frac{(k_{F_3}+k_{F_4})^2 - k_{F_1}^2}{2eB}\right]\frac{\mu_1^*\mu_3^*\mu_4}{k_{F_3}k_{F_4}}T^6\Theta,$$

where $\cos\theta_{14} = (k_{F_1}^2 + k_{F_4}^2 - k_{F_3}^2)/2k_{F_1}k_{F_4}$, and the threshold factor is $\Theta = \theta(k_{F_3} + k_{F_4} - k_{F_1})$, with $\theta(x) = 1\ (x > 0)$, $\theta(x) = 0$ (otherwise) and $T$ is the temperature, $k_{Fi}$ is the Fermi momentum.

## 2. Results

Figure 2 shows the cooling due to the direct Urca process of neutron stars with 1.4 and 1.6 solar masses (continuous and dashed lines, respectively) for the cases $B = 0$ (blue line) and $B(\rho/\rho_0) = B^{surf} + B_0[1 - \exp\{-\beta(\rho/\rho_0)^\gamma\}]$ (red line), where $B^{surf} = 10^8$G and $B_0 = 10^{19}$G are the magnetic fields at the surface and the center of the star respectively, with the parameters $\beta = 10^{-4}$ and $\gamma = 17$, and $\rho_0$ is the saturation density. We can see that the cooling is more intense with the increase in the mass of the star and for the case $B(\rho/\rho_0)$. Theses differences may be attributed to the increase of proton and electron fractions with the mass and magnetic field of the star and to the phase space modifications.

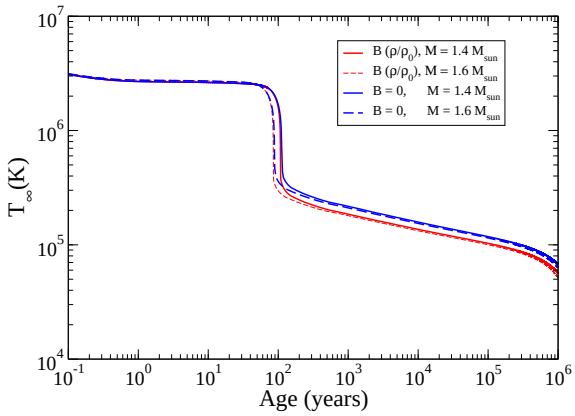


Figure 2. Cooling of a neutron star mass with 1.4 and 1.6 solar masses (continuous and dashed lines, respectively) for the cases $B = 0$ (blue line) and $B(\rho/\rho_0) = B^{surf} + B_0[1 - \exp\{-\beta(\rho/\rho_0)^\gamma\}]$ (red line).

## References

Bandyopadhyay, D., Chakrabarty, S., Dey, P. & Pal, S. 1998, PhRvD, 58, 121301

Chakrabarty, S., Bandyopadhyay, D. & Pal, S. 1997, PhRvL, 78, 2898

Chiapparini, M. et al. 2009, NuPhA, 826, 178

Glendenning, N. K. 1997, "Compact stars. Nuclear physics, particle physics, and general relativity", Springer, Berlin

Kobayashi, M. & Sakamoto, M. 1983, PThPh, 70, 5

*Gravitation, Relativistic Astrophysics and Cosmology*
*Second Argentinian-Brazilian Meeting, 2014*
*G. S. Vila, F. L. Vieyro and J. Fabris, eds.*

# Testing the duality distance relation with galaxy clusters and Type Ia supernovae data: a comparative study

Simony Santos Costa[1] and Rodrigo F. L. Holanda[2]

[1]*UFCG, Campina Grande, PB, Brazil*
[2]*UEPB, Campina Grande, PB, Brazil*

**Abstract.** We aim to compare two tests, cosmological model-independent, for the cosmic distance-duality relation (CDDR), $\eta\,(z) = D_L(z)(1+z)^{-2}/D_A(z) = 1$ where $D_L$ and $D_A$ are, respectively, the luminosity and angular diameter distances. The first test uses angular diameter distances (ADD) of two samples of galaxy clusters obtained by combining their Sunyaev-Zel'dovich effect and X-ray surface brightness and $D_L$ distances provided by two sub-samples of type Ia supernovae (SNe Ia). The second one uses the general expression for X-ray gas mass fraction, $f_{gas}$, of galaxy clusters jointly with type Ia supernovae data. In this case, were considered 38 $f_{gas}$ measurements and two sub-samples of type Ia supernovae for luminosity distances. In both tests, the CDDR is tested by assuming the $\eta$ parameter as a function of the redshift parametrized by two different ways. The results of the gas mass fraction test indicate the existence for new physics, such as photon coupling with particles beyond the standard model of particle physics, while the results for distance measurements test indicate that the validity, or not, of CDDR depends on the starting physical hypotheses describing the galaxy clusters.

## 1. Introduction

The so-called reciprocity relation, proved long ago by Etherington (1933), is a fundamental result for observational cosmology and its most useful version in the astronomical context is defined by

$$\frac{D_L}{D_A}(1+z)^{-2} = 1 \tag{1}$$

which relating the luminosity distance $D_L$ with the angular diameter distance $D_A$.

This equation is completely general, valid for all cosmological models based on Riemannian geometry, and only requires that source and observer be connected by null geodesics in a Riemannian spacetime and that the number of photons be conserved (Ellis, 2007).

If one is able to find cosmological sources whose intrinsic luminosities are known (standard candles) as well as their intrinsic sizes (standard rulers), one can determine both $D_L$ and $D_A$ and, after measuring the redshifts, test Etherington's result above. Although taken for granted in virtually all the analyses in cosmology, some attempts to test the identity (1) have been discussed in the literature. Basically, one assumes that the reciprocity relation can be a function of the redshift, namely:

$$\frac{D_L}{D_A}(1+z)^{-2} = \eta(z), \tag{2}$$

where $\eta(z)$ quantifies a possible epoch-dependent departing of the standard result ($\eta = 1$).

Approaches to test the CDDR in the recent literature assume a cosmological background suggested by a set of observations and check the validity of the CDDR in the context of some astrophysical effect. Examples of these methods are given by Bassett & Kunz (2004), Uzan *et al.* (2004) and Avgoustidis *et al.* (2010). More recently Holanda *et al.* (2011), used the validity of the CDDR in the ΛCDM framework to constrain possible galaxy cluster morphologies, and Nesseris & Garcia-Bellido (2012) tested the CDDR by the reconstruction of the parameter $\eta(z)$ using Genetic Algorithms and BAO data.

In this context, this work shows and compares two cosmological model-independent tests for (1) by using SNe Ia data compilations and galaxy clusters observations, adopting the following parametrizations:

$$\eta(z) = 1 + \eta_0 z \qquad (P1) \qquad\qquad \eta(z) = 1 + \frac{\eta_0 z}{(1+z)} \qquad (P2)$$

## 2. Test 1: diameter angular distance *vs* SNe Ia

The first test to be considered have been proposed by Holanda *et al.* (2010). They constrained the possible values of $\eta_0$ by considering two samples of ADD from galaxy clusters obtained by combining their SZE and X-ray surface brightness observations and two sub-samples of $D_L$ chosen from Constitution data.

The first sample is formed by 25 galaxy clusters from De Filippis *et al.* (2005) sample, that used an isothermal elliptical $\beta$ model to describe the clusters and obtained $D_A$ measurements by combining X-ray and SZE analysis. The second one is defined by the 38 ADD galaxy clusters from the Bonamente *et al.* (2006) sample, where the cluster plasma and dark matter distributions were analyzed assuming the hydrostatic equilibrium model and spherical symmetry.

For the luminosity distances, were chosen two sub-samples of SNe Ia from Constitution SNe Ia data whose redshifts coincide with the ones appearing in the galaxy cluster samples.

### 2.1. Analysis and results

In order to estimate the $\eta_0$ parameter for each sample, in both parametrizations, were used the likelihood estimator, determined by

$$\chi^2 = \frac{\sum_z [\eta(z) - \eta_{obs}(z)]^2}{\sigma^2_{obs}} \tag{3}$$

where $\sigma^2_{obs}$ are the errors associated with the observational techniques and $\eta_{obs}(z) = D_A^{cluster}(z)(1+z)^2/D_L$.

For De Filippis *et al.* was obtained $\eta_0 = -0.28^{+0.44}_{-0.44}$ ($\chi^2_{dof} = 1.02$) for P1 and $\eta_0 = -0.43^{+0.6}_{-0.6}$ ($\chi^2_{dof} = 1.03$) for P2, and for Bonamente *et al.*, was obtained $\eta_0 = -0.42^{+0.21}_{-0.21}$ ($\chi^2_{dof} = 0.88$) for P1 and $\eta_0 = -0.66^{+0.31}_{-0.31}$ ($\chi^2_{dof} = 0.86$) for P2, both in $2\sigma$ confidence level.

## 3. Test 2: gas mass fraction *vs* SNe Ia

The second test was proposed by Gonçalves *et al.* (2010). These authors showed that the model function depends explicitly on the CDDR, differently from most of the analyses discussed in the literature. They constrained the possible values to the parameter $\eta_0$ by using $D_A$ measurements extracted from $f_{gas}$ observations of galaxy clusters and $D_L$ from current SNe Ia data.

The mentioned authors considered two samples of 38 gas mass fraction measurements obtained from X-ray observations, as discussed by La Roque *et al.* (2006) and Ettori *et al.* (2009), plus two sub-samples of the SNe Ia taken from the Union2 compilation (Amanullah et al. 2010).

The gas mass fraction is defined by $f_{gas} = M_{gas}/M_{Total}$, where $M_{gas}$ is the mass of the intracluster medium gas and $M_{Total}$ is the total mass including baryonic mass and dark matter. To determine the gas mass and cluster's total mass followed the procedure of Sasaki (1996), which combined with the spherical $\beta$ model profile (Cavaliere & Fusco-Fermiano, 1976) provides in its more general form $f_{gas} \alpha D_A^{1/2} D_L$.

Furthermore, the authors defined the $f_{gas}$ model function as

$$f_{gas} = N \left[ \frac{D_L^* D_A^{*1/2}}{D_L D_A^{1/2}} \right] \tag{4}$$

where N is a normalization factor and $D_A^*$ ($D_L^*$ ) is the angular diameter (luminosity) distance of the fiducial model. They considered how the fiducial model $\Lambda CDM$, in such a way that the angular diameter distance that was used in analyses is given by

$$D_A(z) = N^{2/3} \left[ \frac{D_A^*}{\eta^{2/3} f_{gas}^{2/3}} \right] \tag{5}$$

It is worth mentioning that La Roque *et al.* (2006) and Ettori *et al.* (2009) used a spherical model to describe the clusters and the fiducial model used in both samples was the $\Lambda CDM$ scenario.

### 3.1. Analysis and results

Again, a possible departure from the CDDR ($\eta = 1$) was parametrized by using two functional forms for $\eta(z)$, how defined earlier.

By combining Eqs. (1) (with $\eta = 1$) and (5), we define

$$\eta_{obs}(z) = \frac{D_L^3 f_{gas}^2}{N^2 (1+z)^6 D_A^{*3}} \tag{6}$$

and the likelihood estimator is defined by $\chi^2$ statistics as in (3) and where $\sigma_{obs}$ takes into account the propagation of the statistical errors in eq. (6).

For La Roque *et al.* samples was obtained $\eta_0 = -0.03^{+1.03}_{-0.65}$ ($\chi^2_{dof} = 1.34$) for P1 and $\eta_0 = -0.08^{+2.28}_{-1.22}$ ($\chi^2_{dof} = 1.34$) for P2 and for Ettori *et al.* samples was obtained

$\eta_0 = -0.97^{+0.54}_{-0.38}$ ($\chi^2_{dof} = 1.12$) for P1 and $\eta_0 = -1.60^{+0.90}_{-0.70}$ ($\chi^2_{dof} = 1.13$) for P2, both in $2\sigma$ confidence level.

Regardless of the CDDR parameterization adopted, we clearly see that the La Roque *et al.* (2006) plus SNe Ia sample is in perfect agreement with the $\eta_0 = 0$ value ($\eta = 1$), which means that CDDR is valid, whereas the Ettori *et al.* (2009) plus SNe Ia data presents a significant conflict.

## 4. Conclusions

In this paper we examined two cosmological model-independent methods to test the CDDR by using galaxy clusters and SNe Ia observations. We also saw that $f_{gas}$ model function depends explicitly on the CDDR, as well as, the CDDR's validity is closely dependent of assumptions used to describe galaxy clusters.

The achieved results by the first method, although independent of any cosmological scenario, depends on the starting physical hypotheses describing the galaxy clusters since their analysis revealed that the isothermal elliptical $\beta$ model is compatible with the CDDR at $1\sigma$ while the non-isothermal spherical model is only marginally compatible at $3\sigma$.

In addition, for all analyses performed in two tests, a negative value of $\eta_0$ is preferred. In principle, this result can be explained in terms of cosmic opacity that can violate the CDDR (Corasaniti, 2006) or the existence of axion-like and mini-charged particles (Avgoustidis *et al.*, 2010).

Therefore, the presented results reinforce the interest in searching for new and independent methods to test the CDDR.

## References

Amanullah, R. et al.. 2010, ApJ, 716, 712
Avgoustidis, A. et al. 2010, JCAP, 024, 1010
Basset, B. A. & Kunz, M. 2004, PRD, 69, 101305
Bonamente, M. et al. 2006, ApJ, 647, 25
Cavaliere, A. & Fusco-Fermiano, R. 1978, A&A, 667, 70
Corasaniti, P. S. 2006, MNRAS, 372, L191
Ellis, G. F. R. 2007, GRG, 39, 1047
Etherington, I. M. H. 1933, Phil. Mag., 15, 761; reprinted in 2007, GRG, 39, 1055
Ettori, S. et al. 2009, A&A, 501, 61
Filippis, E. S. et al., 2005, ApJ, 625, 108
Gonçalves, R. S., Holanda, R. F. L. & Alcaniz, J. S. 2012, MNRAS, 420, L43
Holanda, R. F. L., Lima, J. A. S. & Ribeiro, M. B. 2010, ApJL, 722, L233
Holanda, R. F. L., Lima, J. A. S. & Ribeiro, M. B. 2011, A&A, 528, L14
La Roque, S. J. et al. 2006, ApJ, 652, 917
Mason, B. S. et al. 2001, ApJ, 555, L11
Nesseris, S. & García-Bellido, J. 2012, JCAP, 11, 033
Reese, E. D. et al. 2002, ApJ, 581, 53

Sarazin, C. L. 1988, "X-ray Emission from Cluster of Galaxies", Cambridge University Press, New Jersey

Sasaki, S. 1996, PASJ, 48, L119

Uzan, J. P., Aghanim, N. & Mellier, Y. 2004, PRD, 70, 083533

*Gravitation, Relativistic Astrophysics and Cosmology*
*Second Argentinian-Brazilian Meeting, 2014*
*G. S. Vila, F. L. Vieyro and J. Fabris, eds.*

# Thin-shell wormholes in Einstein-Born-Infeld theory

Ernesto F. Eiroa[1,2] and Griselda Figueroa Aguirre[1]

[1]*Instituto de Astronomía y Física del Espacio, Buenos Aires, Argentina*
[2]*Departamento de Física, FCEN-UBA, Buenos Aires, Argentina*

**Abstract.** We construct spherically symmetric thin-shell wormholes with a generalized Chaplygin gas at the throat, in Born-Infeld electrodynamics coupled to Einstein gravity. We analyze their stability under radial perturbations.

## 1. Introduction

Traversable Lorentzian wormholes (Morris et al. 1988) are theoretical objects with a throat that connects two regions of the same universe or two different universes. They are characterized by being threaded by matter that violates the null energy condition and its amount can be arbitrarily small at the cost of increasing the pressure at the throat. A particular class of wormholes can be obtained by using the thin-shell formalism, i.e. by cutting and pasting two manifolds to construct a new one, with a shell at the joining surface corresponding to the throat (Poisson et al. 1995), which must fulfill the flare-out condition.

Born-Infeld electrodynamics is a non-linear theory proposed in order to avoid the infinite self energies of charged point particles arising in Maxwell theory. Born-Infeld type actions have appeared in low energy string theory, leading to an increasing interest in non-linear electrodynamics. The field equations obtained from the action of Born-Infeld electrodynamics coupled to Einstein gravity have the spherically symmetric vacuum solution (Bretón 2002):

$$ds^2 = -\psi(r)dt^2 + \psi(r)^{-1}dr^2 + r^2(d\theta^2 + \sin^2\theta d\phi^2), \tag{1}$$

$$\psi(r) = 1 - \frac{2M}{r} + \frac{2}{3b^2}\left\{r^2 - \sqrt{r^4 + b^2Q^2} + \frac{\sqrt{|bQ|^3}}{r}F\left[\arccos\left(\frac{r^2 - |bQ|}{r^2 + |bQ|}\right), \frac{\sqrt{2}}{2}\right]\right\}, \tag{2}$$

with $M$ the mass, $Q$ the charge, and $F(\gamma, k)$ the elliptic integral of the first kind.

## 2. Wormhole construction and stability analysis

From the geometry (1) we construct the thin-shell wormholes, by using the Darmois-Israel formalism (Israel 1966). We cut and paste two identical copies of the region $r \geq a$; then at $r = a$ there is a shell where the throat is located. We let $a = a(\tau)$, with $\tau$ the proper time on the shell, and we take $a$ larger than the horizon radius $r_h$, in order to avoid the presence of the horizons and the singularity in the new manifold. The Einstein equations on the shell can be reduced to Lanczos equations that relate the extrinsic curvature with the surface stress-energy tensor $S_{ij} = \mathrm{diag}(\sigma, p_{\hat{\theta}}, p_{\hat{\varphi}})$, with $\sigma$

the surface energy density and $p_{\hat{\theta}}$, $p_{\hat{\varphi}}$ the transverse pressures, from which we obtain

$$\sigma = -\frac{\sqrt{\psi(a) + \dot{a}^2}}{2\pi a}, \tag{3}$$

$$p = p_{\hat{\theta}} = p_{\hat{\varphi}} = \frac{\sqrt{\psi(a) + \dot{a}^2}}{8\pi} \left[ \frac{2}{a} + \frac{2\ddot{a} + \psi'(a)}{\psi(a) + \dot{a}^2} \right]. \tag{4}$$

From Eq. (3) we see that $\sigma < 0$, which indicates the presence of exotic matter at the junction shell. In a previous related work (Richarte et al. 2009), the matter at throat was modelled by a gas with a linearized equation of state; here we adopt a generalized Chaplygin gas (Bento et al. 2002), with an equation of state

$$p = A|\sigma|^{-\alpha}, \tag{5}$$

where $A > 0$ and $0 < \alpha \leq 1$ are constants. The generalized Chaplygin gas has been adopted in current cosmology studies in order to explain the accelerated expansion of the universe. The dynamical evolution of the wormhole throat can be obtained by replacing Eqs. (3) and (4) into Eq. (5) to give

$$\left\{ [2\ddot{a} + \psi'(a)]a^2 + [\psi(a) + \dot{a}^2]2a \right\} [2a]^{\alpha} - 2A[4\pi a^2]^{\alpha+1}[\psi(a) + \dot{a}^2]^{(1-\alpha)/2} = 0. \tag{6}$$

This equation should be satisfied by thin-shell wormholes in Einstein-Born-Infeld theory, threaded by exotic matter with the equation of state of a generalized Chaplygin gas. If static solutions exist, they should satisfy Eq. (6) evaluated at a constant $a_0$. We can obtain $\sigma = \sigma(a)$ by the integration of the equation

$$\dot{\sigma} = -2\,(\sigma + p)\,\frac{\dot{a}}{a}, \tag{7}$$

which comes from the the conservation equation. Then, we replace $\sigma(a)$ in Eq. (4) to find the equation that determines completely the dynamics of the throat:

$$\dot{a}^2 = -V(a) = -\left\{ \psi(a) - [2\pi a \sigma(a)]^2 \right\}, \tag{8}$$

where $V(a)$ can be interpreted as a potential, so it can be expanded in a Taylor series in order to analyze the stability of static solutions. It is not difficult to see that $V(a_0) = V'(a_0) = 0$, so the stability condition is given by $V''(a_0) > 0$, which takes the form (Eiroa et al. 2012)

$$V''(a_0) = \psi''(a_0) + \frac{(\alpha - 1)[\psi'(a_0)]^2}{2\psi(a_0)} + \frac{\psi'(a_0)}{a_0} - \frac{2(\alpha + 1)\psi(a_0)}{a_0^2} > 0. \tag{9}$$

By using Eq. (6) evaluated in $a_0$, we can find the possible throat radii $a_0$, for different values of the Born-Infeld parameter $b$, the constant $A$, the exponent $\alpha$, the mass $M$ and the charge $Q$. These solutions are stable if inequality (9) is fulfilled. The results shown in Figs. 1 and 2 present an important change around $Q_c/M$, where $Q_c$ is the critical charge, corresponding to the extremal value, from which the original metric used in the construction has no horizons. In the plots, the stable solutions are displayed with solid lines, the dotted lines correspond to unstable configurations; and the regions that have no physical meaning are shaded in gray.

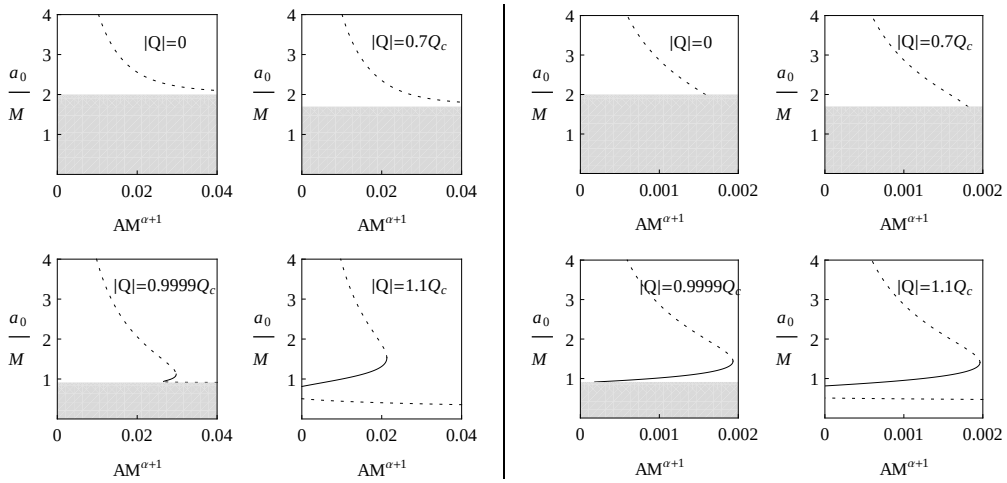


Figure 1. Stability for $b/M = 1$, in this case $Q_c/M = 1.02526$. Left: $\alpha = 0.2$, right: $\alpha = 1$.

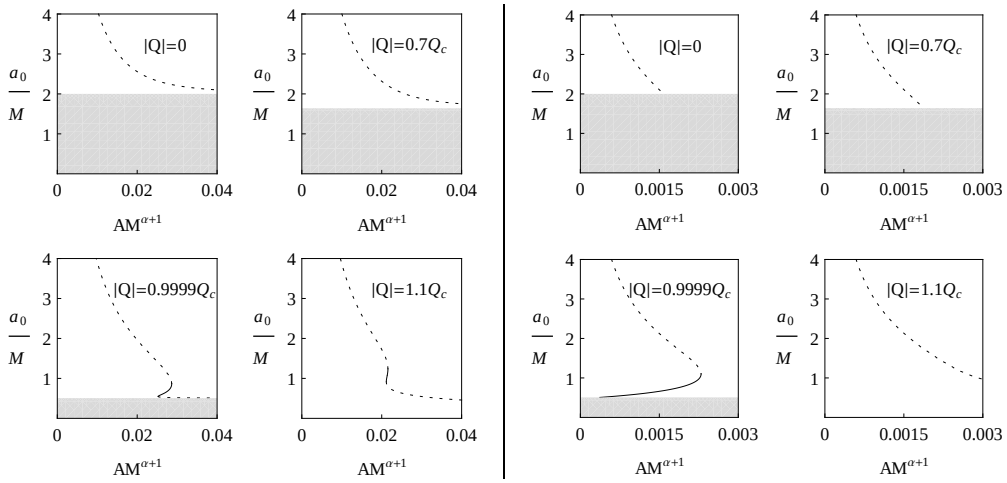


Figure 2. Stability for $b/M = 2$, in this case $Q_c/M = 1.10592$. Left: $\alpha = 0.2$, right: $\alpha = 1$.

- For $b = 0$ (then $Q_c/M = 1$), the Born-Infeld electrodynamics reduces to Maxwell theory, so the Reissner-Nordström solution is used in the wormhole construction (Eiroa, 2009).

- If $0 < b/M \leq 1$ the behavior of the solutions is similar to what is shown in Fig. 1, corresponding to $b/M = 1$ (then $Q_c/M = 1.02526$):

  Case $0 < \alpha < 1$ (for example, $\alpha = 0.2$): For $0 \leq |Q| < Q_c$ and $|Q|$ not very close to $Q_c$, there is one unstable solution for each value of $AM^{\alpha+1}$, and this behavior continues when this parameter grows. For $|Q| \lesssim Q_c$, we find three solutions, one

of them stable; when $AM^{\alpha+1}$ grows there is only one unstable solution close to the radius of the horizon of the original manifold. For $|Q| > Q_c$, there are three solutions, only one of them is stable.

Case $\alpha = 1$: For $0 \leq |Q| < Q_c$ and $|Q|$ not very close to $Q_c$, there is only one solution which is unstable. For $|Q| \lesssim Q_c$, there are two solutions, one stable and the another unstable. For $|Q| > Q_c$, there are three solutions, only one of them is stable.

Comparing the results shown in Fig. 1 with those obtained in Reissner-Nordström case (Eiroa, 2009), we observe a similar behavior when $b = 0$ and when $0 < b/M \leq 1$, for the same values of $\alpha$. The only difference is found in the case $|Q| > Q_c$, where there is a small unstable solutions for $0 < b/M \leq 1$ which is not present in $b = 0$ case.

- From Fig. 2, corresponding to $b/M = 2$ (then $Q_c/M = 1.10592$):

  Case $0 < \alpha < 1$ (for example, $\alpha = 0.2$): For $0 \leq |Q| < Q_c$ and $|Q|$ not very close to $Q_c$, there is always one unstable solution. For $|Q| \lesssim Q_c$ or $|Q| > Q_c$, there exists three solutions, one of them is stable.

  Case $\alpha = 1$: For $0 \leq |Q| < Q_c$ or $|Q| > Q_c$, with $|Q|$ not very close to $Q_c$, there is only one unstable solution. For $|Q| \sim Q_c$, there are two solutions, one of them stable.

- When $b/M$ takes large values (not shown in the figures), for example if $b/M = 5$, (then $Q_c/M = 1.48468$), for any values of $\alpha$ and $Q$ there is only one solution, which is always unstable (Eiroa et al. 2012).

## 3. Conclusions

For small values of $b/M$, the behavior of the solutions resemble the one obtained for Reissner-Nordström metric, except that in the Einstein-Born-Infeld case are found unstable solutions for large values of $|Q|/M$. As $b/M$ increases, i.e. when the theory is distancing itself from Einstein-Maxwell, the stability region becomes smaller. For large values of $b/M$ the stable solutions are not longer present.

**Acknowledgments.** This work was supported by CONICET and UBA.

## References

Bento, M. C., Bertolami, O. & Sen, A. A. 2002, Phys. Rev. D 66, 043507

Bretón, N. 2002, Class. Quantum Grav. 19, 601

Eiroa, E. F. 2009, Phys. Rev. D, 80, 044033

Eiroa, E. F. & Figueroa Aguirre, G. 2012, Eur. Phys. J. C 72, 2240

Israel, W. 1966, Nuovo Cimento B 44, 1; 1967, ibid. 48, 463(E)

Morris, M. S. & Thorne, K. S. 1988, Am. J. Phys. 56, 395

Poisson, E. & Visser, M. 1995, Phys. Rev. D 52, 7318

Richarte, M. G & Simeone, C. 2009, Phys. Rev. D 80, 104033; 2010, ibid. 81, 109903(E)

*Gravitation, Relativistic Astrophysics and Cosmology*
*Second Argentinian-Brazilian Meeting, 2014*
*G. S. Vila, F. L. Vieyro and J. Fabris, eds.*

# Stability of thin disks with a dipolar magnetic field

Vanessa Pacheco de Freitas[1] and Alberto Saa[2]

[1]*Centro Brasileiro de Pesquisas Físicas, Rio de Janeiro, RJ, Brazil*
[2]*Departamento de Matemática Aplicada, UNICAMP, Campinas, SP, Brazil*

**Abstract.** We use the "displace, cut and reflect" method to generate thin disks from Gutsunaev-Manko solution of Einstein Equations. This solution represents a massive object endowed with magnetic dipole moment and our purpose is to study the stability of the disk-like configurations obtained with this method.

## 1. Introduction

Solutions that represents the gravitational field of an object with axial symmetry can be used to model galaxies and accretion disks. Magnetic fields have an important part in the study of astrophysical objects, such as neutron stars, white dwarfs, black holes and of galaxy formation. There is in our analysis, therefore, astrophysical interest in incorporating magnetic fields.

We can obtain solutions of Einstein Equations that correspond to disk-like configurations and these solutions have been studied for many years. Disks without radial pressure were initially studied by Bonnor and Sackfield (Bonnor & Sackfield, 1968) and Morgan and Morgan (Morgan & Morgan, 1969). Static disks with radial pressure were studied by Morgan and Morgan (Morgan & Morgan, 1970). We can also have the superposition of a disk with a black hole (Lemos & Letelier, 1993) and include other physical elements like magnetic fields for example (Letelier, 1990).

## 2. The "displace, cut and reflect" method

We can separate the "displace, cut and reflect" method in three steps: first, we choose an hypersurface that divide the space containing a gravitational source in two, one of which contains this source; second, we discard the part of space with the gravitational source; and third, we reflect the non-singular region across the plane $z = 0$ delimited by our surface. The result of this method will be a space with a singularity of the Dirac delta type with support on the surface $z = 0$ and this is equivalent to make the mathematical transformation $z \to |z| + z_0$ (Vogt & Letelier, 2003).

## 3. Stability analysis

The analysis is made through a perturbation in the energy-momentum tensor and we study the conservation of the perturbed equations of motion. Considering an orthonormal basis of tetrads we can write the energy-momentum tensor as $Q^{\alpha\beta} = (\sigma U^\alpha U^\beta + P_r X^\alpha X^\beta + P_\varphi Y^\alpha Y^\beta)\delta(z)$, where $\sigma, P_r$ and $P_\varphi$ are the energy density, radial and azimuthal pressures, $U^\alpha$ is the quadrivelocity of the fluid and $X^\alpha, Y^\alpha$ are the main time-like

directions of the fluid. For a perturbation like $\delta Q^{\alpha\beta}(t,r,\varphi) = \delta Q^{\alpha\beta}(r)e^{i(k_\varphi \varphi - \omega t)}$. the conservation equations to the perturbed energy-momentum tensor $(\delta Q^{\alpha\beta})_{;\beta} = 0$ are

$$\delta U^r_{,r}(\sigma U^t + \xi_1 P_r X^r) + \delta U^r[F(t,r,\sigma U^t) + \xi_{1,r} P_r X^r + \\ +\xi_1 F(t,r,P_r X^r)] + \delta U^\varphi[ik_\varphi(\sigma U^t + \xi_2 P_\varphi Y^\varphi)] + \delta\sigma(-i\omega U^t U^t) = 0, \tag{1}$$

$$\delta P_{r,r}(X^r X^r) + \delta U^r[-i\omega(\sigma U^t + \xi_1 P_r X^r)] + \delta\sigma(U^t U^t \Gamma^r_{tt}) + \\ +\delta P_r G(r,r,X^r X^r) + \delta P_\varphi Y^\varphi Y^\varphi \Gamma^r_{\varphi\varphi} = 0, \tag{2}$$

$$\delta U^\varphi[-\omega(\sigma U^t + \xi_2 P_\varphi Y^\varphi)] + \delta P_\varphi(k_\varphi Y^\varphi Y^\varphi) = 0, \tag{3}$$

where $\xi_1 = -X_r/U_t, \xi_2 = -Y_\varphi/U_t, F(I,J,K) = K_{,J} + K(2\Gamma^I_{IJ} + \Gamma^\lambda_{\lambda J})$ and $G(I,J,K) = K_{,J} + K(\Gamma^I_{IJ} + \Gamma^\lambda_{\lambda J})$.

For the case of disks with the radial pressure equals to the azimuthal pressure ($P_r = P_\varphi = P$) we have

$$\delta P = \left(\frac{P_{,r}}{\sigma_{,r}}\right)\delta\sigma, \tag{4}$$

and rearranging Equations (1)-(3) we obtain the expression

$$A_S \delta\sigma_{,rr} + B_S \delta\sigma_{,r} + C_S \delta\sigma = 0, \tag{5}$$

where $A_S, B_S$ and $C_S$ depend on the coefficients of these same equations.

For disks without radial pressure ($P_r = \delta P_r = 0$) we obtain from substituting $U^\varphi$ and $U^r$ in Equation (1) a first order differential equation to the perturbation $\delta\sigma$

$$A\delta\sigma_{,r} + B\delta\sigma = 0 \Rightarrow \delta\sigma = e^{\int(-B/A)dr}, \tag{6}$$

where $A$ and $B$ depend on the coefficients of Equations (1)-(3).

## 4. Applications of the method and final remarks

If we apply the method to Schwarzschild solution we observe that the perturbation profiles are stable and have oscillatory form (see Figure 1). Considering the Gutsunaev-Manko case, by analyzing the perturbation profiles we get singularities and could not find any stable modes (see Figure 2).

### 4.1. Schwarzschild solution

Schwarzschild solution in cylindrical coordinates is

$$ds^2 = \frac{\left(1 - \frac{m}{2\sqrt{r^2+z_0^2}}\right)^2}{\left(1 + \frac{m}{2\sqrt{r^2+z_0^2}}\right)^2} dt^2 - \left(1 + \frac{m}{2\sqrt{r^2+z_0^2}}\right)^4 \left[dr^2 + dz^2 + r^2 d\varphi^2\right]. \tag{7}$$

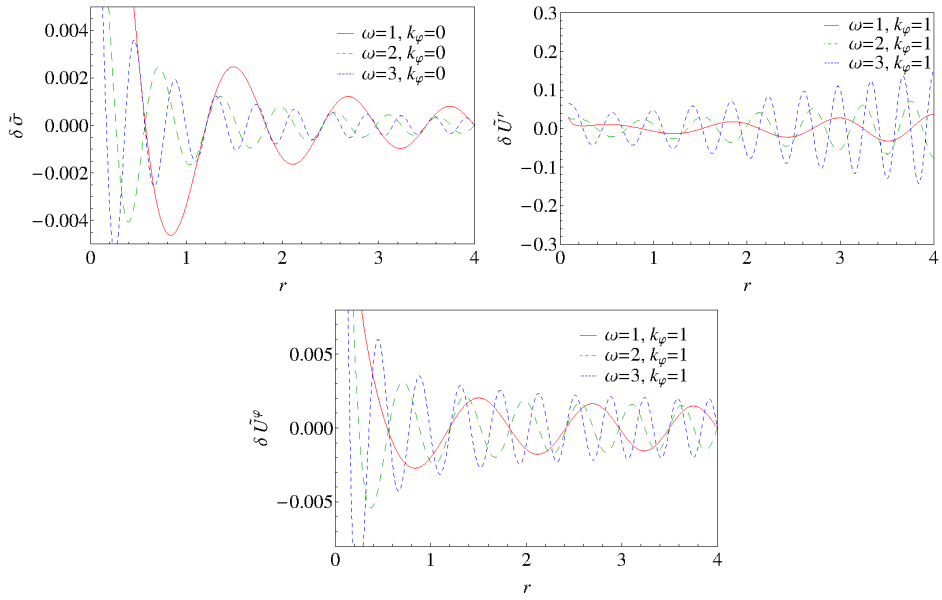


Figure 1. Perturbation profile for the energy density, radial and azimuthal velocity for the parameters $z_0 = 0.5$ and $m = 0, 4$

### 4.2. Gutsunaev-Manko solution

We can include magnetic field using Gutsunaev-Manko solution, which represents a massive object endowed with a magnetic dipole moment (Gutsunaev & Manko, 1987). This solution in prolate ellipsoidal coordinates can be written as:

$$f = \frac{x-1}{x+1}\left[\frac{[x^2-y^2+\alpha^2(x^2-1)]^2+4\alpha^2x^2(1-y^2)}{[x^2-y^2+\alpha^2(x-1)^2]^2-4\alpha^2y^2(x^2-1)}\right]^2, \tag{8}$$

$$e^{2\gamma} = \frac{x^2-1}{x^2-y^2}\frac{\left[[x^2-y^2+\alpha^2(x^2-1)]^2+4\alpha^2x^2(1-y^2)\right]^4}{(1+\alpha^2)^8(x^2-y^2)^8}, \tag{9}$$

where $f = f(r,z)$ and $\gamma = \gamma(r,z)$ are the components of a general axially symmetric metric

$$ds^2 = f\,dt^2 - \frac{1}{f}\left[e^{2\gamma}(dr^2+dz^2)+r^2d\varphi^2\right]. \tag{10}$$

We regain Weyl coordinates with the transformation

$$x = \frac{1}{2k}\left[\sqrt{r^2+(z+k)^2}+\sqrt{r^2+(z-k)^2}\right] \tag{11}$$

$$y = \frac{1}{2k}\left[\sqrt{r^2+(z+k)^2}-\sqrt{r^2+(z-k)^2}\right], \tag{12}$$

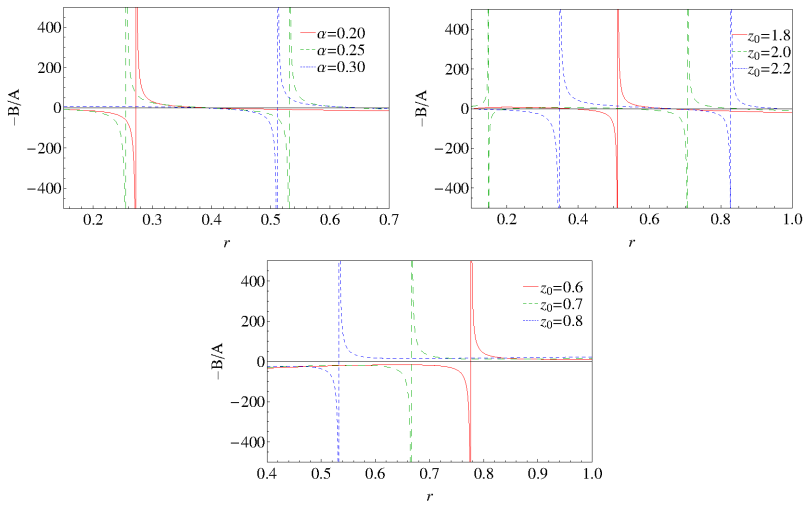


Figure 2. Profile of $(-B/A)$ present in the solution of the perturbation in the energy density for ($z_0 = 1.8, k_\varphi = 0$ and $\omega = 1$), ($\alpha = 0.3, k_\varphi = 0$ and $\omega = 1$) and ($\alpha = 0, k_\varphi = 0$ and $\omega = 1$) with $m = 1$.

with $k = m(1 + \alpha^2)/(1 - 3\alpha^2)$.

## 5. Summary and perspectives

It is important to mention that the electromagnetic potential is continuous and has reflection symmetry across the plane $z = 0$, but the magnetic field posses discontinuities at this surface in such way that our disk presents a superficial monopole density, which impairs us of considering this disk a viable physical solution to describe real astrophysical objects.

A possible extension of this work would be the inclusion of other physical elements, such as rotation. We could also analyse how the magnetic field alters the properties of thick disks.

**Acknowledgments.** Research supported by CNPq.

## References

Bonnor, W. A. & Sackfield, A. 1968, Comm. Math. Phys., 8, 338
Lemos, J. P. S. & Letelier, P. S. 1993, Class. Quantum Grav., 10, L75
Letelier, P. S. 1999, Phys. Rev. D, 60, 104042
Gutsunaev, Ts. I. & Manko, V. S. 1987, Phys. Lett. A, 123, 215
Morgan, L. & Morgan, T. 1969, Phys. Rev., 183, 1097
Morgan, L. & Morgan, T. 1970, Phys. Rev D, 2, 2756
Vogt, D. & Letelier, P.S. 2003, Phys. Rev. D, 68, 104002

*Gravitation, Relativistic Astrophysics and Cosmology*
*Second Argentinian-Brazilian Meeting, 2014*
*G. S. Vila, F. L. Vieyro and J. Fabris, eds.*

# Structure of compact stars in Palatini $f(R)$ gravity

Federico García,[1,2,†] Florencia A. Teppa Pannia,[1,2]
Santiago E. Perez Bergliaffa,[3] Mariana Orellana,[4] and Gustavo E. Romero[1,2]

[1]*Instituto Argentino de Radioastronomía (CCT La Plata, CONICET), C.C.5, (1894) Villa Elisa, Buenos Aires, Argentina*
[2]*Facultad de Ciencias Astronómicas y Geofísicas, Universidad Nacional de La Plata, Argentina*
[3]*Departamento de Física Teórica, Instituto de Física, Universidade do Estado de Rio de Janeiro, Brazil*
[4]*Sede Andina de la Universidad Nacional de Río Negro, Argentina*
[†]*e-mail: fgarcia@iar-conicet.gov.ar*

**Abstract.** The study of the structure of compact objects in modified theories of gravity can be useful to constrain $f(R)$-theories in the strong gravitational regime. In particular, the structure of compact stars in the theory with Lagrangian density $f(R) = R + \alpha R^2$ have been recently explored using the metric formalism.

In this work we analyze configurations of neutron stars in *squared*-gravity using the Palatini formalism, in which the field equations are of second order, and the modified Tolman-Oppenheimer-Volkoff equations for a spherically-symmetric and static metric can be derived without approximation, as in General Relativity.

The numerical integration of the structure equations allows us to study the mass-radius configurations and the characteristics of internal profiles.

We compare our results with those obtained using General Relativity.

## 1. Analytical formulation

The so-called $f(R)$ theories of gravity are obtained when the Ricci curvature scalar, $R$, is replaced, in the Einstein-Hilbert action, by a function of it. In particular, the simplest choice $f(R) = R + \alpha R^2$, also called *squared*-gravity, has been shown to be a viable alternative to General Relativity (GR), which satisfies the current Solar System tests for gravity (Sotiriou & Faraoni, 2010). However, gravity in the strong gravitational regime is largely unconstrained by observations. Hence, the study of the properties of Neutron Stars (NSs) and Quark Stars (QSs) in different gravitational frameworks may help in setting constraints (and eventually discard) alternative theories.

The modified Hilbert-Einstein action for *squared*-gravity in the Palatini formalism is

$$S[g, \Gamma, \psi_{\rm m}] = \frac{1}{16\pi} \int {\rm d}^4x \sqrt{-g}\, f(R) + S_{\rm m}[g_{\mu\nu}, \psi_{\rm m}], \tag{1}$$

where $f(R) = R + \alpha R^2$, $R \equiv g^{\mu\nu} R_{\mu\nu}(\Gamma)$, $R_{\mu\nu}(\Gamma) = -\partial_\mu \Gamma^\lambda_{\mu\nu} + \partial_\lambda \Gamma^\lambda_{\mu\nu} + \Gamma^\lambda_{\mu\nu}\Gamma^\rho_{\nu\lambda} - \Gamma^\lambda_{\nu\rho}\Gamma^\rho_{\mu\lambda}$ and $\Gamma^\lambda_{\mu\nu}$ is the connection. The matter action, $S_{\rm m}$, depends on the matter field, $\psi_{\rm m}$, and the metric, $g_{\mu\nu}$, but is independent of the Christoffel symbols. Here $\alpha$ is a free

parameter of the theory which must be positive due to stability considerations (Sotiriou & Faraoni, 2010). The scalar curvature $R$ can be solved as an algebraic function of the trace $T$ of the energy-momentum tensor as $R = -8\pi T$.

We assume a spherically-symmetric and static metric, $ds^2 = -e^{A(r)}dt^2 + e^{B(r)}dr^2 + r^2(d\theta^2 + \sin^2\theta d\phi^2)$, and we consider a perfect-fluid matter with energy-momentum tensor $T_{\mu\nu} = (\rho + p)u_\mu u_\nu + p g_{\mu\nu}$ (where $\rho$ is the energy density and $p$ is the pressure). With these considerations, the modified Tolman-Oppenheimer-Volkoff (TOV) equations are:

$$\frac{dp}{dr} = -\frac{1}{1+\gamma_0}\,\frac{\rho+p}{r(r-2m)}\left(m + \frac{4\pi r^3 p}{1+2\alpha R} - \frac{\alpha_0}{2}(r-2m)\right), \tag{2}$$

$$\frac{dm}{dr} = \frac{1}{1+\gamma_0}\left(\frac{4\pi r^2\rho}{1+2\alpha R} + \frac{\alpha_0+\beta_0}{2} - \frac{m}{r}(\alpha_0+\beta_0-\gamma_0)\right), \tag{3}$$

where $m(r) \equiv r(1 - e^{-B(r)})/2$. The quantities $\alpha_0$, $\beta_0$ and $\gamma_0$ are functions of $f(R)$ and the derivatives of $f(R)$ with respect to $R$ (which depend on the parameter $\alpha$) and the coordinate $r$ (Olmo, 2008; Barausse et al., 2008).

The above system of differential equations can be solved if an Equation of State (EoS) $p = p(\rho)$ is given. Through this work we use three different EoS: PLY, which is a polytropic EoS of adiabatic index 2; SLY, which is a realistic EoS for nuclear matter (Haensel & Potekhin, 2004); and SQM, which is a simple linear EoS for quark matter (Degrand et al., 1975). The derivatives of $f(R)$ with respect to the coordinate $r$, hidden in the functions $\alpha_0$, $\beta_0$ and $\gamma_0$, are expressed in terms of the first and second derivatives of $p$ with respect to $\rho$, by means of the EoS, as $R$ is related to $T$, contrary to GR, where no derivatives of the EoS are involved. Thus, analytical approximations instead of tabular EoS are needed in order to achieve enough precision.

## 2. Results

Based on a Runge-Kutta numerical scheme, we integrate equations (2) and (3) in the radial coordinate from the center to the surface of the star, with boundary conditions: $m(r = 0) = 0$, $p(r = 0) = p_c$, $\rho(r = 0) = \rho_c$, $p(r = R) = 10^{-12}p_c$ and $m(r = R) = M$. A static configuration of total mass, $M$, and radius, $R$, is obtained for each value of $\rho_c$, and for each EoS adopted.

In Figure 1 we show the family of static configurations for the PLY, SLY and SQM EoS considering several values of the $\alpha$ parameter (see the legend). Whereas for simple polytropic EoS (PLY and SQM), the static configurations are almost indistinguishable from GR ($\alpha = 0$), in the case of the realistic and more complex SLY EoS, relevant differences arise. The maximum mass, $M_{\rm max}$, grows up to $\gtrsim 10\%$ when $\alpha_8 = 10$. Moreover, contrary to what is found by means of a perturbative approach in the metric formalism (Arapoğlu et al., 2011; Orellana et al., 2013), $M_{\rm max}$ increases for $\alpha > 0$.

In Figure 2 we show the internal mass profiles $m(\rho)$ obtained for the SLY EoS using the same values of the $\alpha$ parameter (solid lines, left axis), considering $\rho_c = 2.5 \times 10^{15}$ gr cm$^{-3}$, which corresponds to $\sim M_{\rm max}$. Strong differences with the GR case (thick-solid line) can be noted: (i) a huge difference in the total mass, $M$, of the static configurations arises at densities $\sim 10^{14}$ gr cm$^{-3}$, and (ii) a counter-intuitive feature in the mass profile occurs at densities $\sim 5 \times 10^{11}$ gr cm$^{-3}$, which is seen as a dip in the

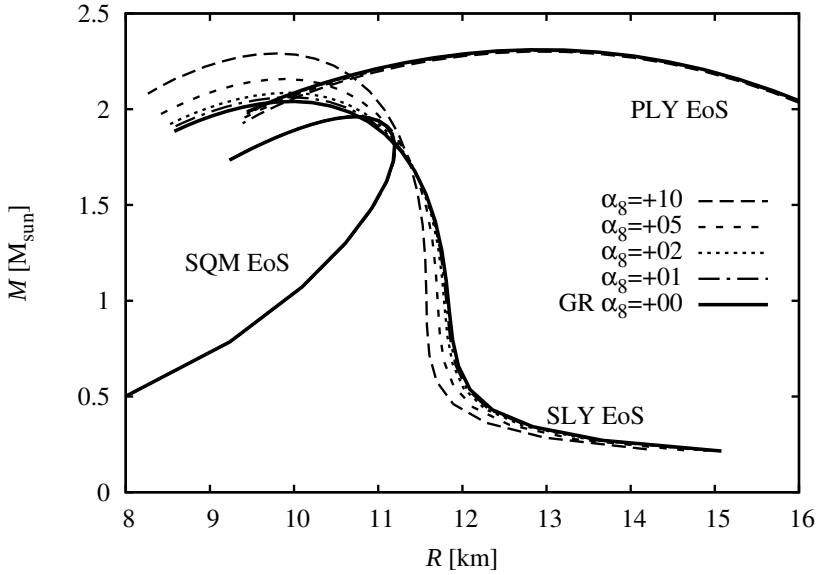


Figure 1. Mass-Radius relations obtained for three EoS considering $\alpha_8 = \alpha/10^8$ cm$^2$ = 10, 5, 2, 1, 0 (GR case).

profile ($dm/d\rho > 0 \rightarrow dm/dr < 0$). The latest behaviour was also pointed out in the metric formalism in Orellana et al. (2013) and it is independent of the value of $\alpha$. In Figure 2, we also plot the logarithmic first and second-order derivatives of the SLY EoS in gray-dashed lines (see right axis), which makes explicit the correlation between this particular behaviour of the profiles and the complexity of the EoS. On the other hand, we found neither counter-intuitive features nor huge differences in the total mass in the internal profiles obtained with PLY and SQM EoS.

## 3. Discussion

We have shown how mass-radius configurations of compact stars are modified under *squared*-gravity in the Palatini formalism. The field equations depend not only on the explicit $p - \rho$ relation (the EoS), but also on the first and second-order derivatives of $p$ with respecto to $\rho$. If a simple polytropic or linear equation is adopted, differences between compact stars in *squared*-gravity and GR are negligible. However, if a realistic EoS, as SLY, is used, the maximum mass achievable can be significantly larger than its value in GR, becoming an observable signature of modified gravity in the strong gravitational regime. Moreover, we also found huge differences in the internal mass profiles, which present a counter-intuitive characteristic ($dm/dr < 0$) in the outer layers of the compact stars.

We shall continue our research by exploring the impact of differentiability constraints on the stellar structure calculations in modified gravity.

**Acknowledgments.** FG, FATP, MO and GER acknowledge support from CONICET. SEPB acknowledges support from FAPERJ and UERJ.

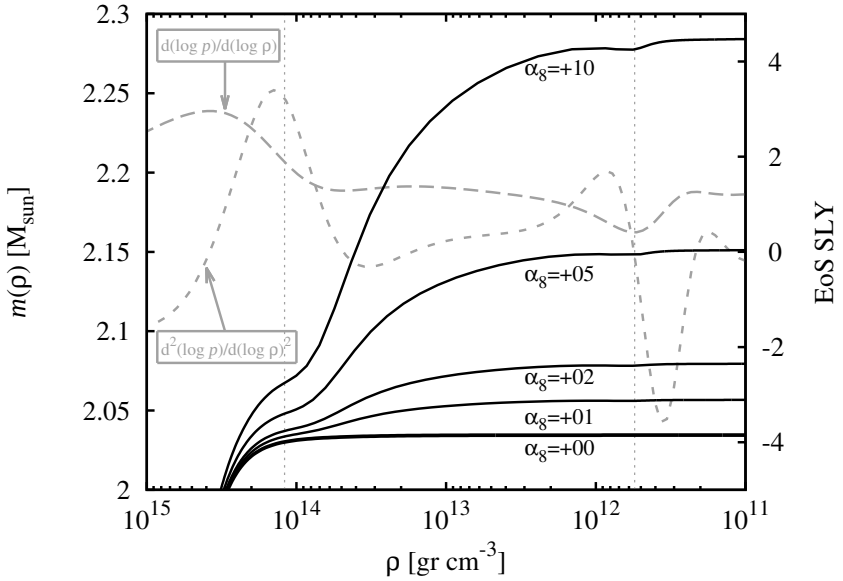


Figure 2. Mass internal profile (black-solid lines, left axis) and logarithmic derivatives of the SLY EoS (gray-dashed lines, right axis) for NS configurations with $\rho_c = 2.5 \times 10^{15}$ gr cm$^{-3}$ and $\alpha_8$ =10, 5, 2, 1, 0 (GR case). Notice the correlation between features on the mass profiles and the high-order derivatives of the realistic EoS, for $\alpha > 0$, at densities $5.5 \times 10^{11}$ and $1.2 \times 10^{14}$ gr cm$^{-3}$ (gray-dotted lines).

## References

Arapoğlu, S. et al. 2011, JCAP, 7, 20

Barausse, E. et al. 2008, C&QG, 25, 062001

Degrand, T., Jaffe, R. L., Johnson, K. & Kiskis, J. 1975, PRD, 12, 2060

Haensel, P. & Potekhin, A. Y. 2004, A&A, 428, 191

Olmo, G. J. 2008, PRD, 78, 104026

Orellana, M. et al. 2013, GR&G, 45, 771

Sotiriou, T. P. & Faraoni, V. 2010, Rev. Mod. Ph., 82, 451

*Gravitation, Relativistic Astrophysics and Cosmology*
*Second Argentinian-Brazilian Meeting, 2014*
*G. S. Vila, F. L. Vieyro and J. Fabris, eds.*

# Vacuum decay and gravitationally particle production leading to cosmic acceleration

L. L. Graef,[1] F. E. M. Costa,[2] and J. A. S. Lima[3]

[1]*Instituto de Física, Universidade de São Paulo, São Paulo, SP, Brazil*
[2]*Universidade Federal Rural do Semi-Árido, Pau dos Ferros, RN, Brazil*
[3]*Departamento de Astronomia, Universidade de São Paulo, São Paulo, SP, Brazil*

**Abstract.** The correspondence between accelerated cosmological models powered by a decaying vacuum energy density and by the gravitationally particle production mechanism is investigated. Although being different in the physics behind them, we show that both classes of models under certain conditions can exhibit the same dynamic and thermodynamic behavior. We also make an observational analysis in order to constraint some classes of these models.

## 1. Introduction

It is well known that the standard model of cosmology, ΛCDM, provides a very good description of the observed Universe. However, despite its observational successes, it suffers from some conceptual problems.

A possible alternative to resolve the cosmological constant problem and the coincidence problem is to suppose that the vacuum energy is not a constant but decays into other cosmic components (Borges & Carneiro, 2005). The usual treatment is to assume that $\Lambda(t) = 8\pi G\rho_v(t)$ is coupled to the other components of the universe thereby producing particles continuously and slowly. In these models the explanation for the present smallness of the vacuum energy density is that it has been decaying during the whole life of the universe, and, as such, the vacuum energy density is small nowadays because the Universe is too old.

Another possibility is the process of matter creation induced by a time varying gravitational field, which is also macroscopically described by a negative pressure (Lima & Germano, 1992). In this kind of model (CCDM models), by assuming that dark matter particles can be produced by a time varying gravitational field, it could be also possible to obtain a late time acceleration in a universe composed only by pressureless fluids, like baryons and cold dark matter (Lima et al. 2008; Fabris et al. 2014; Ramos et al. 2014).

Here we investigate the relations between these two cosmological scenarios, beginning from a dynamical point of view.

Let us consider a generic decaying vacuum model, whose Friedmann equations reduce to:

$$\rho + \Lambda(t) = 3\frac{\dot{a}^2}{a^2} + 3\frac{k}{a^2}\,, \tag{1}$$

$$p - \Lambda(t) = -2\frac{\ddot{a}}{a} - \frac{\dot{a}^2}{a^2} - \frac{k}{a^2}\,, \tag{2}$$

where $\rho$ and $p$ are the energy density and the equilibrium thermostatic pressure of the usual cosmic fluid (baryons, radiation and dark matter) with $p = w\rho$. $a$ is the cosmic scale factor and $k$ is the parameter of curvature. For simplicity, henceforth it will be assumed that the decaying vacuum is coupled only with the dominant component.

The decaying vacuum causes a change in the number of particles of dark matter, so the equation describing particle concentration has a source term, i.e., $N^{\alpha}_{;\alpha} = \dot{n} + 3\frac{\dot{a}}{a}n = n\Gamma$. Where, $\Gamma$ is the rate of change of the number of particles, $n = N/a^3$ is the particle number density and $N^{\alpha} = nu^{\alpha}$ is the particle flux.

By combining Eqs. (1) and (2), or more directly, from the total energy conservation law one finds

$$\dot{\rho} + 3\frac{\dot{a}}{a}(\rho + p) = -\dot{\rho}_{\Lambda} \, . \tag{3}$$

Since the vacuum decay is the unique source of particle creation, we can write $\dot{\rho}_{\Lambda} = -\zeta n\Gamma$, where $\zeta$ is a positive phenomenological parameter.

The second class of scenarios to be considered here are models with gravitationally induced particle production. In this case, the Friedmann equations take the following form

$$\tilde{\rho} = 3\frac{\dot{a}^2}{a^2} + 3\frac{k}{a^2} \, , \tag{4}$$

$$\tilde{p} + p_c = -2\frac{\ddot{a}}{a} - \frac{\dot{a}^2}{a^2} - \frac{k}{a^2} \, , \tag{5}$$

where $p_c$ (creation pressure) is a non-equilibrium correction term describing the particle production. It is given by $p_c = -\alpha\tilde{n}\tilde{\Gamma}/3H$, where $\tilde{\Gamma}$ is the rate of particle creation induced by the varying gravitational field. The particle number density in this case is described by $\tilde{N}^{\alpha}_{;\alpha} = \dot{\tilde{n}} + 3\frac{\dot{a}}{a}\tilde{n} = \tilde{n}\tilde{\Gamma}$. From now on, a tilde denotes the fluid component quantities of the CCDM model in order to distinguish its values from their possible $\Lambda(t)$CDM counterparts.

Combining above equations one finds the conservation equation

$$\dot{\tilde{\rho}} + 3H(\tilde{\rho} + \tilde{p} + p_c) = 0 \, . \tag{6}$$

By comparing the Friedmann equations of the two models we can see that the condition to a dynamic equivalence is given by: $p_c = -(1 + w)\Lambda(t)$. This expression relates $\Lambda(t)$ cosmologies with the corresponding creation pressure of CCDM models.

Special attention has been paid to the process termed "adiabatic" particle production. It means that particles and entropy are produced in the space-time, but the specific entropy (per particle) remains constant ($\dot{\tilde{\sigma}} = 0$). In this case, the parameter $\alpha$ is equal to $(\tilde{\rho} + \tilde{p})/\tilde{n}$, so that the creation pressure reads

$$p_c = -\frac{(\tilde{\rho} + \tilde{p})\tilde{\Gamma}}{3H} = -\frac{(1 + w)\tilde{\rho}\tilde{\Gamma}}{3H} \, . \tag{7}$$

From the equivalence condition together with above equation we find $\Lambda(t) = \tilde{\rho}\tilde{\Gamma}/3H$. By assuming a spatially flat geometry we have that $\tilde{\rho} = 3H^2$, so the equivalence condition reads $\Lambda/H^2 = \tilde{\Gamma}/H$.

## 2. Thermodynamic correspondence

Let us now examine the possibility of a complete thermodynamic equivalence. In order to obtain the thermodynamic description of decaying vacuum-$\Lambda(t)$ models one needs to obtain the evolution equations of the specific entropy ($\sigma = S/N$) and temperature ($T$) of the created component. In this context, the vacuum works like a second component transferring energy continuously to the matter component. We assume that its chemical potential is null ($\mu_v = 0$), so the vacuum equation of state ($p_v = -\rho_v$) implies that $\sigma_v = 0$. Under such conditions, the time-comoving derivative of the entropy flux, which is given by $S^\alpha = n\sigma u^\alpha$, combined with the equation for $N^\alpha_{;\alpha}$, the expression for $\dot{\rho}_\Lambda$, and the Friedmann equations, implies that $\dot{\sigma} + \sigma\Gamma = \Gamma(\zeta - \mu)/T$, where $\mu$ is the chemical potential of the created particles. The temperature satisfies the following evolution law

$$\frac{\dot{T}}{T} = \left(\frac{\partial p}{\partial \rho}\right)_n \frac{\dot{n}}{n} - \frac{\Gamma}{T\left(\frac{\partial \rho}{\partial T}\right)_n}\left[T\left(\frac{\partial p}{\partial T}\right)_n + n\left(\frac{\partial \rho}{\partial n}\right)_T - \zeta n\right]. \tag{8}$$

In the case of CCDM models the specific entropy is given by $\dot{\tilde{\sigma}} + \tilde{\sigma}\tilde{\Gamma} = \tilde{\Gamma}(\alpha - \tilde{\mu})/\tilde{T}$. And the temperature follows the evolution law

$$\frac{\dot{\tilde{T}}}{\tilde{T}} = \left(\frac{\partial \tilde{p}}{\partial \tilde{\rho}}\right)_{\tilde{n}} \frac{\dot{\tilde{n}}}{\tilde{n}} - \frac{\tilde{\Gamma}}{\tilde{T}\left(\frac{\partial \tilde{\rho}}{\partial \tilde{T}}\right)_{\tilde{n}}}\left[\tilde{T}\left(\frac{\partial \tilde{p}}{\partial \tilde{T}}\right)_{\tilde{n}} + \tilde{n}\left(\frac{\partial \tilde{\rho}}{\partial \tilde{n}}\right)_{\tilde{T}} - \alpha\tilde{n}\right]. \tag{9}$$

Comparing the equations above we note that when $\alpha = \zeta$ the two pictures are thermodynamically equivalent. In addition, from the expressions for $\dot{\rho}_\Lambda$ and $p_c$ we also see that such an equality also implies $\dot{\rho}_\Lambda = 3Hp_c$, as should be expected due to the dynamic equivalence.

Now by considering that the particle creation process in both pictures is "adiabatic", some equilibrium relations need to be preserved. In this case the second terms on right-hand side of Eqs. (8) and (9), which correspond to the non-equilibrium contributions, must be identically zero. In this case, it is possible to show that

$$\alpha = \zeta = \frac{\rho + p}{n}. \tag{10}$$

Physically, this relation amounts to saying that ($\dot{\sigma} = 0$). Hence, the equilibrium relations are preserved only if the specific entropy of the created particles is constant. This means that $\frac{\dot{S}}{S} = \frac{\dot{N}}{N} = \Gamma$, for both pictures.

## 3. Unifying the Dark Sector

As seen previously, in vacuum decay models we must consider at least two main components, $\Lambda$ term and dark matter, in which vacuum is decaying. Now, we will interpret the standard model and some $\Lambda(t)$ models that have been discussed in literature in terms of matter creation models. We will restrict ourselves to late time behavior, and, as such, we take $w = 0$.

Firstly, we rewrite Eq. (6) in terms of the interaction rate, i.e.,

$$\dot{\tilde{\rho}} + 3H(\tilde{\rho} - \tilde{\Gamma}H) = 0 \ . \tag{11}$$

Generically, for a given $\Lambda(t)$ model, the corresponding matter creation model is obtained by combining the equivalence condition with (11) and performing the integration.

We are going to consider three particular cases. The Model 1, $\Lambda(t) = cte = \lambda$, corresponds to the standard $\Lambda$CDM model. In this case we have for the corresponding CCDM model, $\tilde{\Gamma} = \lambda/H$, where $\lambda$ is the cosmological constant of the $\Lambda$CDM. Inserting this expression into Eq. (11) and performing the integration, we can find the conservation equation for this model. By substituting the conservation equation into Eq. (4) we can obtain an expression for $H$ as a function of redshift $(z)$, which describes the dynamics of a CCDM scenario that behaves like the $\Lambda$CDM model. Naturally, as discussed in the first sections, due to the thermodynamic and dynamic equivalence it is rather difficult to distinguish observationally between Model 1 and $\Lambda$CDM model.

Through the same method we can obtain the dynamic evolution of the Model 2, described by the simple law $\Lambda = \gamma H$ (Borges & Carneiro, 2005). And also of the Model 3, described by $\Lambda = c + \beta H^2$ (Lima & Maia, 1994).

In our observational analysis we make use of data from SNe Ia (Suzuki et al., 2012) and CMB/BAO ratio, in order to compare the three models through their resulting dynamical equations. We put constraints on the matter density parameters, $\tilde{\Omega}_m$, which quantifies the amount of matter that is clustering in each model, and we also find constraints to the free parameter $\beta$ of Model 3.

For Model 1 we find that the likelihood function peak is at $\tilde{\Omega}_{m1} = 0.282^{+0.014}_{-0.014}$, therefore, in excellent agreement with observations. While for Model 2 the peak is at $\tilde{\Omega}_{m2} = 0.449^{+0.013}_{-0.013}$. This shows that a constant creation rate of particles during the cosmic evolution supplies a current value for $\tilde{\Omega}_m$ higher than the observed. For Model 3 we find $\tilde{\Omega}_{m3} = 0.274^{+0.014}_{-0.014}$ and $\beta = -0.018^{+0.026}_{-0.027}$ at 68.3% confidence level, with $\chi^2_{min} = 563.53$ and $\nu = 581$ degrees of freedom. While the reduced $\chi^2_r \equiv \chi^2_{min}/\nu = 0.97$, thereby showing that the model provides a very good fit to the data.

**Acknowledgments.** L. G. is supported by FAPESP (2012/09380-8).

## References

Borges, H. A. & Carneiro, S. 2005, Gen. Relativ. Gravit., 37, 1385

Fabris, J. C., de Freitas Pacheco, J. A. & Piattella, O. F. 2014, JCAP, 1406, 038

Jesus, J. F., Oliveira, F. A., Basilakos, S. & Lima, J. A. S. 2011

Lima, J. A. S. & Germano, A. S. M. 1992, Phys. Lett. A, 170, 373

Lima, J. A. S. & Maia, J. M. F. 1994, Phys. Rev. D, 49, 5597

Lima, J. A. S., Silva, F. E. & Santos, R. C. 2008, Class. Quant. Grav., 25, 01

Ramos, R. O., Santos, M. V. & Waga, I. 2014, Phys. Rev. D, 89, 083524; Phys. Rev. D, 84, 063511

Suzuki, N. et al. (The Supernova Cosmology Project) 2012, Astrophys. J., 746

*Gravitation, Relativistic Astrophysics and Cosmology*
*Second Argentinian-Brazilian Meeting, 2014*
*G. S. Vila, F. L. Vieyro and J. Fabris, eds.*

# Comparison of predictions from alternative cosmologies with Cosmic Microwave Background data

María Pía Piccirilli,[1] Gabriel León,[2] and Susana J. Landau[2]

[1]*Grupo de Astrofísica, Relatividad y Cosmología, Facultad de Ciencias Astronómicas y Geofísicas, Universidad Nacional de La Plata, Paseo del Bosque S/N, (1900) La Plata, Provincia de Buenos Aires, Argentina*
[2]*Departamento de Física, Facultad de Ciencias Exactas y Naturales, Universidad de Buenos Aires, Ciudad Universitaria - PabI, (1428) Buenos Aires, Argentina*

**Abstract.** The emergence of the seeds of cosmic structure from a perfect isotropic and homogeneous Universe has not been clearly explained by the standard version of inflationary models. We consider alternative scenarios where the emergence of an anisotropic and inhomogeneous Universe from an initial isotropic and homogeneous state can be explained by the of introduction the "self-induced collapse hypothesis", a scheme in which an internally induced collapse of the wave function of the inflaton field is the mechanism by which inhomogeneities and anisotropies arise at each particular length scale. Our aim is to test these models through statistical analysis comparing them with recent data of the Cosmic Microwave Background and galaxy surveys. This procedure will restrict the value of free parameters and test the viability of each scheme using the results of latest observational experiments.

## 1. Introduction

Observations of the Cosmic Microwave Background (CMB) radiation are the most powerful tools to study the early Universe and establish the value of cosmological parameters. In the last decade, there have been great advances concerning the CMB data due to a remarkable increase in the accuracy of observational techniques. Furthermore, the agreement between theory and observations has strengthened the theoretical status of inflationary scenarios among cosmologists.

In the standard inflationary paradigm the emergence of all structures in our Universe like galaxies and galaxy clusters is described by a featureless stage represented by a background Friedmann-Robertson-Walker (FRW) cosmology with a nearly exponential expansion driven by the potential of a single scalar field and from its quantum fluctuations characterized by a simple vacuum state. However, when the scenario is considered more carefully, a conceptual problem emerges regarding a change in the initial symmetries of the Universe. Indeed, the dynamics of quantum unitary evolution cannot explain how an inhomogeneous and anisotropic Universe originates from a completely homogeneous and isotropic initial situation. Dr. Sudarsky and collaborators have developed one proposal to handle these shortcomings (Sudarsky, 2011). To deal with the problem a new ingredient is introduced into the inflationary account of the origin of cosmic seeds: *"the self-induced collapse hypothesis"*. In this scheme an internally induced collapse of the wave function of the inflaton field is the mechanism by which inhomogeneities

and anisotropies arise at each particular length scale. We do not know exactly what kind of physical mechanism would lie behind what looks like a spontaneous collapse of the wave function, as there is no "observer" who can possible "measure" the Universe. We assume that the effect is caused by an unknown quantum aspect of gravitation.

## 2. Collapse models

We consider the action of a scalar field minimally coupled to gravity:

$$S[\phi, g_{ab}] = \int \mathrm{d}^4x\sqrt{-g}\Big(\frac{1}{16\pi G}R[g_{ab}] - \frac{1}{2}\nabla_a\phi\nabla_b\phi g^{ab} - V(\phi)\Big), \tag{1}$$

where $\phi$ is the inflaton field and $g_{ab}$ is the metric. Fields are separated into their homogeneous ("background") part and the perturbations ("fluctuations"). Conformal Newton gauge is the most appropriate choice for this scheme.

Einstein's equations are followed up to the first order and scalar field perturbations are quantized in the framework of a semi-classical gravitation theory (Wald, 1994) $G_{ab} = 8\pi G < \hat{T}_{ab} >_{\phi}$. Hypothesis are: (i) given a value $\eta_k^c$ of conformal time the state collapses to a different one ($\vec{k}$ is not longer in its vacuum state), (ii) the inflaton's wave function is initially the vacuum state, this implies that the metric perturbations are null before the collapse, (iii) each collapse mode represents beginning of inhomogeneities and anisotropies at the characteristic scale of that mode, and (iv) it is possible to describe the state of the system if collapse modes at each time and previous collapse state are known. Primordial power spectrum can be expressed:

$$P(k) = C(k)A_s\left(\frac{k}{k_0}\right)^{n_s-1}, \tag{2}$$

where $C(k)$ is a function that depends on the scheme under which the collapse hypothesis is taking place. In this work we will show results from three different collapse models depending on which variable changes as result of collapse: inflaton field, canonical conjugate momentum or both. It follows from Unánue & Sudarsky (2008) and Landau et al. (2012) that the primordial power spectrum is nearly scale invariant if the time of collapse of each mode can be expressed as:

$$\eta_k^c = \frac{A}{k} + B, \tag{3}$$

where $A$ and $B$ are constants (which value must be constrained). The case where $B = 0$ reduces $P(k)$ to a constant, giving a perfectly scale invariant primordial power spectrum ($n_s = 1$ for the standard model, see De Unáue & Sudarsky, 2008 for $C(k)$ expressions). Therefore, we take this expression for the collapse time in order to start with a scale invariant power spectrum and study small deviations with respect to the standard model. Let us now define a fiducial model, which will be taken just as a reference to discuss the results we obtain for the collapse models. The fiducial model is a $\Lambda$CDM model with the following cosmological parameters: $\Omega_b h^2 = 0.021$, $\Omega_c h^2 = 0.119$, $H_0 = 70$, $\tau = 0.084$, $n_s = 0.96$. The temperature anisotropy for the collapse models together with the prediction for the fiducial model is shown in Figs. 1 and 2.

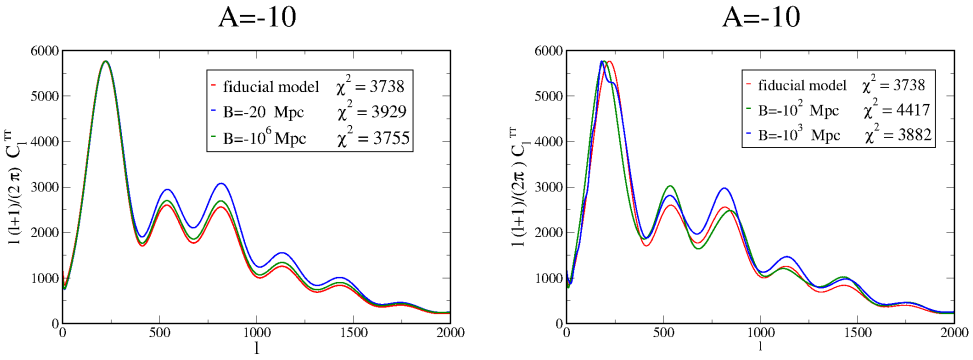


Figure 1. **Model I (left)**: Both expectation values for the field and its canonical conjugate momentum collapse. This plot compares the temperature anisotropy predictions for different values of the collapse conformal time with the fiducial model. For values $|A| > 20$, collapse model I is indistinguishable from the standard one. **Model II (right)**: Only the conjugate momentum changes its expectation value after the collapse. A comparison of the temperature anisotropy predictions for different values of the collapse conformal time is shown. Landau et al. (2012). Reprinted with permission from Physical Review D85, 123001 (2012). Copyright(2012) by the American Physical Society.

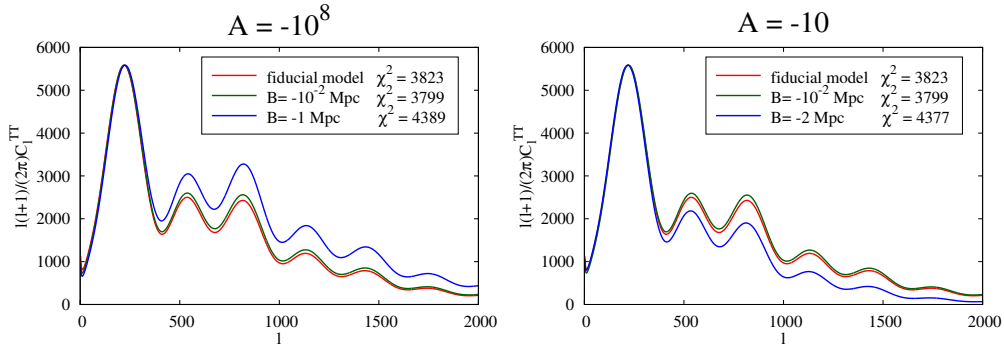


Figure 2. **Model III**. Both field and its canonical conjugate momentum are affected by the collapse following a correlation described by a *Wigner's distribution function*. Both plots compare the temperature anisotropy predictions for different values of the collapse parameters with the fiducial model.

It follows from Fig. 2 that not every value of $\eta_k^c$ gives a good fit to the observational data (represented by the fiducial model). This gives predictability to the model, as not every pair of values for $A$ and $B$ will do. However, there are certain values for the collapse conformal time that fit observational data just as well as the standard paradigm. Once our free parameters are constrained with CMB observations, we will end up with a cosmological model that can explain in a more feasible way the origin of cosmic structures.

## 3. Conclusions

The emergence of the seeds of cosmic structure, from a perfect isotropic and homogeneous Universe, has not been clearly explained by the standard version of inflationary models as the dynamics involved is not capable of breaking the initial symmetries of the system. The *self induced collapse hypothesis* attempts to deal with this problem. The proposal incorporates two free parameters which are to be constrained using the latest CMB data available. Figs. 1 and 2 show that not all the values are viable and some of them must be ruled out. In order to constrain the values of the free parameters $A$ and $B$ we need to perform a statistical analysis with the latest CMB data.

Previous works show that collapse models I and II can explain with enough accuracy the observations provided by WMAP 7-year release. Our aim now is to compare models I, II and III with WMAP 9-year release and Planck data. We are working on different schemes for collapse and also some cutting edge modifications to previous models, such as the possibility of collapse occurring during the radiation era.

**Acknowledgments.** This research is developed in the framework of a CONICET doctoral fellowship, and supported by CONICET PIP 0152/10 and UNLP project 11/G119 grants. We thank Federico Bareilles for computational support.

## References

de Unánue, A. & Sudarsky, D. 2008, Phys. Rev. D, 78, 043510

Landau, S. J., Scóccola, C. G. & Sudarsky, D. 2012, Phys. Rev. D, 85, 123001

Landau, S. J., León, G. & Sudarsky, D. 2013, Phys. Rev. D, 88, 023526

León, G., de Unánue, A. & Sudarsky, D. 2011, Classical and Quantum Gravity, 28, 155010

Perez, A., Sahlmann, H. & Sudarsky, D. 2006, Classical and Quantum Gravity, 23, 2317

Sudarsky, D. 2011, International Journal of Modern Physics D, 20, 509

Wald, R. M. 1994, "Quantum field theory in curved spacetime and black hole thermodynamics", Chap. 4, The University of Chicago Press

*Gravitation, Relativistic Astrophysics and Cosmology*
*Second Argentinian-Brazilian Meeting, 2014*
*G. S. Vila, F. L. Vieyro and J. Fabris, eds.*

# Study of pulse structure of long GRBs: radiative mechanisms associations and geometry of the emission

Jonathan Quirola and Nicolás Vásquez

*Physics department, Escuela Politécnica Nacional, Quito, Ecuador*

**Abstract.** Gamma Ray-Bursts (GRBs) are considered one of the most enigmatic events as well as one of the oldest known in the Universe. In this work, we have studied ten different GRBs detected by Swift mission with redshift between $z = 0.69$ and $z = 3.60$. We have used the pulse model proposed by Norris (2005) for each GRB in four different energy bands to fit only regular pulses. The analysis suggests that there are two type of pulses associated with two specific radiation mechanisms which remain invariant to different ages of the Universe. In fact, it confirmed that GRBs are candidates to standard candles. We have analyzed light curves from different pulses and spectral lag of each GRB. Also, we have determined correlations between spectral lag with some others spectral parameters. We verified if the GRB's analysis is consistent with the two types of pulses defined by the physical classification (Zhang 2009), and the relation of these with the geometry during its emission founded.

## 1. Introduction

GRBs are bringing important information about the expansion of the Universe (Piran 2004, Zhang & Mészáros 2004) as distances and cosmological effects (Piran 2004). GRBs with known redshift are useful distance indicators of primordial stars, and could help to track the history of the star formation in the Universe. One characteristic of GRB prompt emission is the spectral lags (Norris et al. 2005, Arimoto et al. 2010) which is the time delay in the arrival of low-energy emissions relative to high-energy emissions ($\tau_{lag} = t_{peak,low} - t_{peak,high}$). We proposed to obtain spectral lag (between six energy bands) with Norris' model (Norris et al. 2005, Arimoto et al. 2010). Furthermore, we found possible correlations between spectral lags and other spectral parameters.

## 2. Prompt emission

The GRB prompt emission is believed to have a non-thermal origin spectroscopically. The emission is believed to originate from relativistic electrons and positrons accelerated in relativistic outflows. The radiation is generated in strong magnetic fields. In addition, the most natural emission mechanism should be Synchrotron and a well stablish model is the fireball (Resmi & Zhang 2012). This model considers that internal shocks are created by collisions between relativistic shells with different Lorentz factors ejected by a central engine (Zhang & Mészáros 2004). Internal shocks are candidates for fermions acceleration and is associated to a non-thermal emission. The most natural mechanism for non-thermal emission is Synchrotron (Zhang & Mészáros 2004). Nevertheless, there are some evidence that a simple Synchrotron spectrum does not fit all bursts (Resmi

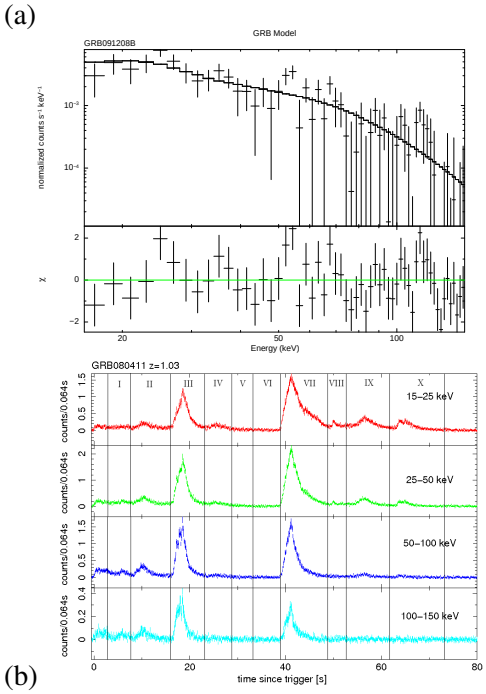


Figure 1. (a) Band Model spectrum of GRB 091208B and (b) GRB 080411 in four different energy bands.

& Zhang 2012). Others candidate mechanisms are inverse Compton and Synchrotron self-Compton (Piran 2004). Different kinds of physical process can be involved such as particle acceleration, magnetic field amplification, among others.

## 3. Methodology

We chose ten GRBs with redshift between $z = 0.69$ and $z = 3.60$. We extracted light curves and spectrum using Heasoft 6.15.1 and the specific tools for *Swift* analysis. Additionally, we used light curves with a binsize of 0.125 seconds. In order to extract the spectral lag for each GRB, we generated four light curves in the following bands: 15-25 keV, 25-50 keV, 50-100 keV and 100-150 keV.

### 3.1. Pulse fitting

To determine the spectral lag we have compared the shape of the pulses in four different energy bands. We have used the pulse model proposed by Norris et al. (2005), which is presented as follows:

$$I(t) = A \exp(2\sqrt{\tau_1 \tau_2}) \exp(\tau_1/t - t/\tau_2).$$

The maximum amplitude of the pulse is determined by the expression: $t_{peak} = \sqrt{\tau_1 \tau_2}$. The spectral lag is defined as the difference between maximum amplitudes in low and high energy bands: $\tau_{lag} = t_{low} - t_{high}$ (Arimoto et al. 2010). Using Norris' model for this analysis, we found that the gamma-rays arrived before x-rays in 90% of pulses.

### 3.2. Spectral Fitting

For spectral analysis, we used three different spectral models for each GRB and its regions. We used *Power law model* in regions with low signal to noise ratio. However, regions with regular pulses we used the *Band Model* and *Cutoff power law model* normalized to 50 keV.

## 4. Results

We studied the spectral lag associated to individual GRB's pulses. In this research, we defined six different spectral lags based on the four energy bands chosen. Figure 2(a) shows two different kind of emissions associated with two photon indices for GRB 080411. The analysis of seventeen pulses is presented in Figure 2(b), where is possible to observed that the luminosity are divided in two groups of pulses with short and long lags. One group is associated with short lags and the release of high energies. On the other hand, a second group is related to long lags, low energies and is related with an interaction with the circumburst medium. Furthermore, we found a possible correlation between low photon index and short spectral lag.
In the analysis, we are found pulses that appeared in low energy bands and vanished in high energy bands. We observed that high energy photons arrived before low energy photons because the burst must be related with the geometry of the emission.

Table 1 shows the spectral fitting parameters such as photon index, luminosity and energy peak for regions of GRBs. Gamma-ray burst had regions with regular pulses and others regions without pulses. Therefore, in regions without pulses (low signal to noise ratio) we applied Power law model and regions with regular pulses we used the normalized model or Band model.

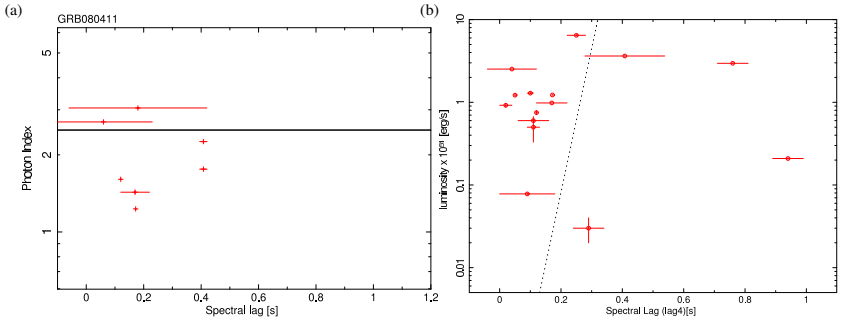


Figure 2. (a) GRB 080411: $t_{lag}$ vs Photon Index and (b) $t^4_{lag}$ ($\tau_{50-100}$ − $\tau_{25-50}$) vs Luminosity [$10^{51}$erg/s].

## 5. Conclusions

We found two different kind of pulses with short and long spectral lags. The bimodality of pulses suggest two or more different radiation mechanisms occurring within the fireball expansion. One group of pulse are characterized by short lags, high luminosities and low photon index, a second group are characterized by longer lags, short luminosities

Table 1. Spectral fit for each GRB's region.

| GRB | $z$ | Region | Model | Photon Index | $E_p$[KeV] | $\chi^2$/DoF | Luminosity[$10^{51}$ erg/seg] |
|---|---|---|---|---|---|---|---|
| 070306 | 1.49 | I | Normalized | 1.49±0.12 | 146.55±62.80 | 0.81/55 | 0.60±0.02 |
| | | II | Power law | 1.81±0.18 | - | 0.92/56 | 0.03±0.01 |
| 071010B | 0.94 | I | Normalized | 1.59±0.11 | 46.11±0.92 | 0.68/55 | 0.594±0.002 |
| | | II | Power law | 2.70±2.15 | - | 0.98/56 | 0.01±0.001 |
| 080411 | 1.03 | I | Power law | 1.22±0.04 | - | 1.13/56 | 0.982±0.004 |
| | | II | Power law | 1.43±0.02 | - | 0.98/56 | 1.226±0.005 |
| | | III | Normalized | 1.230±0.001 | 179.96±22.18 | 0.64/55 | 3.63±0.03 |
| | | IV | Power law | 1.759±0.002 | - | 1.03/56 | 0.75±0.04 |
| | | V | Power law | 2.2534±0.0009 | - | 0.91/56 | 0.61±0.01 |
| | | VII | Normalized | 1.606±0.001 | 92.19±5.83 | 0.58/55 | 4.11±0.02 |
| | | VIII | Power law | 2.654±0.002 | - | 1.17/56 | 0.87±0.02 |
| | | IX | Power law | 2.6889±0.0005 | - | 0.76/56 | 1.179±0.001 |
| | | X | Power law | 3.050±0.002 | - | 0.95/56 | 0.74±0.01 |
| 080413B | 1.10 | I | Normalized | 1.17±0.17 | 65.43±5.26 | 0.54/55 | 1.29±0.03 |
| | | II | Power law | 4.55±3.91 | - | 1.37/56 | 0.02±0.02 |
| 080916A | 0.69 | I | Normalized | 0.61±0.13 | 149.38±14.17 | 0.86/55 | 0.209±0.004 |
| | | II | Normalized | 1.09±0.19 | 52.34±3.03 | 1.06/55 | 0.078±0.002 |
| | | III | Power law | 2.34±0.39 | - | 1.08/56 | 0.0061±0.0001 |
| 091020 | 1.71 | I | Normalized | 1.30±0.17 | 146.08±62.32 | 0.59/55 | 0.92±0.05 |
| | | II | Power law | 1.87±0.22 | - | 1.05/56 | 0.08±0.03 |
| 091208B | 1.06 | I | Normalized | 0.64±0.71 | 51.26±7.93 | 1.05/55 | 0.50±0.17 |
| | | II | Power law | 1.71±0.07 | - | 0.76/56 | 1.22±0.04 |
| | | III | Power law | 2.32±0.79 | - | 1.07/56 | 0.04±0.01 |
| 100704A | 3.6 | I | Normalized | 0.90±0.13 | 120.56±12.68 | 0.93/55 | 2.96±0.04 |
| | | II | Power law | 1.51±0.5 | - | 0.85/56 | 0.129±0.002 |
| 110503A | 1.61 | I | Normalized | 0.73±0.14 | 112.67±8.23 | 1.25/55 | 6.46±0.13 |
| | | II | Power law | 1.50±0.59 | - | 1.51/56 | 0.13±0.01 |
| 110715A | 0.82 | I | Normalized | 1.09±0.07 | 89.5±13.5 | 1.08/55 | 2.52±0.01 |
| | | II | Power law | 2.25±0.41 | - | 0.80/56 | 0.09±0.02 |

and high photon index. The number of pulses with short lag is greater than the pulses with long lag. The short lag pulses have a high luminosity and they are associated with photon indexes close to 2. We suggest that gamma radiation should originate from pulses with low photon index and short spectral lag, but in order to confirm the emission mechanisms. Simulations of Inverse Compton like possible mechanism must be performed in a future research.

**Acknowledgments.** The authors acknowledge financial support from Escuela Politécnica Nacional and the *Swift* team to make the data public.

## References

Arimoto, M. et al. 2010, PASJ, 62, 487-499

Norris, J. P., Bonnell, J. T. et al. 2005, ApJ, 627, 324-345

Resmi, L. & Zhang, B. 2012, MNRAS, 426, 1385-1395

Zhang, B. & Mészáros, P. 2004, Int. J. of Mod. Phys. A, 19, 2385-2472

*Gravitation, Relativistic Astrophysics and Cosmology*
*Second Argentinian-Brazilian Meeting, 2014*
*G. S. Vila, F. L. Vieyro and J. Fabris, eds.*

# Thermal emission and line profiles from magnetized accretion disks

Ignacio F. Ranea-Sandoval[1] and Federico García[2]

[1]*Grupo de Gravitación, Astrofísica y Cosmología, Facultad de Ciencias Astronómicas y Geofísicas - Universidad Nacional de La Plata. Paseo del Bosque S/N (1900). La Plata, Argentina*
[2]*Instituto Argentino de Radioastronomía, CCT La Plata - CONICET, C.C. 5 (1984) Villa Elisa, Buenos Aires, Argentina; Facultad de Ciencias Astronómicas y Geofísicas, Universidad Nacional de La Plata. Paseo del Bosque S/N 1900. La Plata, Argentina*

**Abstract.** Observations of X-ray binary systems provide strong evidences of the existence of compact objects too massive to be explained by current neutron star models. When these systems are in the thermal (*high/soft*) state their emission spectra in the $0.1 - 5$ keV range can be modeled by means of the thermal radiation of an accretion disk formed around super-compact objects. The profile of the fluorescent iron line is useful to get insight related with the nature of the compact object.

In this work we developed a numerical scheme able to calculate thermal spectra of magnetized Page-Thorne accretion disks formed around both rotating black holes and naked singularities as seen by an arbitrary distant observer. We incorporated two different magnetic field configurations: uniform and dipolar, using a perturbative scheme in the coupling constant between matter and magnetic field. Under the same assumptions we obtained observed synthetic line profiles of the 6.4 keV iron line.

We show that the presence of an external magnetic field produces potentially observable modifications on both the thermal energy spectrum and fluorescent iron line profile.

## 1. Introduction

Thermal spectra of X-ray binary systems in the (*high/soft*) state can be explained by the emission of accretion disks formed around ultra-compact objects (McClintock et al., 2006). Furthermore, the shape of the fluorescent iron line present on these spectra can be useful to constrain physical parameters of these systems (Reynolds & Fabian, 2008).

Accretion disks and magnetic fields are two different phenomena intimately related with ultra-compact objects. The structure of the magnetic field in the neighborhood of the system formed by the compact object plus the accretion disk is extremely complex. In a series of works that ended with Contopoulos & Papadopoulos (2012), the authors proposed that the mechanism called the Poynting-Robertson Cosmic Battery (CB) could be responsible of generating *in situ* and maintaining a central dipolar magnetic field. Another viable magnetic field configuration is one that presents almost no changes through the equatorial region where the disk develops.

A central ingredient in simple models of accretion disks (Page & Thorne, 1974) are circular equatorial geodesics. In Ranea-Sandoval & Vucetich (2014), the authors investigated the effects caused on the circular trajectories of charged test particles by the presence of an external magnetic field. In order to calculate these orbits around both Kerr black holes (BHs) and naked singularities (NSs), they used a perturbative approach on the coupling constant between the effective charge of the matter that forms the disk and the magnetic field strength, $\lambda$.

Based on these results, in this work we introduce our study of the observed thermal emission and line profiles produced by a magnetized accretion disk formed on a Kerr spacetime with arbitrary spin parameter, $a$.

## 2. The model

Using the magnetic field solutions on a Kerr background (Petterson, 1975), we developed magnetized versions of Page-Thorne's accretion disks under two different external magnetic field configurations: uniform and dipolar. We assumed that the geometrically thin but optically thick accretion disks extend from the innermost stable circular orbit, $r_{\rm isco}$, to $r_{\rm out} = 11 r_{\rm isco}$ (Dove et al., 1997).

Once we obtained the structure of the disk, we calculated observed thermal energy spectra and fluorescent $K\alpha$ iron line profiles. We incorporated a ray-tracing technique to evaluate the geodesics of photons between a plaque placed at observer's position and the surface of the disk where photons are emitted. For this purpose, we adapted the public-code YNOGK (Yang & Wang, 2013), which includes all the relativistic effects suffered by photons: Doppler boosting, gravitational redshift and gravitational light bending.

## 3. Results

Using a perturbative approach we were able to analytically reproduce previously reported numerical results for the radii of the most relevant circular orbits of charged particles orbiting a Kerr BH with an external uniform and/or dipolar magnetic field, also extending them to the super-spinning Kerr NS case. Our results are in agreement with those obtained by Iyer et al. (1985); Prasanna & Vishveshwara (1978); Wiita et al. (1983) in the weak coupling ($\lambda \ll 1$) regime.

Assuming a black-body emissivity law, we calculated observed thermal energy spectra for magnetized accretion disks. In Figure 1 we show non-absorbed thermal energy spectra of a BH (black lines) and a NS (grey lines) considering non-magnetized ($\lambda = 0$) and uniform ($\lambda_{\rm U} = 0.1$) and dipolar ($\lambda_{\rm D} = 0.1$) magnetized accretion disks. Thermal emission from NS are harder and brighter than those from BH. The presence of an external magnetic field modifies the shape of the spectra, peak intensities and cut-off energies.

Now we focus on the effects caused by the inclusion of an external magnetic field on the profiles of emission lines formed on the surface of the disk, assuming a power-law emissivity $r^{-p}$. First, in the top panels of Figure 2 we plot our results for the uniform magnetic field configuration, considering $\lambda_{\rm U} = 0.05$ and 0.1 (dashed lines), and fixing $p = 3$ and $i = 30°$. As a reference we also plot the non-magnetized case (solid lines). From left to right we plot the line profiles obtained for $a = 0.5$, 0.99 and 1.2. For small

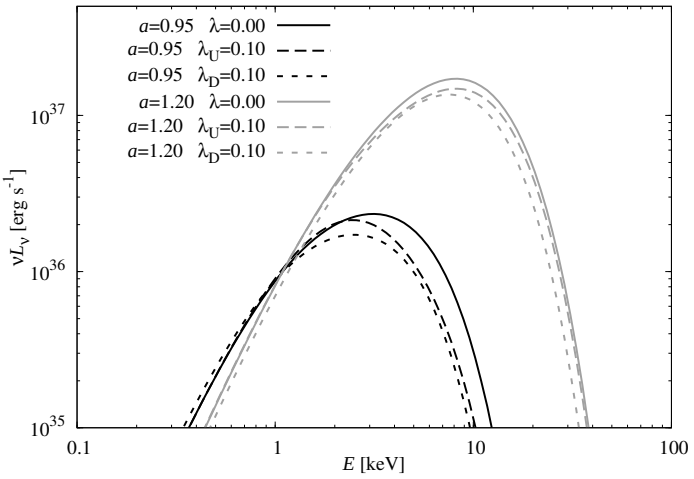


Figure 1. Thermal spectra of magnetized accretion disks surrounding a BH ($a = 0.95$) and a NS ($a = 1.20$) as seen by a distant observer with inclination $i = 80°$.

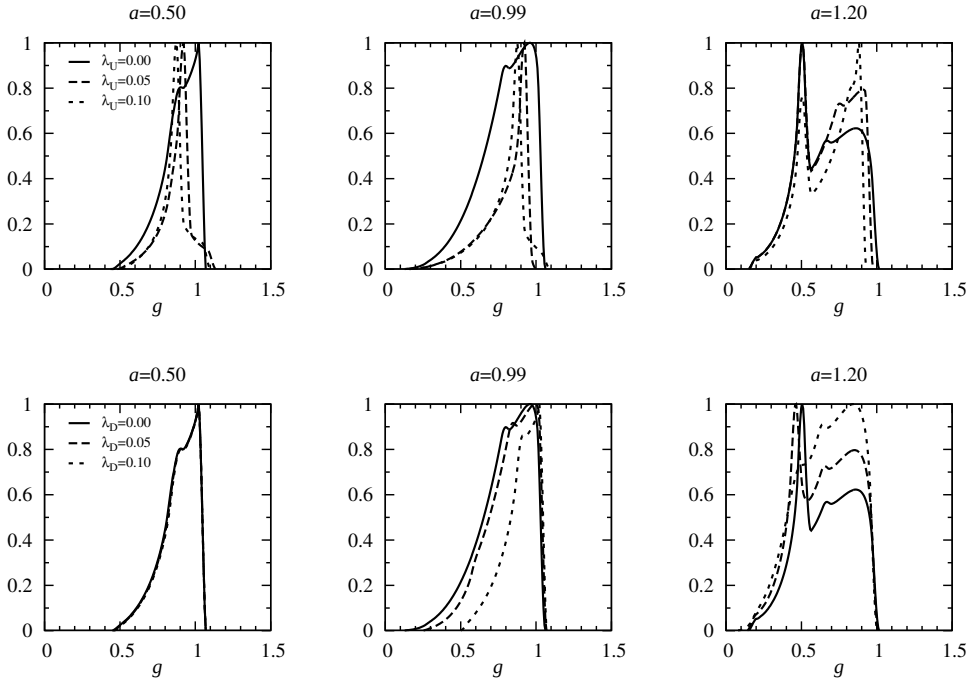


Figure 2. Emission line profiles of magnetized accretion disks as seen by a distant observer with inclination $i = 30°$. Top (bottom) panels correspond to uniform (dipolar) magnetic field configurations.

values of the spin parameter, $a$, accretion disks extend to outer regions where the effects of the uniform magnetic field strongly affect the trajectories, and thus, the emission line

profiles. On the contrary, as $a$ grows, and the disks shrink, the effects become less relevant, but still noticeable for these values of $\lambda_{\rm U}$.

Secondly, in the bottom panels of Figure 2 we present, for the same parameters, our results corresponding to the dipolar magnetic field configuration. In this case, contrary to the uniform one, dipolar magnetic field dominates in the inner regions of the disks and thus the major changes in the shape of the line profiles occur for values of $a \sim 1$, as $r_{\rm isco} \to 1$. This explains why line profiles of magnetized accretion disks for $a = 0.5$ are almost indistinguishable from the non-magnetized case. As $a$ grows, this characteristic changes radically, and emission line profiles become more sensitive to the value of $\lambda_{\rm D}$. In the case of extremely spinning BHs, the effect of the dipolar magnetic field on the line profile dominates in the red wings, while for NSs, the blue-shifted peak becomes brighter.

Comparison between observational data from X-ray binary systems and our model can be used as a tool to get insight regarding physical properties of the compact object and also to probe cosmic censorship conjecture (Penrose , 1998) in astrophysical environments. Moreover our results can be implemented to estimate the magnetic field strength and geometry in the neighbourhood of accretion disks.

**Acknowledgments.** We thank Prof. Dr. H. Vucetich for reading the original manuscript and Dr. M. M. Miller Bertolami for borrowing us the computer with which we performed most of our calculations. IFRS and FG are fellows of CONICET.

## References

Contopoulos, I. & Papadopoulos, D. B. 2012, MNRAS, 425, 147

Dove, J. B. et al. 1997, ApJ, 487, 759

Iyer, B. R. et al. 1985, Pramana-J.Phys., 25, 2, 135

McClintock, J. E., Shafee, R., Narayan, R., et al. 2006, ApJ, 652, 1, 518

Page, D. N. & Thorne, K. S. 1974, ApJ, 191, 499

Penrose, R. 1998, Black Holes and Relativistic Stars, 103

Petterson, J. A. 1975, Phys. Rev.D, 12, 2218

Prasanna, A. R. & Vishveshwara, C. V. 1978, Pramana, 11, 359

Ranea-Sandoval, I. F. & Vucetich, H. 2014, "Relativity and Gravitation", in Bičák J. and Ledvinka T. (eds.), Springer Proceedings in Physics Vol. 157, 435

Reynolds, C. S. & Fabian, A. C. 2008, ApJ, 675, 1048

Wiita, P. J. et al. 1983, Journal of Physics A Mathematical General, 16, 2077

Yang, X. & Wang, J. 2013, ApJS, 201, 6

*Gravitation, Relativistic Astrophysics and Cosmology*
*Second Argentinian-Brazilian Meeting, 2014*
*G. S. Vila, F. L. Vieyro and J. Fabris, eds.*

# The incidence of the host galaxy light in the polarized emission of the blazars 1959+650 and 2201+044

M. S. Sosa,[1,2] S. A. Cellone,[1,2] I. Andruchow,[1,2] and C. von Essen[3]

[1]*Facultad de Ciencias Astronómicas y Geofísicas, UNLP, Argentina*
[2]*Instituto de Astrofísica La Plata, CONICET-UNLP, Argentina*
[3]*Institut für Astrophysik Göttingen, F.-Hund-Pltz. 1, Germany*

**Abstract.** We present a study carried out to determine variations in scales ranging from hours to days, both in the total flux and optical linear polarization in two blazars: 1959+650 and 2201+044. Both blazars are relatively nearby active galactic nuclei, so their host galaxies are well resolved, having accurately measured photometric parameters. This allowed us to apply models that take into account the depolarizing effect introduced by the (un-polarized) light of the galaxy, and, at the same time, to evaluate any spurious variation in polarization time-curves due to variable seeing conditions, that affect differently the (point-like) core and the (extended) host galaxy. Our results provide information on the optical behaviour of high energy blazars, taking advantage of a scarcely explored technique as optical polarimetry with high-temporal resolution.

## 1. Introduction

Blazars constitute the most extreme subclass of active galactic nuclei (AGN). We present results from a study of two of them: 1959+650 and 2201+044. The first is a High-energy peaked BL Lac (HBL), detected at TeV energies by HESS and *Fermi*-LAT, at redshift $z = 0.048$, while the second is a Low-energy peaked BL Lac (LBL) at $z = 0.027$. Isolated polarimetric measurements ($P$) can be found in the literature for both objects: $P = 2.92\%$ for 1959+650, $P = 1.1 - 1.5\%$ for 2201+044; however these relatively low polarization percentages have not been corrected by the effect of unpolarized host galaxy light.

We report here the results obtained from our observational campaign designed to study the polarized emission of blazars. These data will help us to understand the optical variability of the polarized emission. In addition, we study the effects of the host galaxy light on polarization measurements of blazars.

## 2. Observations

The instrument used for the study was the Calar Alto Faint Object Spectrograph (CAFOS) in its imaging polarimetric mode, at the Calar Alto (Spain) 2.2 m telescope.[1] This instrument has a Wollaston prism plus a rotatable half-wave plate (Patat & Taubenberger, 2011), producing two orthogonally polarized images, ordinary (O) and

[1]The observations were carried out in the framework of a collaboration with researchers from University of Hamburg, Germany.

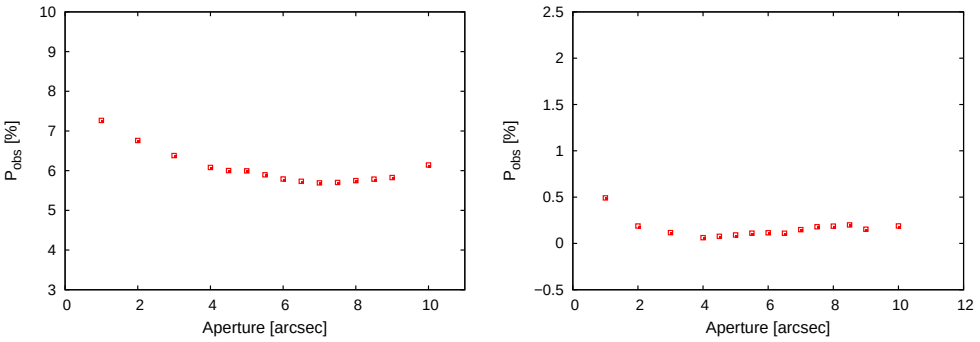


Figure 1. Curve of the polarization degree $\langle P_{\rm obs}\rangle$ as a function of the photometric apertures. *Left:* 1959+650 *Right:* 2201+044.

extraordinary (E), of each object on the focal plane. In addition, a mask with alternate blind and clear stripes is placed before the detector. This procedure improved the signal to noise ratio (S/N), although half of the field is lost.

## 3. Analysis

We obtained the linear polarization and position angle ($\theta$) for both blazars using equations that can be found in e.g. Lamy & Hutsemékers (1999). For each object in the field, including the blazars, we computed the average polarization ($P_{\rm obs}$) (in the $Q$, $U$ plane) for a 3 arcsec radius photometric aperture (which maximizes the S/N, see Howell 1989). We estimated a value of the Galactic polarization ($P_{\rm Gal}$) considering field stars with a polarization vector almost parallel to each other and much smaller than the polarization of the blazar.

Using a 3 arcsec aperture radius, we obtained $\langle P_{\rm obs}\rangle$= 6.41 ± 0.26 % and $\langle P_{\rm Gal}\rangle$ = 0.73 % for 1959+650 and $\langle P_{\rm obs}\rangle$ = 0.16±0.28 % and $\langle P_{\rm Gal}\rangle$ = 0.28 % for 2201+044. We explored the depolarizing effect of the host galaxy by plotting $P_{\rm obs}$ against the aperture radius (Fig. 1). As expected, the observed polarization decreases for large apertures, for which the contribution of unpolarized flux from the host galaxy dominates. Note that for 2201+044, while for the larger apertures its polarization is consistent with 0%, a low but significant polarization ($\sim$ 0.5%) is measured through the smallest aperture.

On the other hand, since the brightness distributions of the host galaxy and the nucleus are different, any seeing variation will affect each component in different proportions. Hence, spurious effects on the polarization variability may be induced by changes in the atmospheric seeing, which affects the relative contribution of (partially polarized) AGN and (unpolarized) host within the aperture. We checked for this effect by comparing the variations in time of the polarization with the behaviour of the FWHM. No significant seeing-induced spurious variations in $P$ were detected.

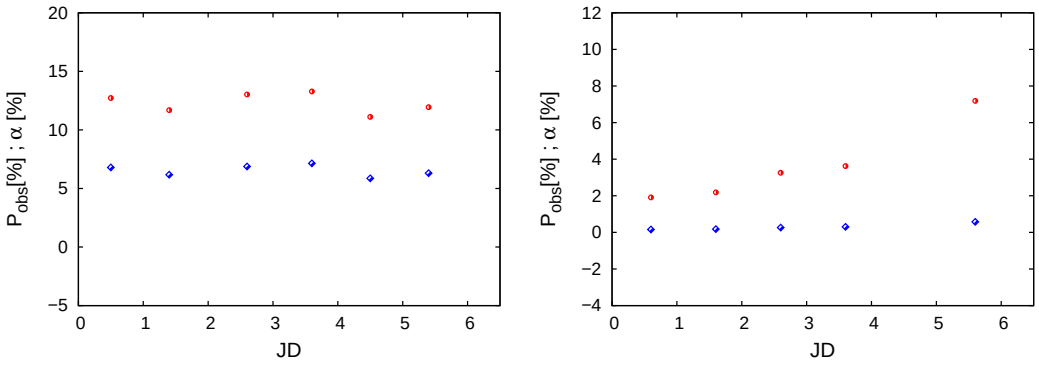


Figure 2. Temporal behaviour of the degree of polarization $P$ (blue) and the $\alpha$ parameter (red). *Left:* 1959 +650. *Right:* 2201+044.

## 4. Results

The blazar 1959 +650 shows significant inter-night variability, while 2201 +044 seems to be steady.

We modelled the flux distribution of the blazar+host and seeing (Andruchow et al. 2008) in order to estimate and subtract the depolarizing effect of the host galaxy, thus recovering the intrinsic polarization of the blazar and, at the same time, removing any spurious variability induced by seeing variations. The results are shown in Fig. 2, where the $\alpha$ parameter quantifies the intrinsic polarization of the nucleus. On one hand, we can see that for 1959 +650 $\alpha$ is $\approx 7\%$ larger than $P$, while the former closely follows the behaviour of the latter with time. This behaviour is expected since the FWHM remained almost constant during the observations. On the other hand, for 2201+044, $\alpha$ departs systematically from the curve corresponding to $\langle P_{\rm obs} \rangle$. This can be explained because this AGN was observed at the end of each night of observation, when the seeing was not stable. Results for this object should be taken with care, and a more accurate modelling of its host galaxy is needed to recover the nuclear polarization.

As an alternative approach in the case of 1959 +650, we use the total contaminating fluxes (host galaxy + nearby companions) estimated by Nilsson et al. (2007) to obtain the blazar's polarization $\alpha$, applying Eq. 1 from Andruchow et al. (2008):

$$P_{\rm obs}[\%] = \frac{\alpha \, F_{\rm AGN}}{F_{\rm AGN} + F_{\rm Gal}}, \tag{1}$$

thus obtaining $\alpha \sim 7.55\%$. This value is lower than that obtained by the model ($\alpha = 11.94\%$), but this difference can be attributed to the fact that 1959 +650 is variable and the magnitude of the blazar used in the model may not be the actual magnitude at the moment of the observations.

## 5. Conclusions

We estimated the polarization degrees of the blazars 1959 +650 and 2201 +044. We conclude that the HBL is a high polarization object, while in the case of the LBL under study its polarization is close to zero. We analyzed the behaviour of the polarization

degree as a function of the photometric apertures to check if there was any spurious effect on the polarization variability due to atmospheric changes. Finally, we applied a mathematical model with the aim to recover the intrinsic AGN polarization, and, at the same time, remove any change in $P$ induced by seeing variations.

On the one hand, for 1959 +650, for which the FWHM remained almost constant during the observation, both the intrinsic ($\alpha$) and observed ($P$) polarization degrees follow the same behaviour. We also estimated a value of the intrinsic polarization using the total contaminating fluxes (host galaxy + nearby companions) tabulated by Nilsson et al. (2007). We obtained a lower value of intrinsic polarization as compared with the model results, thus underlining the need to use accurate parameters for both AGN and host in order to obtain reliable results. On the other hand, for 2201 +044, $\alpha$ departs systematically from the curve corresponding to $\langle P_{\rm obs} \rangle$. This can be explained because this AGN was observed during the part of the night with less stable seeing.

As a general conclusion we stress that an accurate subtraction of contamination by the host galaxy is very important for optical polarimetric studies of blazars, especially for those detected at high-energies, because they are found at relatively low redshifts.

**Acknowledgments.** Lic. M. S. Sosa thanks Dr. J. N. González Pérez and Prof. J. H. M. M. Schmitt for their collaboration. This work was partially financed by PICT 2008-0627 ANPCyT.

## References

Andruchow, I. et al. 2008, MNRAS, 388, 1766

Howell, S. B. 1989, PASP, 101, 616

Lamy, H. & Hutsemékers, D. 1999, The Messenger, 96, 25

Nilsson, K. et al. 2007, A&A, 475, 199N

Patat, F. & Taubenberger, S. 2011, A&A, 529A, 57P

*Gravitation, Relativistic Astrophysics and Cosmology*
*Second Argentinian-Brazilian Meeting, 2014*
*G. S. Vila, F. L. Vieyro and J. Fabris, eds.*

# Primordial gravitational waves with decaying vacuum cosmologies

David Tamayo,[1] J. A. S. Lima,[2] and D. Bessada[3]

[1]*Instituto de Física, Universidade de São Paulo, São Paulo, Brazil*
[2]*Instituto de Astronomia, Geofísica e Ciências Atmosféricas, Universidade de São Paulo, São Paulo, Brazil*
[3]*Universidade Federal de São Paulo - UNIFESP, Campus Diadema, Brazil*

**Abstract.** The production of primordial gravitational waves (GWs) is discussed in the framework of a flat FRW cosmology with decaying vacuum energy density. The gravitational wave equation is established and its time-dependent part is analytically solved for different epochs. Unlike the standard ΛCDM cosmology (no interacting vacuum), we show that GWs can be produced during the radiation era. However, high frequency modes are damped out even faster than in the standard cosmology both in the radiation and matter dominated epoch. The power and energy density spectrum generated at different cosmological eras are also explicitly evaluated.

## 1. Introduction

The study of the primordial GWs is of great interest for cosmology since its possible observation may provide fundamental informations about the physical conditions in the very early Universe. Important clues about inflation, high energy physics and the quantum gravity regime are expected from its direct detection. The generation of cosmological GWs was extensively studied since long ago by many authors (see Grishchuk 1993 for a review; also de Garcia Maia & Lima 1996). Here we focus on decaying vacuum cosmologies where the Λ-term is a time dependent quantity, $\Lambda = \Lambda(H)$. The interacting $\Lambda(H)$ models alleviate the cosmological constant and coincidence problems, and some models are also in agreement with the available astronomical observations. The kind of decaying vacuum energy density adopted here is also supported by dimensional arguments and the renormalization group approach (Carvalho et al 1992; Lima et al. 2013).

## 2. Cosmological gravitational waves

We are interested in the evolution of the GWs, i.e. tensor perturbations of the spacetime itself. A classical tensor metric perturbation in FRW can be described as $ds^2 = a^2(\eta)[-d\eta^2 + (\delta_{ij} + h_{ij})dx^i dx^j]$ by satisfying the gauge conditions: $|h_{ij}| \ll 1$, $h_{0\mu} = h^i_i = \nabla^j h_{ij} = 0$. At first order the equation of evolution of the tensor perturbation $h_{ij}$ is given by (Tamayo et al. 2014):

$$h_i^{j\,\prime\prime} + 2\frac{a'}{a}h_i^{j\,\prime} - \nabla^2 h_i^j = 0. \tag{1}$$

Making the expansion

$$h_{ij}(\eta,\mathbf{x}) = \frac{\sqrt{16\pi G}}{(2\pi)^{3/2}}\int d^3\mathbf{n}\sum_{r=+,\times}\overset{r}{\epsilon}_{ij}(\mathbf{n})[\overset{r}{h}_n(\eta)e^{i\mathbf{n}\cdot\mathbf{x}}\overset{r}{c}_{\mathbf{n}} + c.c]$$

we obtain:

$$\overset{r}{h}_n(\eta)'' + 2\frac{a'}{a}\overset{r}{h}_n(\eta)' + n^2\overset{r}{h}_n(\eta) = 0 \tag{2}$$

$$\Rightarrow \qquad \overset{r}{\mu}{}'' + \left(n^2 - \frac{a''}{a}\right)\overset{r}{\mu} = 0, \overset{r}{\mu}_n(\eta) = a(\eta)\overset{r}{h}_n(\eta).$$

The term $V(\eta) = a''/a$ is called the "potential" in analogy with the stationary Schrodinger equation. It drives the evolution of the amplitude $\overset{r}{h}_n(\eta)$ giving up the *gravitational wave amplification* as described in figure 1. When the perturbations are quantized, all $\overset{r}{c}_{\mathbf{n}}$ are promoted to be the creation and annihilation operators, $[\overset{r'}{c}_{\mathbf{n}}, \overset{r}{c}{}^{\dagger}_{\mathbf{m}}] = \delta_{r'r}\delta^3(\mathbf{n}-\mathbf{m})$, thereby defining the vacuum state for a specific time and mode, $\overset{r}{c}_{\mathbf{n}}|0\rangle_{\mathbf{n}} = 0$. We do not have an unique vacuum state because $c_{\mathbf{n}}|0\rangle_{\mathbf{m}} \neq 0$ (the index $r$ was suppressed for notation). Consequently we have particle (graviton) creation due the expansion of the Universe because the number operator gives $N_{\mathbf{n}}|0\rangle_{\mathbf{m}} = c^{\dagger}_{\mathbf{n}}c_{\mathbf{n}}|0\rangle_{\mathbf{m}} \neq 0$. With this we can easily calculate the *power spectrum* of the GWs $\mathcal{P}(n,\eta)$ and the *energy density spectrum* $\Omega_{\rm gw}(n,\eta)$:

$$\mathcal{P}(n,\eta) \equiv \frac{d\langle 0|h_{ij}(\eta,\mathbf{x})h^{ij}(\eta,\mathbf{x})|0\rangle}{d\ln n} = \frac{32G}{\pi}n^3|h_n(\eta)|^2, \tag{3}$$

$$\Omega_{\rm gw}(n,\eta) \equiv \frac{1}{\rho_{\rm crit}}\frac{d\langle 0|\rho_{\rm gw}(\eta)|0\rangle}{d\ln n} = \frac{8\pi G}{3\mathcal{H}^2(\eta)}\frac{n^3}{2\pi^2}(|h_n'(\eta)|^2 + n^2|h_n(\eta)|^2). \tag{4}$$

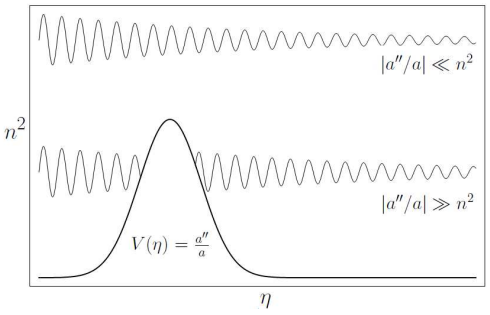


Figure 1. GW amplification. High frequencies, $|a''/a| \ll n^2 \Rightarrow \mu \propto e^{-in\eta}$ i.e $h \propto a^{-1}$, the perturbations decay with the cosmic expansion. Low frequencies $|a''/a| \gg n^2 \Rightarrow \mu \propto a$ i.e. $h \propto constant$ the perturbations do not "feel" the cosmic expansion, this is the basic principle of the GW amplification.

### Scale factor

Let us now consider a decaying vacuum cosmology driven by $\Lambda(H) = \Lambda_0 + 3\beta H^2$. By using the equation of state, $p = \omega\rho$, one may show that the evolution equation for the scale factor reads:

$$aa'' + (\Delta - 1)a'^2 - \frac{1+\omega}{2}\Lambda_0 a^4 = 0, \quad \Delta = \frac{3(1+\omega)(1-\beta) - 2}{2}. \tag{5}$$

At early times, the term involving $\Lambda_0$ in the above equation of motion can be neglected. So, by integrating it, we find that the solutions of the scale factor for the different cosmic eras (inflation, radiation & Matter) can be written as:

$$a(\eta) = \begin{cases} -l_i\eta^{-1}, & \eta \leq \eta_1 \quad \eta < 0, & \text{inflation} \\ l_i a_{0r}(\Delta_{\rm rad}\eta - \eta_{\rm rad})^{1/\Delta_{\rm rad}}, & \eta_1 \leq \eta \leq \eta_{\rm eq}, & \text{radiation} \\ l_i a_{0m}(\Delta_{\rm mat}\eta - \eta_{\rm mat})^{1/\Delta_{\rm mat}}, & \eta \geq \eta_{\rm eq}, & \text{matter} \end{cases} \tag{6}$$

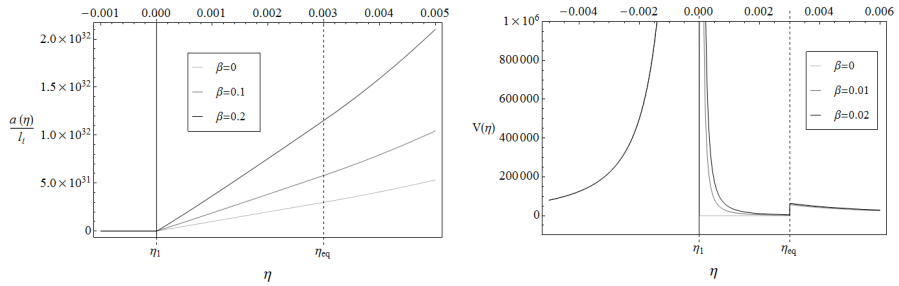


Figure 2. *Left:* Evolution of the scale factor $a(\eta)$ for some selected values of $\beta$, the expansion rate is faster for higher values of $\beta$. *Right:* of $\beta$, note that $V = 0$ only for $\beta = 0$.

## 3. Results

The inflation era is independent of $\beta$ so that we have the well-known solution $\mu_{\rm inf} = \frac{e^{-in\eta}}{\sqrt{2n}}(1 - \frac{i}{n\eta})$. However, new results are present during the radiation and matter era. The main result is that in the radiation era we have $V = 2\beta\frac{a'}{a}$. Therefore, unlike in the standard ΛCDM model, where $V = 0$ (see Figure 2), we obtain that for $\beta \neq 0$ the GW amplification occurs even during the radiation phase. In Figures 3 and 4 we show the behavior of the modulus of the perturbations $|h|$ in the radiation and matter era. Finally, in Figures 5 and 6, the results for the power and energy density spectra are also presented.

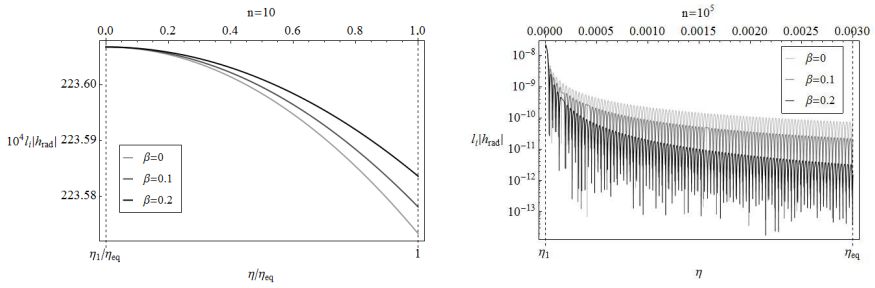


Figure 3. *Left:* $|h_{\rm rad}|$ as a function of the conformal time for some values of $\beta$ and a fixed $n = 10$. *Right:* $|h_{\rm rad}|$ for high frequency $n = 10^5$. In the low frequency regime the decaying vacuum amplify the perturbations since the amplitude is higher in comparison to the case $\beta = 0$. The high frequency modes are always damped out regardless of the value of $\beta$.

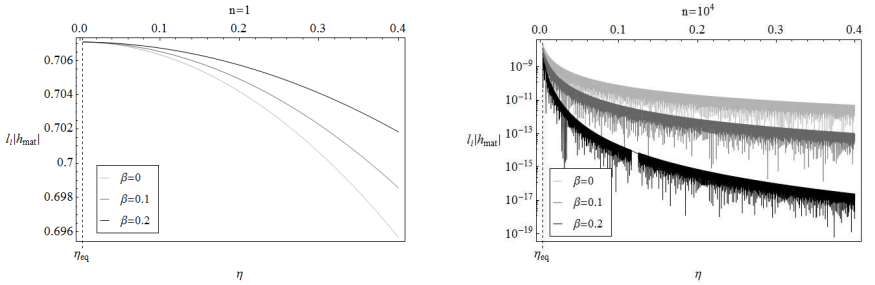


Figure 4. *Left:* $|h_{\rm mat}|$ as a function of the conformal time for some selected values of $\beta$ and a fixed $n = 1$. *Right:* $|h_{\rm mat}|$ for a high frequency, $n = 10^4$. We have the same features of the radiation era.

## 4. Basic conclusions

- In decaying $\Lambda$ models, the GW amplification (graviton creation) can occurs even during the radiation era. In general, for $\Lambda(t)$-models, the "Schrodinger potential", $V(\eta) = a''/a$, is usually different from zero.
- For a $\Lambda = 3\beta H^2$ model discussed here, the graviton production is also a low frequency phenomenon.
- For de Sitter inflation, $\omega = -1$, the initial spectrum is independent of the parameter $\beta$.
- The amplitude, power spectrum and energy density of cosmological GWs were explicitly calculated and compared with the standard case ($\beta = 0$).

**Acknowledgments.** DT and JASL are grateful to CAPES and CNPQ (Brazilian Research Agencies), respectively.

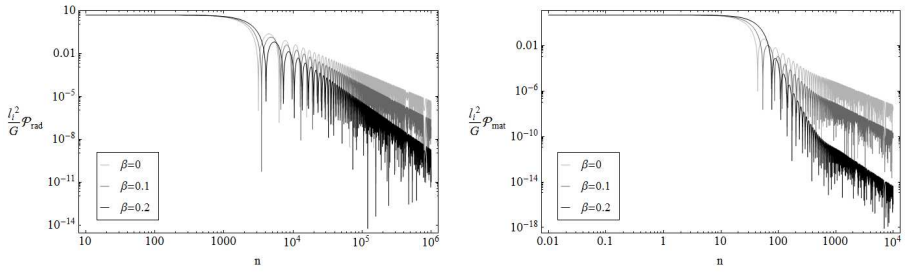


Figure 5. *Left:* $\mathcal{P}_{\rm rad}$ as a function of $n$ for a fixed time. The spectrum is practically flat until some transition frequency when begins to decrease being slightly larger as $\beta$ increases. $\Lambda(t)$ contributes to the creation of low-frequency gravitons. Note that after some $\beta$-dependent transition frequency the waves are strongly damped. This means that the decaying vacuum in this regime contributes more to increase the scale factor than to the production of gravitons. *Right:* $\mathcal{P}_{\rm mat}$ as a function of $n$ for a fixed time. With the same high and low frequency general properties of the radiation era, it starts with an almost flat spectrum and also decreases faster as long as the vacuum contribution is relatively larger (higher values of $\beta$).

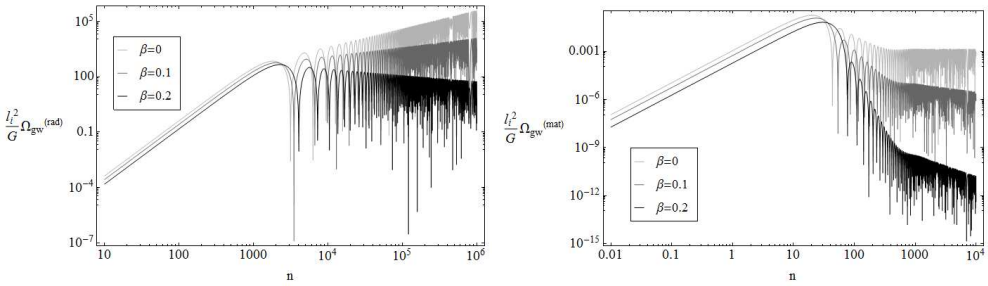


Figure 6. *Left:* $\Omega_{\rm gw}^{\rm (rad)}$ as a function of $n$ for a fixed time. If $\beta_1 > \beta_2$ then $\Omega_{\rm gw}^{\rm (rad)}(\beta_1) < \Omega_{\rm gw}^{\rm (rad)}(\beta_2)$ for all frequencies. $\Omega_{\rm gw}^{\rm (rad)}$ grows as a power-law being weakly dependent on the value of $\beta$, but a more strong dependence is obtained at the high frequency limit. *Right:* $\Omega_{\rm gw}^{\rm (mat)}$ follows a similar trends, if $\beta_1 > \beta_2$ then $\Omega_{\rm gw}^{\rm (mat)}(\beta_1) < \Omega_{\rm gw}^{\rm (mat)}(\beta_2)$, with some peculiarities at the high frequency limit where the spectrum always decreases but varies differently in function of $\beta$. The basic reason for such a behavior is because when $|h'|^2 \ll |h|^2$ the energy density spectrum is $\Omega_{\rm gw} \propto n^5|h|^2\mathcal{H}^{-2}$, where $\mathcal{H} = a'/a$ (see expression (4) for the power-spectrum). At this limit, the factor $\mathcal{H}^{-2}$ determines the behavior of $\Omega_{\rm gw}^{\rm (mat)}$.

## References

Carvalho, J. C., Lima, J. A. S. & Waga, I. 1992, Phys. Rev. D, 46 2404

de Garcia Maia, M. R. & Lima, J. A. S. 1996, Phys. Rev. D, 54, 6111

Grishchuk, L. P. 1993, Class. Quant. Grav., 10, 2449

Lima, J. A. S., Basilakos, S. & Solà, J. 2013, MNRAS, 431, 923

Tamayo, D., Lima, J. A. S. & Bessada, D. 2014, "Primordial Graviton Production and Decaying Vacuum Energy Density", submitted

*Gravitation, Relativistic Astrophysics and Cosmology*
*Second Argentinian-Brazilian Meeting, 2014*
*G. S. Vila, F. L. Vieyro and J. Fabris, eds.*

# Study of the chemical composition of high energy cosmic rays using the muon LDF of EAS between $10^{17.25}$ eV and $10^{17.75}$ eV

A. Tapia,[1] D. Melo,[1] F. Sánchez,[1] A. Sedoski Croce,[1] J. M. Figueira,[1] B. García,[2] N. González,[1] M. Josebachuili,[1] D. Ravignani,[1] B. Wundheiler,[1] and A. Etchegoyen[1]

[1]*ITeDA (CNEA, CONICET, UNSAM), Buenos Aires, Argentina*
[2]*ITeDA (CNEA, CONICET, UNSAM), Mendoza, Argentina*

**Abstract.** We explore the feasibility of estimating primary cosmic ray composition at high energies from the study of two parameters of Extensive Air Showers (EAS) at ground and underground level with Monte Carlo simulations using the new EPOS and QGSJETII hadronic models tuned with LHC data. Namely, the slope and density at a given distance of the muon lateral distribution function are analysed in this work. The power to discriminate primary masses is quantified in terms of merit factor for each parameter. The analysis considers three different primary particles (proton, iron and gamma), four different zenith angles (0°, 15°, 30° and 45°) and primary energies of $10^{17.25}$ eV, $10^{17.50}$ eV and $10^{17.75}$ eV.

## 1. Introduction

The particle lateral distribution of EAS is the key quantity for cosmic ray ground observations at energies greater than $10^{15}$ eV, from which most observables are derived. An EAS is initiated by a high energy cosmic ray interacting in the top of the atmosphere and creating a multitude of secondary particles, which arrive at ground nearly at the same time. Secondary particles are distributed over a large area perpendicular to the direction of the cosmic ray primary. The disc of secondary particles may extend over several hundred meters from the shower axis, reaching its maximum density in the center of the disc, which is called the shower core. The density distribution of particles within the shower disc can be used to derive information on the primary particle. EAS measurements at ground level are carried out using arrays of individual detectors, which take samples of the shower disc at several distances from the shower core [1].

It is known that the muonic component of EAS carries information about the identity of the primary particle [2]. In this work we study two parameters sensitive to primary masses: the slope of the Muon Lateral Distribution Function (MLDF) and the density of muons at a certain distance from the core. The underlying idea is that showers originated by heavy nuclei produce more muons than lighter ones (therefore the absolute muon density at fixed distance will be higher for heavy nuclei) but the MLDF will be less steep. For the presented analysis the response of any detector is not taken into account.

## 2. Monte Carlo simulations

For this work we generated a library of EAS using AIRES 2.8.4a [3] which make use of QGSJET-II-03 [4] as hadronic model and CORSIKA 7.3700 [5] which make use of QGSJET-II-04 [4] and EPOS-LHC [6] as hadronic models. In both programs, we set a statistical thinning of $10^{-6}$. For each hadronic model we consider three types of primaries (proton, iron and gamma), four zenith angles (0°, 15°, 30° and 45°) and three energies ($10^{17.25}$ eV, $10^{17.50}$ eV and $10^{17.75}$ eV). For each energy, zenith angle and primary type a total of 120 showers were produced, considering an uniform azimuthal distribution between 0° and 360°. During the EAS simulations only muons with energies above 55 MeV have been taken into account to assess the MLDF at different depths between 0 and 2.5 m using the same set of showers.

## 3. $\beta$ and $\rho_\mu(500)$ parameters

Once the EAS is simulated, the muon lateral density is fitted event-by-event with a KASCADE-Grande like MLDF [7] :

$$\rho_\mu(r) = N_\mu \left(\frac{r}{r_0}\right)^{-\alpha} \left(1 + \frac{r}{r_0}\right)^{-\beta} \left(1 + \left(\frac{r}{10r_0}\right)^2\right)^{-\gamma}, \quad (1)$$

where $r$ is core distance in the shower plane. The values of $\alpha$, $\gamma$ and $r_0$ are fixed in 0.75, 3 and 320 m, respectively, and $N_\mu$ and $\beta$ are the free parameters.
The MLDF is simulated at ground with AIRES and CORSIKA and afterwards propagated underground. In the last case, two depths have been used: 1.3 m and 2.5 m. The layer of soil is used as a shielding against the electromagnetic component of the EAS, allowing only the muons of energy greater than 0.52 and 1 GeV to arrive to the desired depths respectively. For each event simulated, $\beta$ and $\rho_\mu(r = 500)$ are obtained from Eq. (1). For the energies considered, the distance of 500 m is close to the distance where the fluctuations over the MLDF are minimized if the any detector response is not taken into account. However, Fig. 1 (*Right*) show a wide range in distance with similar fluctuations values.

## 4. Muons propagation through the soil

Muons lose a fraction of their energy when they propagate through the soil, mainly due to ionization. Therefore, we assume as a first-order approximation that the energy loss is proportional to the muon track length and constant with energy. Then the energy of a muon that traveled a distance $x$ through the soil is: $E_\mu(x) = E_{\mu 0} - \alpha \rho x$, where $E_{\mu 0}$ is the initial energy of the muon, $\rho = 1.8 \times 10^6$ g m$^{-3}$ is the density of a soil with standard rock and $\alpha = 1.808 \times 10^{-7}$ GeV m$^2$ g$^{-1}$ is the fractional energy loss per grammage depth. As an example, in Fig. 1 we show a fit of the muon lateral density for one vertical proton with energy of $10^{17.75}$ eV and QGSJET-II-03 hadronic model. In this case, the slope values were $\beta = 2.44 \pm 0.38$, $\beta = 2.67 \pm 0.43$ and $\beta = 2.93 \pm 0.49$, and the density values were $\rho_\mu(500) = 0.81 \pm 0.12$ m$^{-2}$, $\rho_\mu(500) = 0.62 \pm 0.09$ m$^{-2}$, and $\rho_\mu(500) = 0.48 \pm 0.07$ m$^{-2}$, for ground, 1.3 m and 2.5 m underground, respectively.
In order to validate the first-order approximation, we use the GEANT4 package to perform a complete simulation of particles arriving to different depths. The results are equivalent because the ionization is the main process of energy loss.

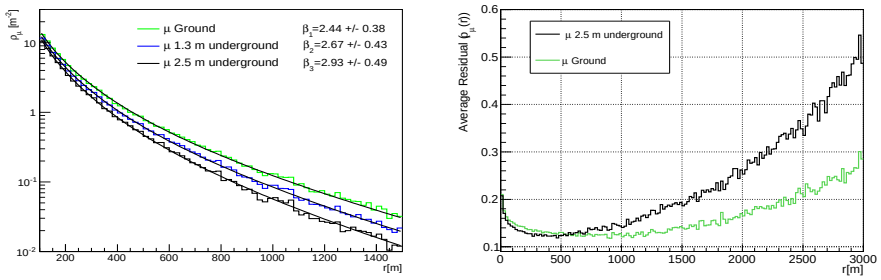


Figure 1. *Left:* MLDF of one vertical proton of $10^{17.75}$ eV at different soil levels. The muons propagation was performed using the firs-order approximation. *Right:* The mean spread in $\rho_\mu(r)$ for 120 showers initiated by proton with energy of $10^{17.50}$ eV and zenith angle of 30°.

## 5. Data Analysis

In order to quantify the discrimination power of $\beta$ and $\rho_\mu(500)$ parameters, we constructed the distributions of these two parameters for each primary type, energy and zenith angle, at ground and underground levels, respectively. As an example, in Fig. 2 the distributions of $\beta$ and $\rho_\mu(500)$ are shown for $E = 10^{17.75}$ eV and zenith angle 0°. The power of discrimination is measured calculating the Merit Factor (MF) between the distributions defined as: $MF = |\langle A\rangle - \langle B\rangle|/\sqrt{\sigma_A^2 + \sigma_B^2}$, where $\langle A\rangle$ and $\langle B\rangle$ are the mean values of the $A$ and $B$ distributions, and $\sigma_A$ and $\sigma_B$ their respective standard deviations (because no detector is considered in this work, these fluctuations correspond only to shower-to-shower fluctuations). MFs lower than 1 indicate very poor discrimination power (roughly because mean values are less than $1\sigma$ apart from each other).

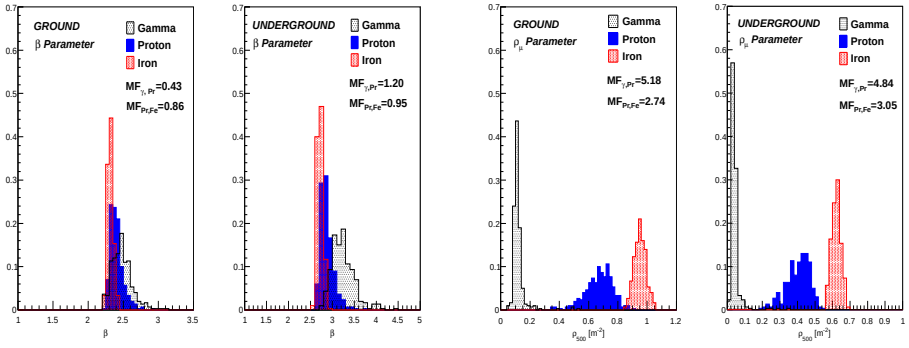


Figure 2. *Left:* $\beta$ parameter distributions corresponding to 120 vertical EAS at ground and 2.5 m underground levels, with energy of $10^{17.75}$ eV and QGSJET-II-03 hadronic model. *Right:* The same for $\rho_\mu(500)$ parameter distributions.

## 6. Merit factor and primary mass discrimination

The MFs dependence with energy, hadronic model and zenith angle was the main goal of this work. In Fig. 3 we show the results for case of 2.5 m underground. From both

plots it can be seen that the discrimination power of $\beta$ is not very good. On the other hand, $\rho_\mu(500)$ shows a MF greater than 2 and is practically independent of the energy and zenith angle. Therefore this parameter has the potential to discriminate the mass of primaries cosmic rays. A similar behavior was seen at 1.3 m underground level.

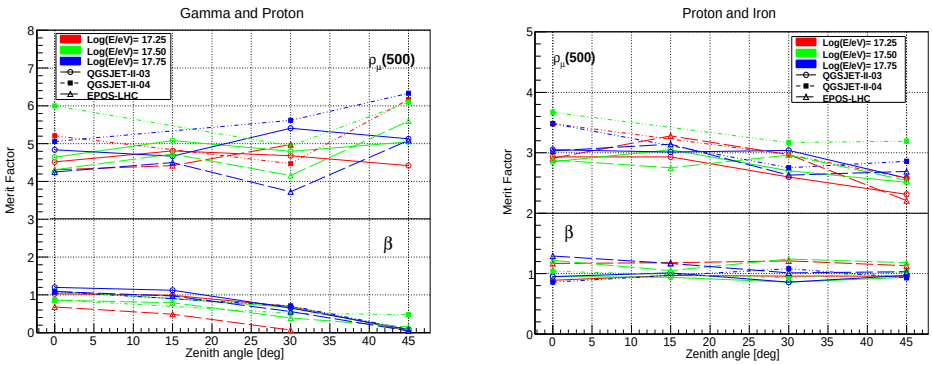


Figure 3. Merit factor of the $\rho_\mu(500)$ and $\beta$ parameter at 2.5 m underground level as function of primary energy and zenith angle. *Left:* For Gamma and Proton. *Right:* For Proton and Iron.

## 7. Conclusions

In this work we performed a study of the merit factor of $\beta$ and $\rho_\mu(500)$ parameters obtained from MLDFs. We used proton, iron and gammas as primary cosmic ray, three hadronic models and different ground levels. The muons propagation through of soil was performed using an approximation which only took into account the continual energy loss. For energies and zenith angles studied, the $\beta$ parameter has a merit factor $\leq 1$, and therefore it is not a good mass discriminator, while the $\rho_\mu(500)$ parameter has a merit factor $> 2$ (if Poissonian fluctuations are not taken into account). In each case, the merit factor does not show a significant difference with the three hadronic models considered.

## References

[1] Letessier-Selvon, A. & Stanev, T. 2011, Rev. Mod. Phys., 83, 907

[2] Supanitsky, A. D. et al. 2008, Astropart. Phys., 29, 461

[3] Sciutto, S., "AIRES user's Manual", http://www.fisica.unlp.edu.ar/auger/aires.

[4] Ostapchenko, S. 2011, Physical Review D, 83, 014018

[5] Heck, D. et al. 1998, "CORSIKA: a Monte Carlo Code to Simulate Extensive Air Showers", FZKA, 6019

[6] Pierog, T. et al. 2013, arXiv:1306.0121 [hep-ph]

[7] KASCADE-Grande Collab. 2005, Proc. $29^{th}$ ICRC, 6, 301

*Gravitation, Relativistic Astrophysics and Cosmology*
*Second Argentinian-Brazilian Meeting, 2014*
*G. S. Vila, F. L. Vieyro and J. Fabris, eds.*

# Inflation in inhomogeneous spacetimes: bubble evolution

Florencia A. Teppa Pannia[1,2] and Santiago E. Perez Bergliaffa[3]

[1]*Instituto Argentino de Radioastronomía (CCT La Plata, CONICET), C.C.5, (1894) Villa Elisa, Buenos Aires, Argentina*
[2]*Facultad de Ciencias Astronómicas y Geofísicas (UNLP), Paseo del Bosque S/N, B1900FWA La Plata, Argentina*
[3]*Departamento de Física Teórica, Instituto de Física, Universidade do Estado de Rio de Janeiro, Brazil*

**Abstract.** The evolution of a vacuum bubble embedded in an inhomogeneous spacetime is relevant for the modelling of inflation in the presence of inhomogeneities. We developed a numerical scheme based on Israel's matching conditions to solve the evolution of the bubble for spherically symmetric inhomogeneous backgrounds. Particular attention is paid to spacetimes with perfect fluid with non-zero pressure as a source, which are described by Lemaître solution of Einstein's equations. As a previous step that serves as a check of the numerical scheme, we present here the case of a bubble evolving in a FLRW metric with radiation as a source.

## 1. Motivations

Although inflation is specifically designed to solve some of the problems of the standard cosmological model, it is not free of its own problems. Among these, perhaps the most relevant ones are those related to the beginning of inflation in the presence of inhomogeneities, and the evolution of an inflating region in an inhomogeneous ambient. Regarding the first problem, numerical (Goldwirth & Piran, 1989) and analytical (Perez & Pinto Neto, 2011) studies show that spacetime has to be homogeneous and isotropic to a high degree for inflation to start. Regarding the second problem, an inflating region may stop inflating in particular ambient spacetimes, as discussed in (Fischler et al., 2009; Rakic et al., 2009) for the FLRW and LTB cases.

The question of whether an inflating region can continue to inflate if the ambient region is inhomogeneous has been explored by several authors for different backgrounds (Goldwirth & Piran, 1989; Fischler et al., 2009; Rakic et al., 2009). In all these cases, the inflating region was modelled by a vacuum bubble, separated from the exterior by a thin wall. The results show that the presence of matter slows down (and may even stop) the expansion of the bubble. An inhomogeneous outer spacetime was only studied for spherically symmetric dust (Fischler et al., 2009; Rakic et al., 2009), which is a first step aiming at a more realistic description in terms of ultrarelativistic matter. We intend here to undertake this latter task.

## 2. General framework

A propagating bubble divides the space-time into three regions:

1. The inner region, which is described by a de Sitter spacetime in the case at hand.

2. The bubble, which is assumed to be a thin-shell, with a perfect fluid energy-momentum tensor with an equation of state (EoS) given by $P = w\sigma$. It is described by the hypersurface $\Sigma$ with geometry

$$ds^2|_\Sigma = d\tau^2 - \rho^2(\tau)d\Omega^2. \tag{1}$$

3. The background, which will be assumed to be spherically symmetric and filled with a perfect fluid with non-zero pressure ($T_{\mu\nu} = (\epsilon + p)u_\mu u_\nu - p g_{\mu\nu}$). This back is described by Lemaître's solution of Einstein's equations, which in comoving coordinates takes the form

$$ds^2 = e^{A(t,r)}dt^2 - e^{B(t,r)}dr^2 - R(t,r)^2 d\Omega^2. \tag{2}$$

Einstein's equations for this geometry are given by

$$\kappa R^2 R_{,r}\epsilon = 2M_{,r} \tag{3}$$
$$\kappa R^2 R_{,t} p = -2M_{,t}, \tag{4}$$

where $M(t,r)$ is defined by

$$2M = R + Re^{-A}R_{,t}^2 - e^{-B}R_{,r}^2 R - \Lambda R^3/3. \tag{5}$$

Using the conservation of $T_{\mu\nu}$, we obtain

$$A_{,r} = -2p_{,r}/(\epsilon + p) \tag{6}$$
$$e^B = \frac{R_{,r}^2}{1+2E}\exp\left(\int_{t_0}^{t}\frac{2R_{,t}}{[\epsilon+p]R_{,r}}p_{,r}d\tilde{t}\right), \tag{7}$$

where $E(r)$ is an arbitrary function related to the local curvature (Bolejko et al. 2006). Note that in the case of dust, the above equations reproduce the LTB model, where $e^A = 1$ and $e^B = R_{,r}^2/(1+2E)$. The FLRW limit is obtained when $R(t,r) \to a(t)r$, $M \to M_0 r^3$ and $E \to E_0 r^2$.

## 3. Numerical scheme

In order to describe the evolution of the bubble we use the general thin-wall formalism based on the Israel's junction conditions (Israel, 1966; Berezin & Kuzmin, 1987; Visser, 1996). They relate the discontinuity in the extrinsic curvature to the energy-momentum tensor of the bubble across the hypersurface $\Sigma$ which separates two given spacetimes. The outer coordinates are related to the comoving time of the bubble by $d\tau^2 = e^A dt^2 - e^B dr^2$. Since the coordinates $r$ and $t$ are both functions of $\tau$ on the shell, the evolution of the radius of the bubble $\rho(\tau)$ can be parameterized by the function $\tilde{r} = r(t)|_{shell}$, with $\rho(\tau) = R(t, \tilde{r}(t))$.

The equations that govern the evolution of the radius and the density of the bubble are

$$\left(\frac{d\tilde{r}}{dt}\right)^2 (R_{,\tilde{r}^2} + e^B(R^2C^2 - 1)) + 2R_{,t}R_{,\tilde{r}}\left(\frac{d\tilde{r}}{dt}\right) + R_{,t}^2 - e^B(R^2C^2 - 1) = 0, \tag{8}$$

$$\frac{\mathrm{d}\sigma}{\mathrm{d}t} + \frac{2R_{,t}}{R}\sigma(1+w) - \left[e^{A/2}e^{B/2}(\epsilon+3p)\left(\frac{\mathrm{d}\tilde{r}}{\mathrm{d}t}\right)\right] \Big/ \sqrt{e^{A} - e^{B}(\mathrm{d}\tilde{r}/\mathrm{d}t)^2} = 0, \qquad (9)$$

where

$$C^2 = \frac{\Lambda_{in}}{3} + \left[\frac{\sigma}{4} + \frac{1}{\sigma}\left(\frac{\Lambda_{out} - \Lambda_{in}}{3} + \frac{2M}{R^3}\right)\right]^2 .$$

These expressions depend on the background geometry and are general in the sense that they can be used for FLRW, LTB or Lemaître backgrounds by calculating the corresponding metric functions $A$ and $B$, and using a proper EoS for the perfect fluid on the shell.

The evolution of a bubble of vacuum on a background with a non-zero pressure fluid and non-zero $\Lambda$ will substantially depend on the pressure balance and on the relation of the surface tension to the difference in inner and outer $\Lambda$, and dust density (Rakic et al., 2009). This can be seen from the equation for the acceleration of the radius of an initially comoving bubble, which in the FLRW case is given by

$$\ddot{r}|_{\dot{r}=0} = \frac{1}{a}\left(\frac{\Lambda_{out} - \Lambda_{in}}{24\pi\sigma} - 2\pi\sigma - \frac{2\rho + \alpha p}{3\sigma}\right), \qquad (10)$$

where $\alpha$ is a numerical coefficient. It follows from this equation that both the density and the pressure of the external fluid tend to slow down the expansion of the bubble.

## 4. Results and discussion

We obtained a system of ordinary differential equations which determines the evolution of the shell based in the Israel's junction conditions. These general expressions allow us to analyze several combinations of background metrics and/or matter content, and different EoS for the matter on the shell.

A numerical scheme was developed to solve the problem for different choices of the initial conditions and the parameters which describe the shell and the background. The goal of the analysis is to determine if the outer non-zero pressure fluid can slow down the bubble and eventually stop the inflation of the vacuum region in inhomogeneous backgrounds. We will also investigate if the external inhomogeneities leave any traces in the region contained in the bubble.

The case of an homogeneous background with radiation fluid as a source is presented as an example. The outer FLRW metric is described by $\Lambda = 3 \times 10^{-5}$, curvature function $E(r) = -kr^2$ with $k = 4 \times 10^{-6}$, $\rho_{rad} = A/a^4(t)$ with $A = 1 \times 10^{-3}$, and the initial condition $a_0 = 1$. The evolution of the radius of the bubble for several initial sizes and different choices of the EoS is shown in Fig. 1. As a test for our code, and for comparison with the radiation case, the curves for the dust case presented in Fischler et al. (2009) are also displayed in the Figure. The plots show that the evolution of the bubble when pure radiation is considered is qualitatively the same as in the case of pure dust.

We are presently exploring the evolution of the bubble for different curvature profiles for inhomogeneous backgrounds described by the Lemaître metric (i.e. spherically symmetry and non-zero pressure perfect fluid as a source). We are also deducing a theoretical expresion for the acceleration of the bubble, that will generalize Eq. (10) in order to gain insight on the role of the density and pressure in the evolution equations.

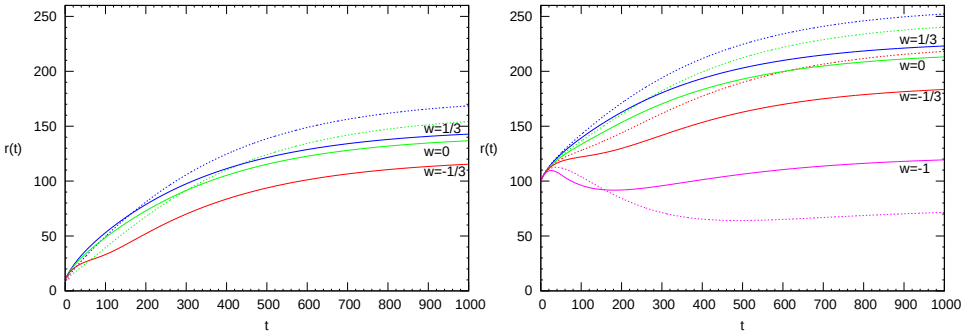


Figure 1. A closed FLRW background with perfect fluid as a source that will eventually asymptote to a de Sitter spacetime is considered. Solid and dashed lines indicate, respectively, the pure radiation and the pure dust cases. The two panels show the evolution for different initial radius of the bubble ($\tilde{r}_0 = 10, 100$, respectively). The initial density of the shell is $\sigma_0 = 1 \times 10^{-3}$ and several values of the parameter $w$ of the EoS are considered. Qualitatively, the asymptotic behaviour of the comoving bubble coordinate $\tilde{r}(t)$ does not depend on the initial conditions or on the EoS of the bubble.

**Acknowledgments.** FATP acknowledges support from CONICET. SEPB would like to acknowledge support from FAPERJ and UERJ.

## References

Berezin, V. A. & Kuzmin, V. A. 1987, PRD, 36, 2919-2944

Bolejko, K. et al. 2010, "Structures in the Universe by Exact Methods: Formation, Evolution, Interactions", Cambridge University Press

Fischler, W. et al. 2009, JHEP05, 041

Goldwirth, D. S. & Piran, T. 1989, PRD, 40, 3263-3279

Israel, W. 1966, Nuovo Cim., B44S10

Perez, R. S. & Pinto Neto, N. 2011, Grav. & Cosm., 17, 136-140

Rakic, A. et al. 2009, PoS (Cosmology)

Visser, M. 1996, "Lorentzian Wormholes: From Einstein to Hawking", Chapter 15

*Gravitation, Relativistic Astrophysics and Cosmology*
*Second Argentinian-Brazilian Meeting, 2014*
*G. S. Vila, F. L. Vieyro and J. Fabris, eds.*

# Exploring cosmic rays ionization power

Matias Tueros,[1] Ma. Victoria del Valle,[1] and Gustavo E. Romero[1,2]

[1]*Instituto Argentino de Radioastronomía, C.C.5, (1894) Villa Elisa, Buenos Aires, Argentina*
[2]*Facultad de Ciencias Astronómicas y Geofísicas, Universidad Nacional de La Plata, Paseo del Bosque S/N, (1900) La Plata, Argentina*

**Abstract.** After the so-called cosmic recombination the expanding universe entered into a period of darkness, since most of the matter was in a neutral state. However, about a billion years later the intergalactic space was once again ionized. The process, known as the cosmic reionization, required the operation of mechanisms that are not well understood. Among other ionizing sources, Population III stars, mini-quasars, and X-ray emitting microquasars have been invoked. All these models relay on the ionizing power of photons. But what about charged particles?. In this contribution we quantify the ionization power of cosmic rays (electrons and protons) in the primordial intergalactic medium.

## 1. Introduction

Around 380000 yr after the Big Bang, the combination of protons and electrons formed neutral gas allowing the radiation to decouple from matter. The universe entered then in a “dark age", that lasted up to about a billion years (e.g., Ellis, Maartens & MacCallum 2012). How the universe was reionized is a major topic in current cosmology. The formation of the first stars of zero metallicity, at redshift $z \sim 20$, resulted in the injection of a large number of ultraviolet (UV) photons (e.g., Loeb 2010). However, it seems difficult for these photons to interact with neutral gas at large distances from the stars, given the high-column densities of the primordial star-forming clouds. Recently, Mirabel et al. (2011) have proposed that X-rays from accreting black holes in early binary systems might have played a crucial role, because of the longer mean free path with respect to the UV radiation.

The first generations of microquasars should have not only produced copious X-rays, but also relativistic particles through their jets. Moreover, unlike the X-rays from the disk that are injected in the vicinity of the star, the jets can propagate hundreds of parsecs and escape the original cloud where the star formation took place. Once the jets were in what would become into the intergalactic medium, the termination shocks can re-accelerate protons and electrons up to relativistic energies. Then, these particles would diffuse, ionizing the medium they encountered. In this contribution we offer a quantitative estimate of the ionizing power of these particles as they diffused through the early universe.

In the next section we describe the simulations of cosmic ray (CR) propagation in the early universe. Then, in Section 3 we discuss the obtained results. We close with implications of our results in Section 4.

## 2. Simulations

In order to estimate the ionization power of electrons and protons injected directly into the intergalactic medium (IGM) we have used a heavily modified version of the AIRES code (see AIRES Manual). AIRES is a particle cascade simulation suite originally designed to simulate particle cascades initiated by CRs on Earth's atmosphere. We have modified AIRES propagation routines to simulate the conditions of the primigineous IGM. We have added a redshift-dependent monochromatic photon field to simulate the cosmic microwave background (CMB) and a material medium of hydrogen atoms with redshift-dependent number density. We added inverse Compton scattering and $e^{\pm}$ photo-pair production for electrons, positrons and photons. Neutron decays have been also included.

When a particle cascade develops, most of the ionization in the traversed medium is produced by low energy particles, especially electrons and photons in and below the keV energy range. Unfortunately, the full simulation of all processes leading to particles in and below the keV range would require humongous amounts of CPU time. To circumvent this problem, the generation of particles below a certain threshold (100 keV for electrons and photons, and 500 keV for other particles) has not been directly simulated. Instead, the generation of low energy particles is represented by an averaged energy loss per amount of traversed matter, that has been subtracted from all charged particles during their propagation.

As low energy particles lose most of their energy through ionization, the subtracted energy has been considered to be ultimately deposited in the traversed medium through ionization. The number of ions that would have been generated by these low energy particles can then be estimated using the mean energy loss per ionization event $I_{\rm H}$. We take $I_{\rm H}$ to be $\approx 36$ eV, considering that 10.2 eV goes to ionize the atom and $\approx 25.8$ eV corresponds to the average kinetic energy of the outgoing electron, of which 22.3 eV are lost in exitations of atomic levels and 3.4 eV in heating of the gas (Spitzer & Tomasko 1968).

To further speed up the simulations, we have discarded particles that fell below the low energy threshold during their propagation. The energy carried away by these particles has also been considered to be ultimately deposited in the medium through ionization.

The IGM has a redshift dependence. We have adopted a density of the primordial IGM of $n_{\rm H} = 2.5 \times 10^{-30}(1+z)^3$ g cm$^{-3}$ (e.g., Ellis et al. 2012). The CMB has been considered monoenergetic with photon energy $E_{\rm CMB} = 3.75 \times 10^{-4}(1+z)$ eV, and a photon density $u_{\rm CMB} = 0.05\,(1+z)^3$ cm$^{-3}$. For the magnetic field of the IGM we have taken the value $B = 10^{-17}$ G (e.g., Stacy & Bromm 2007; Loeb 2010; Bromm 2013). The model we have used for the evolution of the universe is that of the standard spatially-flat six-parameter $\Lambda$CDM cosmology, with a Hubble constant $H_0 = 67.3 \pm 1.2$ km s$^{-1}$ Mpc$^{-1}$ and a matter density parameter $\Omega_{\rm m} = 0.315 \pm 0.017$, in accordance with latest results from the Planck Collaboration (2014).

Under these assumptions, simulations of electrons in the 1 MeV - 100 TeV and protons in the 1 GeV - 100 TeV energy range have been generated. Particles start at redshift $z = 19$ and they are propagated through the IGM until they reach $z = 5$, the epoch at which the reionization is considered to be complete (Loeb 2010). During this lapse, particles traverse up to $\sim 3.1$ g cm$^{-2}$ of matter.

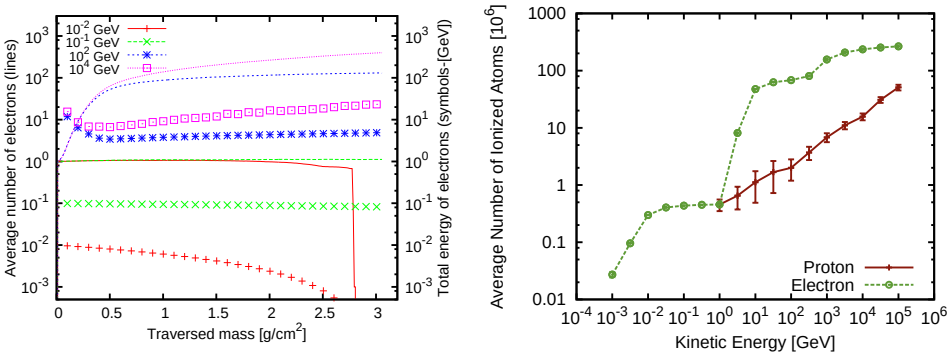


Figure 1. (left) Average longitudinal development of electrons and (right) total ionization power of particles injected in the IGM at redshift $z = 19$ and propagated through redshift $z = 5$

## 3. Results

Our simulations for electrons primaries show that below the energy threshold for interactions with the CMB, - roughly 1 GeV - no particle cascades are produced. An example of the average longitudinal development of 10 MeV electrons is shown in Figure 1 (left). At these energies, electrons propagate loosing their energy mainly by ionization of the hydrogen atoms they encounter on their path.

Electrons below 10 MeV loose all their energy in the IGM before the reionization epoch ends, producing a number of ionizations (i.e. an ionization power) proportional to their initial energy. This is evidenced as a unitary slope in the low energy end of Fig. 1 (right).

Above 10 MeV, electrons survive the reionization epoch, as can be seen on the average longitudinal profile for 100 MeV electrons shown in Fig. 1 (left). This gives a plateau in the ionization power for electrons between 10 MeV and 1 GeV seen in Fig. 1 (right). The energy deposited through ionization by a single particle for a fixed amount of traversed matter has little dependency on its energy.

Once the energy of the primary electrons reach the threshold of inverse Compton with the CMB, particle cascades start being generated. The number of particles quickly rises and so does the total energy lost through ionization. At some point these particles start having enough energy to survive the reionization epoch. This gives the second plateau in Fig. 1 (right).

A second sudden but smaller rise in the ionizing power is produced when secondaries also reach the CMB interaction threshold, triggering more cascades. An example of this type of cascades is given in Fig. 1 (left) for 10 TeV electrons, where it can be seen that the number of electrons and the energy they carry continues to rise, in contrast with the 100 GeV case.

For proton primaries we started our calculations at 1 GeV. At these energies protons have a big variability in their ionization power as the 3.1 g cm$^{-2}$ of traversed matter is well below the mean free path of $p - p$ interactions. Protons that do not interact survive the reionization epoch and deposit very little energy, giving a small ionization power. Protons that do interact generate pions that promptly decay into muons, electrons and

photons that in turn generate cascades that do have a big ionization power. This yields a big variability in the ionization power of protons, specially at low energies, and a slope lower than 1 in the ionization power as can be seen in Fig. 1 (right).

## 4. Conclusions

Only low energy lectrons have a ionization power per unit energy comparable with UV or X-Ray photons, i.e. in the order of 20 ionizations per keV. However, microquasar jets inject particles with a power law spectrum making low energy particles dominate the microquasar total ionizing power. Furthermore, these particles would be injected directly into the IGM, bringing directly where UV photons cannot reach. The contribution from protons would be a hundred times lower, but their bigger gyroradius make them diffuse faster and deeper into the IGM.

**Acknowledgments.** We thank Alejandra Kandus for insightful discussions on primordial magnetic fields. This work was supported by PICT 2012-00878, Préstamo BID (ANPCyT) and grant AYA 2013-47337-C3-1-P (MINECO, Spain).

## References

AIRES Manual, Sciutto, S., *www2.fisica.unlp.edu.ar/auger/aires*

Alvarez, M. A., Busha, M., Abel, T. & Wechsler, R. H. 2009, ApJ, 703, L167

Bromm, V. 2013, Rep. Progr. Phys., 76, 112901

Ellis G., Maartens, R. & MacCallum, M. 2012, "Relativistic Cosmology", Cambridge University Press, Cambridge

Spitzer, L. & Tomasko, M., 1968, ApJ, 152, 971

Loeb, A. 2010, "How Did the First Stars and Galaxies Form?", Princeton University Press, Princeton

Madau, P., Rees, M. J., Volonteri, M., Haardt, F. & Oh, S. P. 2004, ApJ, 604, 484

Mirabel, I. F., Dijkstra, M., Laurent, P., Loeb, A. & Pritchard, J. R. 2011, A& A 528, A149

Planck Collaboration 2014. arXiv:1303.5076

Stacy, A. & Bromm, V. 2007, MNRAS, 382, 229

# List of Authors